OPEN ACCESS

University of BRISTOL

This electronic thesis or dissertation has been downloaded from Explore Bristol Research, http://research-information.bristol.ac.uk

Author:
Diteesawat, Richard Suphapol

Title:
Development of Soft Artificial Muscles towards a Smart Assistive Suit

General rights
Access to the thesis is subject to the Creative Commons Attribution - NonCommercial-No Derivatives 4.0 International Public License. A copy of this may be found at https://creativecommons.org/licenses/by-nc-nd/4.0/legalcode This license sets out your rights and the restrictions that apply to your access to the thesis so it is important you read this before proceeding.

Take down policy
Some pages of this thesis may have been removed for copyright restrictions prior to having it been deposited in Explore Bristol Research. However, if you have discovered material within the thesis that you consider to be unlawful e.g. breaches of copyright (either yours or that of a third party) or any other law, including but not limited to those relating to patent, trademark, confidentiality, data protection, obscenity, defamation, libel, then please contact collections-metadata@bristol.ac.uk and include the following information in your message:

• Your contact details
• Bibliographic details for the item, including a URL
• An outline nature of the complaint

Your claim will be investigated and, where appropriate, the item in question will be removed from public view as soon as possible.

Development of Soft Artificial Muscles towards a Smart Assistive Suit

By

Richard Suphapol Diteesawat

Department of Aerospace Engineering
University of Bristol
Department of Engineering Design and Mathematics
University of the West of England

A dissertation submitted to the University of Bristol in accordance with the requirements for award of the degree of Doctor of Philosophy in the Faculty of Engineering.
June 2020.

Word count: Fifty-eight Thousand Six Hundred and Ninety-two

Abstract

Impaired mobility is one of the major issues in human life, affecting and limiting independent living, especially for older adults. Although many conventional rigid exoskeletons and soft orthoses have been developed to strengthen the human body for workers, and improve the mobility of people with disabilities, there remain many challenges to overcome before we can create an assistive suit for healthy elderly individuals. Advanced wearable assistive devices should have light weight, low cost, high flexibility, and high adaptability. This will enable them to fit the user's body while remaining inconspicuous (possibly being embedded with standard clothing), and also provide sufficient mechanical power to maintain effective and safe assistance to the body. To achieve these required features, this thesis describes the study and development of novel artificial muscles based on two potentially disruptive technologies: pneumatically-driven and electrically-driven soft actuators.

First, a lightweight, flexible, inexpensive pneumatic actuator, namely Bubble Artificial Muscle (BAM), was developed. BAMs are capable of generating either high contraction or high tensile force, by adjusting their material properties. This provides BAMs with high flexibility, allowing them to be designed to suit the various capabilities of human muscles. An actuation model was developed to predict the real-world performance of BAMs, and a design methodology to maximise BAM performance metrics is presented. A mobility assistance demonstrator was built to investigate how an effective orthosis can theoretically reduce muscle work of a user while walking. BAMs were used to create soft orthoses to assist two human locomotion movements:. walking and sit-to-stand transition, providing support forces and assisting the lower limb's motions. However, since the BAM is pneumatically driven, it has a major drawback due to its associated air power source, e.g. a large, heavy, noisy pump or compressor for actuation. This limits the portability and fast actuation response of a BAM-driven orthotic. To address this limitation, electrically-driven actuators were investigated.

The electro-ribbon actuator (ERA) is an electrostatic zipping actuator, which exhibits high stress and contraction, along with fast actuation speed and low power consumption. This actuator was studied to overcome the disadvantages associated with pneumatic actuators. In this research, an effective control algorithm was developed to improve the controllable actuation range of the ERA. Alternative materials and fabrication methods were also explored, resulting in a new version of the ERA with wider designs and

applications, including three-dimensional motion. The ERA was developed further by fully encapsulating the zipping mechanism, leading to a novel lightweight, soft pneumatic pump, the Electro-pneumatic Pump (EPP). The EPP is capable of exerting air pressure and pumping its internal air volume to a connecting device. EPPs allow for high-flow-rate continuous pumping while being portable and controllable, and showing low power consumption. Combining the EPP and the BAM together results in an entirely soft pneumatic actuation system, which can deliver high contraction and mechanical work as a wearable device for assisting human body movement. This new electropneumatic system fulfils the ultimate research outcome and has high potential as a future robotic device and artificial muscle, paving the way for the creation of a smart assistive suit that will restore the independence of older adults and people living with disabilities.

Acknowledgement

I would like to take this opportunity to express my gratitude to everyone who advised and supported me in completing this research study. It would not have been possible without their assistance and guidance.

I would like to express my deepest appreciation to my supervisors, Prof Jonathan Rossiter, Dr Tim Helps and Dr Majid Taghavi, for their supervision, inspiration, and expertise, which helped me to accomplish the goal of this research. A special thanks to the technicians at Bristol Robotics Laboratory (BRL), University of Bristol and Unversity of the West of England who advised, helped and provided me with invaluable experience improving my mechanical skills and offered me the use of the laboratory facilities.

A very warm thanks to my cohorts and colleagues from the FARSCOPE program and the Soft Robotics group at BRL for wonderful time, sharing of knowledge and joy, and encouragement throughout this research. Last, I would like to thank my family for their continued understanding, motivation and support.

This research was supported by the Engineering and Physical Sciences Research Council (EPSRC) through the EPSRC Centre for Doctoral Training in Future Autonomous and Robotic Systems (FARSCOPE), grants EP/M026388/1 (Wearable Soft Robotics for Independent Living) and EP/S026096/1 (FREEHAB: accessible, comfortable and adaptable wearable rehabilitation and assist devices), and Royal Society Grant (TA\R1\170060).

Author's Declaration

I declare that the work in this dissertation was carried out in accordance with the requirements of the University's *Regulations and Code of Practice for Research Degree Programmes* and that it has not been submitted for any other academic award. Except where indicated by specific reference in the text, the work is the candidate's own work. Work done in collaboration with, or with the assistance of, others, is indicated as such. Any views expressed in the dissertation are those of the author.

SIGNED: _____ DATE: _____

Contents

List of Figures

List of Tables

List of Symbols

a	elasticity of the actuator's membrane
A	cross-sectional area
$\alpha, \theta, \beta, \gamma$	generic symbols for angle
c, C	contraction
$c_{optimal}$	optimal contraction of the BAM
C_i	initial contraction of the EPP
C_a	actuated contraction of the EPP at applied voltage V
ΔC	contraction change of the EPP
e	input error of the ERA's controller
E	Young's modulus
$\mathrm{E}(\varphi/m)$	elliptic integral function of the second kind
$\mathrm{F}(\varphi/m)$	elliptic integral function of the first kind
F, F_t	tensile force
φ, φ_R	dominant parameter referring to angle of the PPAM's actuator membrane
g	acceleration of gravity
h	height of the ERA
I	moment of inertia
K_p, K_i, K_d	proportional, integral and derivative terms used in the PID controller of the ERA
l, L	length
l_i, L_i	initial length
l_a, L_a	actuated length
L_{actual}	actual actuator length of the PPAM
$L_{actuator}$	initial actuator length of the BAM
L_{bubble}	inflated unit length of the BAM at maximum shape expansion
L_{fold}	length of folded membrane of the BAM from an actuator end
$L_{inactive}$	length of an inactive region in the BAM
$L_{optimal}$	optimal unit length of a single contractile-unit BAM
L_{unit}	initial unit length of a single contractile-unit BAM
ΔL	actuator stroke

m	dominant parameter defining shape of the PPAM
m	load mass
P	pressure
P_i	initial pressure of the EPP
$P_a(V)$	actuated pressure of the EPP at applied voltage V
ΔP	pressure change of the EPP
r, R	radius
r_i	membrane radius from the axial line of the PPAM at given contraction
r_{max}	maximum actuator radius
R_{bubble}	inflated unit radius of the BAM at maximum shape expansion
$R_{material}$	material radius of retaining rings used to fabricate BAMs
$R_{optimal}$	optimal ring radius of a single contractile-unit BAM
R_{ring}	ring radius of a single contractile-unit BAM
ε	strain (in pneumatic actuators)
ε	dielectric constant (in electrostatic actuators)
$s_{material}$	material thickness
SR	slenderness ratio
t	time
T	torque
x_i	axial distance from the actuator centre of the PPAM at given contraction
V	applied voltage
$V_{pull-in}$	pull-in voltage when the ERA starts zipping
V_c	constant voltage used as an additional term in the PID controller of the ERA
v	volume
v_{in}	injected air volume of an atmosphere air at room temperature
W	weight (force of gravity) of the mass

List of Abbreviations

BM	body mass
BAM	Bubble Artificial Muscle
COG	centre of gravity
COM	centre of mass
DEA	Dielectric Elastomer Actuator
DOF	degree of freedom
EAP	Electroactive Polymer
EMG	Electromyography sensor
ERA	Electro-ribbon Actuator
EPP	Electro-pneumatic Pump
FPBA	foldable pneumatic bending actuator
GC	gait cycle
GLW	ground-level Walking
GRF	ground reaction force
HASEL	Hydraulically Amplified Self-healing Electrostatic actuator
IMU	inertial measurement unit
MEMS	Microelectromechanical systems
PAM	Pneumatic Artificial Muscle
PPAM	Pleated Pneumatic Artificial Muscle
PLA	polylactic acid
PVC	plasticized polyvinyl chloride
ROM	range of motion
SEA	Series Elastic Actuator
sEMG	Surface electromyography sensor
SMA	Shape Memory Alloy
sPAM	series Pneumatic Artificial Muscle
STS	sit-to-stand transition
STW	sit-to-walk movement
TPU	thermoplastic polyurethane
VSA	Variable Stiffness Actuator
WAD	Wearable Assistive Device

Chapter 1

Introduction

Wearable Assistive Devices (WADs) have been developed over decades with the purpose in assisting and improving human mobility [1]. Although existing WADs and conventional exoskeletons can aid patients with mobility disabilities for rehabilitation, and strengthen the human body for industrial and military purposes, they are still not suitable for healthy able-bodied subjects and older adults [2]. A flexible, lightweight, comfortable, effective WAD with adaptability, quiet operation, low cost and safety is required [2,3]. This thesis focuses on developing novel artificial muscles for mobility assistance, and addressing the ongoing challenges of WADs. A major outcome of this research is the achievement of innovated lightweight, inexpensive pneumatic and electrostatic artificial muscles, which can perform human body assistance such as walking motion, sit-to-stand transition, and arm movement. This shows their potential for use in a smart assistive suit in the future. Development, characteristic analysis and performance evaluation of these new artificial muscles and their demonstrations as assistive devices are presented in this thesis.

1.1 Motivation

The number of older adults has been increasing, and they have become a majority in the global population [4]. Getting older results in body impairments and muscle weaknesses, reducing capabilities to perform daily activities [5]. Mobility degeneration is one of the most serious problems faced by people, causing disabilities as they reach middle age and beyond. Without appropriate healthcare and regular physical exercise, older adults may face difficulties to maintain quality of life [6]. Lower-body degeneration does not only affect and limit independent living of elderly and disabled people, but also impacts their family, physical therapists and caregivers.

From past to present, many exoskeletons and orthoses were invented in order to strengthen the human body and address mobility limitations. These assistive devices were characterised into two main groups: performance-augmenting exoskeletons for en-

hancing body strength and active orthoses for assisting individuals with disabilities due to severe mobility disorders such as spinal cord injuries and stroke [7]. The former exoskeletons were developed for healthy people to perform more effective locomotion such as the RoboKnee [8] or to handle heavy tasks and be capable of load carriage in industrial and military applications with low fatigue, for example, BLEEX [9]. On the other hand, the latter exoskeletons were built for rehabilitative purposes [10–12]. One example is ReWalk, a commercial wearable assistive product, which was designed to enable disabled and paralysed patients to be able to walk again [13]. Generally, these exoskeletons and orthoses are composed of rigid elements, which allow them to fully support and power the entire body to achieve the desired tasks. However, there are remaining challenges in regard to weight, portability, effective autonomous control, user interface, resistance of natural movements and joint misalignment which can cause injuries and safety problems [7,14,15].

Soft robotics has the potential to overcome the limitations of the conventional rigid robots due to its typical low mass, inherent compliance and flexibility to interact with human body safely [16]. Soft Wearable Assistive Devices (WADs) have been developed towards a flexible power suit with the concept of providing an extra power for either normal or older adults in order to perform more effective movement and attain daily activities with more comfort and less fatigue. For example, Exosuits developed at Harvard University [14, 15, 17] were one of the early soft WADs that could partially assist an able-bodied wearer. In addition, several soft orthoses were invented by using pneumatic artificial muscles as an actuator to assist movement of human body [18,19]. Nevertheless, current WADs still lack flexibility and adaptability for safe interaction, and may be obtrusive drawing unwanted attention to users. The future smart assistive device must be easily embedded in normal clothing [2]. Moreover, sensing and control systems require further development for reliability in body assistance without any harm.

This thesis focuses on developing artificial muscles which can partially aid individual subjects to perform human movement activities, such as walking, sitting and standing, while solving remaining challenges of WADs. Studying the anatomy of human body and its fundamental biomechanics in locomotion will help understanding the requirements of the desired assistive device. Comparing performance and suitability of existing soft actuators and exploring alternative materials and designs will result in the creation of new soft artificial muscles, toward the development of the future smart assistive suit.

1.2 Research Questions

The ultimate goal of this thesis is to innovate novel artificial muscles for creating a smart assistive suit, which can autonomously assist people to perform better locomotion, and maintain their independence. The suit is proposed to provide extra power to the human body, which can conserve their muscle energy, to raise their abilities to conduct their work longer and faster, and to ensure that they do not become fatigued easily. Hence, the novel artificial muscles must be able to function similar to the human muscle and perform in the same range of muscle work. They must be lightweight, flexible, comfortable and safe for the user, adaptable, portable, and embeddable within normal clothing to be suitable for creating the ideal WAD. To achieve these requirements, this thesis concentrates on investigating and addressing the following research questions.

- What kind of existing artificial muscles can be developed to achieve the research requirements? What are the advantages of their further developments?
- How can the selected artificial muscles be improved (for example, by exploring alternative materials, designs and fabrication approaches)?
- Which part of lower limbs should be assisted to improve human mobilities, and what is the required motion and force to achieve walking motion and sit-to-stand transition?
- What type of evaluation can be used to assess mobility assistance of the invented artificial muscles, particularly walking motion and sit-to-stand transition?

1.3 Contributions

In addressing the above questions, this thesis makes the following contributions.

- An innovation of a lightweight, inexpensive, effective pneumatic artificial muscle, called Bubble Artificial Muscle (BAM), which can generate either high contraction or tension depending on design and material optimisation to match the desired working range (Chapter 3).
- The mathematical model predicting BAM actuation when constraining actuator's size and materials for practical usage, and the method to design the optimal BAM which always maximises its contraction and tension (Chapter 3).
- Development of Electro-ribbon Actuators (ERAs) by developing their control algorithm increasing their working range and by deploying alternative flexible materials and improved fabrication method, creating several conceptual designs for various applications, enabling three-dimensional motions including contraction, extension and bending (Chapter 5).

- An innovation of Electro-pneumatic Pump (EPP), a flexible electrostatic actuator, developed based on the ERAs, which uses Dielectrophoretic Zipping Liquid (DLZ) to generates pneumatic pressure, inflating a connected pneumatic device and working as a soft pump (Chapter 6).
- Understanding of functions and biomechanics of human lower limbs regarding locomotion and how to assist lower limbs (Chapter 4).
- Concepts and mathematical models of knee flexion/extension assistance for human locomotion (Chapter 4).
- Demonstration of the BAMs in performing walking motion and sit-to-stand transition on human-like mechanisms (chapter 4) and the combined EPP-BAM system, an entire soft pneumatic system, in performing arm flexion with potentials to become a portable WAD (Chapter 6).

1.4 Publications

The following peer-reviewed works have contributed to this thesis.

Journals

- **Diteesawat RS**, Helps T, Taghavi M, Rossiter J. Characteristic Analysis and Design Optimisation of Bubble Artificial Muscles (BAMs). *Soft Robotics* 2020.
- **Diteesawat RS**, Helps T, Taghavi M, Rossiter J. Electro-pneumatic Pumps for Soft Robotics. Submitted to *Science Robotics* in April 2020
- **Diteesawat RS**, Fishman A, Helps T, Taghavi M, Rossiter J. Closed-loop Control of Electro-ribbon Actuators. Submitted to *Frontier in Robotics and AI* under the research topic of "Advances in Modelling and Control of Soft Robot", in April 2020. *Diteesawat RS and Fishman A contributed equally in this work.*
- Chen HY, **Diteesawat RS**, Haynes A, Partridge AJ, Simons MF, Werner E, Garrad M, Rossiter J, Conn AT. *RUBIC: An Untethered Soft Robot With Discrete Path Following.* Frontiers in Robotics and AI. 2019;6:52. *Chen HY, Diteesawat RS, Haynes A, Partridge AJ, Simons MF and Werner E contributed equally and are joint first authors.*

Co-author at conferences

- **Diteesawat RS**, Helps T, Taghavi M, Rossiter J. High strength bubble artificial muscles for walking assistance. *IEEE International Conference on Soft Robotics (RoboSoft)* 24 April 2018 (pp. 388-393).

- Cao C, **Diteesawat RS**, Rossiter J, Conn AT. A Reconfigurable Crawling Robot Driven by Electroactive Artificial Muscle. *2nd IEEE International Conference on Soft Robotics (RoboSoft)* 14 April 2019 (pp. 840-845). *Cao C and Diteesawat RS contributed equally and are joint first authors.*

1.5 Outline of the Thesis

The structure of the thesis is described below, and the overall research outcomes presented in this thesis can be illustrated in fig. 1.1.

- Chapter 2 discusses the effects of ageing on human mobility and muscle strength. Reviews of existing rigid exoskeletons, soft wearable assistive devices and current soft actuators with potential to be used for mobility assistance are included. The concept of the future smart assistive suit is also introduced in this chapter.

- Chapter 3 presents a novel, lightweight pneumatic actuator, namely Bubble Artificial Muscle (BAM). It was developed from existing pneumatic actuators by improving flexibility and performance in generating high contraction and tension. BAM characterisation, the effects of varying its fundamental parameters and its performance compared to existing pneumatic actuators are discussed. A mathematical model predicting BAM actuation was built for real-world applications, and design optimisation was introduced to advise how to build the optimal BAM based on selected material properties.

- Chapter 4 presents biomechanics of human locomotion and human mobility assistance using BAMs. Lower-limb degeneration and comparison of the range of motion (ROM) of lower limbs between a healthy able-bodied subject and researched data of older adults are discussed. The concept of ground-level walking assistance, focusing on the knee, is introduced as well as designs and model analysis of the BAM orthoses and human-like leg mechanisms. Demonstration and evaluation of BAM assistance on ground-level walking and sit-to-stand transition are included.

- The development of Electro-ribbon Actuators (ERAs), an electrostatic zipping actuator, is presented in chapter 5. Closed-loop control of ERAs was developed, increasing their working capabilities and achieving different patterns of controlled contraction. New ERAs were improved by using alternative materials, allowing simpler fabrication and more adaptability while producing similar performance as the original ERAs. Various conceptual designs of the new ERAs are illustrated, enabling three-dimensional motions for wider soft robotic applications.

- According to the development of the BAM and the ERA, chapter 6 introduces Electro-pneumatic Pump (EPP), the first flexible, lightweight, pneumatic pump.

The principal concept, fabrication and characterisation of the EPP and a EPP-BAM system are presented. Capabilities and demonstrators of the EPP for use as an antagonistic mechanism, a wearable robotic device for arm flexion and a continuous-pumping system are included.

- Chapter 7 concludes all works presented in this thesis. Limitations, contributions towards Soft Robotics and wearable assistive devices, future work and how to improve the developed technologies are discussed in this chapter.

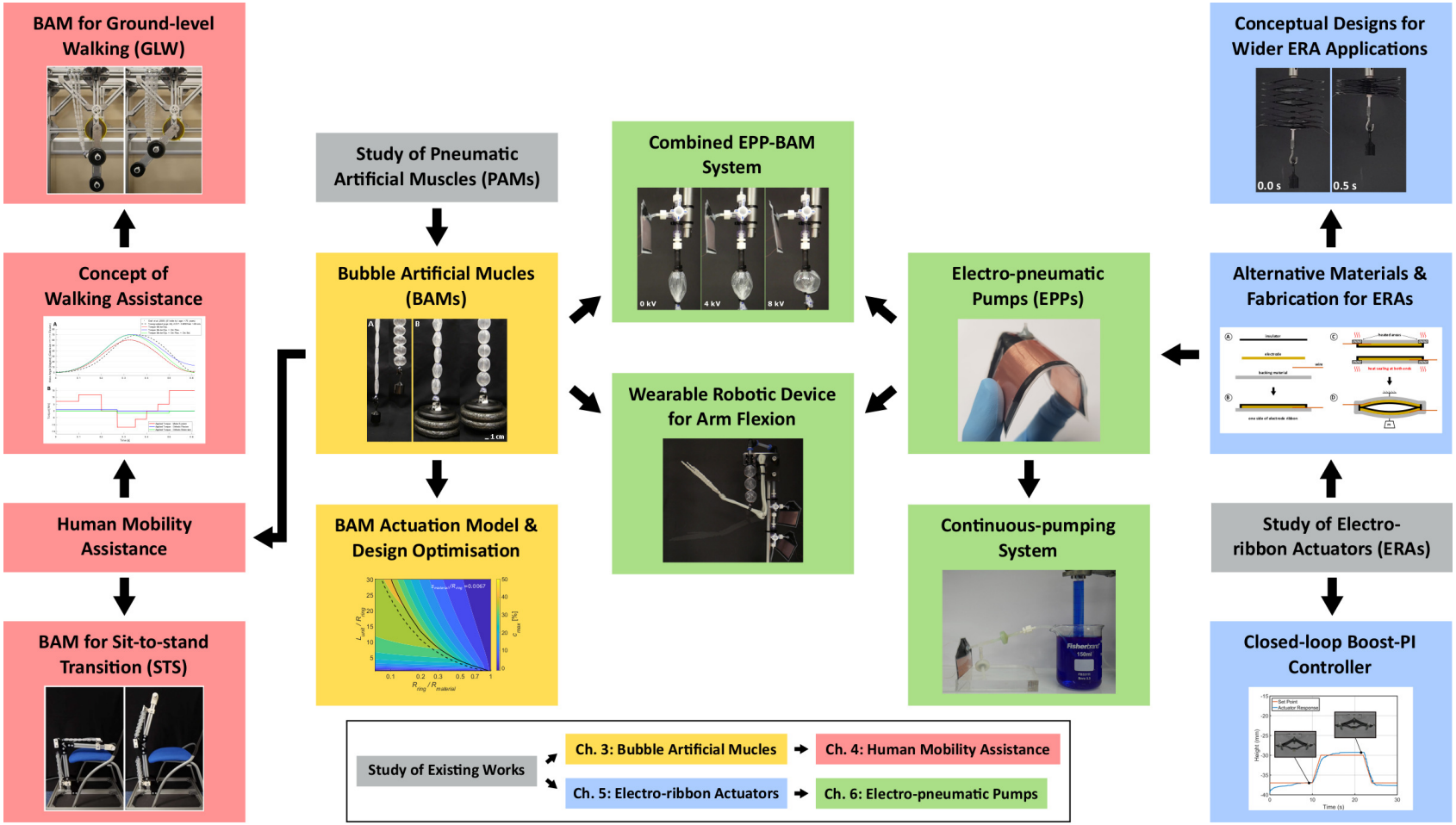

Figure 1.1: Diagram of overall research outcomes. Inset box illustrates the progress of the research contributions, starting from independently studying two potential artificial muscles to create an advanced assistive suit, i.e. pneumatic and electrostatic actuators, (grey boxes) and finally resulting in a novel artificial muscle featuring combined advantages of these two technologies. Colours indicate contributions from different chapters.

Chapter 2

Background

Several exoskeletons have been developed to strengthen human muscles and improve mobility. Healthy older adults prefer a wearable assistive device, which is simple and inconspicuous, but still provide additional power to improve or maintain their locomotion capabilities. A flexible, effective artificial muscle is needed for the development of a smart assistive suit. Understanding muscle weaknesses and biomechanics involving human locomotion will lead to a solution in mobility assistance.

In this chapter, biomechanics of human locomotion and muscle degeneration due to ageing are first introduced. This is followed by the review of conventional exoskeletons and wearable assistive devices, the concept and requirements to create the future smart assistive suit and the progress of current soft actuators. A discussion on selecting the assistance location for the lower limbs, and soft actuators to be developed is included.

2.1 Biomechanics and Terminology of Human Mobilities

This thesis focuses on assisting walking, sitting and standing motions. Therefore, the understanding of biomechanics and terminology using in ground-level walking (GLW) and sit-to-stand transition (STS) are necessary.

Human locomotion occurs with the cooperation of the muscles along a hip, knee and ankle. The movements of these joints in three planes, i.e. sagittal plane, coronal plane and transverse plane, can be illustrated in fig. 2.1. The combination of the movements in sagittal plane leads to walking motion, sit-to-stand transition and other locomotion activities such as stair climbing and running. The knee has only one degree of freedom (DOF) in the sagittal plane, performing knee flexion/extension, while the hip and ankle have 3 DOF in all three planes, which can perform movements in three axes.

2.1.1 Ground-level Walking

A gait cycle (GC) can be simply divided into two major phases: a stance phase and a swing phase (fig. 2.2). The stance phase starts when a heel strikes the ground as an initial

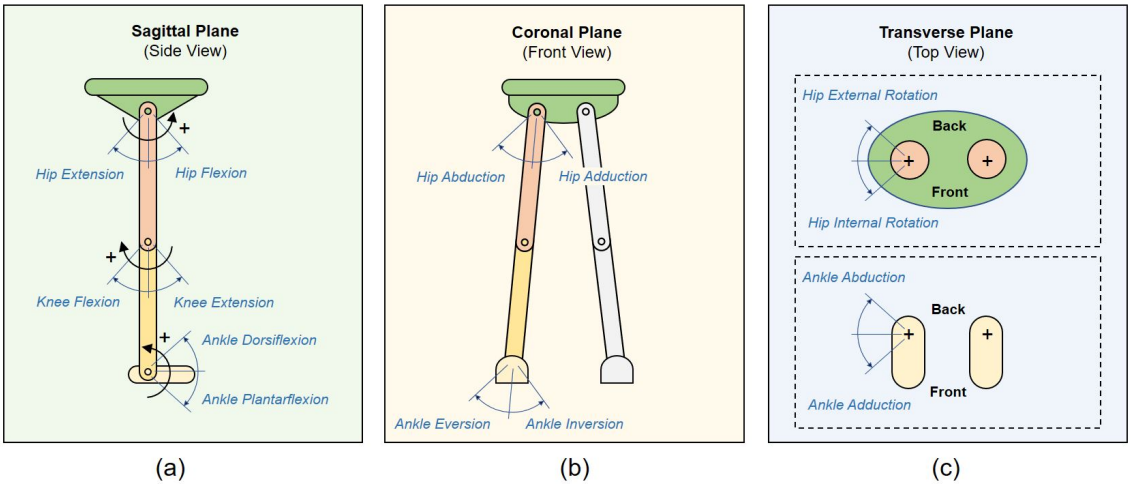

Figure 2.1: The movement of hip, knee and ankle joints in three planes: (a) sagittal plane, (b) coronal plane and (c) transverse plane.

contact at 0% of GC. During this stance phase, the foot maintains on the ground until a toe takes off at approximately 62% of GC, which is the beginning of the swing phase. On the other hand, the swing phase is when the foot is in the air to perform a swing motion. This phase will end when the heel strikes the ground again at 100% (or 0%) of GC. These two phases are responsible for walking motion which requires to achieve three fundamental tasks during a gait cycle: weight acceptance, single limb support and limb advancement. Additionally, the stance phase can be separated into four periods: loading response, mid stance, terminal stance and pre-swing. Swing phase can be divided into three periods: initial swing, mid swing and terminal swing [20].

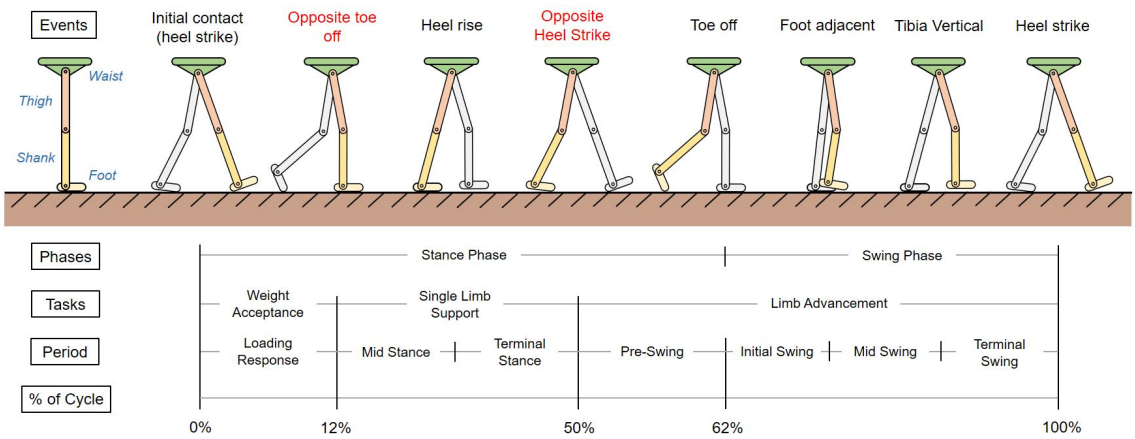

Figure 2.2: A gait cycle of human walking describing events, phases, tasks, periods and percentage of a gait cycle of a colourful leg. Adapted from [7, 20, 21]

step length, *stride length*, *stride time*, *cycle time* and *cadence* are gait terms used to calculate *walking speed* [20]. *step length* is the distance travelled by each foot in the forward direction within one step, for example, left *step length* and right *step length*. *stride length* is the distance travelled by the feet for the entire gait cycle: the sum of left and right

step lengths. *stride time* or *cycle time* is the time of the whole gait cycle, whereas *cadence* is the number of steps the walker can perform within one minute. Accordingly, *walking speed* can be derived from the following equations:

$$walking\ speed\ [cm/s] = \frac{stride\ length\ [cm]}{stride\ time\ [s]} \tag{2.1}$$

$$walking\ speed\ [cm/s] = stride\ length\ [cm] \times \frac{cadence\ [step/min]}{120} \tag{2.2}$$

2.1.2 Sit-to-stand Transition

Sit-to-stand transition was divided into four phases: a flexion-momentum phase, a momentum transfer, an extension phase and a stabilisation phase [22], as shown in fig. 2.3. The flexion-momentum phase (Phase I) starts from upright sitting posture and ends at lift-off, where buttocks are about to be lifted from the chair. During this phase, a subject moves his trunk forward, caused by the flexion of trunk and hip, generating initial momentum in the horizontal direction for rising. This phase is followed by the momentum-transfer phase (Phase II), happening at lift-off and ending when maximum ankle dorsiflexion is reached. The initial forward momentum of the upper body transfers to forward and upward momentum of the entire body in this phase. Maximum hip flexion, trunk flexion and ankle dorsiflexion are attained sequentially, causing a transition from dynamic to quasi-static stability, in preparation for standing up. The center of mass (COM) of the whole body shifts horizontally closer to the feet during Phase I and diagonally upwards over the feet during Phase II. After maximum ankle dorsiflexion is completed in Phase II, the body will extend to an upright standing posture during the extension phase (Phase III). Trunk, hip and knee extension are achieved in this phase. It ends when the hip angular velocity firstly reaches zero, where the stabilisation phase (Phase IV) occurs. During the last phase, the trunk and hip continue moving to balance the entire body till body stabilisation is settled.

According to the STS experiments in [22], nine healthy young subjects with an average age of 29 achieved STS within 1.95 seconds. Their extension phase (Phase III) corresponded to 54% of the required time spent in the first three phases, whereas that of their flexion momentum and momentum transfer (Phase I and II) were 28% and 18%. Forward momemtum generated in Phase I significantly helped subjects to achieve STS by reducing an effort to perform upward motion compared to those without forward momentum. In addition, sitting posture, involving the height of a chair and the angle of ankle dorsiflexion, strongly affected the STS performance.

The phase division shown in fig. 2.3 can be used in clinical analysis of elderly patients to observe causes of STS inabilities, such as insufficient forward momentum generation in Phase I, lack of balance control when shifting the COM in Phase II and ineffective muscle extension for standing up in Phase III [23]. Some researches combined Phase I and II, and Phase III and IV together to have only two major phases: a forward-moving phase and an upward-moving phase [24].

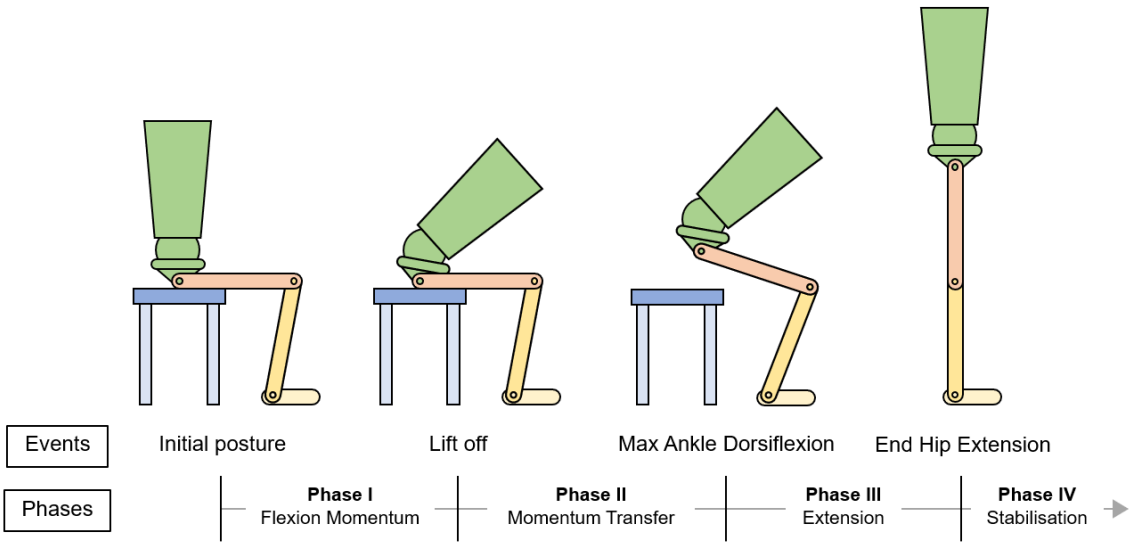

Figure 2.3: Events and phases during sit-to-stand transition (STS). Adapted with permission from [22]

2.2 Lower Limb Degeneration and Mobility Impairment

In this section, we studied the effect of lower limb degeneration on the efficiency of mobile capabilities due to ageing, muscle weakness and other factors. The decrease in muscle activities of lower limbs in performing ground-level walking (GLW) and sit-to-stand transition (STS), and the causes of these reductions as well as changes in body movement patterns of elderly subjects are discussed. Then, we will describe the functional roles and the impact of the knee as an essential joint in achieving both GLW and STS.

2.2.1 Ground-level Walking

Impaired mobility is one of the major issues within the elderly population, since it affects and limits their locomotion and daily activities. This disability occurs as a result of the degeneration of lower limbs and muscle weakness with increasing age. Walking speed is one of the methods used to evaluate walking efficiency and detect mobility disorders [25]. 156 healthy subjects within the age range between 50 and 79 performed walking tasks to measure the factors that affected their maximum and comfortable walking speed. As a result, gender, body weight and hip flexion strength was found to correlate with the reduction of gait speed, especially maximum walking speed. Further experiments were performed with 230 active individuals from a wider age range between 20 and 79, discovering that walking speed, in fact, declined mainly because of ageing [26]. Also, height and knee flexion strength substantially influenced the decreases in maximum and comfortable walking speed. Although comfortable walking speed slightly decreased, maximum walking speed considerably reduced with an increasing age, as shown in fig. 2.4. A six-minute walking experiment was performed by 51 healthy elderly subjects to measure their walking

efficiency, and the results showed that age was the main factor that reduces gait speed [27].

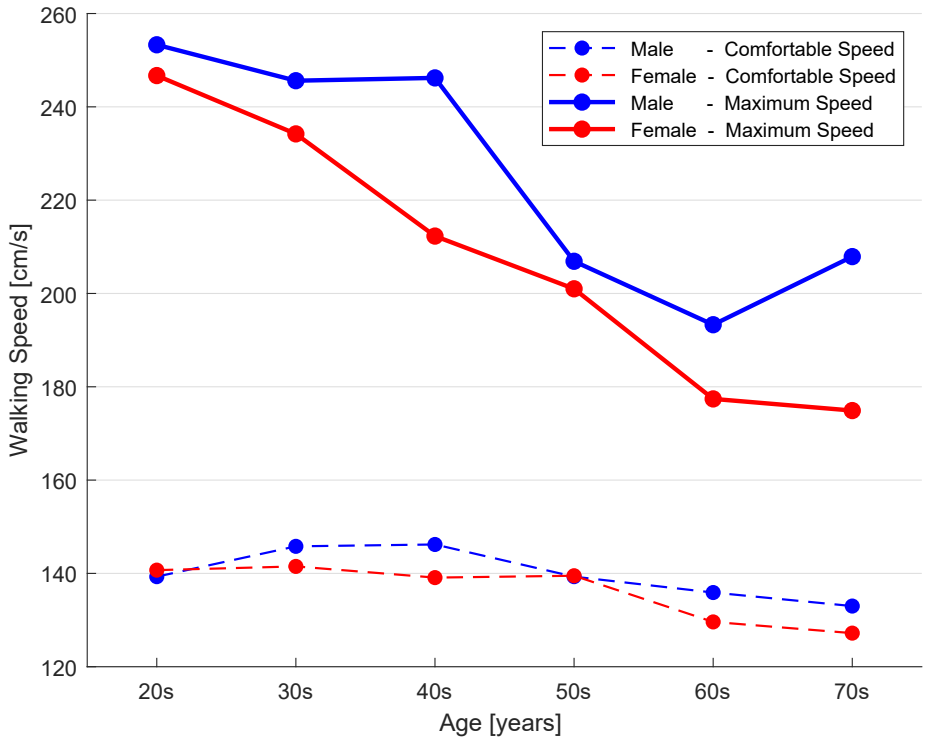

Figure 2.4: The reduction of the maximum and comfortable walking speed in male and female healthy subjects by age. Solid lines show maximum walking speed of male (blue) and female (red) healthy subjects, while dashed lines show comfortable walking speed. Adapted with permission from [26]

Gait kinematics of 136 healthy subjects with different ages between 18 and 97 was studied and measured by portable inertial measurement units (IMUs) [5]. The range of motion (ROM) of thigh, shank and knee started decreasing at the age of 60 and were significantly different in subjects beyond the age of 80, for example, the knee ROM as shown in fig. 2.5. A gradual increase in stride time and a decrease in stride length with age caused the decreases in lower limb advancement and walking velocity, which could be because of the reduction of peak muscle power. Other researchers compared gait patterns of 60 active young and old subjects and evaluated the ROM of their lower limb, i.e. hip, knee and ankle, and the walking velocity, as well as stride time and length [28]. They used videotapes to capture 2-dimensional walking motion with six reflective markers along the lateral side of the lower limb. The computer-analysed gait characteristics revealed that peak knee extension and stride length of the older group were greatly less than those of the younger group, which led to a slower walking speed. Besides muscle weakness, the walking speed of older adults was possibly reduced due to an attempt to ensure stable locomotion and to prevent falling [29]. Gait characteristics of elderly subjects tended to concentrate more on stability and safety while walking by increasing a duration of double leg support

during stance phase and decreasing push-off power during re-swing period. Consequently, these changes shortened the step length of elderly subjects and thus declined walking velocity and limb advancement.

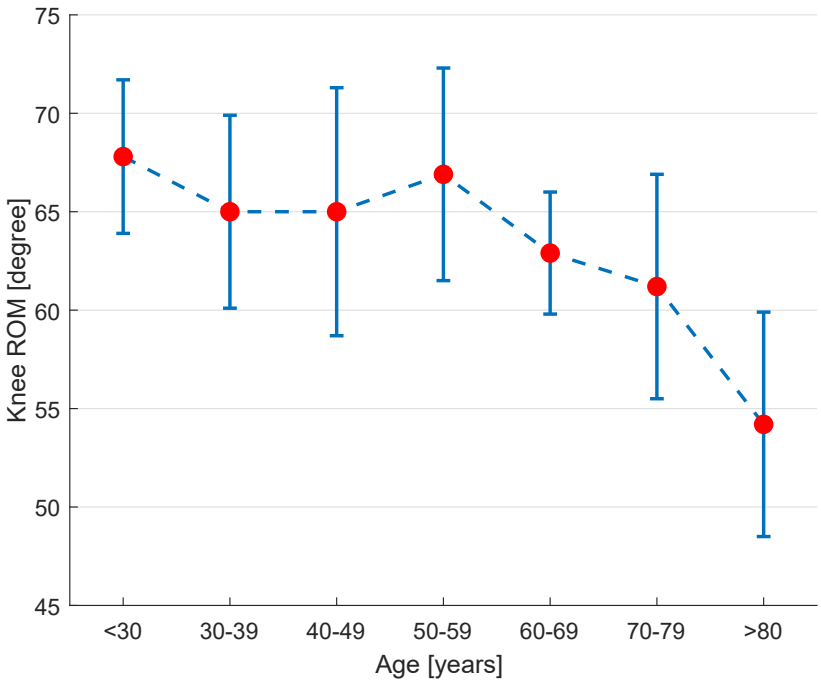

Figure 2.5: The relationship between the knee ROM and age. Red dots are the mean knee ROM of the healthy subjects in different age ranges, and the standard deviation is represented as vertical blue errorbars. The blue dashed line shows the trend of the decrease in the knee ROM with age. Adapted from [5]

Fear of falling is another major cause of slow walking in elderly population [30]. Falling can happen with people in all age ranges. One research study demonstrated that falling occured more frequently with age: 18% in young, 21% in middle-aged and 35% in older adults [31]. This could result from many factors such as environmental factors, unpredicted accidents, balance impairment, muscle weakness and injuries in their lower limbs. In consequence, it led to a fear of falling in older adults. For instance, 30% of 100 elderly subjects, aged beyond 75 years, were found to be impacted by fear of falling while walking, which resulted in slow gait speed [32]. A self-selected gait speed and a stride length of older adults who was fearful of falling significantly reduced at approximately 38 cm/s and 31 cm, respectively, compared to a fearless group, whereas their double leg support duration during a stance phase increased [31]. The decrease in walking speed could stem from changes in a gait pattern and biological mechanism in order to improve body balance for a stable gait [32].

All of this evidence leads to a conclusion that walking efficiency and gait speed decrease because of ageing, muscle weakness, fear of falling and the concentration on body balance, which limit lower limb advancement during the swing phase of a gait cycle.

2.2.2 Sit-to-stand Transition

Sit-to-stand transition (STS) is another major challenge limiting independent living of older adults. 42% of 379 elderly and arthritic subjects, mostly aged between 50 and 80 years, were found to experience difficulty in rising from a chair easily [33]. Importantly, about half of this group were unable to get up from a chair without supports, such as armrests or helps from another person.

In general, there are two major factors affecting the STS strategy and performance: STS speed and sitting posture. Ten healthy adults, aged between 26 and 38 years, performed STS experiments at three different standing speeds: slow, natural and fast [34]. When increasing STS speed, the trajectory of their body COM changed, and the total travelling distance of their body COM decreased. The peak linear momentum in both horizontal and vertical directions became higher and occurred earlier for faster STS. Moreover, when comparing between slow and fast STS, the increase in the peak vertical momentum was more than three times greater than that of the peak horizontal momentum (an increase of 40 and 12 $kg{\cdot}m/s^{-1}$, respectively). Further experiments were undertaken by the same research group with eight healthy subjects with the same age range while constraining the same seat height and initial seated position [35]. Their average time spent for STS transfers at slow, natural and fast speeds were 1.2±0.2, 1.6±0.2 and 2.5±0.3 seconds, respectively. The peak joint torques of knee extension was found to increase with an increasing STS speed (from averaged 111 Nm for slow STS to 184 Nm for fast STS, and around 150 Nm for natural speed) while that of hip flexion and ankle dorsiflexion only differed between slow and fast STS speeds. The other joint torques showed no significant change. These generated torques, however, can be altered when the subject concentrates in body balance, causing an increase in hip extension and ankle plantarflexion torques to brake the forward momentum in Phase II [35].

Ten young subjects with an average age of 25 years undertook STS experiments with two different initial knee flexion angles: 105 degree (15-degree ankle dorsiflexion) and 75 degree (15-degree ankle plantarflexion), meaning that the feet were horizontally forward or backward from the knee position, respectively, [36]. The peak hip-flexion moment was considerably greater for forward feet position since the subjects were required to generate larger forward momentum to break stability for rising from a chair. Some subjects also threw their arms forward to aid forward momentum. Another experiments were performed by varying sitting postures regarding the initial ankle-dorsiflexion angle and the seat height [37]. When increasing the initial ankle-dorsiflexion angle (moving the feet backward, closer to the body COM), the horizontal trajectory of the body COM was shorter, resulting in lower required forward momentum (lower hip flexion) and thus lower hip-extensor joint moment but higher required knee-extensor joint moment due to lower initial knee-extension angle. When increasing the seat height, the vertical trajectory of the body COM decreased, requiring lower hip-extensor joint moment for upward motion. When increasing both

initial ankle-dorsiflexion angle and seat height, although the knee-extensor joint moment was still higher compared to when initialising STS with only lower ankle-dorsiflexion angle, the total moments of all lower-limb joints became lowest, especially for the hip extensor. All of these experiments were based on healthy young adults; the factors impacting the STS of elderly subjects (muscle weakness, additional supports, intention of faster STS achievement, sitting posture and concentration on body balance) are discussed below.

Muscle weakness in lower extremity was commonly found in elderly individuals, especially with an average age over 84, who participated in STS experiments [24]. This resulted in slower STS speed, difficulty in body balance and a change in STS strategies and the ROM of all lower-limb joints during STS. The elderly group spent average time of 1.83 second to complete the entire STS at comfortable speed, which was 0.27 second longer than that of a young group. This time difference was mainly from moving trunk forward in forward-momentum and momentum-transfer phases (Phase I and II), while their spending time in moving upward (Phase III) was comparable to the young group. When using armrests, both groups attained STS within similar spending time of 1.57 second [24]. However, an improper-designed chair, for example, incorrect heights of the armrest and seat, could result in damage to the elderly person's body while performing STS [33]. In addition, the older group performed consistently larger knee extension than the young group in STS with and without using armrests, whereas the ROM of their hip flexion was larger only when not using armrests, and there were small changes for that of their ankle flexion for both cases [24]. This increased knee extension was a result of the the interaction between body weight and the older group's weaker muscles.

Another nine healthy elderly individuals, aged between 61 and 74 years, performed STS experiments initialising with 18-degree ankle dorsiflexion and without the use of arms [23]. The recorded data was compared with the data of the young group previously collected in [22]. As a result, there was no significant difference in the sequence of kinematic events between two groups although the older group completed most of the STS events slower, and their total time spent to complete the entire STS was slightly longer than that of the young group (1.95 and 1.86 seconds respectively). Moreover, the head movement of the elderly group was altered, which could be clinically implied as an effect of loss of balance and an adjustment in the STS strategy to compensate body balance, preventing falling. In addition, the collected data showed that the elderly group required higher maximum knee torque than the young group to achieve STS, while that of their hip was lower.

Eight healthy elderly subjects voluntarily performed STS under different conditions by changing movement speeds (self-selected and fast speed) and initial angles of ankle dorsiflexion (5 and 18 degree) [38]. In the fast speed condition, their muscles activated more rapidly, resulting in shorter period of forward body movement (Phase I and II) and the total time spent. They generated higher vertical force to attain STS without any change in muscle activity. In contrast, STS with lower initial angle of ankle dorsiflexion caused modification of their muscle activity. When the feet were initially placed further

from the body (5-degree ankle dorsiflexion), elderly subjects necessarily moved their trunk faster to produce higher forward momentum to lift their buttocks from the chair and shift the COM of their entire body over their feet rapidly. Consequently, they spent a longer time for the muscles to counteract this increased forward momentum in Phase II to prevent falling and to generate enough forces for upward extension in Phase III. However, failure to perform sufficiently fast forward movement and activate muscular extensors powerfully at an appropriate time could lead to STS failure.

Similarly, 18 elderly subjects and 9 healthy young adults with average age of 74 and 22 years, respectively, participated in sit-to-walk (STW) experiments by performing STW at different speeds [39]. Although the older group moved their centre of gravity (COG) forward less at lower velocity and generated lower muscular force than the young group at any speed tasks due to their physical limitation, they was able to adjust their STS strategy to catch up with the STS speed of the young group. As a results, the total time required to complete STW at comfortable and maximal speeds between two groups was similar.

Overall, it can be concluded that muscle degeneration in older adults led to changes in STS strategy in order to balance their body and prevent falling during STS. It caused reduction in their STS speed and alteration in the ROM and generated force of lower-limb joints. Although some elderly adults were able to achieve STS as quickly as healthy young adults by altering their STS strategies: exerting higher muscle power or rising with some assistance, the majority of older adults still faced difficulties in STS, limiting their independent living. In the next section, we will consider the important of the knee joint in performing human locomotion over other lower-limb joints and how to assist the knee in order to improve human mobility, particularly GLW and STS.

2.3 Importance of Knee in Human locomotion

Fundamentally, human locomotion is the production of the cooperation between hip flexion/extension, knee flexion/extension and ankle plantarflexion/dorsiflexion (as shown in fig. 2.1). The knee joint is the primary focus of this research since it has only one DOF, i.e. flexion and extension, which simplifies control and mobility assistance for wearable devices. The knee is also an essential joint in achieving both ground-level walking and sit-to-stand transition as discussed follows.

For ground-level walking, the knee-acting muscles in the sagittal plane, i.e. flexors and extensors, are responsible for three main functions: control balance, foot clearance and shock absorption [40]. First, control balance happens because of the cooperation between knee flexors and extensors during single limb support to attain stability and weight transfer between two legs. Second, foot clearance occurs during a pre-swing phase by knee flexors to prevent the foot from dragging. It requires approximately 60 degree of knee flexion during the swing phase to produce at least 1.29 cm height so as to avoid

foot dragging [41]. The reduction of the knee flexion can be because of a decrease in hip flexion moment, an increase in toe-off hip flexion velocity and an overactivity of the rectus femoris muscle[1], which result from changes in muscle activities. This leads to lower foot clearance and higher chance of falling. Last, both knee flexors and extensors absorb the shocks at the heel strike and toe-off phases to facilitate forward propulsion. Although the knee is proposed to accomplish these three tasks during walking, elderly subjects are likely to preform less knee functions than young subjects. Their knee flexors and extensors generally focus on control balance to perform a stable gait, which results in shorter stride length and lower walking speed [42]. Elderly subjects also lack limb advancement, which might be because of muscle weakness and the concentration merely on control balance. To sum up, the knee is the main biological joint to produce walking motion, and the degeneration of knee muscle power and knee flexion/extension certainly affect the gait pattern, and limit limb advancement.

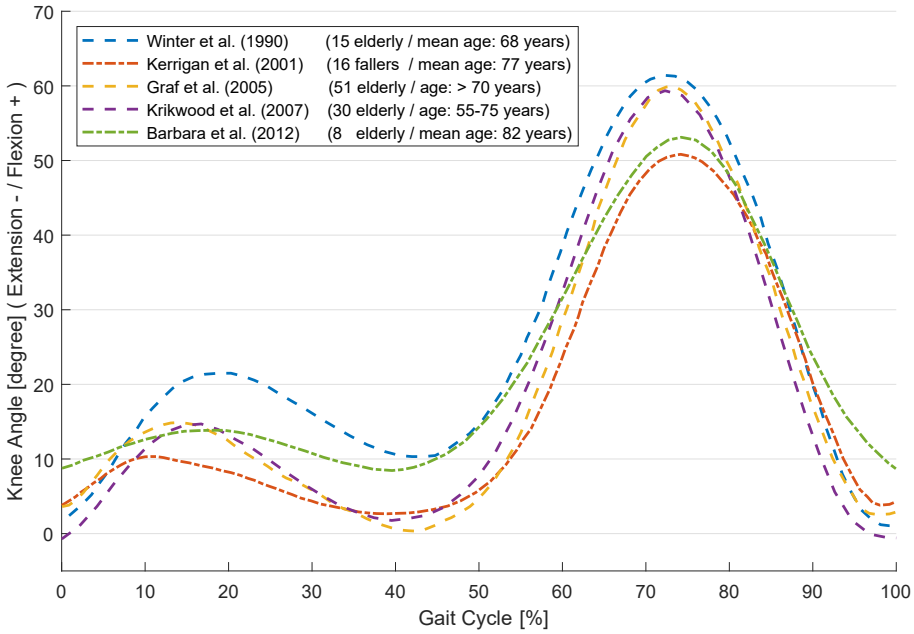

Figure 2.6: The recorded angle of the knee flexion/extension in the sagittal plane during a gait cycle of elderly subjects. Adapted from [29, 43–46]

According to several papers researching knee behaviour of elderly subjects during a gait cycle [29, 43–46], their knee angle in the sagittal plane can be shown in fig. 2.6. The peak knee flexion of the elderly subjects with a falling history or aged over 80 years (dash-dot lines) decreased about 10 degrees compared to healthy elderly subjects with lower age (dashed lines). The knee flexion of elderly subjects with all conditions (fig. 2.6) follows the decreasing trend of the knee ROM with age shown in fig. 2.5 and are all less than that of young healthy subjects (for example, 67.8 degrees for adults with the age below

[1]Rectus femoris muscle is a quadricep muscle of the lower limb, used to perform a knee extension and located at the front of the thigh.

30, acquired from [5]).

A summary of previously discussed research on knee torque in sit-to-stand transition is presented here. Older adults typically required higher maximum knee torque than young adults to achieve STS [23]. In order to increase STS speed, humans normally exert much higher momentum in vertical direction, which mainly results from increasing knee-extension torque while other joint moments are dedicated for body balance [34, 35]. Some healthy elderly subjects were able to deliver fast STS as young adults by exerting higher muscle power or standing up with some assistance [39]. When performing fast STS or STS with the feet positioned further from the body, elderly subjects had to move forward faster and exert higher vertical force for lifting their body and standing up [38]. With or without the use of armrests, elderly subjects always performed STS with larger knee extension and higher knee torque than young subjects [24]. Also, the moments of hip flexion and extension can be reduced by simply adjusting the sitting postures, i.e. increasing an ankle-dorsiflexion angle or a seat height [36, 37]. These evidences lead to a conclusion that knee extension is the most important movement for achieving effective sit-to-stand transitions in elderly individuals.

Based on this conclusion, the knee is selected as the joint to be assisted. The design and development of knee-flexion and knee-extension orthoses which can effectively improve walking motion and sit-to-stand transition is chosen as a research focus. To further support for this decision, a recent review of 52 existing exoskeletons for lower-limb assistance and rehabilitation revealed that the majority were built to support the knee (71% of exoskeletons, where those built for the hip and ankle are 50% and 63%, respectively) [47], as shown in fig. 2.7. This ensures an important of the knee to be assisted.

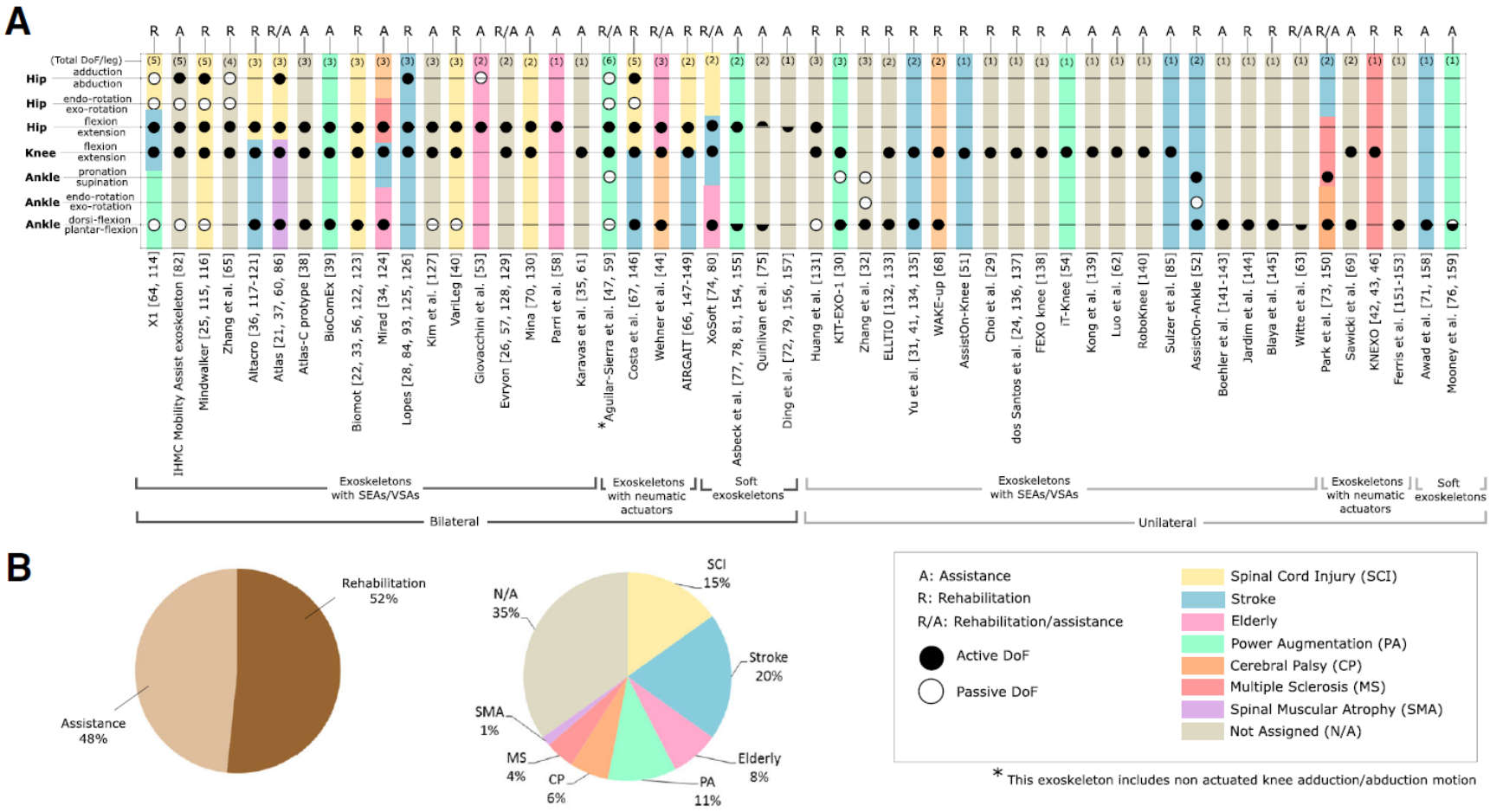

Figure 2.7: Classification of 52 lower limb exoskeletons. (A) They are classified into function (i.e. rehabilitation (R) and assistance (A)), number of active and passive DOF in parenthesis, targeted pathologies, actuation system (i.e. SEAs, VSAs and PAMs) and configuration (i.e. unilateral and bilateral). (B) A breakdown of the individual system's information shown. Reproduced with permission from [47] (CC by 4.0)

2.4 Conventional Exoskeletons and Wearable Assistive Devices

This section reviews conventional rigid exoskeletons and soft wearable assistive devices, which were developed to improve human mobility. The advantages and disadvantages of conventional assistive devices and their remaining challenges requiring further developments are given.

Existing exoskeletons can be classified based on their components regarding actuators and body attachments, worn on a user's body. 52 compliant lower-limb exoskeletons were reviewed and divided into three categories: exoskeletons with compliant actuators and rigid attachments (85%), exoskeletons with rigid actuators and soft attachments (11%), and exoskeletons with complaint actuators and soft attachments (4%) [47], as shown in fig. 2.7. Examples of compliant actuators are series elastic actuators (SEAs), variable stiffness actuators (VSAs) and pneumatic actuators, which can work smoothly and not resist natural human body motion. Textile/fabric or soft components are considered as soft attachments, providing comfort for a user's body. In this thesis, all exoskeletons are divided into only two groups: rigid exoskeletons (with compliant actuators and rigid structure) and soft wearable assistive devices (exoskeletons with soft attachments and entirely soft structure).

2.4.1 Rigid Exoskeletons

Rigid exoskeletons have been continuously invented and developed for many decades in order to improve human capabilities. Traditional exoskeletons were characterised into two main types: performance-augmenting exoskeletons for enhancing body strength, and active orthoses for assisting individuals with disabilities owing to severe mobility disorders such as spinal cord injuries and stroke [7]. These rigid exoskeletons were typically designed to operate in parallel with a lower limb to provide power for a user to achieve desired tasks such as load carriage, better locomotion and rehabilitation, as shown in fig. 2.8.

First, performance-augmenting exoskeletons were mainly invented to enable a wearer to accomplish difficult missions more easily and safely such as load carriage and long-distance locomotion at high walking speed. They were used for many purposes, particulary for military and industrial applications. The Berkeley Lower Extremity Exoskeleton (BLEEX) is an example of an energetically autonomous wearable device developed to increase physical performance to carry an external payload while ground-level walking [9]. It was designed to provide torques at the hip, knee and ankle for four movements, i.e. hip flexion/extension, hip abduction/adduction, knee flexion/extension and ankle dorsiflexion/plantarflexion, driven by linear hydraulic actuators. This exoskeleton allowed the wearer to walk at 0.9 m/s with a 75-kg payload or at 1.3 m/s without any loads. Another example is the RoboKnee exoskeleton that was developed to enable the user to perform

high-speed walking (up to approximately 2.5 m/s), stair climbing and squatting with a heavy payload (60-kg) [8]. This device attached to the thigh and shank and used a series elastic actuator to apply external torque to the knee during a swing phase of a gait cycle.

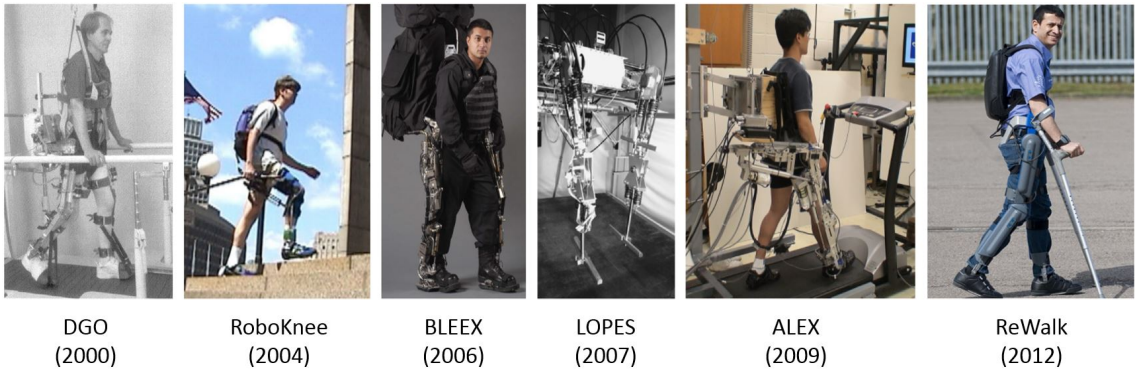

Figure 2.8: Conventional rigid exoskeletons developed to augment human performance to perform more effective locomotion and achieve difficult tasks (RoboKnee and BLEEX), and to recover mobility of disable patients (DGO, LOPES, ALEX and ReWalk). Reproduced from [8–12, 48]

Other active orthoses were developed for the rehabilitative purpose to improve the locomotion of elderly individuals and patients with impaired mobility. For example, a Driven Gait Orthosis (DGO) was able to recover walking of paralysed patients on a treadmill with partial body-weight support [10]. It was designed to aid physical therapists to automatically train the patients to walk following physiological gait patterns. Similarly, the LOPES exoskeleton was created to assist the hip and knee [12]. It could operate with two modes to effectively treat disabled patients: a "patient-in-charge" mode and a "robot-in-charge" mode. The Active Leg Exoskeleton (ALEX) could resist undesirable gait patterns and help patients to walk with desirable gait characteristics [11]. In addition, ReWalk is a commercial wearable assistive product that can restore the locomotion for disabled and paralysed patients, which can be used either personally or clinically [13]. From these examples of active orthoses, patients can experience more effective walking rehabilitation to obtain greater mobility improvement.

Although many rigid exoskeletons succeeded in assisting users to handle difficult tasks and helping disabled patients to walk again, they still require further developments to accomplish ongoing challenges such as heavy weight, portability, effective autonomous control, user interface, self-adjustment, resistance of natural movements and joint misalignment, which can cause injuries and safety problems [7, 14, 15]. Some of these challenges can be solved by using soft robotic technologies, which can exhibit light weight, adaptability and safe interaction. The next section will present examples of soft wearable assistive devices (WADs), which were developed to address human immobility.

2.4.2 Soft Wearable Assistive Devices

Soft robotics is alternative technology which has the potential to overcome the limitations of conventional rigid robots because of its typical low mass, inherent compliance and flexibility [16]. Resistance of the natural movements is one of the critical safety issues in using rigid exoskeletons. It happens as a result of joint misalignment of exoskeletons while actuated along the leg. This therefore leads to negative gait patterns and muscular injuries. Importantly, if rigid exoskeletons operating with high power fail, they can possibly damage the lower limb of the user. In contrast, soft robotics enables safe interaction with human body.

Soft wearable assistive devices have been developed with the aim of creating a flexible power suit, which provides extra power for healthy young or elderly able-bodied people to perform higher-performance locomotion and achieve daily activities with more comfort and less fatigue as well as rehabilitative purposes to maintain high mobile efficiency (fig. 2.9). Knee-ankle-foot orthosis (KAFO) was one of the early soft WADs employing pneumatic artificial muscles (PAMs) to assist the knee and ankle of a wearer (fig. 2.9a). It could produce high ankle dorsiflexion/plantarflexion and knee flexion/extension during normal-speed walking [49]. An active soft orthotic device was developed by applying PAMs to control the ankle movement stably without any resistance (fig. 2.9b) and was used to improve a gait of the patients with neuromuscular disorders [50].

In 2012, an active modular elastomer sleeve (fig. 2.9c) was invented using series McKibben pneumatic actuators and hyper-elastic strain sensors embedded inside an elastomer sheet [18]. It could assist the knee to function various motions, for example, contraction and bending, by activating a combination of McKibben muscles with shape control. However, it required further improvements to succeed in full walking assistance in terms of control strategies, fabrication and miniaturisation of muscle cells. Researchers at Harvard University have innovated two types of soft exoskeletons, called exosuits (fig. 2.9d). The first exosuit applied McKibben muscles to aid the hip, knee and ankle [14]. The second one was operated by geared motors with Bowden cables, transferring generated forces to lower limbs through garments and providing assistive torques for the ankle and hip [15]. Comparing these two exosuit types, the McKibben-type exosuit could maintain constant metabolic cost of walking (MCW) of a wearer at comfortable walking speed, whereas the cable-driven exosuit slightly increased the MCW while walking and carrying a 24.5-kg payload [17]. In the meantime, Japanese researchers at Chuo University invented an orthosis using straight-fibre PAMs (fig. 2.9e) to assist the hip [19]. This orthosis could increase the step length for longer forward swing, but some user's muscles generated more energy to compensate the body balance after the longer swing motion, measured by electromyography (EMG) devices. Thus, it required further improvement regarding accurate control, appropriate activation timing and assistance without impacts on lower limb muscles.

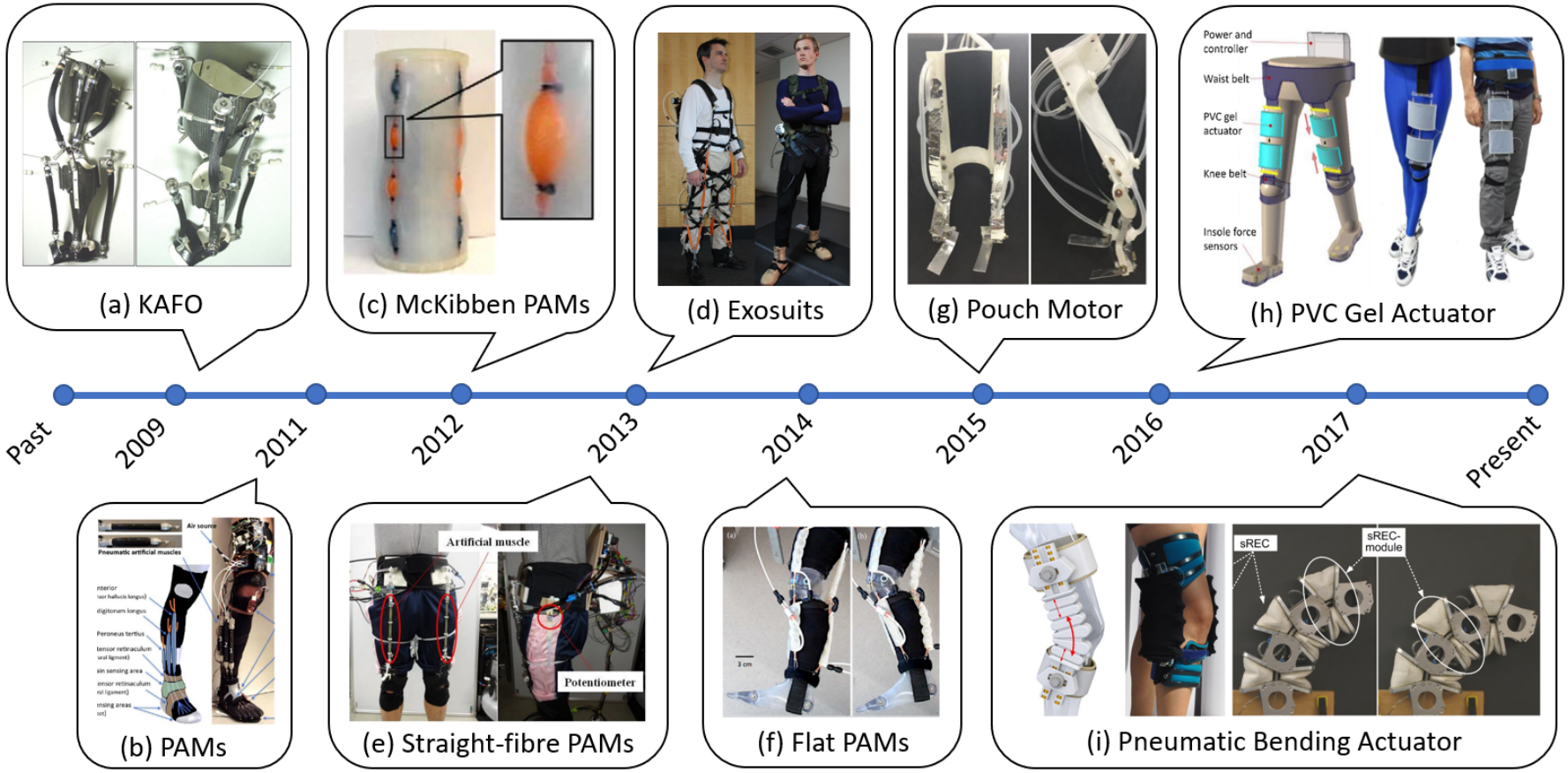

Figure 2.9: The history and development of soft wearable assistive devices (WADs) with some examples: (a) knee-ankle-foot orthosis (KAFO) actuated by pneumatic artificial muscles (PAMs), (b) active soft orthotic device with PAMs, (c) series McKibben PAMs, (d) McKibben-type and cable-type exosuits, (e) straight-fibre PAMs, (f) elastomeric flat PAMs, (g) series pouch motors, (h) PVC gel actuators, and (i) pneumatic bending actuators. Reproduced with permission from [15, 19] © 2013 IEEE, [18] © 2012 IEEE, [49] (CC by 2.0), [50] © 2011 IEEE, [17, 51] © 2014 IEEE, [52] © 2015 IEEE, and [53, 54]

In 2014, an orthosis consisting of eight elastomeric flat PAMs aligned in series along the lower limb was built to facilitate the knee motion for infant-toddler rehabilitation (fig. 2.9f). These series actuators could generate maximum force and contraction of 38 N and 22.5%, respectively, at an operating pressure of 104 kPa. It therefore could perform knee flexion and extension on a 3-dimensional (3D) printed leg model with 0.39 kg weight to a maximum angle of 37 and -5 degrees, referred to the vertical line of the sagittal plane, respectively [51]. Afterwards, a wearable small-size device was developed for rat gait rehabilitation using pouch motors [52]. This orthosis was designed to restore the mobility of paralysed rats, and it showed the potential to assist and control hip motion during the rat walking (fig. 2.9g). The pouch motor is considerably lightweight, low-cost, and easily fabricated. It is made of inextensible materials and can be designed to either contract or bend when inflated [55–57].

Plasticised polyvinyl chloride (PVC) gel soft actuator was another artificial muscle applied to create a hip assistive orthosis (fig. 2.9h), using electricity as a power source [53]. The PVC gel orthosis was able to reduce the muscle activities of rectus femoris during walking [58]. The major features of this actuator are its compliance, light weight, simple structure, stable actuation, lower power consumption and no noise during actuation, and the orthosis can be easily put on and taken off, increasing its feasibility for daily usage [53]. In addition, a pneumatic bending actuator for a rehabilitation orthosis (fig. 2.9i) was developed to assist walking, sitting and standing of elderly individuals [54]. This orthosis was made of series rotary elastic chambers attached at the side of the knee. It was able to deliver a polycentric motion and self-adjustment to fit with the knee, preventing from joint misalignment and any damage while operating.

The concept of the exosuit, an exoskeleton driven by a cable/tendon mechanism transmitting generated forces to a user's body through textile garments [15], has been expanded, resulting in further developments of this type of exoskeleton to improve walking performance and minimise the metabolic energy cost of healthy able-bodied users and patients with impaired mobilities (fig. 2.10). This type of exoskeleton was defined as soft exoskeletons comprising rigid actuators and soft attachments by [47]. The original exosuit was capable of assisting 18% and 30% of ankle and hip moments required for normal walking, respectively, using an on-board actuation unit loaded on the user's back, as shown in fig. 2.10A.

This exosuit had been developed further, embedding joint force and motion sensors and driven by an off-board actuation with a two-layer control system (fig. 2.10B). It was reported that this new tethered exosuit succeeded in decreasing the metabolic cost of walking up to 22.83%, recorded from experiments of seven healthy young subjects (average age of 26.7 years), comparing between an active mode and a power-off mode [59]. Similarly, a tethered ankle-assisting exosuit (fig. 2.10C) was built to aid ankle plantarflexion and dorsiflexion during stance and swings phases, respectively, to improve walking behaviour of healthy poststroke patients on a treadmill, resulting in a 32±9% reduction

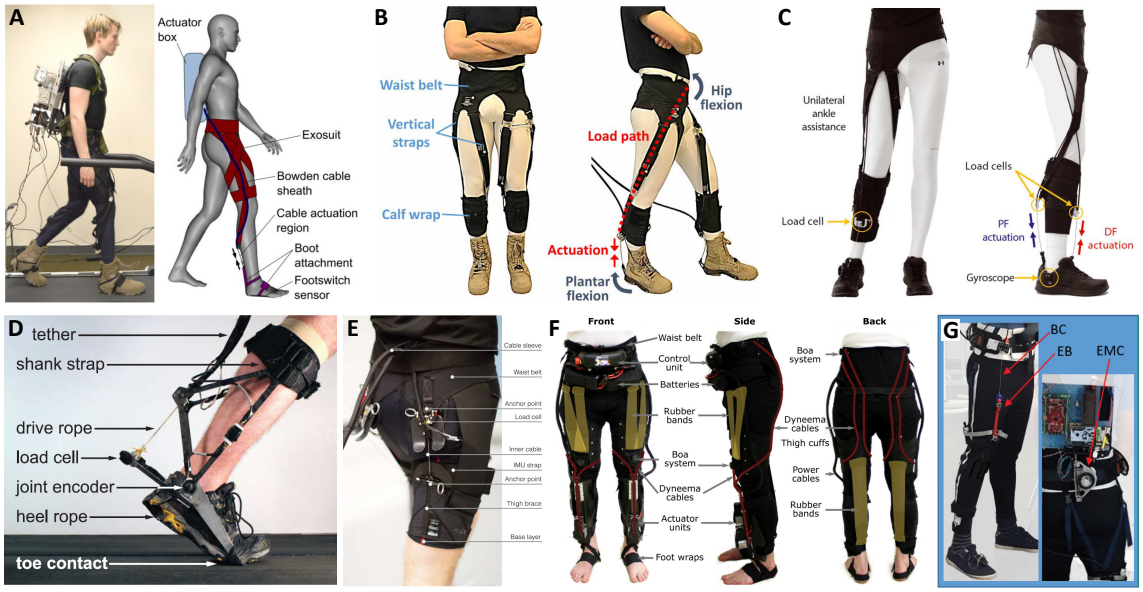

Figure 2.10: Development of cable/tendon-driven exoskeletons: (A) the original hip/ankle-assisting exosuit with an on-board actuation unit loaded on a user's back for walking assistance [15], new versions of (B) the hip/ankle-assisting exosuit for healthy able-bodied subjects and (C) the ankle-assisting exosuit for poststroke patients with off-board actuation units [59, 60], (D) a tethered ankle exoskeleton [61], (E) a tethered hip exosuit [62], (F) untethered Myosuit assisting hip and knee extension/flexion for STS assistance [63] and (G) XoSoft untethered hip exoskeleton [64]. Reproduced with permission from [15] © 2013 IEEE, [59–62], [63] (CC by 4.0), [64] © 2018 IEEE

in their metabolic energy cost [60]. Also, a proof of concept and walking evaluation of an untethered ankle-assisting exosuit loading a cable-driven actuator and a battery pack on a user's waist were presented in [60]. In the meantime, another tethered ankle exoskeleton with an off-board motor and control system (fig. 2.10D) was built to operate on a treadmill [61]. This system applied a new self-updating control algorithm, called human-in-the-loop optimisation, to optimise a walking assisting strategy. In general, controlling the human mobility assistance is challenging although a walking model is well simulated, because human walking pattern can be changed over time or influenced by environments. Human-in-the-loop optimisation is the method that a controller of exoskeletons can automatically update its control algorithm based on current human walking performance and continuously adapt to maximise their assistance and minimise the user's metabolic energy cost during walking, as shown in fig. 2.11. This approach resulted in the greatest reduction of the metabolic energy cost compared to other existing exoskeletons (average of 24.2±7.4% compared to no torque assistance or approximately 14% compared to normal shoes, acquired from experiments of 11 healthy subjects with an average age of 27 years) and also large reduction of the lower limb's muscle activity.

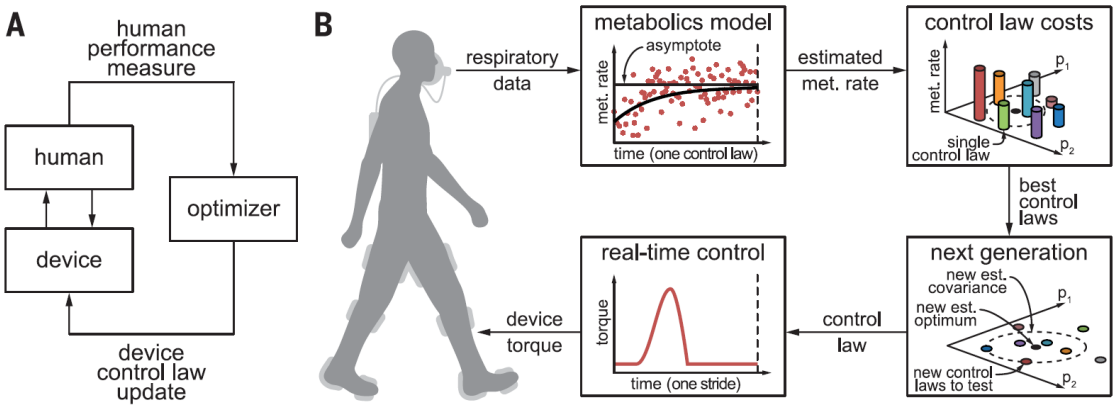

Figure 2.11: Human-in-the-loop optimisation. (A) Measurements of human performance are used to update device control so as to improve performance in the human portion of the system. (B) A method for minimising the energy cost of human walking, in which various control laws are applied, metabolic (met.) rate is quickly estimated (est.) for each, costs are compared, and an evolution strategy is used to generate a new set of control laws to be tested, all during walking. p_1 and p_2 are hypothetical control parameters. Reproduced with permission from [61]

Despite a success in the highest decrease in the metabolic cost and muscle activity [61], this control optimisation required long empirical walking protocol (over an hour) to identify controlled parameters for optimised walking, which can negatively cause fatigue and inaccurate measurement. Later, human-in-the-loop Bayesian optimisation was derived and used in a soft textile-based hip-assistive exosuit driven by an off-board actuation unit (fig. 2.10E). This control algorithm was able to minimise convergence time of the optimised control to average 21.4±1.0 min with decreased metabolic cost of 17.4±3.2 (compared to no exosuit worn) of eight healthy participants (an average age of 30 years), where the peak assistive force was fixed to 30% of the participant's body weight for safety and comfort [62].

In addition, a new exoskeleton was designed to assist extension of both hip and knee with the purpose to complete three tasks: sit-to-stand transition, ground-level walking and stair ascent [65]. This conceptual design was implemented for STS assistance, creating Myosuit (fig. 2.10F), an untethered bilateral exoskeleton with the total weight of 4.6 kg. It consisted of active and passive components to assist extension and flexion of both hip and knee, respectively [63, 65]. XoSoft was another untethered cable-driven exoskeleton invented, employing soft clutches to support hip flexion [64], as shown in fig. 2.10G. Its first prototype was able to reduce biological energy consumption during walking. These two untethered exoskeletons, i.e Myosuit and XoSoft, also included on-board sensors and control systems, enabling accurate and effective assistance and portability.

Most of these cable-driven exoskeletons comprise textile attachments and force transmissions with approximately 0.9 kg weight loaded on a user's body while their actu-

ation units are off-board, leading to an impressive walking improvement, suitable for clinical-based treatments. The minimum weight of the portable exoskeletons with entirely on-board actuation units loaded on the user's body, reviewed in this thesis, is 4.1 kg (XoSoft [64]), which was considerably reduced from that of the original exosuit (12.15 kg [15]). Decreasing their weight to improve assistance efficiency for ambulatory applications requires advanced developments in current technologies to create much lighter actuation units and power sources. Moreover, despite the capabilities in effectively assisting human locomotion, the force transmissions on the suits remain rigid and could lead to unpredicted damages to human skins and muscles.

Recently, several soft pneumatic exoskeletons were invented, as shown in fig. 2.12. Multifilament muscles consisting of several compliant, flexible, thin McKibben muscles (fig. 2.12A) were developed and used as human-like thigh and shank muscles to drive a musculoskeletal lower-limb robot and fully control knee and ankle motions [66]. These thin McKibben muscles were also used to create a lightweight, flexible muscle textile and a upper-limb assistive suit [67], as shown in fig. 2.12B. Moreover, McKibben muscles were integrated with planar fabrics embedding soft sensors to facilitate surface-induced deformations and thus bending motions of a mounted joint [68] (fig. 2.12C). Although this actuator was designed for typical continuum robots, it possesses high flexibility, adaptability and easiness of donning/doffing, showing a potential actuator design to be implemented in human mobility-assisting applications.

Two soft, lightweight, fabric-based knee assistive devices were lately created for walking rehabilitation, including compact sensor and control systems using external air suppliers (fig. 2.12, D and E). First, a soft-inflatable exosuit was created for knee-extension assistance using soft I-shaped cross-section inflatable actuators (fig. 2.12D) made of heat-sealable thermoplastic polyurethane (TPU) sheets, located at the back of the knee joint [69]. This soft exosuit has light weight of 0.16 kg including on-board electronics for motion capturing, worn on the knee using an elastic fibre (neoprene) sleeve for comfort, together with an independent insole sensor for gait event detection. An off-board electro-pneumatic system was used to control the actuation, and the soft exosuit was initially designed to assist 20% of the required knee-extending moment during a swing phase, corresponding to 4.4 Nm. It was used to aid walking at 0.5 m/s and was able to reduce 7% of the muscle activity in the rectus femoris muscles. This soft-inflatable exosuit was developed further using wireless IMUs and smart shoe insole sensors for real-time knee motion monitoring and gait event detection, respectively, with an off-board control unit [70], as shown in fig. 2.12D. The actuator was operated using an external air compressor for inflation and a vacuum pump for deflation. A two-layer control algorithm was implemented: a low-level closed-loop controller accurately driving the actuator at required pressure and a high-level controller setting the required pressure to improve walking assistance based on the updated gait behaviour acquired from IMUs and smart shoe insole sensors (ground reaction force (GRF) sensors). The assisted knee-extending moment was increased to 25%

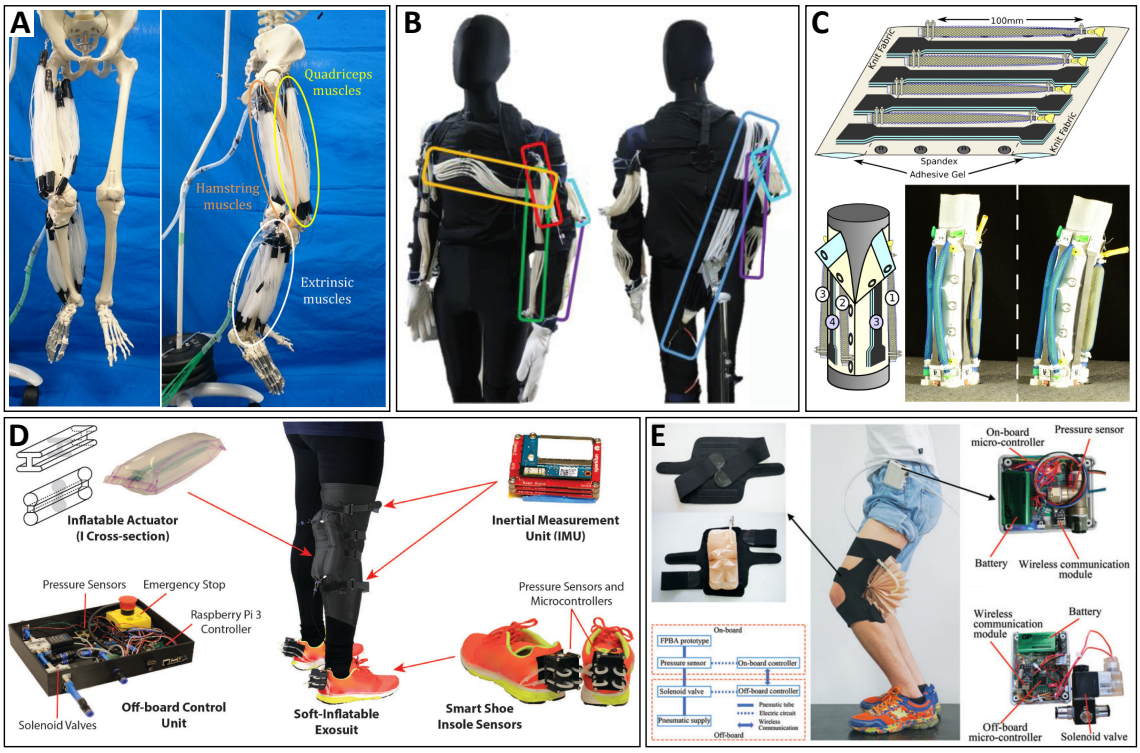

Figure 2.12: Recent development of soft pneumatic exoskeletons: (A-B) multifilament muscles consisting of several thin McKibben muscles for (A) a musculoskeletal lower-limb robot [66] and (B) an upper-limb exoskeleton [67], (C) a planar fabric-based McKibben-driven device including soft sensors [68], (D) a soft inflatable exosuit [69, 70] and (E) a knee assistive device driven by a foldable bending actuator [71]. Reproduced from [66, 70] (CC by 4.0), [67, 68] © 2018 IEEE, [71]

of the requirement, and this exosuit was capable of decreasing 30-57% of the muscle activities in the quadriceps femoris muscle group for knee extension, comparing between active and inactive worn exosuit while walking at 0.5 m/s, despite increasing muscle activities in hamstrings group. This negative increase could be because of the delay in actuator deflation, restricting efficient knee flexion.

Second, a lightweight knee assistive device [71] was created, driven by a foldable pneumatic bending actuator (FPBA), sewn to a knee elastic fabric sleeve embedding an on-board pressure-sensing system, leading to the total weight on a user's leg of 0.30 kg (fig. 2.12E). The FPBA was inspired by an accordion bellow; it was made of TPU sheets, a flexible, inextensible fabric material, and fabricated by a heat-sealing method without any rigid mechanical structures. The device was operated using an off-board controller and pneumatic source for controlling input/output airflow and FPBA actuation. It was used to rehabilitate five static knee postures, i.e. forward and barbell lunges, and half, deep and bulgarian deep squats. It was also succeeded in prolonging persistence time and reducing muscle activities while performing these five knee postures, comparing between wearing the device with and without assistance.

The weight loaded on a user's body of these two soft pneumatic exoskeletons are at least three times less than that of tethered cable-driven exosuits with off-board actuation units. Importantly, they highly respond to low pressure actuation, operating below 40 kPa for knee assistance, highlighting safety. They also behave as soft springs, preventing from restrictions in natural lower-limb movements. Despite these advantages of soft pneumatic exoskeletons, there are two remaining problems: (1) their air supply sources, i.e. a large, bulky, heavy external compressor or pump, which limits their portability and are only practical at clinical or rehabilitation bases, and (2) their actuation speed due to large air volume consumption, limiting effective assistance for normal-speed locomotion. As same as the cable-driven exoskeletons, more improvements are required to reduce the load of their on-board air-supplying units. More details in the development and trend of pneumatic exoskeletons can be found in [72]. Next section will conclude the principal concepts of the future smart assistive suit as a guideline in developing current exoskeletons.

2.5 Concept of the Future Smart Assistive Suit

Exoskeletons and wearable assistive devices have received significant attention over the last two decades. These technologies have been developed to improve and recovere human mobilities in a wide range of applications from partial supports for healthy able-bodied users, maintaining or enhancing their mobility efficiency, to full body supports for patients with mobile disabilities. However, most of the current exoskeletons comprise rigid elements in either actuation units or body attachments, making them uncomfortable, heavy, bulky and impossible to be integrated with normal clothing. Currently, they are restricted to operate only at clinical platforms since they are bulky, operate at a limited time, and generally are not optimised for ambulatory applications. More developments in multiple aspects of these technologies are required to deliver practical usage for real-world applications. As shown in table 2.1, orthosis stakeholders' needs and the associated actuator requirements are summarised and listed in [73] as a guideline for improving the current technologies with the aim of making them suitable for exoskeletons and wearable assistive devices.

Clothing has been using in everyone's daily life, but has not been changed in terms of its general form and design throughout many centuries in human history. A smart assistive suit is the future generation of an intelligent clothing which possesses advanced features improving human mobile abilities including: (1) consistently monitoring body motions, evaluating muscle efficiency and detecting undesired disabling symptoms while performing daily activities, (2) automatically adapting body-assisting strategies to continuously provide effective, harmless assistance, and (3) simultaneously harvesting and reusing restored energy from body movements to maintain daily operations. Achieving this future smart assistive suit requires considerable progress in technological developments and long-time evolutions in all robotic fields. This research aims to tackle some challenges in this

field with developing new technologies, paving the way to deliver fully-functional smart assistive suits.

Exoskeletons or wearable assistive devices are generally composed of four key components: (1) an actuation unit, (2) body attachments and garments, (3) a sensing system and (4) an off-board body motion simulation and a control algorithm. These components have been reviewed with respect to the guidelines (table 2.1) towards the smart assistive suit for healthy able-bodied users as follows.

Table 2.1: Summary of orthosis stakeholder needs (first row) and actuator requirements (second row) to meet these needs. Stakeholders are the definition of orthosis users, their family, clinicians and care givers. Adapted with permission from [73]

Category		Needs/Requirements
Orthosis stakeholder needs		affordability, durability, easy to maintain/repair, effectiveness, operability (controllability and adaptability), comfort/acceptance (ease of donning/ doffing, fit, appearance and sound), portability, reliability, and safety
Actuator requirements	performance	compliance, high specific power and force, natural motion characteristics, infinitely variable backdrivability, ease of control, and efficiency
	key physical	low mass, slim form, low cost, modularity, environmental compatibility, and quietness
	safety	sanitary cleanliness, safe exposed parts, and limited range of motion, speed and force

Actuation Unit

The actuation unit is the essential part in exoskeletons to provide sufficient support for human body to attain desired mobile functions. Actuators are generally required to produce specific power and force as high as human muscle while being lightweight and delivering smooth assistance for natural body movements [73]. Series elastic actuators (SEAs) and variable stiffness actuators (VSAs) are one solution to achieve these requirements, which are often used in the existing exoskeletons (83% [47]). They ensure high force and power transmission to the user's body. They also provide smooth actuation operated by sophisticated controllers, enabling backdrivability to avoid restricting natural body motions for safety purposes. However, they still contain rigid components, which could possibly damage human body. Compliance is one of the most important required features in exoskeletons to facilitate adaptability, comfort and safe interaction [73].

Level of compliance of exoskeletons varies depending on the usage purposes. Rigid exoskeletons can replace muscle functions and rehabilitate mobilities of patients with severe

mobile disabilities at a clinical base, whereas compliant exoskeletons are more suitable for healthy able-bodied people or patients after recovering from stroke or mobile impairments, who require less supports to maintain effective locomotions [60]. It is suggested in [71] that partial assistance is enough to enhance human mobility of healthy people since fully replacing their lower-limb muscle functions can lead to muscle atrophy or other side effects.

Compliant actuation systems can massively reduce exoskeleton's weight, enabling its portability. An active undressing trouser is an example of soft exoskeletons with potential to integrate with normal clothing, activated using a soft pneumatic smart adaptive belt to expand and loose the belt to undress the trouser [74]. This device possesses portability due to its on-board, lightweight air source, comprising a compressed gas cartridge, a valve and a small power supply with the total weight less than 100 g. Nevertheless, there is a compensation between compliance of actuators and their high assistive force generation. Increasing compliance can decrease force generation/transmission, bandwidth and accuracy of the actuation system [73].

In addition to compliance and high force generation, high actuation speed is a significant factor to produce compatible assistance with natural body movements. Asynchronous actuation can increase muscle power consumption and fatigue of users and can negatively alter patterns of their body movements. Moreover, exoskeletons are required to limit the range of motion of assisted lower-limb joints, for example, to prevent knee hyperextension.

Body Attachments and Garments

Ideally, people prefer to wear normal clothing which can intuitively provide them with desired assistance while being aesthetic and inconspicuous. A guideline in designing wearable assistive devices regarding their weight and size is provided in [73]. External loads on trunk and each foot should be less than 15% and 1.25% of the user's body weight, respectively. The thickness of wearable devices located along lower limbs should be less than 30 mm, and the total available volume of the energy source located on the user's back is limited to 0.023 m^3.

Body assistance while joint misalignment occurs is one of the most serious issues in wearable assistive devices since it can restrict natural body movements and cause ineffective assistance, discomfort, muscle injuries and skin damages, raising safety problems. Conventional rigid exoskeletons addressed this issue using a misalignment compensation [75]. An example of this mechanism can be found in a full-DOF hip exoskeleton comprising additional three rotational hinges and three perpendicular sliders which can passively adjust joint-assisted alignments to minimise undesired interaction forces [76]. Another example is iT-Knee, a 6-DOF self-aligning knee exoskeleton, allowing autonomous adaptability to a user's body and pure knee assistance decoupling from other joint motions [77]. However, these compensation mechanisms negatively added complexity and rigidity to exoskeletons.

Alternatively, textiles and flexible fabric materials, such as soft braces and straps, are the most promising solutions in creating compliant body attachments or garments providing compatibility with human body motions, increasing comfort and safety [47]. They can efficiently transmit assistive force to the body and decrease undesired misalignments during assistance. Key anchor is defined as an effective location for wearing assistive devices to attach on since it has the thinnest skin above the bone compared to surrounding area, for example, shoulder, iliac crest of hips and the bottom of feet, which can prevent misalignments while transmitting assistive forces through the body [14].

As mentioned in the actuation section above, although a totally soft assistive suit can reduce misalignments and has possibility to be integrate with normal clothing, it can cause ineffective power transmission, affecting controllability. However, in the future generations, actuation units and body attachments can be combined together, creating a multifunctional assistive suit capable of stiffness variability and morphology deformation. Every area on the suit can contain multiple layers for actuating, sensing and control units, operating synchronously to deliver the optimal assistance. These small areas must also be able to independently adapt their stiffness and locally deform. For example, at no assistance, the entire suit turns soft and harvests energy from shape deformation and heat loss released from the body surface. At the assisting mode for walking, certain regions of the suit on one leg become stiffer to aid a single leg support. Parts of suit on the other leg vary their stiffness to perform contraction and elongation to assist a swing motion while the regions around key anchors temporally turn rigid for efficient force transmission. These functions also enable adaptability and self-fitting to the user's body. For example, an inactive suit can be oversized for ease in donning/doffing and activated to firmly fit the user's body. Moreover, the shape changing capability of the suit can be used to expand it, e.g. by air inflation, when unpredicted falling is detected in order to absorb reaction force when hitting the ground, reducing body injuries.

In addition, the suit must be breathable to allow humidity and temperature exchanges on the skin surface for comfortable wearing. For example, the suit could have a self-deformable function, which is sensitive to surface's temperature and passively change its structure to inhale/exhale, interacting with surrounding air for cooling/warming the suit.

Sensing System

A sensing system in wearable devices is responsible for three main functions: (1) measuring force generation, (2) monitoring body motions and detecting locomotion activities and events, (3) evaluating assistance efficiency. First, an actuation unit requires force sensors, e.g. load cells, and strain sensors to measure actuator's outputs as a feedback input for a controller to deliver required force and strain accurately. They are also used to prevent undesired damage to the user's body, for instance, stopping actuation when high forces and out-of-range lower-limb's motions are detected.

Second, body-motion-capturing sensors (e.g. IMUs) and force/pressure insole sensors must be integrated with an assistive suit to indicate precise lower-limb's kinematic data, e.g. angle and velocity, and current state/event of locomotions as well as a ground reaction force for reversely calculating kinetic data. Different sensors can be used to obtain the required data. For example, IMUs with a gait prediction model can be used to acquire lower limb's kinematic data and recognition of locomotion. Three IMUs were attached to subject's thigh, shank and foot to predict walking activities, gait phases and events with high accuracy over 99% and within 240 ms for ground-level walking, ramp ascent and descent activities [78, 79]. A single IMU attached to the subject's thigh was able to recognise activity states and transition phases during sit-to-stand or stand-to-sit transitions with 100% accuracy within 50 ms [80]. These systems are highly accurate, fast, robust to disturbed noise and adaptable to variety of user's requirements, and also simplify a sensing system for wearable assistive devices. Recently, a soft multi-bend/shape sensor was invented, which is capable of measuring its deformed shape [81]. This device can be employed as one layer of the future suit/garment, which can simulate the entire garment's shape to predict locomotion activities, phases and events. Detecting force distribution over the user's skin surface is also necessary to be included in the suit for assessing compressed pressure and skin's damage, adjusting the assisting strategy and altering the garment's structure for user's comfort and safety.

Last, efficiency of mobility assistance can be evaluated by several methods: reduction of the metabolic energy cost and muscle activities, as well as heart rate [61]. Currently, the metabolic cost can be recorded at experimental and clinical platforms, and muscle activities can be detected using surface-electromyography (sEMG) sensors, measuring electric signals released from muscles when contracting. In the future technologies, all of these sensors need to become softer and beautifully embedded with normal clothing or garments, resulting in a super slim suit consisting of multiple layers of sensing devices, which can monitor entire wearer's body information.

Body Motion Simulator and Control Algorithm

Ideally, a virtual locomotion simulation can be simultaneously created using body data, acquired from sensors, to understand and analyse a suit wearer's locomotion pattern, while assisting body motion, with the aim of detecting muscle degeneration and mobility disorders, referring clinical information, and exploiting the optimal assisting strategy. A sophisticated controller is required to control a wearable device to generate right amount of assistive forces at right assistance timing [60].

Human-in-the-loop optimization is an example of a current advanced control algorithm which can significantly improve walking performance of users [61, 62]. These advanced controllers consist of two-level functions: a low-level control for producing required actuation outputs accurately, and a high-level control for adjusting actuator's requirements accord-

ing to the updated locomotion performance. The new generation of controllers must be self-adaptable to suit the variety of user's locomotion and consistently optimised based on current locomotion pattern to maximise assistance. Moreover, they must be capable of self-learning to create long-time strategies to improve or rehabilitate user's locomotion with remote communication with physical therapists. In future technologies, a soft high-speed computing microcontroller with the features described above needs to be embedded into the smart assistive suit.

This research mainly focuses on developing novel soft artificial muscles to create an advanced actuation unit. The next section reviews current state-of-the-art soft technologies and introduces potential soft actuators suitable for the future smart assistive suit and wearable robotic devices, which will be studied and developed further in this research.

2.6 Current Soft Actuators

As described before, soft actuators benefit from their typical light weight, inherent compliance, and high flexibility to adapt to surrounding environments, leading to safe interaction with human body, while producing large power-to-weight ratio and range of motions [16, 82]. They are widely used across healthcare, industrial and robotic sectors [16, 83–85]. In this thesis, three types of soft technologies are studied based on their power sources: thermal, pneumatic/hydraulic and electrical actuators. They have been reviewed in multiple literature, for example, Zhang et al [82] discusses their key performance metrics which are compared with human skeletal muscle (fig. 2.13). There are also other types of actuation technologies which are driven by chemical reactions, such as, Octobot [86], or environmental variation, including shape-changing smart materials triggered by water [87] and humidity [88]. More examples of soft actuation technologies are described in [85].

Soft thermally-driven actuators

Shape memory alloy (SMA) and shape memory polymer (SMP) are two examples of soft thermally-driven actuators, which can deform at low temperature and reverse to their memorised shapes when heated. SMA produces very high stress and power density compared to most soft actuators but very low strain, whereas SMP delivers higher strain but lower stress and power density than SMA [82]. Super-coiled polymer (SCP) is another thermally-driven actuator having higher linearity than the former actuators [82]. It is twisted polymer filaments, contracting when heated [89, 90]. It generates higher strain and stress than SMA and SMP, respectively, (fig. 2.13) and has been used to develop wearable arm assisting devices [91,92]. However, these thermally-driven actuators have low bandwidth, considerable hysteresis and extremely low efficiency because of slow thermal change and heat loss.

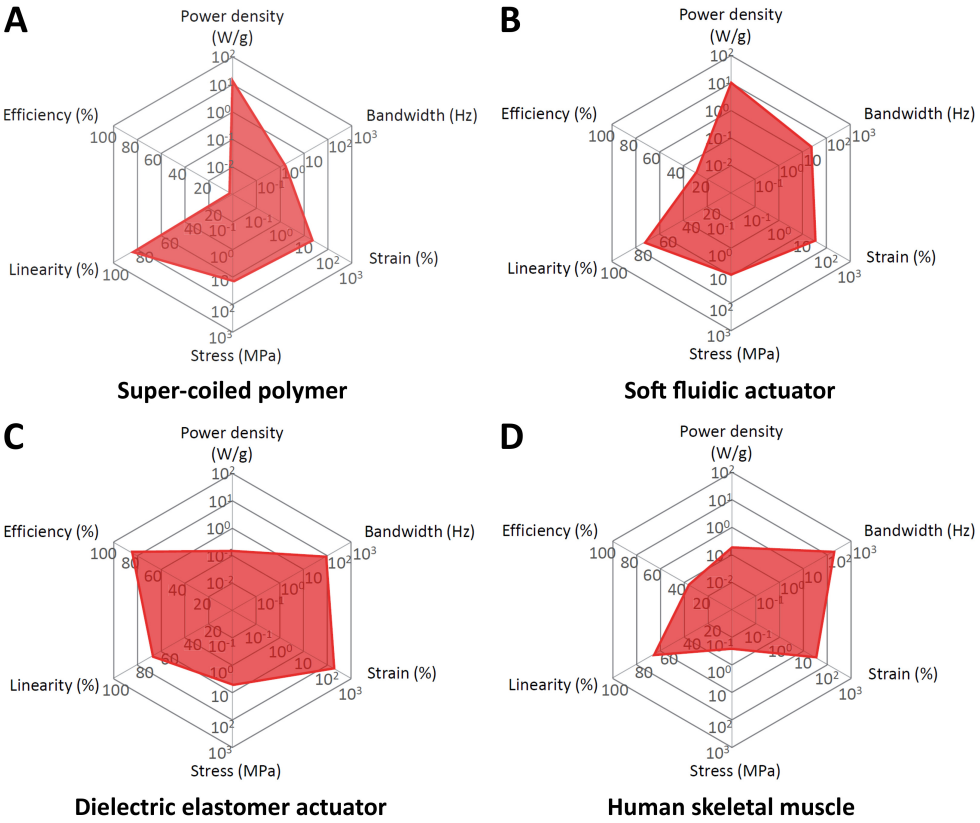

Figure 2.13: Comparison between (A) super-coiled polymer, (B) soft fludic actuators, (C) dielectric elastomer actuators and (D) human skeletal muscle regarding key performance metrics: stress, strain, bandwidth, power density, efficiency and linearity. Reproduced with permission from [82] © 2019 IEEE

Pneumatic Artificial Muscles

Soft fluidic actuators can produce sufficient stress and strain, compared to human muscles, although they have low efficiency (around 30%) during fluidic to mechanical energy conversion [82] (fig. 2.13). Soft pneumatic actuators operate at lower bandwidth than soft hydraulic actuator due to gas compression, but have lower weight, and are more suitable for wearable assistive devices (WADs).

Pneumatic Artificial Muscles (PAMs) have been consistently used in building WADs [72], for example, McKibben muscle [14], pleated PAM (PPAM) or straight-fibre muscle [19] and Pouch Motor [52]. Their major characteristics are their typical lightweight (excluding the weight of air sources), inherent compliance, backdrivability, low cost and high specific force and power [47]. The McKibben muscle (fig. 2.14A) is made of a length of elastic tubing enclosed by a stiff braided sleeve, which contracts to form a cylindrical shape under high pressure [93,94]. Similarly, straight fibre PAMs (fig. 2.14B) use an elastic tube featuring reinforced fibres to increase membrane strength and form a spherical shape when actuated [95–98]. In contrast, Pleated PAMs (PPAMs) only use a high-strength inexten-

sible material as an actuator membrane constrained by special end fittings to create equal radial pleats at the actuator ends, contracting to an elliptical shape under pressure [99], as shown in fig. 2.14C. Pouch Motors (fig. 2.14D) use a commercial flexible plastic material to create a lightweight series contractile actuator, allowing low-pressure actuation [55]. The two latter actuators take advantage of their inelastic material's strength, leading them to operate under pressure and produce contraction and tensile force.

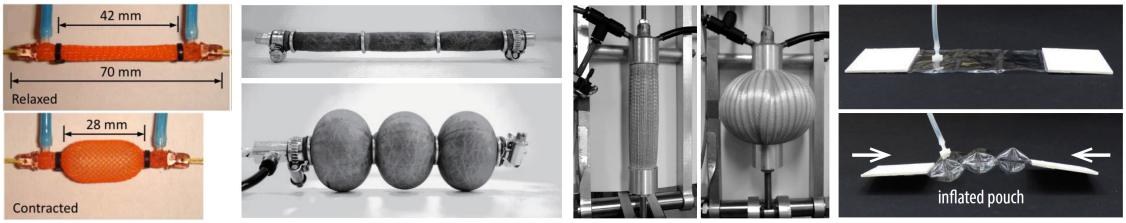

(a) McKibben Muscle (b) Straight fibre PAM (c) Pleated PAM (d) Pouch motor

Figure 2.14: Pneumatic artificial muscles commonly used for WADs: (a) McKibben PAM, (b) Pleated PAM, (c) straight-fibre muscle and (d) Pouch Motor. Reproduced from [18] © 2012 IEEE, [97], [100] © 2001 IEEE, [55] © 2014 IEEE

Table 2.2 compares the performance of these four PAMs. McKibben muscle and straight-fibre muscle can produce considerable tensile force, but operate at a high pressure range, which can be dangerous to use with human body. The PPAM has the highest contraction because of its maximum expanded shape and starts actuation at low pressure while exerting high maximum tensile force. However, these three PAMs contain rigid components, especially end fittings in order to withstand high pressure, reducing their compliance. On the other hand, the pouch motor is easily fabricated using only a flexible low-cost plastic sheet, allowing low pressure operation and high compliance, but it generate lower tension and contraction than the other PAMs due to a limited pressure range. In conclusion, the PPAM is the most suitable PAM design for developing wearable assistive devices due to its high tension and contraction. Deploying a softer material as used in pouch motor to fabricate the PPAM can simplify fabrication, generates compliant structure and possibly delivers a desired performance.

Soft Electrical Actuators

Soft electrical actuators have potential to become future robotic technology for WADs due to their high actuation performance, fast and quiet operation, and high efficiency [73, 82]. Electroactive polymers (EAPs) are active polymers which can change their shape when electrically charged, such as dielectric elastomer actuator (DEA) and ionic polymer-metal composite (IPMC).

Table 2.2: Comparison between potential Pneumatic Artificial Muscles (PAMs) for developing a wearable assistive device. (Th.) and (Ex.) indicate data sources from either theoretical calculation or experimental collection, respectively. Volume consumption is related to shape change of the actuators, and compliance refers to materials used to fabricate the actuators. Fabrication process and cost compares the level of difficulty in building each actuator and availability of the materials. Green and red colours represent, respectively, advantages and disadvantages of each actuator compared to the other PAMs presented here.

	McKibben muscle (since 19th century) [94, 97]	Straight-fibre muscle (since 2003) [96, 97, 101]	Pleated PAM (since 1999) [100]	Pouch motor (since 2014) [55, 56, 97]
Max tensile force [N]	650 (Ex.)	3,000 (Th.)	3,500 (Th.)	50-100 (Ex.)
Max contraction [%]	30 (Ex.)	35 (Ex.)	54.3 (Th.), 42 (Ex.)	36.34 (Th.), 28-30 (Ex.)
Pressure range [kPa]	100 - 500	100 - 300	10 - 300	0 - 40
Initial shape (0 kPa)	Cylinder	Cylinder	Cylinder	Flat
Maximum inflated shape	Cylinder	Circle	Ellipse	Circle
Volume consumption	Low	High	High	Medium
Material	Silicone tube + braided sleeve + metal connector	Reinforced carbon fibre + rubble tube + metal connector	Kevlar49 fabric + polypropylene film + mental end fitting	PVC or polyethylene sheets formed by heat sealing
Weight [g]	32	45	60	< 20
Compliance	Low	Low	Low	High
Fabrication process	Medium	Hard	Hard	Easy
Cost	Medium	Medium	High	Low

DEA is made of an elastomeric sheet sandwiched between stretchable electrodes. When charged, an electric field is generated between two opposing electrodes, causing Maxwell stress which compress the sheet, leading to contraction in thickness direction and surface expansion. It can produce high strain, bandwidth and efficiency (fig. 2.13) [82], and is widely used in robotic applications [102–104]. The main drawbacks of DEAs are high voltage requirement for actuation and technological limitations in fabricating stretchable electrodes. Low voltage actuation is achieved in IPMC actuator. When charged, ions inside the ionic polymers move between two opposing electrodes, resulting in a bending motion. However, it produces low stress and has low power density [82].

Recently, dielectric fluid electrostatic actuators have been introduced in dielectrophoretic liquid zipping actuator [105] and hydraulically amplified self-healing electrostatic (HASEL) actuators [106]. They add dielectric liquid between two opposite insulated electrodes to amplify the electrostatic force, resulting in high-performance zipping or hydraulic actuation. They are easily fabricated using inexpensive materials and have potential to be investigated for developing WADs.

2.7 Discussion

This chapter described the biomechanics of human mobilities and reduced locomotion efficiencies because of ageing, muscle weakness and change in lower-limb motion strategies to concentrate on body balance and prevent falling. The knee joint was concluded to be the most essential joint responsible for walking motion and sit-to-stand transition. It was selected to primarily design and develop an orthotic prototype improving human locomotion due to its simple one degree of freedom. Rigid and soft exoskeletons were reviewed in this chapter, showing their progressive developments, achievements in strengthening human body, restoring mobility disabilities, and remaining challenges. Demand for the wearable assistive devices and detailed technical requirements are listed and discussed as a guideline for developing the future smart assistive suit suitable for daily use.

Comparing the main soft actuation technologies, soft pneumatic and electrical actuators have an overall performance closest to human skeletal muscles (fig. 2.13) and high potential to address the user's needs and actuation requirements. Therefore, they are selected to be studied and developed towards the future smart assistive suit. The following chapters will present novel soft actuators developed in this research: Bubble Artificial Muscle (BAM) and BAM orthotic prototypes for human mobility assistance, Electro-ribbon Actuator (ERA) and Electro-pneumatic Pump (EPP).

Chapter 3

Bubble Artificial Muscle

The work described in this chapter has been submitted to the following peer-reviewed venue as:

- **Diteesawat RS**, Helps T, Taghavi M, Rossiter J. High Strength Bubble Artificial Muscles for Walking Assistance. *IEEE International Conference on Soft Robotics (RoboSoft)* 24 April 2018 (pp. 388-393).
- **Diteesawat RS**, Helps T, Taghavi M, Rossiter J. Characteristic Analysis and Design Optimisation of Bubble Artificial Muscles (BAMs). *Soft Robotics* 2020.

In this chapter, we introduce a novel pneumatic actuator, namely Bubble Artificial Muscle (BAM). This actuator is a lightweight, compliant, effective pneumatic muscle, designed to have similar structure and function as the conventional PPAM whilst being considerably simpler and less expensive. It is made of a thin, flexible inelastic tubing and stiff retaining rings. This grants the BAM flexibility and low- to high-pressure actuation to deliver either high contraction or high tensile force depending on the thickness and stiffness of the tubing material (fig. 3.1). The BAM can be designed to deliver the most suitable mechanical assistance for different parts of human body, which require different amounts of tensile forces and contractions. To enable this design flexibility, here we present characteristic analysis and design optimisation of Bubble Artificial Muscles, develop an actuator model encompassing the unique buckled folds at the rings and verify the model against experimentation with a range of BAM actuators.

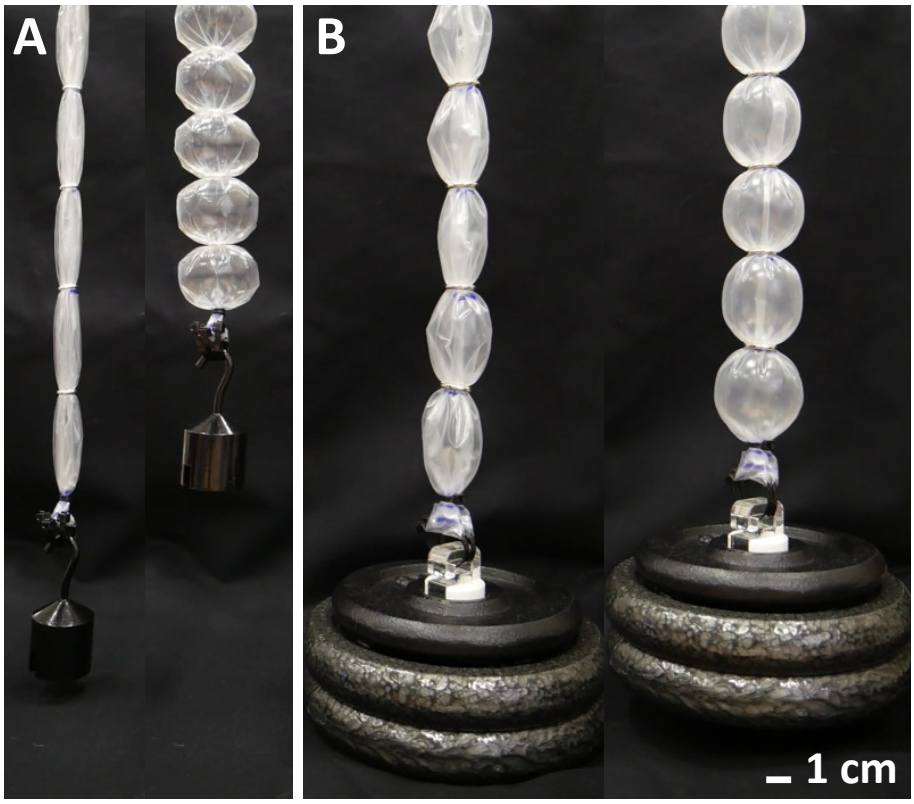

Figure 3.1: Actuation of Bubble Artificial Muscles (BAMs). (A) A BAM made of thin material (30.0 μm) delivers high contraction of 37.04% while lifting 0.5 kg. (B) A BAM made of thicker material (125.0 μm) delivers high tensile force, lifting 3.0 kg at contraction of 10.22%.

3.1 Previous Pneumatic Artificial Muscles (PAMs)

The BAM was developed applying the actuation behaviour of the Pleated Pneumatic Artificial Muscle (PPAM), but using a more compliant material as its main body, which is a plastic tubing as used in Pouch Motor. It was fabricated similar to the series Pneumatic Artificial Muscle (sPAM) but using metal retaining rings to effectively form the actuator shape instead of a rubber o-rings used in the sPAM. This allows the BAM to achieve higher contraction than the PPAM and higher tension than the sPAM, and results in a simple, low-cost fabrication. To derive the actuation model of the BAM, the understanding in the mathematical model of the PPAM and sPAM is required as follows. The PPAM model is summarised and modified for simplicity in derivation of the BAM model as follows.

3.1.1 Pleated Pneumatic Artificial Muscle

The Pleated Pneumatic Artificial Muscle (PPAM) was invented by Frank Daerden in 1999 [99]. PPAM is a muscle-like actuator operated by pressurised air as demonstrated in fig. 3.2A. It is made of a polymer with high tensile strength and high flexibility (actuator membrane – pink in fig. 3.2A) connected to two end fittings (actuator ends – grey in fig.

3.2A). The end fittings are specially made to feature several radial teeth, which create a series of pleats with equal spacing around the actuator end (cross-section area i in fig. 3.2A). When inflated, these pleats unfold, allowing the actuator membrane to expand circumferentially and radially, reaching a maximum inflated radius at the actuator centre (see cross-section area i, ii, iii and iv). Unfolding of these pleats happens with negligible friction and energy loss.

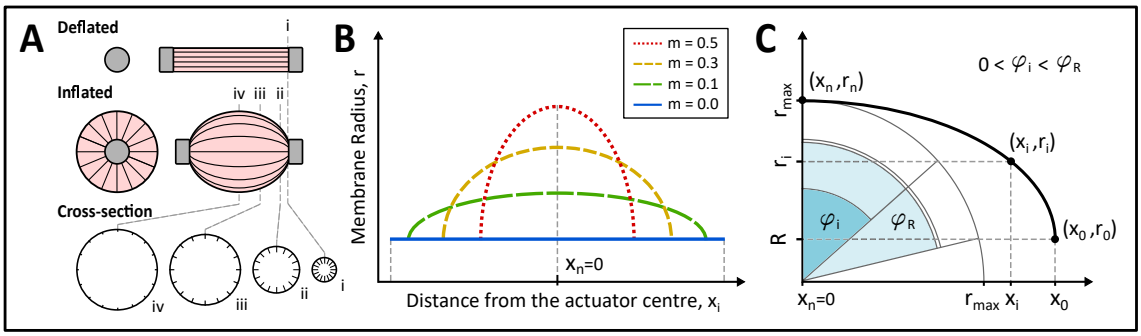

Figure 3.2: Fundamental concepts of Pleated Pneumatic Artificial Muscles (PPAMs). (A) The deflated and inflated shapes of the PPAM in top and side views with selected cross-sections perpendicular to the actuator axis. (B) Profile of the PPAM at different contractions simulated using different m values. (C) The definition of the parameters on the membrane surface, x and r, as a distance from the actuator centre and a membrane radius. Adapted from [99]

The characteristics of the PPAM are based on actuator length L, actuator radius R and applied pressure P, with the assumption of inelastic material behaviour. The PPAM mathematical model was derived using the elliptical integral with m and φ_R as dominant parameters to determine the actuator shape at any contraction c [99]. $\mathrm{F}(\varphi_R/m)$ and $\mathrm{E}(\varphi_R/m)$ are the elliptic integrals of the first kind and the second kind used to model the PPAM, which can be solved with the use of MATLAB (a numerical computing program).

$$\mathrm{F}(\varphi/m) = \int_0^{\varphi} \frac{1}{\sqrt{1 - msin^2\theta}} d\theta$$
$$\mathrm{E}(\varphi/m) = \int_0^{\varphi} \sqrt{1 - msin^2\theta} d\theta$$

m defines the actuator's shape and contraction, as demonstrated in fig. 3.2B. For example, an actuator at zero contraction ($c = 0$, blue solid line in fig. 3.2B) has an m value equal to zero, while the actuator at maximum contraction ($c = c_{max}$, red dotted line in fig. 3.2B) has an m value equal to 0.5 ($0 \leq m \leq 0.5$). φ_R is a characteristic angle mathematically related to the shape of the actuator membrane, and depends upon m, where $0 \leq \varphi_R \leq \frac{\pi}{2}$. φ_R can be calculated from eq. (3.1) by substituting L, R and m. This results in a φ_R value for each m value at any contraction for a single PPAM.

$$\frac{R}{\sqrt{m}\cos\varphi_R}\mathrm{F}(\varphi_R/m) = L \tag{3.1}$$

The contraction c and the tensile force F_t of the PPAM with the actuator size, L and R, and the shape at certain m and φ_R values when using an applied pressure P can be calculated from the following equations.

$$c = 1 - \frac{2R}{L}\left(\frac{\mathrm{E}(\varphi_R/m) - \frac{1}{2}\mathrm{F}(\varphi_R/m)}{\sqrt{m}\cos\varphi_R}\right) \tag{3.2}$$

$$F_t = \pi\ PR^2 \frac{1-2m}{2m\cos^2\varphi_R} \tag{3.3}$$

The actuator shape at a given contraction c is defined by x_i and r_i ($i = 0, 1, \ldots, n$), representing a point on the actuator surface as a horizontal axial distance from the actuator centre and a membrane radius from the axial line, respectively, as shown in fig. 3.2C. Each point on the actuator surface can be acquired by solving eq. (3.4) and (3.5) with constant R, m and φ_R, and different φ, varying from 0 to φ_R ($0 \leq \varphi \leq \varphi_R \leq \frac{\pi}{2}$). For instance, when $\varphi = \varphi_R, (x_i, r_i)$ is equal to (x_0, r_0), where x_0 is at the actuator end and $r_0 = R$. When $\varphi = 0, (x_i, r_i)$ is equal to (x_n, r_n), where x_n is at the actuator centre ($x_n = 0$) and $r_n = r_{max}$.

$$x_i = \frac{R}{\sqrt{m}\cos\varphi_R}\left(\mathrm{E}\left(\varphi/m\right) - \frac{1}{2}\mathrm{F}\left(\varphi/m\right)\right) \tag{3.4}$$

$$r_i = \frac{R}{\cos\varphi_R}\cos\varphi \tag{3.5}$$

The maximum actuator radius r_{max} at the actuator centre is as follows.

$$r_{max} = \frac{R}{\cos\varphi_R} \tag{3.6}$$

In addition to the actuator shape, the actuator volume v at any contraction c can be calculated using the following equation:

$$v = \frac{\pi R^2 L}{6m\cos^2\varphi_R}\left(1 - (1-2m)(1-c) + \frac{2R}{L}\sqrt{1 - \left(1 - 2m\sin^2\varphi_R\right)^2}\right) \tag{3.7}$$

Eq. (3.1), (3.2) and (3.3) are the main equations used to design the BAM. These equations were summarised from [99] and their simpler derivation are presented in the following section.

3.1.1.1 PPAM Mathematical Model

Three main equations of the PPAM mathematical model can be derived as follows.

Angle (φ_R)

Considering the actual membrane length of the actuator L_{actual} when dL is a small length along the actuator surface from $-x_0$ to x_0 (fig. 3.2C), therefore

$$L_{actual} = \int_{-x_0}^{x_0} dL$$

This integration can be solved with the use of the elliptical integral of the first kind $\mathrm{F}(\varphi_R/m)$ [99].

$$L_{actual} = \frac{R}{\sqrt{m}\cos\varphi_R}\mathrm{F}(\varphi_R/m) \tag{3.8}$$

Assuming that L_{actual} is different from the resting actuator length L due to a membrane strain ε caused by a meridional stress under an applied pressure P.

$$\varepsilon = \frac{L_{actual} - L}{L}$$
$$L_{actual} = L(1+\varepsilon)$$

The strain ε can be converted to a function of a, m and φ_R [99]. Therefore,

$$L_{actual} = L\left(1 + \frac{a}{2mcos^2\varphi_R}\right) \tag{3.9}$$

Where a implies the elasticity of the actuator's membrane, which is a function of an applied pressure P, an actuator radius R, a cross-sectional area at the actuator end A and Young's Modulus E of the actuator's membrane as follows.

$$a = \frac{\pi P R^2}{AE}$$

From eq. (3.8) and (3.9),

$$\frac{R}{\sqrt{m}\cos\varphi_R}\mathrm{F}(\varphi_R/m) = L\left(1 + \frac{a}{2mcos^2\varphi_R}\right) \tag{3.10}$$

Eq. (3.10) is used to calculate the angle φ_R of the PPAM with elasticity assumption of the actuator's membrane. When assuming that the membrane is inelastic, a becomes zero, and thus the equation with inelastic assumption is eq. (3.1) as follows.

$$\frac{R}{\sqrt{m}\cos\varphi_R}\mathrm{F}(\varphi_R/m) = L$$

Contraction (c)

Consider the contraction c in the axial direction of the actuator when L is the actuator length and x_0 is half of the axial actuator length when the actuator is inflated (fig. 3.2). Therefore,

$$c = \frac{L - 2x_0}{L}$$

$$x_0 = \frac{L}{2}(1-c) \tag{3.11}$$

x_0 can be derived by the elliptical integrals of the first kind $\mathrm{F}(\varphi_R/m)$ and second kind $\mathrm{E}(\varphi_R/m)$ [99] as follows.

$$x_0 = \frac{R}{\sqrt{m}\cos\varphi_R}\left(\mathrm{E}(\varphi_R/m) - \frac{1}{2}\mathrm{F}(\varphi_R/m)\right) \tag{3.12}$$

From eq. (3.11) and (3.12),

$$\frac{L}{2}(1-c) = \frac{R}{\sqrt{m}\cos\varphi_R}\left(\mathrm{E}(\varphi_R/m) - \frac{1}{2}\mathrm{F}(\varphi_R/m)\right)$$

Converting this equation leads to eq. (3.2) as follows.

$$c = 1 - \frac{2R}{L}\left(\frac{\mathrm{E}(\varphi_R/m) - \frac{1}{2}\mathrm{F}(\varphi_R/m)}{\sqrt{m}\cos\varphi_R}\right)$$

Tensile Force (F_t)

PPAM tensile force F_t at a given contraction c, derived from a pair of m and φ_R, can be calculated when knowing R and P [99] as follows.

$$F_{t,constant} = \pi P R^2 \frac{1-2m}{2m\cos^2\varphi_R}$$

According to the PPAM, when having constant pressure $P_{constant}$, the predicted tension to achieve a given contraction (from Equation (3.2) with a pair of m and φ_R value) can be calculated as follows.

$$F_{t,constant} = \pi P_{constant} R^2 \frac{1-2m}{2m\cos^2\varphi_R} \tag{3.13}$$

In contrast, when having constant tension $F_{t,constant}$, the predicted pressure to achieve a given contraction can be calculated as follows.

$$P = \frac{F_{t,constant}}{\pi R^2} \cdot \frac{2m\cos^2\varphi_R}{1-2m} \tag{3.14}$$

The PPAM mathematical model can be solved to obtain contraction and tensile force (for a given pressure) or applied pressure (for a given tensile force) as summarised in fig. 3.3; the actuator length L and actuator radius R are initial parameters. The BAM applies this mathematical model by substituting an initial unit length L_{unit} and a ring radius R_{ring} instead of L and R.

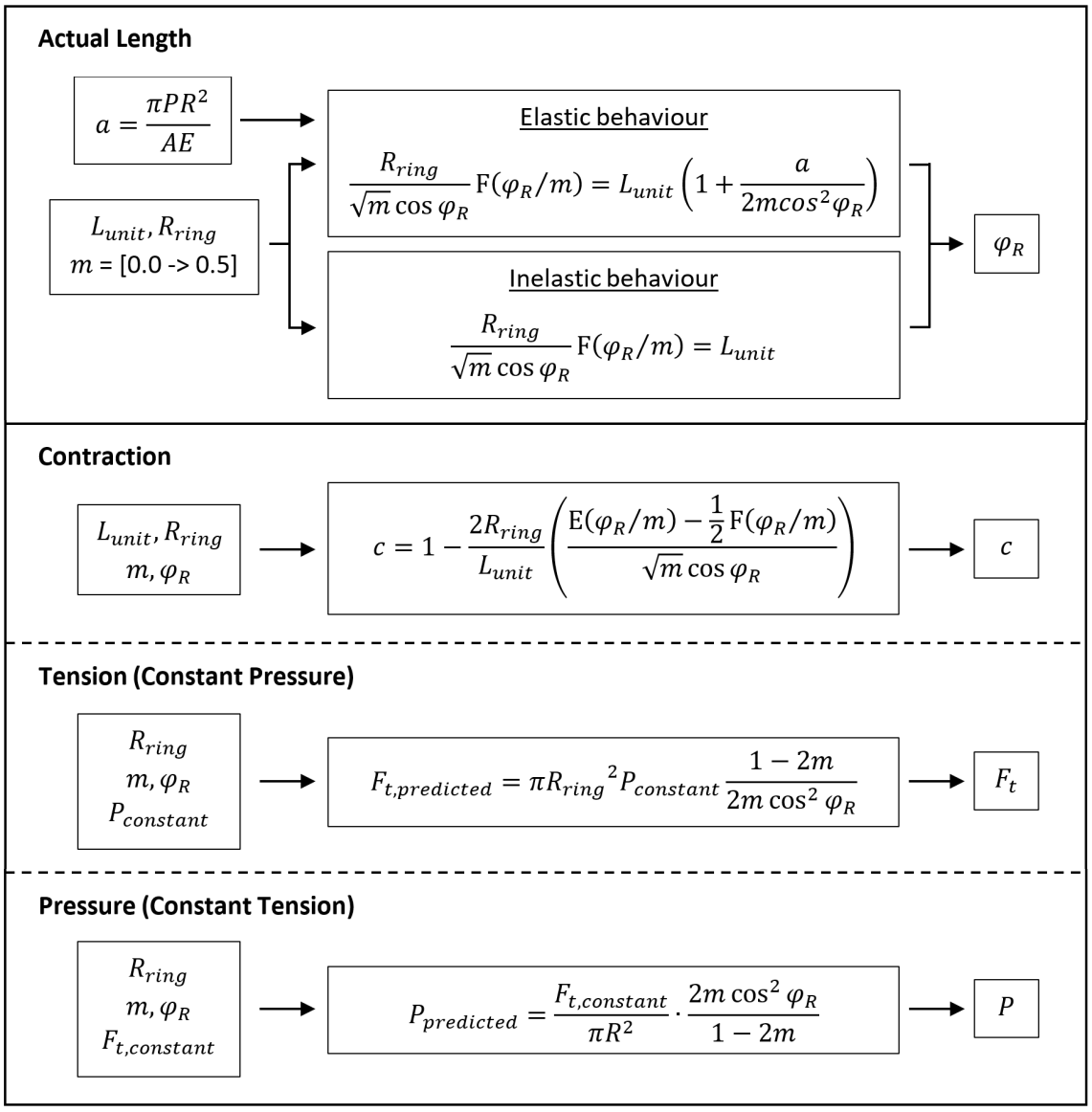

Figure 3.3: Conclusion of the PPAM mathematical model with input and output parameters.

For modelling the BAM with elastic behaviour, an applied pressure is necessarily assumed for calculating an elasticity of the actuator's membrane a before other following calculations. Therefore, the last equation calculating P (eq. (3.14)) cannot be used.

3.1.2 series Pneumatic Artificial Muscle

The Series Pneumatic Artificial Muscle (sPAM) is made of a long plastic tubing and rubber O-rings, creating a series of pneumatic actuators similar to the PPAM [107]. The sPAM was mainly designed for a pneumatic continuum robot with a sophisticated control system, allowing it to move in a three dimensional space while lifting a maximum load of 200 g. Unlike the PPAM, an inactive region appears in the sPAM when actuator length of the sPAM is greater than a certain threshold. This occurs when the inflated actuator

radius reaches the maximum material radius (the radius of the plastic tubing used to build the sPAM), causing the actuator to form a cylindrical region at the middle of the actuator. This region prevents the generation of further contraction and thus limits the overall contraction ratio. It is called as an inactive region. Although each contractile unit of the sPAM generates high contraction close to that of the PPAM model, it produces much lower tensile force than the PPAM due to its low material strength which limits high pressure operation. This actuator shows the potential to be used as an artificial muscle for wearable soft exoskeletons; however, it is necessary to improve tensile force and contraction.

3.2 Principal Characteristics and Concepts of Bubble Artificial Muscle (BAM)

Building upon the PPAM and sPAM designs, the Bubble Artificial Muscle (BAM) was developed to deliver high tensile force while maintaining high contraction. This is achieved by introducing stiff retaining rings and strong actuator material, allowing the BAM to sustain high pressure. The BAM is made using a polyethene plastic tubing and metal retaining rings (fig. 3.4A). Two metal rings (grey in fig. 3.4A) are inserted along the plastic tubing (pink in fig. 3.4A) to create a single contractile unit. These metal rings constrain the tubing to form a tight folded shape within the ring radius (cross-section AA in fig. 3.4A). Non-uniform folding of the plastic tubing extends along the actuator in the axial direction (red dashed lines in fig. 3.4A). These induced folds function similarly to the pleats in the PPAM. The result is a pneumatic artificial muscle that is considerably lower cost and easier to manufacture compared to the PPAM, whilst exhibiting higher tensile force compared to the sPAM.

When inflating the BAM by pressurised air, the actuator membrane unfolds and expands radially, and thus the actuator contracts, forming different expanded shapes, i.e. a vertical elliptical shape, a circular shape and a horizontal elliptical shape, depending on the level of applied pressure P (fig. 3.4B). Increasing the applied pressure results in an increase in actuator contraction. This increase happens only in the inelastic phase, whereby the membrane flexes and the actuator changes shape, with negligible elastic stretching of the membrane. If the pressure is increased beyond the point of maximum contraction, behaviour enters an elastic phase. In this phase, increasing the applied pressure causes the actuator membrane to stretch, inflating like a balloon, which results in a decrease in contraction. The optimal contraction happens when the actuator forms a horizontal elliptical shape in the inelastic phase, which resembles a “bubble”, leading to the name of the actuator, “Bubble Artificial Muscle”.

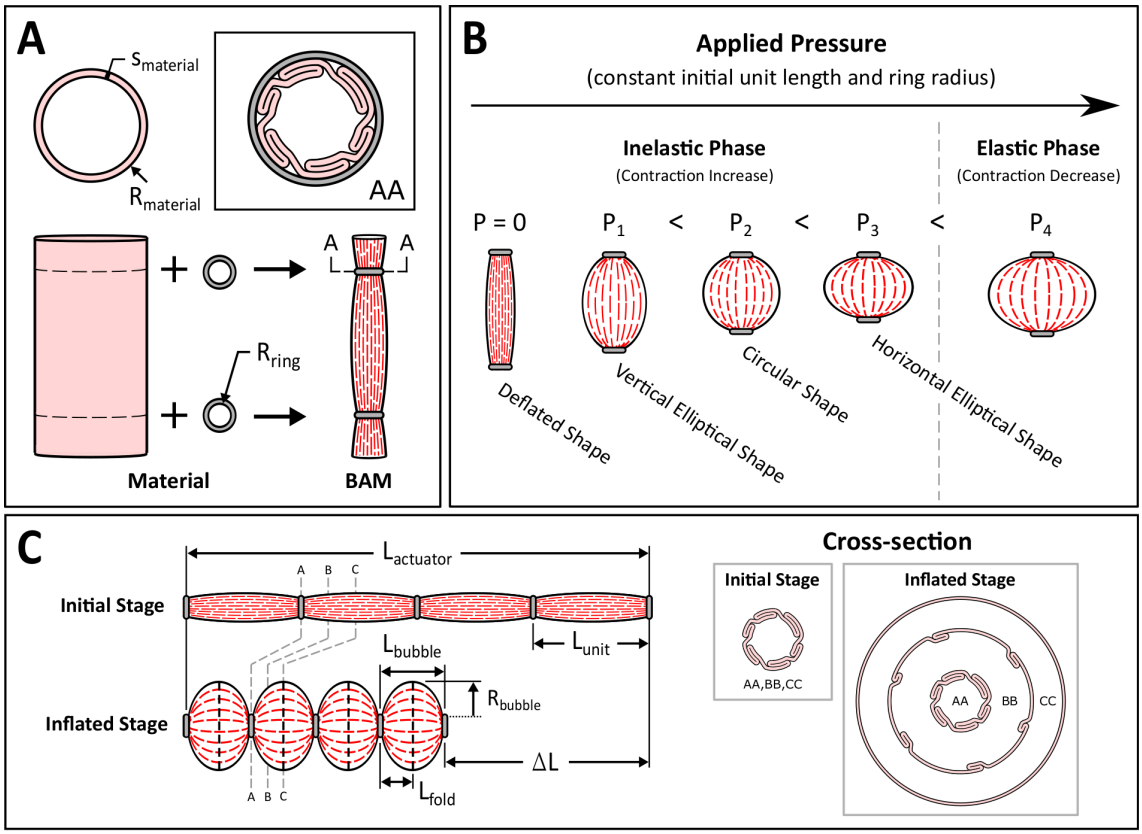

Figure 3.4: Fundamental concepts of Bubble Artificial Muscles (BAMs). (A) Components of a single-unit BAM: a plastic tubing and two metal rings, and the cross-section of the BAM at the actuator end (AA). (B) BAMs at different applied pressure, demonstrating the inelastic and elastic phases. (C) Definitions of BAM parameters, diagrams showing an optimal BAM at the initial stage and the inflated stage, and the cross-section of the actuator of these two stages at different points along the actuator (AA, BB and CC).

As shown in fig. 3.4A, the BAM is fabricated from an inelastic plastic tubing with a maximum material radius $R_{material}$ and a material thickness $s_{material}$ and metal rings with ring radius R_{ring}. With this design and fabrication method, the BAM can comprise of many contractile units aligned in series as demonstrated in 3.4C, enabling it to achieve any desired total strokes. For example, the BAM in 3.4C consists of four contractile units; therefore, it can produce a maximum stroke four times that of a single unit. At the initial stage, the length of the entire series of actuators is defined as an initial actuator length $L_{actuator}$, while that of each contractile unit is defined as an initial unit length L_{unit}. When inflated, the BAM contracts by stroke ΔL and a total contraction c, where $c = \Delta L / L_{actuator}$. Its inflated unit length and inflated unit radius are defined as a bubble length L_{bubble} and a bubble radius R_{bubble} at maximum shape expansion ($m = 0.5$), respectively.

The optimal contraction $c_{optimal}$ can be delivered by a BAM which has L_{unit} equal to the optimal unit length $L_{optimal}$, actuated at the maximum applied pressure that retains

inelastic behaviour (resulting in maximum shape expansion). At any applied pressure P, a folded membrane around the metal rings always exists, forming an actuator shape as in cross-section AA in 3.4C. However, when the optimal BAM is inflated, the amount of folded membrane reduces incrementally with distance from the metal rings until there is no folded membrane at the actuator centre as can be seen in cross-sections AA, BB and CC.

A fold length L_{fold} describes the length of the folded region of the BAM (red dashed lines in fig. 3.5) at maximum shape expansion in the axial direction, beginning from the actuator end and ending at the point where no folding appears on the membrane surface, shown as a black dashed line. Therefore, for the optimal BAM, L_{fold} is equal to half of L_{bubble} (or $L_{bubble} = 2L_{fold}$) as shown in fig. 3.5, left. L_{fold} varies depended on the ring radius R_{ring}, material radius $R_{material}$ and material thickness $s_{material}$ causing a different amount of folding at the actuator ends. Besides the optimal BAM, other expanded shapes can be obtained at the maximum applied pressure, depending on L_{unit}, R_{ring} and $R_{material}$. For example, when L_{unit} is too long, an inactive region occurs. $L_{inactive}$ defines the axial length of the inactive region (blue area in fig. 3.5, middle), and L_{fold} has the same length as that of the optimal BAM; therefore, $L_{bubble} = 2L_{fold} + L_{inactive}$. Alternatively, for shorter initial unit lengths, an overlapped region (red area in fig. 3.5, right) occurs due to the crossover of folding from both actuator ends ($L_{bubble,predicted} < 2L_{fold}$). This results in a considerably stiffer actuator membrane, leading to partial shape expansion at the maximum applied pressure ($R_{bubble,actual} < R_{material}$) and lower contraction ($L_{bubble,actual} > L_{bubble,predicted}$).

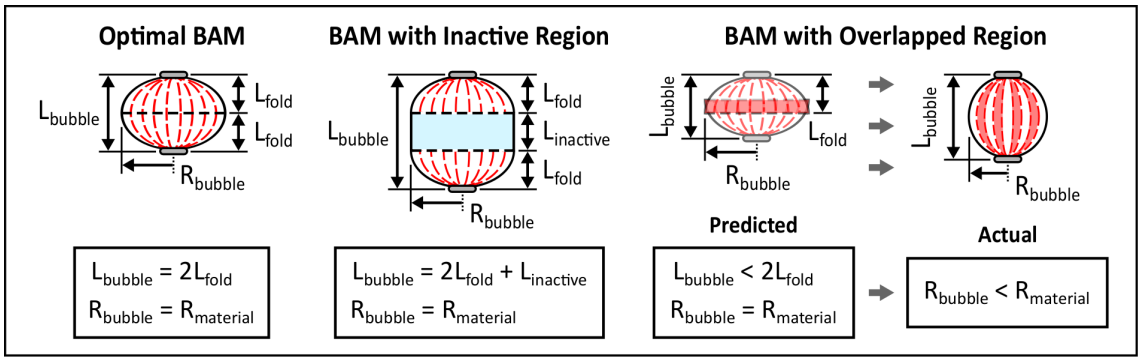

Figure 3.5: Different expanded shapes of different single-unit BAMs at maximum applied pressure in the inelastic phase, illustrating L_{bubble} and R_{bubble} at maximum shape expansion of (left) an optimal BAM, (middle) a BAM with an inactive region (blue area) and (right) a BAM with an overlapped region (red area).

Bubble Artificial Muscles are designed to produce sufficiently high force and contraction to drive an orthosis to assist human muscles. As described above, BAM characteristics depend on an initial unit length L_{unit}, a ring radius R_{ring}, an applied pressure P and a material thickness $s_{material}$. For instance, the optimal "bubble" shape expansion and high

contraction can be attained by carefully selecting L_{unit} and R_{ring} to avoid an overlapped region or an inactive region, while high force generation can be achieved by increasing $s_{material}$ and maximising P. Varying these four parameters leads to different performance of the BAM.

3.3 Effects of varying Fundamental Parameters on BAM's Performance

3.3.1 Experimental Setup

Several experiments were conducted to investigate the effects of P, L_{unit}, R_{ring} and $s_{material}$ and evaluate the resulting BAM performance. Three commercially available low-density polyethylene (LDPE) layflat tubes (Young's Modulus $E = 0.3$ GPa) with different thicknesses ($s_{material} = 30.0$, 62.5 and 125.0 μm) and similar radii (approx. 17 mm) were selected for fabrication into BAMs as shown in table 3.1 (LFT2120STK, LFT2250STK and LFT2500STK, Polybags Ltd, UK). The metal rings were made of metal with a thickness of 1.30 mm and internal radius of 4.5 mm (Oracle Jewellery, UK).

Table 3.1: The specifications of three selected LDPE layflat tubes used to fabricate BAMs.

Material thickness $s_{material}$ [μm]	Material radius $R_{material}$ [mm]
30.0	16.9
62.5	17.2
125.0	17.8

To evaluate the BAM performance, two types of experiments were undertaken: an isometric test and an isotonic test. For isometric testing, the BAM was oriented vertically, with the top end mounted on an acrylic frame connected to a 1kN load cell (700 Series S Beam Load Cell, Load Cell Shop, UK) and the bottom end attached to a linear actuator (LACT8P, Concentric International, USA). The tensile force was measured by the load cell through a load cell amplifier (RW-ST01A, SMOWO, China), and the actuator stroke was controlled by the linear actuator and recorded by a laser displacement sensor (LK-G152, Keyence, Japan). Pressurised air was supplied by an air compressor (CW 100/24 AL, Werther International S.p.A., Germany) connected to the actuator through a pressure regulator (AR20-F02H010B, SMC, UK) and a solenoid valve (WZ-98302-46, Cole-Parmer, UK), which were used to regulate the pressure level and inflate and deflate the actuator. A pressure sensor (HSCDANN030PGAA5, Honeywell, US) was located close to the actuator to measure the applied pressure. For isotonic testing, the bottom end of the actuator was disconnected from the linear actuator and a test mass was hung instead. The rest of the test environment was identical to the isometric test.

All tested BAMs consisted of four contractile units, excluding the optimal-unit-length

experiment. Isometric tests were used to investigate the effects of varying P, L_{unit}, R_{ring} and $s_{material}$ of BAMs. For example, fig. 3.6 illustrates the relationship between tensile force and contraction of BAMs made of the same $s_{material}$ while varying other parameters, and fig. 3.7 shows the relationship between tensile force and pressure of BAMs made of different $s_{material}$ with constant L_{unit} and R_{ring}. Isotonic tests were used to investigate the maximum contraction of BAMs while holding external loads, resulting in the relationship between contraction and pressure. The results of these experiments lead to the conclusion of the BAM characteristics presented in the following sections.

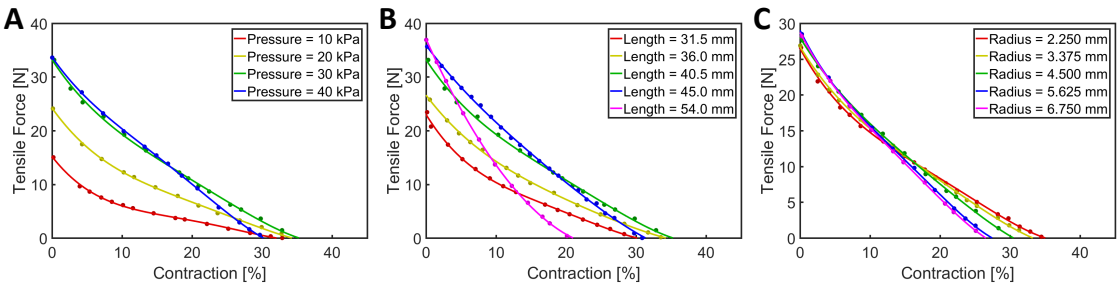

Figure 3.6: The relationship between tensile force and contraction of BAMs acquired from the investigation of the effect of (A) increasing applied pressure, (B) varying initial unit length and (C) varying ring radius at any stroke ΔL when other parameters are constant (L_{unit} = 40.5 mm, R_{ring} = 4.5 mm and P = 30 kPa). The dots and lines represent the experimental data and fitting curve, respectively.

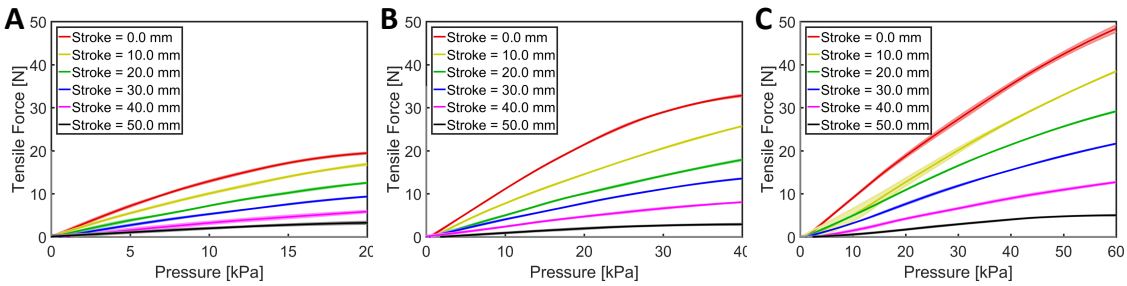

Figure 3.7: The relationship between tensile force and pressure of the BAMs with L_{unit} = 40.5 mm, R_{ring} = 4.5 mm and different $s_{material}$ = (A) 30.0, (B) 62.5 and (C) 125.0 μm from the isometric tests, when fixing the actuator at different strokes. Different thickness BAMs are inflated to a different maximum pressure. The solid line is the mean of the three trials for each condition, and the faded area defines the total range (min to max) of the experimental results.

In the experimental results that follow, maximum contraction c_{max} is the contraction at zero tensile force ($F_t = 0$) and maximum tensile force $F_{t,max}$ is the tensile force at zero stroke ($\Delta L = 0$). A fourth-degree polynomial curve fitting was used to match the experimental data from the relationship between tensile force and contraction (e.g. fig 3.6), using the MATLAB "*fit*" function with method of 'poly4'.

3.3.2 Increasing Applied Pressure (P)

A BAM with L_{unit} = 40.5 mm, R_{ring} = 4.5 mm and $s_{material}$ = 62.5 μm is first considered as an example to show the effect of increasing P. As shown in fig. 3.8, the contraction and tensile force of the BAM increases with an increasing pressure. It achieves a maximum contraction of 32.01%, 34.23% and 35.23% at P = 10.0, 20.0 and 30.0 kPa, respectively, with maximum contraction decreasing to 30.15% at P = 40 kPa. This reduction can be explained by the progression from the inelastic phase to the elastic phase as presented in fig. 3.4B. Increasing applied pressure over a certain threshold (between 30 and 40 kPa in this case) causes the actuator membrane to stretch (behaviour enters the elastic phase) and results in a decrease in the maximum contraction. Further increasing pressure would lead to irrecoverable plastic deformation and ultimately rupturing, therefore experiments were halted when elastic behaviour occurred, prior to rupture. This stretching behaviour can occur at any contraction, not only at zero tensile force, affecting the actuation behaviour of the BAM when exceeding the pressure threshold, for example, the BAM actuated at 40 kPa as shown in fig. 3.6A.

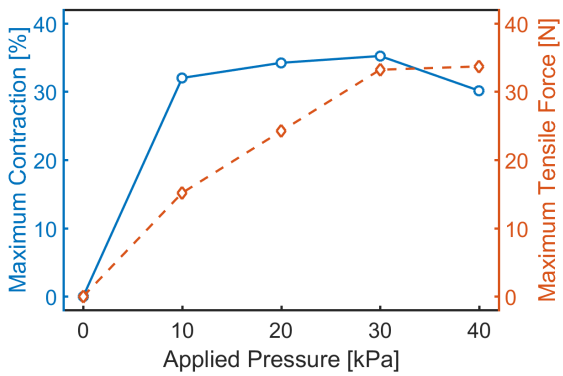

Figure 3.8: Effects of varying applied pressure P on BAM's Performance. Maximum contraction (left y-axis) and maximum tensile force (right y-axis) of a BAM with L_{unit} = 40.5 mm, R_{ring} = 4.5 mm and $s_{material}$ = 62.5 μm, operated at different P.

3.3.3 Varying Initial Unit Length (L_{unit})

Five BAMs with L_{unit} of 31.5, 36.0, 40.5, 45.0 and 54.0 mm but constant R_{ring} of 4.5 mm (slenderness ratio $SR = L_{unit}/R_{ring}$ = 7, 8, 9, 10 and 12) and $s_{material}$ of 62.5 μm were tested to demonstrate the effect of varying L_{unit}. Constant P of 30.0 kPa was used to inflate the BAMs without stretching behaviour. As shown in fig. 3.9a, the greatest maximum contraction occurs at L_{unit} = 40.5 mm (SR = 9). Lower maximum contraction appears at shorter L_{unit} (SR = 7 and 8) and longer L_{unit} (SR = 10 and 12) due to the appearance of the overlapped region and the inactive region, respectively. This supports the hypothesis that the BAM contraction is optimal at only one initial unit length where $L_{unit} = L_{optimal}$.

In contrast, the maximum tensile force increases when L_{unit} is higher. This is because the BAM has larger membrane surface area at $\Delta L = 0$ (membranes surface area is roughly equal to $2\pi R_{ring} L_{unit}$). The fluid pressure is applied over a larger surface, resulting in higher total radial force and thus higher tensile force.

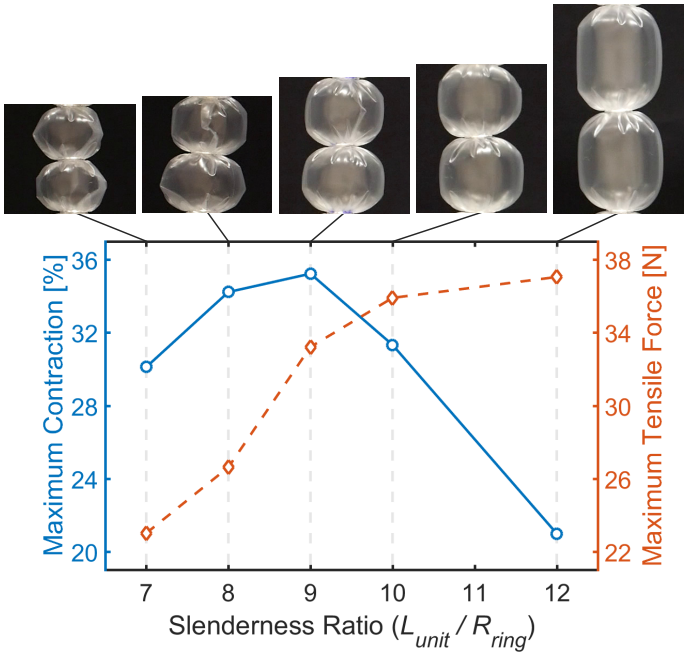

(a) Varying L_{unit}

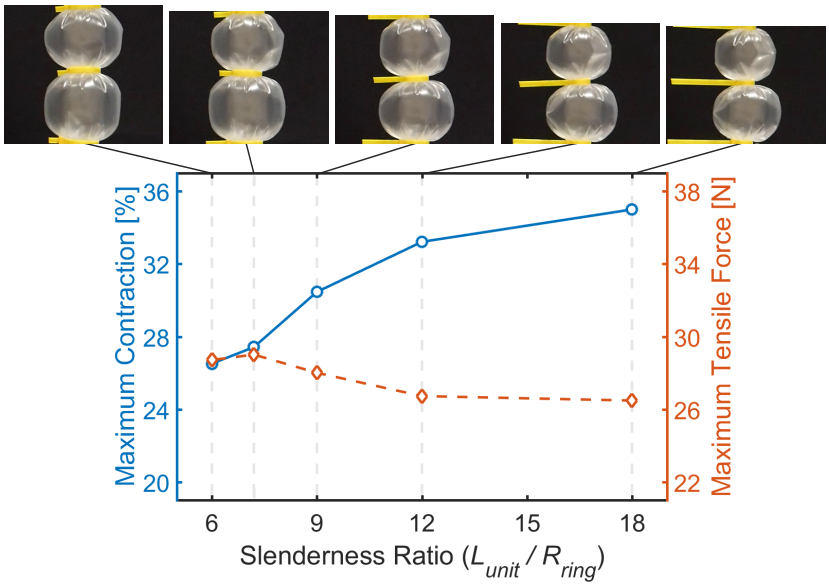

(b) Varying R_{ring}

Figure 3.9: Effects of varying L_{unit} and R_{ring} on BAM's Performance. The BAMs made of $s_{material} = 62.5$ μm with different slenderness ratios $SR(L_{unit}/R_{ring})$, where (a) $R_{ring} =$ 4.5 mm and (b) $L_{unit} = 40.5$ mm, actuated at $P = 30.0$ kPa (images show the maximum expanded shape of the middle two contractile units of the tested BAMs).

3.3.4 Varying Ring Radius (R_{ring})

A BAM with constant L_{unit} of 40.5 mm and $s_{material}$ of 62.5 μm was created by using plastic cable ties in place of metal rings because of the ease in controlling internal radius. Ring radii of 6.750, 5.625, 4.500, 3.375 and 2.250 mm (SR = 6, 7.2, 9, 12 and 18) were selected to investigate the effect of varying R_{ring}. The actuators were inflated at constant P = 30.0 kPa. From fig. 3.9b, decreasing R_{ring} results in higher maximum contraction and reduction of the inactive region. However, an overlapped region occurs when the BAM has too small R_{ring}, causing lower contraction than predicted by the PPAM model. As in the prior length-varying tests (fig. 3.9a), the maximum tensile force increases with a ring radius because of the larger membrane surface area at $\Delta L = 0$.

3.3.5 Optimal Unit Length($L_{optimal}$)

The effects of the overlapped region and the inactive region, which influence $L_{optimal}$, were studied further with the BAM made of the thinnest material, providing the actuator membrane with flexibility to easily unfold and expand. A series of BAM units with different L_{unit} from 20.0 to 60.0 mm at increments of 5.0 mm were built as a single long actuator. Metal rings with R_{ring} = 4.5 mm and a thin plastic tubing with $s_{material}$ = 30.0 μm were selected for fabrication. The experimental procedure involved inflating the BAM at P = 10 kPa, measuring its inflated length (using a calliper) and deflating. This experiment was repeated three times for each L_{unit}, and no external load was applied on the actuator. The maximum measured contraction of each single-unit BAM is presented in fig. 3.10.

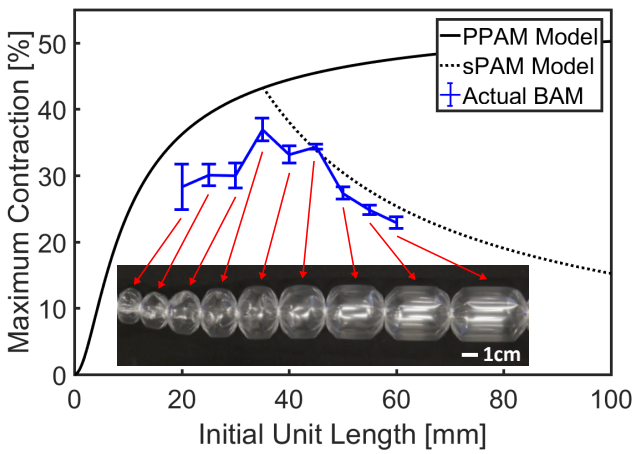

Figure 3.10: Maximum contraction of a series of BAMs with different L_{unit} but constant R_{ring} = 4.5 mm and $s_{material}$ = 30.0 μm, actuated at P= 10.0 kPa (the PPAM and sPAM models are plotted, and the image of the actual BAMs is inset).

The largest contraction (mean at 36.94% and maximum at 38.71%) was observed for the BAM with L_{unit} = 35.0 mm, which is close to the predicted $L_{optimal}$ (35.2 mm, where $R_{bubble} = R_{material}$). The BAMs with $L_{unit} < L_{optimal}$ follow the general trend of the

PPAM model [99], but there is an offset (a reduction in contraction) as a result of the overlapped membrane. The BAMs with $L_{unit} > L_{optimal}$ follow the general trend of the sPAM model [107] since the inactive region appears.

3.3.6 Varying Material Thickness ($s_{material}$)

Isotonic and isometric tests were performed to evaluate the BAM capability to produce contraction with external load of 1 kg and maximum tensile force at $\Delta L = 0$ mm, respectively. The experimental results for BAMs with the same $L_{unit} = 40.5$ mm and $R_{ring} = 4.5$ mm but different material thicknesses of $s_{material} = 30.0$, 62.5 and 125.0 μm are presented in fig. 3.11. The predicted PPAM contraction (which neglects the thickness of the actuator membrane) is included in fig. 3.11A: the PPAM model predicts infinite tensile force at zero contraction so this is not included in fig. 3.11B.

Overall, BAMs with thicker membranes produces less contraction and generally less tensile force at the same applied pressure, deviating increasingly from the PPAM model prediction (as shown in fig. 3.11A). However, since BAMs with thicker membranes were able to withstand higher pressure, their maximum contraction and tension surpassed that of the BAMs with thinner membrane. From fig. 3.11B, the tensile force of each BAM tends to decrease due to stretching behaviour when applied pressure approaches maximum pressure; increasing applied pressure further can cause the BAM to burst. The results of the isometric test measuring tensile force of the three BAMs at strokes other than zero are previously shown in fig. 3.7.

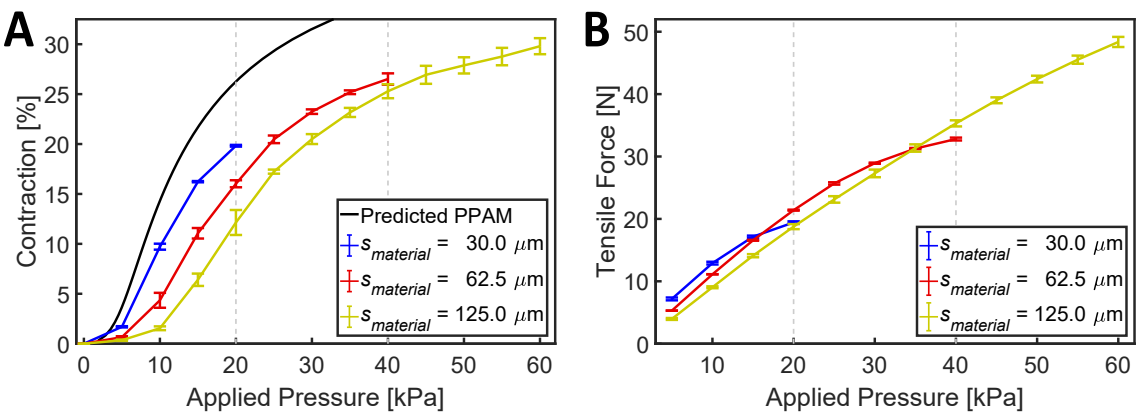

Figure 3.11: Contraction and tensile force of BAMs ($L_{unit} = 40.5$ mm and $R_{ring} = 4.5$ mm) with three different $s_{material}$ were measured from (A) isotonic testing while with a 1 kg load and (B) isometric testing with $\Delta L = 0$ mm; operated from 0 kPa to maximum pressures of 20, 40 and 60 kPa, respectively, depending on $s_{material}$. The two vertical grey dashed lines indicate the maximum tested pressure of the BAMs made from 30 μm and 62.5 μm thick material, respectively. The predicted PPAM model is included only in the contraction-pressure relationship (A).

Further isometric tests were performed to obtain the relationship between tensile force and contraction of BAMs with different $s_{material}$, as shown in fig. 3.12A. They were tested with different P of 10, 30 and 50 kPa, based on their $s_{material}$, well below the maximum pressures observed in fig. 3.11. As a result, the thin-membrane BAM can produce the highest contraction of 39.48% due to its membrane flexibility in unfolding and expanding, and the thick-membrane BAM can generate the highest tensile force up to 56.90 N.

Fig. 3.12B shows the effect of decreasing R_{ring} upon maximum contraction for BAMs made from three different $s_{material}$. BAMs made from L_{unit} = 40.5 mm and R_{ring} = 6.750, 5.625, 4.500, 3.375 and 2.250 mm were evaluated under zero tensile load. P was chosen to be well below the maximum pressure of each material. The theoretical maximum contraction of the PPAM and sPAM are also shown and are listed in table 3.2. As can be seen in fig. 3.12B, discrepancy between the PPAM and sPAM models is maximised at high R_{ring} due to the inactive region. Decreasing R_{ring} reduces the size of the inactive region, and the sPAM model more closely matches the PPAM model. Decreasing R_{ring} increases the maximum contraction of the actual BAMs. However, it also results in a higher reduction in BAM contraction compared to the sPAM model due to the material thickness (both the PPAM and sPAM models assume a zero-thickness membrane). This behaviour occurs with all $s_{material}$ but is more pronounced with higher $s_{material}$. The sPAM model includes only the effect of the inactive region, but higher fold lengths, and a consequential overlapped region, are more likely to appear in actual BAMs with higher $s_{material}$. Consequently, to more accurately capture BAM actuation we must include these effects in the model.

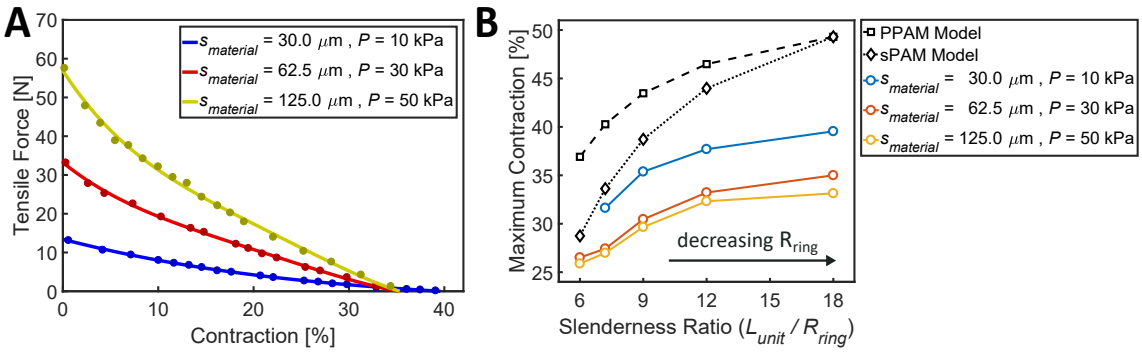

Figure 3.12: (A) The relationship between tensile force and contraction of the BAMs with different $s_{material}$ but the same L_{unit} = 40.5 mm and R_{ring} = 4.5 mm, operated with different applied pressure P. Dots indicate measured data from experiments, to which curve-fitting lines have been added. (B) Maximum contraction of the BAMs made using cable ties with L_{unit} = 40.5 mm, with different slenderness ratios SR (L_{unit}/R_{ring}), R_{ring} and $s_{material}$, actuated at different P. PPAM model (dashed line) and sPAM model (dotted line) predictions are also shown.

Table 3.2: Theoretical maximum zero-tension contraction of the PPAM and sPAM with constant L_{unit} = 40.5 mm, but various R_{ring}, where $L_{optimal}$ is based on $s_{material}$ = 62.5 μm and $R_{material}$ = 17.2 mm. (* shows that $c_{sPAM} = c_{PPAM}$ since $L_{unit} < L_{optimal}$).

R_{ring}	$L_{optimal}$ [mm]	at $L_{optimal}$	at L_{unit} = 40.5 mm	
		c_{PPAM} [%]	c_{PPAM} [%]	c_{sPAM} [%]
2.250	40.57	49.30	49.29*	49.29*
3.375	38.32	46.48	46.88	43.98
4.500	36.07	43.47	44.57	38.71
5.625	33.81	40.27	42.36	33.62
6.750	31.54	36.91	40.25	28.74

3.4 BAM Performance

Typical pneumatic actuators can deliver a maximum contraction of around 25-35%, e.g. McKibben muscle and Pouch Motor [55, 94]. Since the maximum expanded shape of the PPAM, sPAM and BAM actuators is the horizontal ellipse (fig. 3.4B), they can all feasibly reach a maximum contraction of 45.5% [108]. A single-contractile-unit PPAM with $L_{actuator}$ = 100.0 mm, $R_{actuator}$ = 12.5 mm and weight of 58.3 g was able to deliver a maximum contraction of 41.5% and a maximum tension of 3,500 N under P = 300 kPa [99]. An sPAM with R_{ring} = 2.5 mm can deliver a maximum contraction and tension of approximately 40% and 9 N, respectively, actuated at P = 10.34 kPa [107].

Compared to these PAMs, the BAM can be designed to deliver either high contraction when using the thinnest $s_{material}$ and the smallest R_{ring} or high tension when using the thickest $s_{material}$ and operating under high P. The highest contraction of 43.11% was delivered by the BAM with $s_{material}$ = 30.0 μm, L_{unit}= 40.5 mm, R_{ring} = 2.0 mm and an actuator weight of 2.83 g while producing a maximum tensile force of 13.25 N (fig. 3.13). A BAM with L_{unit} = 40.5 mm, R_{ring} = 4.5 mm and higher $s_{material}$ of 125.0 μm delivered a maximum tensile force of 56.9 N (= 0.894 MPa), which corresponds to lifting a load 1,000 times its own weight (5.39 g), and deliver a maximum contraction of 35.2% when operated at a pressure of 50.0 kPa (fig. 3.12A). The specific force and energy were calculated from the maximum tensile force and the relationship between tensile force and contraction of the BAM with $s_{material}$ = 125.0 μm (fig. 3.12A), respectively. Its average and peak specific powers were calculated from an isotonic test of the BAM loaded 1 kg weight, actuated up to 50 kPa. The specific power can be increased by using a higher power air source for faster BAM actuation. Compared to human muscle, the BAM can produce higher performance, as shown in table 3.3. However, these specific values consider merely the weight of the actuator, excluding air sources. When the additional mass and volume of a heavy air supply (pump or pressure vessel) is included, total system performance will be lower than that of human muscle.

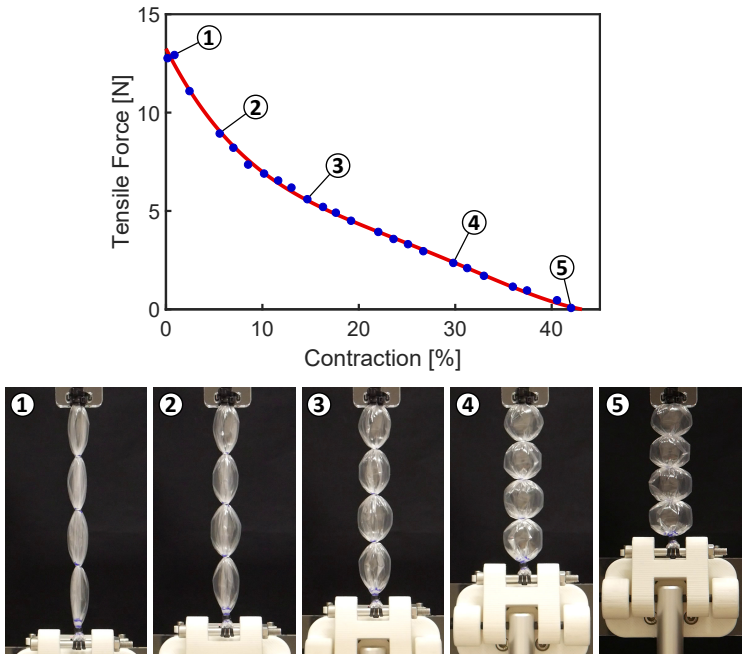

Figure 3.13: The BAM made of $s_{material}$ = 30.0 μm, L_{unit}= 40.5 mm and R_{ring} = 2.0 mm delivered the highest contraction up to 43.11% and the highest tensile force of 13.25 N, operated at 10 kPa, during an isometric test. Images illustrate the BAM at different contraction.

Table 3.3: Comparison of the key performance metrics between mammalian/human muscles [73, 109] and Bubble Artificial Muscles (BAMs). *Specific power of the BAMs are presented as average (peak); the peak specific power was considered from the generated potential energy of every 0.01 second. Specific values consider only the weight of the BAM, excluding air sources.

Key performance	Mammalian/human muscles	Bubble Artificial Muscles
Maximum stress (MPa)	0.35	0.894
Maximum Strain (%)	>40	43.1
Specific force (N/kg)	1,000	10,557
Specific energy (J/kg)	8	108
Specific power (W/kg)	50	48 (79)*

The weight of the BAM is less than one tenth that of the PPAM because of its simpler actuator ends and lighter materials. Although the BAM produces less tension than the PPAM, its actuation is more sensitive to an applied pressure, enabling it to initialise contraction at low pressure, whereas the PPAM can effectively operate at the pressure over 100 kPa [108]. Three BAMs made of the same actuator design and materials had similar tension-contraction relationship; the sample variation is shown in fig. 3.14.

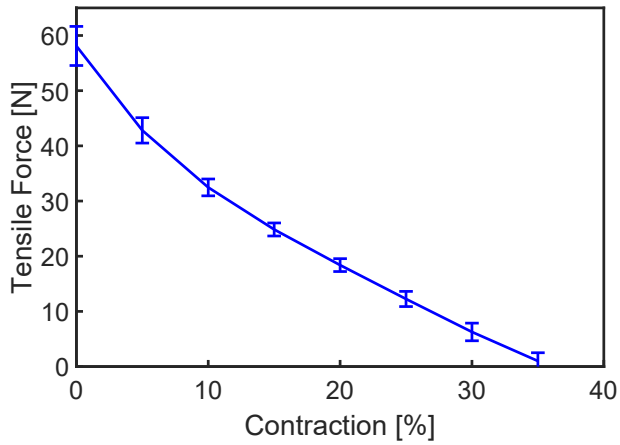

Figure 3.14: Sample variation of three BAMs, made of the same $s_{material}$ = 125.0 µm, L_{unit} = 40.5 mm and R_{ring} = 4.5 mm, actuated at P = 50 kPa, showing tension-contraction relationship.

3.4.1 Comparison between BAM and other PAMs

Although the BAM superficially resembles the PPAM, they have different fundamental structures due to different actuator ends: a special end fitting for the PPAM and a metal ring for the BAM (fig. 3.15). The PPAM has uniform pleats in the radial direction, whereas the folds of the BAM are in lateral direction. These lateral folds are freely and non-uniformly folded around the metal ring, creating a region of overlapping folds, which naturally resists the radial expansion of the BAM. As membrane thickness increases, the amount of lateral folds also increases (fig. 3.16), increasing resistance to BAM shape expansion and reducing contraction and tension. However, higher thickness materials can withstand higher applied pressures, leading to higher expanding force and thus higher tensile force and maximum contraction of the BAM when loaded (fig. 3.11).

When the BAM is inflated, the folds unfold by sliding and bending to expand the actuator shape (fig. 3.15), approaching the circular actuator cross-section (CC in fig. 3.4C). The thickness of the folded membrane along the actuator axis x may be defined as the bubble surface thickness $s_{bubble}(x_i)$, where x_i is the distance from the actuator centre (fig. 3.2). $s_{bubble}(x_0)$ is highest at the actuator ends (higher than $s_{material}$), where many overlapping folds occur, and reduces toward the middle of the actuator where no overlapping folds occur such that $s_{bubble}(x_n) = s_{material}$ when inflated (fig. 3.15). Unlike the BAM, the PPAM has no overlapping folds due to its radial folding structure, resulting in zero-friction shape expansion when inflated.

While the sPAM and BAM share some functionality, the sPAM was designed to control the movement of lightweight continuum robots. In contrast, the BAM was designed as a high-power artificial muscle (e.g. for wearable assistive applications), necessitating higher contraction and tension. Various aspects of the BAM design result from these higher

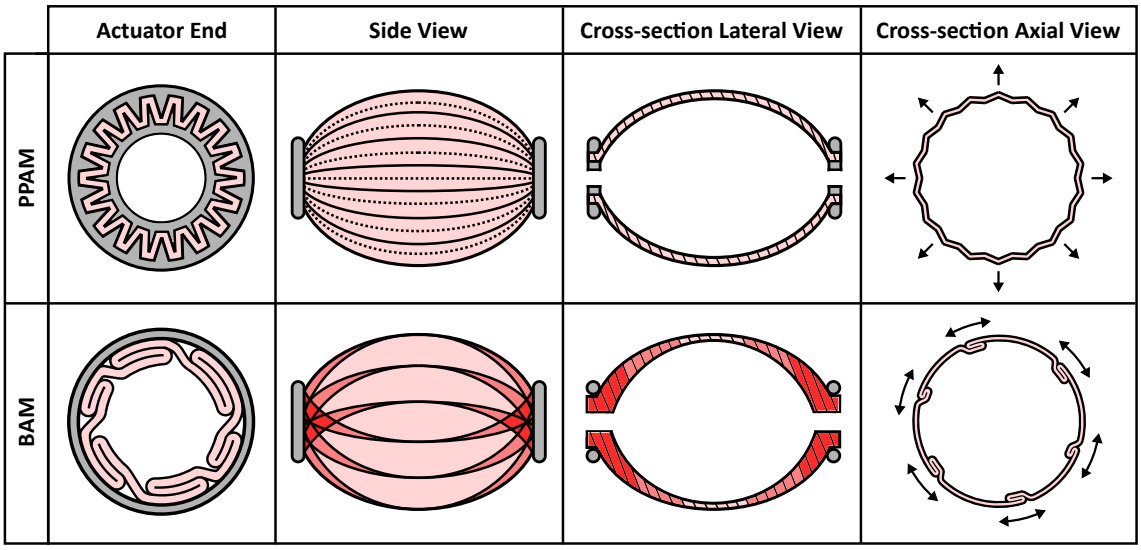

Figure 3.15: Cross-section view of the actuator end, side view, cross-section lateral view, and cross-section axial view showing membrane expansion, comparing the PPAM and BAM. The pink area is the actuator's material, and the grey area is the actuator ends: the special end fitting for the PPAM and the metal ring for the BAM. A pink colour indicates thin membrane, while a red colour indicates where multiple membrane folds occur.

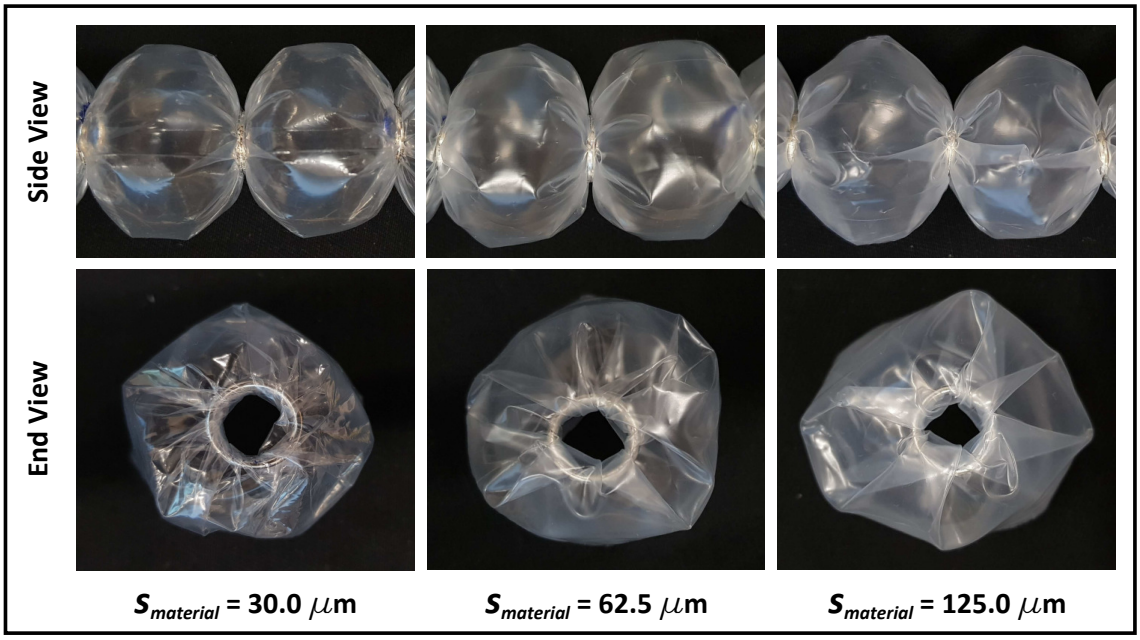

Figure 3.16: Actuator side and end views of BAMs with different $s_{material}$ = 30.0, 62.5 and 125.0 μm, but the same L_{unit} = 40.5 mm and R_{ring} = 4.5 mm. As material thickness is increased, the increase in fold length is clearly visible.

required performance metrics (high-thickness plastic tubing that allows for considerably higher applied pressure, metal retaining rings that withstand high radial force and folding analysis). An isotonic test using a load of 1 kg demonstrates the difference in performance

between these two actuators (fig. 3.17). With the BAM, the metal rings maintained an effective actuator shape, resulting in the BAM contraction following theoretical PPAM contraction. In contrast, the rubber rings of the sPAM stretched as applied pressure was increased, inducing an inactive region and causing large deviation from the PPAM model. Maximum BAM contraction was 26.5% at 40 kPa, significantly larger than the sPAM contraction of 18.2% at the same pressure.

3.4.2 BAM Characterisation

Bubble Artificial Muscle introduces new behaviour, an overlapped region, which, together with the inactive region present in the sPAM (fig. 3.5), reduces maximum contraction and causes deviation from the PPAM mathematical model. The overlapped region occurs when there is a large amount of folds around the actuator ends, causing crossover of the folds from two ends and overlapped membrane across the actuator. It increases the membrane stiffness and difficulty in unfolding and bending of the folded membrane, and reduces the bubble radius R_{bubble}. This stops the actuator reaching its optimum shape, leading to partial shape expansion and lower maximum contraction.

When fixing R_{ring} and varying L_{unit} (fig. 3.18A), the optimal "bubble" shape with $c_{optimal}$ can be achieved when the BAM possesses $L_{unit} = L_{optimal}$ as shown in fig. 3.18A, column A2. Decreasing L_{unit} below $L_{optimal}$ ($L_{unit} < L_{optimal}$) causes a partial shape expansion, creating overlapping of the membrane on the actuator surface, shown as red area in fig. 3.18A, column A1. On the other hand, increasing L_{unit} over $L_{optimal}$ ($L_{unit} > L_{optimal}$) causes an inactive region, shown as blue area in fig. 3.18A, column A3.

Likewise, the overlapped region and the inactive region occur when varying R_{ring} (fig. 3.18B). When fixing L_{unit} and increasing R_{ring}, the radius of the actuator ends approaches the maximum material radius $R_{material}$, reducing the amount of folding at the actuator ends and the fold length L_{fold} until $L_{fold} = 0$ at $R_{ring} = R_{material}$, as shown in column B1, B2, B3 and B4, respectively (the black dashed line shows the end of the folds). This leads to the inactive region shown in fig. 3.18B, column B3 and eventually no contraction in column B4. L_{fold} is unaffected by L_{unit} (fig. 3.18A). Although the inactive region can be addressed by decreasing R_{ring}, too small R_{ring} can result in the overlapped region as shown in Figure 7B, column B1. The optimal ring radius $R_{optimal}$ will create neither an inactive region nor an overlapped region, and will deliver the highest contraction (Figure 7B, column B2). The approach to calculate $L_{optimal}$ and $R_{optimal}$ to design the optimal BAM, which produces $c_{optimal}$, is presented in following section.

Besides, the PPAM never experiences the effect of the overlapped and inactive regions, shown as a predicted shape in fig. 3.18. This is because it has very large $R_{material}$, resulting from special end fittings which create large number of pleats, and its expanded membrane never reaches its maximum material radius.

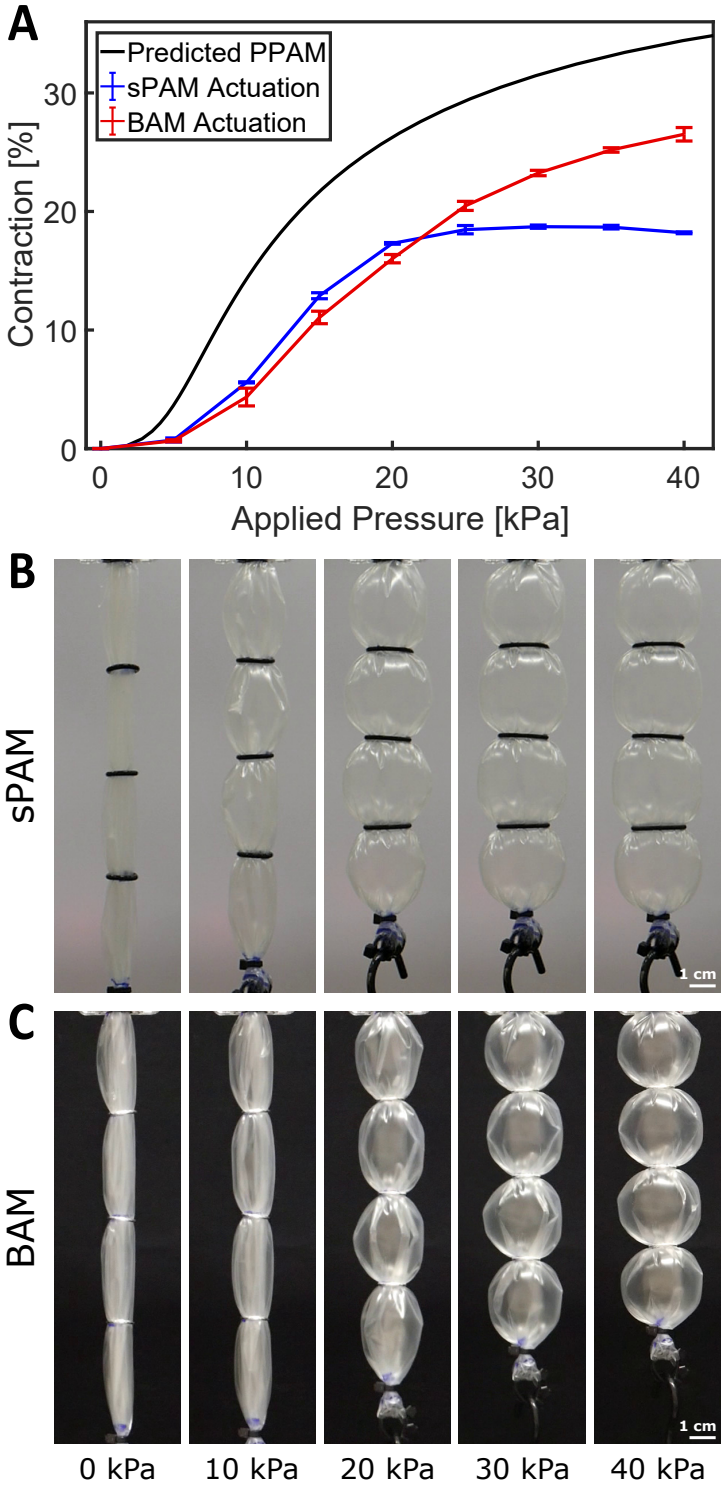

Figure 3.17: (A) Comparison between theoretical PPAM contraction, actual sPAM contraction and actual BAM contraction, during an isotonic test with a load of 1 kg. Both the sPAM (B) and BAM (C) were made of a plastic tubing with $s_{material} = 62.5$ μm and $L_{unit} = 40.5$ mm, and rubber rings (sPAM) or metal retaining rings (BAM) with the same $R_{ring} = 4.5$ mm. The sPAM rubber rings had ring thickness of 2 mm, while the BAM metal rings had ring thickness of 1.3 mm.

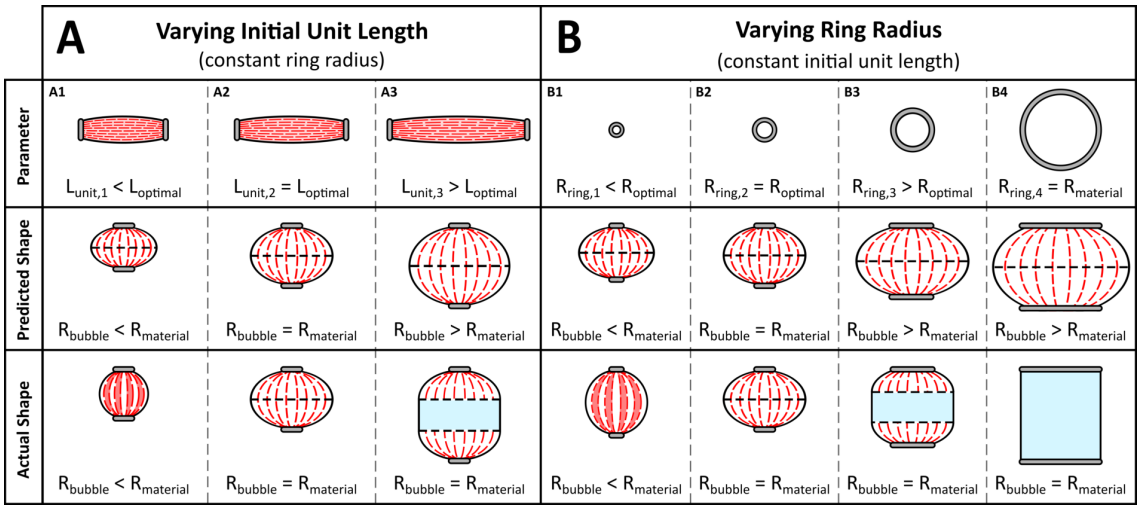

Figure 3.18: The BAM parameter (top row), the predicted PPAM shape (middle row) and the actual BAM shape (bottom row) at maximum shape expansion when (A) varying L_{unit} with constant R_{ring} and (B) varying R_{ring} with constant L_{unit}.

3.4.3 BAM Optimal Unit Length and Optimal Ring Radius

The optimal BAM is the BAM with either optimal unit length $L_{optimal}$ or optimal ring radius $R_{optimal}$, forming the maximum expanding shape ($m = 0.5$) resembling a bubble (when $R_{bubble} = R_{material}$ or $L_{bubble} = 2L_{fold}$). It achieves $c_{optimal}$ without the existence of an overlapped region or an inactive region as shown in fig. 3.18 (column A2 and B2). For the optimal BAM with $L_{optimal}$, $L_{optimal}$ and $c_{optimal}$ can be calculated by firstly selecting R_{ring} and $R_{material}$ of the BAM and using eq. (3.1) and (3.6) as follows.

First, calculate $\varphi_{R,L_{optimal}}$ when $R_{bubble} = R_{material}$ using eq. (3.6),

$$R_{bubble} = R_{material} = \frac{R_{ring}}{\cos \varphi_{R,L_{optimal}}}$$

Therefore,

$$\varphi_{R,L_{optimal}} = \cos^{-1}\left(\frac{R_{ring}}{R_{material}}\right) \tag{3.15}$$

Substitute R_{ring}, $\varphi_{R,L_{optimal}}$ (calculated from eq. (3.15)), and $m = 0.5$ (maximum shape expansion) in eq. (3.1) to obtain $L_{optimal}$,

$$L_{optimal} = \frac{R_{ring}}{\sqrt{m}\cos \varphi_{R,L_{optimal}}} \mathrm{F}(\varphi_{R,L_{optimal}}/m)$$

This equation can also be considered as the ratio of $L_{optimal}/R_{ring}$ as the following equation.

$$\frac{L_{optimal}}{R_{ring}} = \frac{\mathrm{F}\left(\varphi_{R,L_{optimal}}/m\right)}{\sqrt{m}\cos \varphi_{R,L_{optimal}}} \tag{3.16}$$

$c_{optimal}$ can be derived by using selected R_{ring}, calculated $L_{optimal}$ and $\varphi_{R,L_{optimal}}$, and m

$= 0.5$ with eq. (3.2).

$$c_{optimal} = 1 - \frac{2R_{ring}}{L_{optimal}} \left(\frac{\mathrm{E}\left(\varphi_{R,L_{optimal}}/m\right) - \frac{1}{2}\mathrm{F}\left(\varphi_{R,L_{optimal}}/m\right)}{\sqrt{m}\cos\varphi_{R,L_{optimal}}} \right) \tag{3.17}$$

Alternatively, the optimal BAM with $R_{optimal}$ can be created when initially selecting L_{unit} and $R_{material}$ to calculate $R_{optimal}$. First, using an unknown $R_{optimal}$ instead of R_{ring} in eq. (3.15) as follows,

$$\varphi_{R,R_{optimal}} = \cos^{-1}\left(\frac{R_{optimal}}{R_{material}}\right) \tag{3.18}$$

Rearrange eq. (3.1) to calculate $R_{optimal}$,

$$R_{optimal} = \frac{L_{unit}}{\mathrm{F}(\varphi_{R,R_{optimal}}/m)}\sqrt{m}\cos\varphi_{R,R_{optimal}} \tag{3.19}$$

Substituting $\varphi_{R,R_{optimal}}$ from eq. (3.18) as a function of an unknown $R_{optimal}$ in eq. (3.19) and using MATLAB result in the optimal ring radius $R_{optimal}$. This approach is more complicated than the former one since eq. (3.18) and (3.19) are interdependent. Subsequently, the optimal contraction of the BAM with $R_{optimal}$ can be calculated from eq. (3.2) by using $L_{unit}, R_{optimal}, \varphi_{R,R_{optimal}}$ and $m = 0.5$. As a result, these two methods (using $L_{optimal}$ or $R_{optimal}$) allow us to design the BAM, which delivering the highest contraction, when knowing $R_{material}$ and constraining either only L_{unit} or R_{ring}, easily applying to desired applications.

In reality, the actual BAM contraction can be lower than this calculated $c_{optimal}$ according to the difficulty and friction in unfolding of the actuator membrane. The following sections will introduce an actuation model of the BAM modified from the PPAM and sPAM models and derived based on the empirical results to predict the real-world BAM performance and also design optimisation which includes the effect of material thickness to create the optimal BAM.

3.5 BAM Actuation Model

Although the BAM produces lower performance than the PPAM theoretical maximum (fig. 3.11 and 3.12) because of the fundamental difference in their folding structure, they share the same ideal behaviour of shape expansion (fig. 3.4B). Accordingly, the BAM mathematical model is built on the PPAM model with the addition of the inactive region modelled by the sPAM model, and modifications to model the effects of material thickness. The PPAM and sPAM models overestimate BAM performance in terms of contraction and tensile force, as they do not account for material thickness, a major factor in BAM actuation. This deviation can be reduced by modifying the inelastic PPAM model with an additional term based on experimental observation. The effect of the inactive region from the sPAM model, which can limit the maximum contraction, is also included in the BAM model. The process of deriving the BAM model are shown as a diagram (fig. 3.19) and flow chart (fig. 3.20).

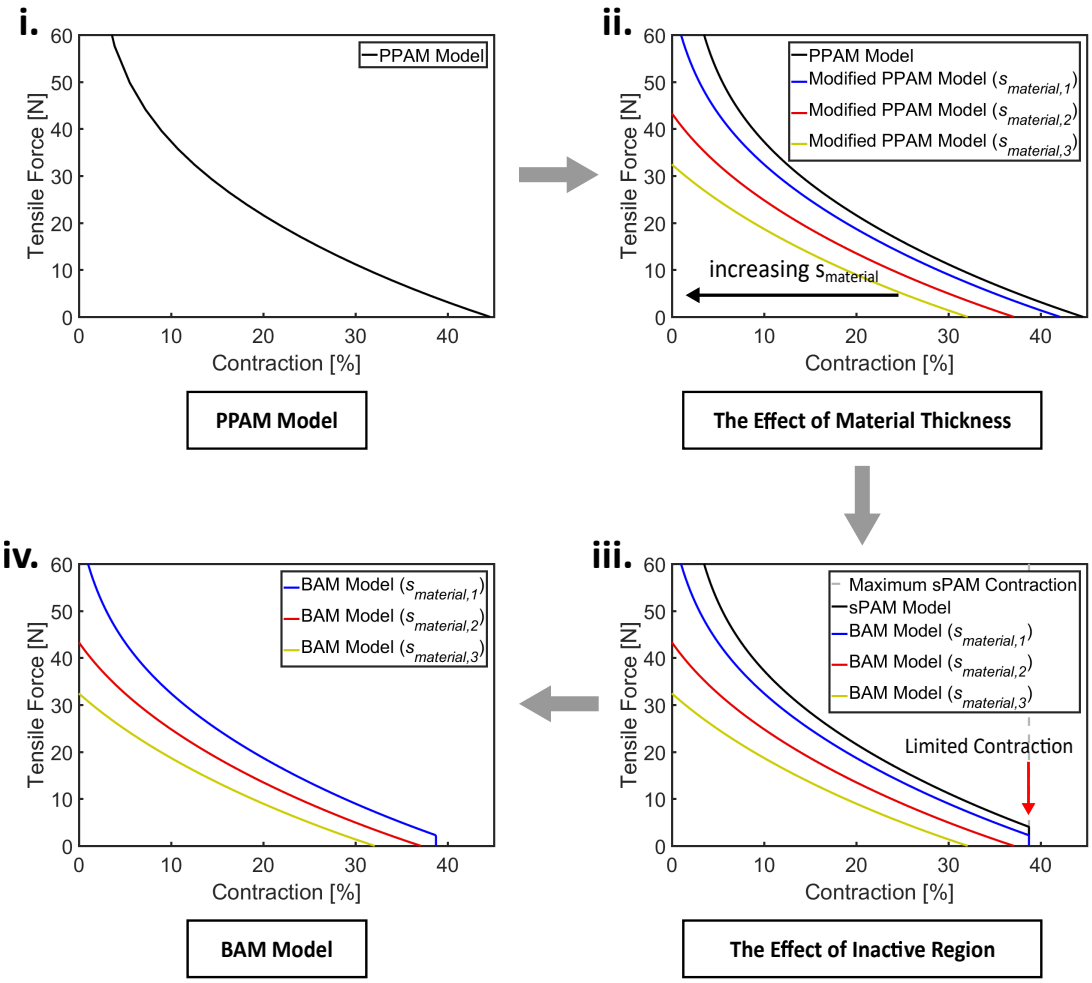

Figure 3.19: Summary of the BAM model: (i) calculating the relationship between tensile force and contraction from the PPAM model, (ii) applying the effect of material thickness ($s_{material,1} < s_{material,2} < s_{material,3}$), (iii) applying the effect of the inactive region, limiting the maximum contraction, and (iv) the resultant BAM model.

As illustrated above in fig. 3.12B, the ratio of the material thickness and the ring radius ($s_{material}/R_{ring}$) and the ratio of the material radius and the ring radius ($R_{material}/R_{ring}$) are likely to be dominant factors in determining the reduction in the BAM performance compared to the PPAM model. As such, the loss in contraction c and tensile force F_t can be described by the following equation, where A and n are constant.

$$loss \propto A * \left(\frac{s_{material}}{R_{ring}} \cdot \frac{R_{material}}{R_{ring}} \right)^n \tag{3.20}$$

This loss term was applied subtractively and multiplicatively to modify the PPAM-predicted tension-contraction relationship and contraction-pressure relationship, respectively, to match the experimental data of the BAM. As a result, the BAM performance regarding the tension-contraction and contraction-pressure relationships can be modelled as follows.

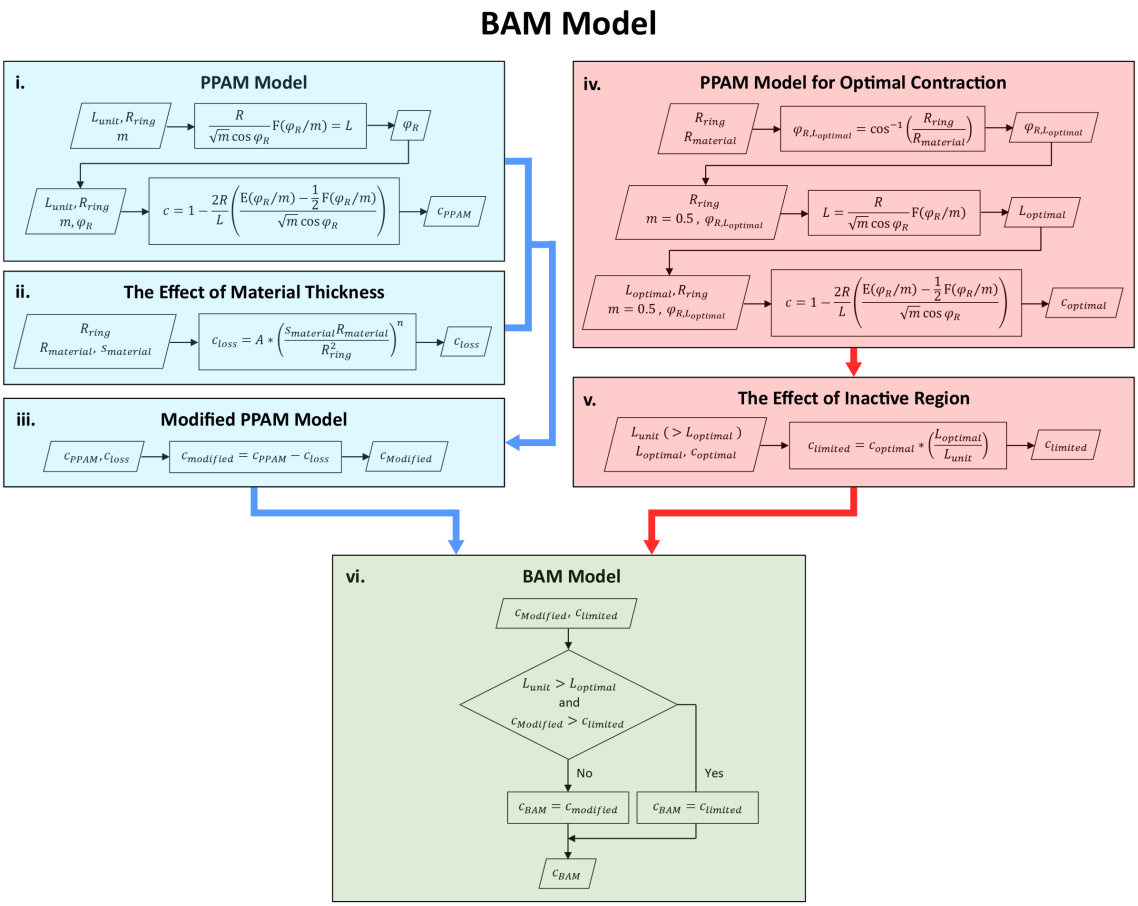

Figure 3.20: Flow chart of the BAM model for the relationship between tensile force and contraction, calculating BAM contraction c_{BAM}. Tensile force F_t can be calculated from the PPAM model.

3.5.1 Tension-contraction Relationship

The relationship between tensile force and contraction of the BAM (fig. 3.12A) can be modified from the PPAM model by using the subtractive contraction loss c_{loss}, applying from eq. (3.20). Therefore, the BAM contraction c_{BAM} can be derived from eq. (3.21), where c_{PPAM} is the PPAM contraction, and where A and n have been chosen to fit experimental data.

$$c_{BAM} = c_{PPAM} - c_{loss}$$

when

$$c_{loss} = 21.35 * \left(\frac{s_{material} R_{material}}{R_{ring}^2} \right)^{0.25} \tag{3.21}$$

The comparison between the PPAM model, the sPAM model, the modified model for the BAM and the experimental data of the BAM ($s_{material} = 62.5$ μm from fig. 3.12A) is presented in fig. 3.21. Applying c_{loss} from eq. (3.21) causes shifting of the PPAM model

to match the BAM experimental data (fig. 3.19). Although not required for the results in fig. 3.21, the BAM model also includes the limitation on maximum contraction due to the inactive region, first described in the sPAM model (fig. 3.19 and 3.20). The BAM model for the BAMs made of different $s_{material}$ (fig. 3.12A) can be seen in fig. 3.22a. This model can also be used to predict the real-world contraction of the BAM with constant $s_{material}$ at various applied pressures (fig. 3.22b).

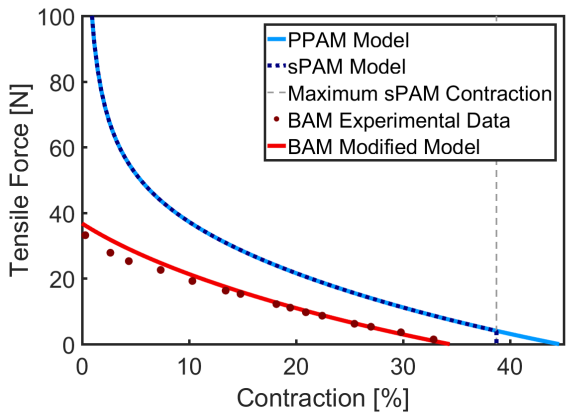

Figure 3.21: Comparison between the PPAM model, sPAM model and BAM model of a BAM with L_{unit} = 40.5 mm, R_{ring} = 4.5 mm and $s_{material}$ = 62.5 μm operating at P = 30 kPa, showing the relationship between tensile force and contraction. The maximum sPAM contraction without an inactive region occurring, and the BAM experimental data included.

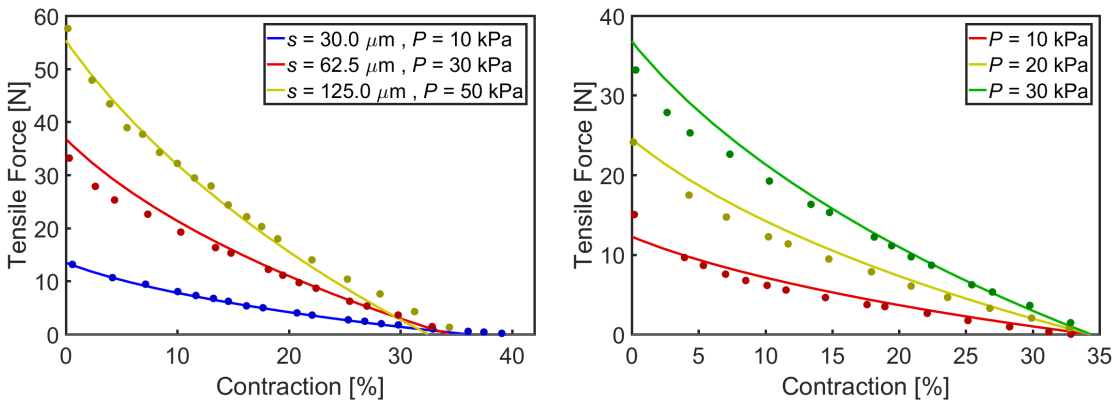

(a) (b)

Figure 3.22: BAM model applying subtractive contraction loss (lines) and experimental results (dots) of BAMs with L_{unit} = 40.5 mm and R_{ring} = 4.5 mm, showing the relationships between tensile force and contraction when (a) varying $s_{material}$ and P and (b) having constant $s_{material}$ = 62.5 μm but operating at different P.

3.5.2 Contraction-pressure Relationship

The relationship between contraction and pressure (fig. 3.11A) is better modelled by applying a multiplicative tension loss, $F_{t,loss} = 1/\eta_{loss}$, to PPAM tension $F_{t,PPAM}$ as in eq. (3.22). As previously shown experimentally, the BAM requires higher applied pressure P than predicted by the PPAM model to deliver desired F_t and c. Conversely, this means that c_{BAM} is less than c_{PPAM} at the same P and F_t. Fig. 3.23 illustrates the increasing divergences of c_{BAM} from c_{PPAM} with $s_{material}$ while loaded with $F_t = 1$ kg.

$$F_{t,BAM} = \frac{1}{\eta_{loss}} * F_{t,PPAM}$$

when

$$\eta_{loss} = 4.39 * \left(\frac{s_{material} R_{material}}{R_{ring}^2} \right)^{0.31} \tag{3.22}$$

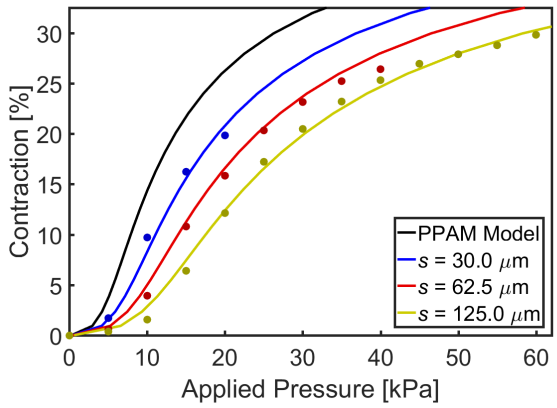

Figure 3.23: BAM model applying multiplicative tension loss (lines) and experimental results (dots) of the BAMs (L_{unit} = 40.5 mm and R_{ring} = 4.5 mm) from fig. 3.11A, showing the relationship between contraction and pressure when varying $s_{material}$ and operating at different P.

3.6 Design Optimisation

As previously described in section 3.4.2, the optimal BAM is the BAM with $L_{optimal}$ delivering maximum contraction without the appearance of the overlapped region or the inactive region. To model the optimal BAM, contractions of BAMs made from different actuator designs and material properties were simulated using the BAM actuation model presented in section 3.5. Analysis summarised in fig. 3.24 shows how the BAM actuator differs from the PPAM and the sPAM, and how it can be optimised to achieve high contraction by choosing three ratios of material properties: L_{unit}/R_{ring}, $R_{ring}/R_{material}$ and $s_{material}/R_{ring}$.

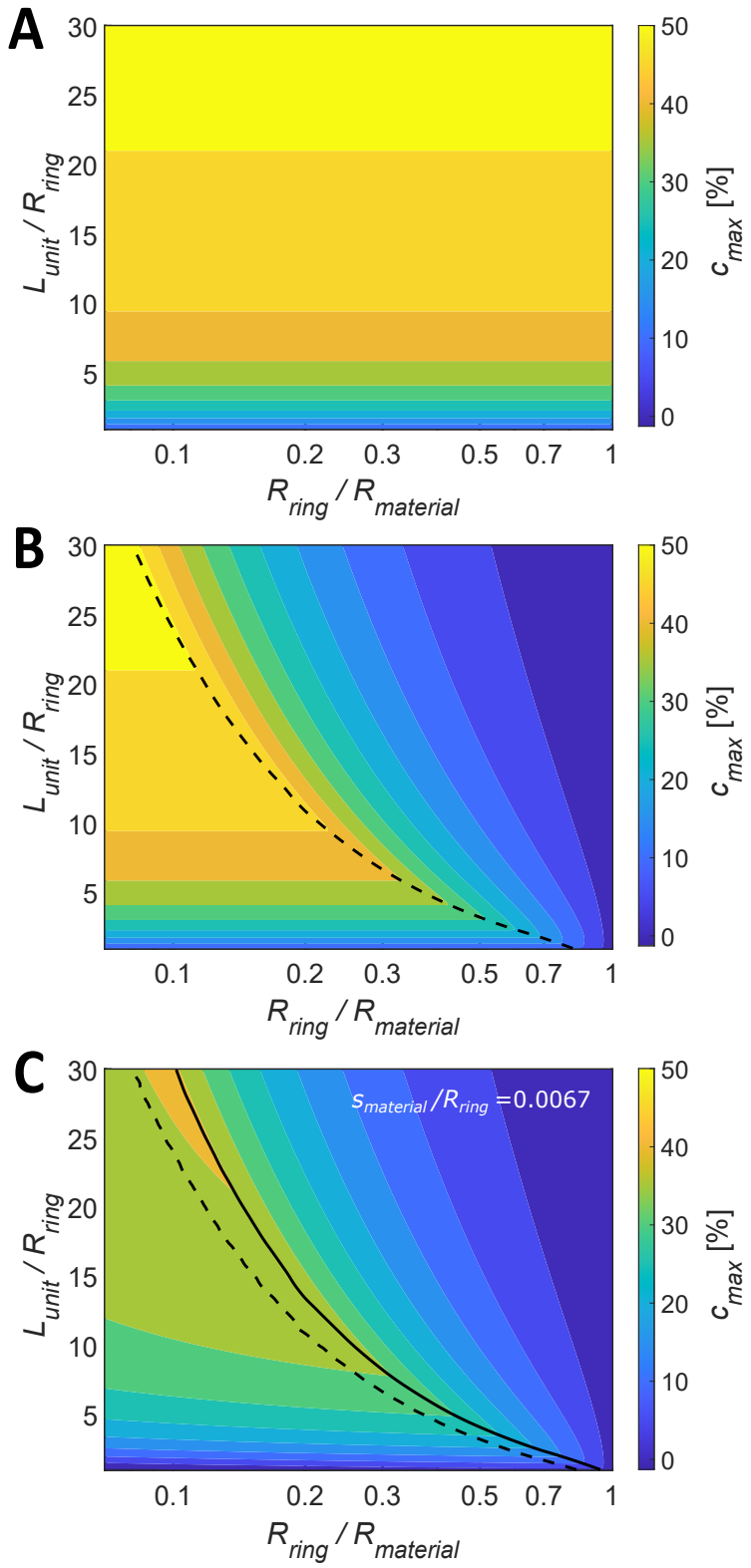

Figure 3.24: Model-predicted maximum contraction of (A) PPAM, (B) sPAM and (C) BAM made of $s_{material} = 30.0$ μm. Colour shows the maximum contraction c_{max} of the actuators as L_{unit}/R_{ring} and $R_{ring}/R_{material}$ are varied. For each $R_{ring}/R_{material}$, dashed and solid lines indicate the location where maximum contraction is highest based upon the sPAM and BAM model respectively.

Fig. 3.24A shows maximum contraction predicted by the PPAM model, simulated by substituting L_{unit}/R_{ring} in eq. (3.1) and (3.2). It does not show an overlapped region or an inactive region since the PPAM actuator membrane is uniformly folded and its actuation never reaches maximum shape expansion. Therefore, its contraction is maximised as L_{unit}/R_{ring} and does not depend on $R_{ring}/R_{material}$. Fig. 3.24B shows maximum contraction predicted by the sPAM model. At any $R_{ring}/R_{material}$, the sPAM contraction increases with L_{unit}/R_{ring} until reaching a maximum when $L_{unit} = L_{optimal}$. If L_{unit}/R_{ring} is further increased, contraction reduces due to the inactive region. Neither the PPAM nor the sPAM models account for the effect of $s_{material}$, which is a significant factor influencing the contractile performance. Fig. 3.24C shows the BAM model developed in this research. The effect of material thickness slightly reduces maximum contraction, and slightly increases the optimal L_{unit}/R_{ring} at each $R_{ring}/R_{material}$ compared with the sPAM model, leading to a new optimal design. The optimal design of the BAM made of different $s_{material}$ is shown in fig. 3.25.

To sum up, theoretically, decreasing $R_{ring}/R_{material}$ can increase the fold length L_{fold} (fig. 3.18) and lead to an increase in $L_{optimal}$ and higher contraction. In reality, the BAM exhibits non-uniform folding near the rings, creating a region of higher stiffness and friction, and restricting inflation. Therefore, low $R_{ring}/R_{material}$ can limit BAM actuation as shown in fig. 3.24C. Furthermore, although the BAM with higher $s_{material}$ can produce higher tensile force due to higher operating pressure, the material resists unfolding and bending, leading to lower maximum contraction (fig. 3.12B). In contrast, the BAM with very thin $s_{material}$ will have low effect on the actual fold length and maintain its contractile capability as predicted. Therefore, the BAM with either high $R_{material}/R_{ring}$ or $s_{material}/R_{ring}$ will experience greater folding and thus lower contraction. Accordingly, when designing the actuator in these conditions, the BAM may exhibit an overlapped region, causing partial shape expansion and shifting of $L_{optimal}$ as shown in fig. 3.24C. These can be solved by increasing L_{unit} until no overlapping occurs and there is no inactive region, thereby achieving optimal contraction.

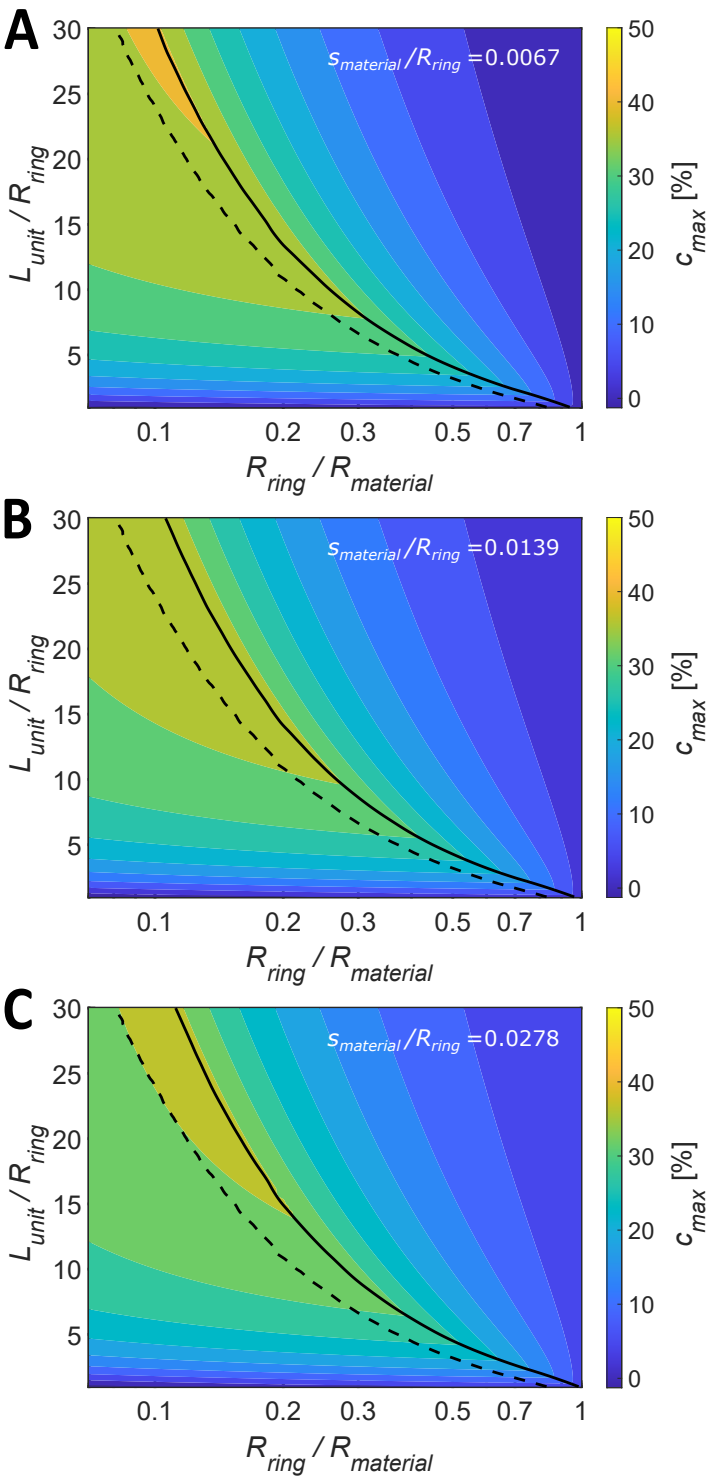

Figure 3.25: Model-predicted maximum contraction for BAM made of different $s_{material}$: (A) 30.0 μm, (B) 62.5 μm and (C) 125.0 μm. Colour bar shows the maximum contraction c_{max} of actuators as L_{unit}/R_{ring} and $R_{ring}/R_{material}$ are varied. For each $R_{ring}/R_{material}$, dashed and solid lines indicate the location where maximum contraction is highest based upon the sPAM and BAM model respectively.

3.7 BAM Improvement

The performance of the BAM can be improved by several approaches. First, better quality fabrication and a method for creating uniformly lateral folding along the actuator are required so that the BAM can unfold and expand more easily with lower friction. Uniform folding can increase BAM contraction and decrease the deviation between the mathematical model and the practical performance.

Second, for the current design, the rings are placed without any attachments to the tubing. After repeated actuation, the rings tend to be fixed in place by the shape adopted by the folded membrane. As $R_{material}$ is much larger than R_{ring}, the folded membrane passively bends around the ring, helping to constrain the movement of the rings. If the BAMs are to be integrated into a robotic system without prior actuation, the rings can be fixed in place by adhesive to prevent slippage. Alternatively, one future BAM design could have no rings but would use its own actuator membrane to form the "bubble" shape, for example, by applying origami or kirigami methods so that the bubble shape naturally emerges.

Last, using high strength inelastic materials, the BAM can operate under higher applied pressure to deliver higher tensile force. The ideal actuator membrane should possess high young's modulus and extremely high tensile strength to withstand high pressure for high tensile force, have low interfacial friction and be very thin and very flexible in order to expand easily at low-pressure actuation and deliver high contraction.

3.8 Discussion

The Bubble Artificial Muscle is one of the most lightweight pneumatic actuators (less than 6 g for the BAMs consisting of four contractile units), which can deliver either high contraction or high tension depending on the actuator's size and thickness and the stiffness of the constituent material. A thicker actuator membrane allows the BAM to operate under higher applied pressure to produce higher tensile force, while metal rings can maintain the actuator radius, delivering desired contraction when operated at high pressure. Despite having different folding pattern to the PPAM, the BAM can form a similar inflated shape and function but with considerably simpler and low-cost fabrication (less than £1 for four-contractile-unit BAMs). The optimal BAM can be achieved by choosing the initial unit length and ring radius to suit the material radius and thickness, avoiding both an overlapped region and an inactive region.

The BAM actuation model was built based on the PPAM model with an additional loss term, modifying the model to match the BAM experimental results. This model can predict the real-world performance for BAMs made from different material thicknesses and operated at different applied pressures. In this research, the loss term was empirically derived, and demonstrates how BAM and sPAM behaviour differ and how BAM perfor-

mance can be improved. A future development is to derive a BAM loss term from first principles and compare this theoretical model with the empirically derived model.

The BAM can be improved further by exploiting actuator materials which possess high strength and flexibility to achieve for higher tension and contraction, removing the requirement of retaining rings by using its own material as the structure to form a contractile shape, and improving fabrication quality to create uniform folding for lower-friction shape expansion. The BAM was intentionally designed to interact with the human body in the form of a wearable exosuit or orthosis. In the next chapter, the developed BAMs were used as an assistive device to perform human locomotions, especially walking motion and sit-to-stand transition (Chapter 4).

Chapter 4

Human Mobility Assistance

Parts of the work described in this chapter have been published and submitted as:

- **Diteesawat RS**, Helps T, Taghavi M, Rossiter J. High Strength Bubble Artificial Muscles for Walking Assistance. *IEEE International Conference on Soft Robotics (RoboSoft)* 24 April 2018 (pp. 388-393).
- **Diteesawat RS**, Helps T, Taghavi M, Rossiter J. Characteristic Analysis and Design Optimisation of Bubble Artificial Muscles (BAMs). *Soft Robotics* 2020.

Lower limb degeneration and mobility impairment are mainly due to ageing and are unavoidable in human life. These make it difficult for older adults and disabled people to maintain their independent living and perform daily activities. Many exoskeletons have been developed either to recover the mobility of affected people through rehabilitation or to improve the body strength and working performance of able-bodied wearers for industrial applications. However, current exoskeletons are still too large, heavy and visible for practical usage by older adults.

To meet the requirement for more useable and practical exoskeletons, the Bubble Artificial Muscle (BAM) was developed, as presented in the previous chapter. The BAM is a lightweight, flexible, inexpensive, effective pneumatic muscle-like actuator, which can be optimised for either high contraction or high tension. It is scalable, can contract at low pressures, and can generate sufficient tension and contraction for human mobility assistance. It therefore has high potential to be used to create a wearable assistive device providing extra power to lower limbs of a wearer in order to prolong their locomotion performance, and hence maintain independence, with less fatigue.

This chapter presents how the BAM can be used to support human mobilities, mainly focusing on ground-level walking (GLW) and sit-to-stand transition (STS). Mathematical leg models were derived to calculate the contraction and force for BAM orthoses needed to achieve GLW and STS. Human-scale leg mechanisms were designed and built to mimic biological leg structures and were used to evaluate the efficiency of the BAM actuators in performing human body movements. In addition, the differences between GLW of a

young healthy subject and elderly subjects, and the concept of timed GLW assistance, were studied.

4.1 BAM Assistance on Ground-level Walking (GLW)

This section firstly introduces the difference between GLW of young and elderly subjects, followed by the design of leg pendulum model and the concept of timed GLW assistance. Subsequently, the design and analysis of a soft orthosis based on the biomechanics of the lower limb are presented. As previously described in section 2.3, the knee is an important joint for maintaining human locomotions. It is easier to support and control through an orthosis than other related joints due to its one relatively constrained, DOF motion. Therefore, the leg model and BAM orthosis in this chapter were based on the functions of the knee joint. Lastly, experiments evaluating the performance of the orthosis are presented and results are analysed.

4.1.1 Range of Motion of the Knee

The range of motion (ROM) of the knee with respect to age and the knee angle of elderly subjects during a gait cycle in a sagittal plane can be found in fig. 2.5 and 2.6, respectively. Fig. 2.5 shows that the knee ROM for people under 30 is between approximately 64 and 72 degrees, and mean ROM reduces to below 55 degrees after the age of 80. The difference in the mean knee flexion between younger and older groups can be used as a target for an orthosis that will assist the knee mobility of an older subject.

To understand the time-varying flexion pattern of the knee, walking data, including joint angle, angular velocity and angular acceleration was captured for a young healthy subject using two different approaches. The first method was to track the body movement using an Xsens suit, a 3D motion tracking technology. Xsens allows the user to capture full-body movement by using inertial measurement units (IMUs) mounted on all body segments. This suit can produce the 2D and 3D motions and kinematic data of the entire body (fig. 4.1a). The second method was to use the Computer Assisted Rehabilitation Environment (CAREN). This technology can capture body movement on a treadmill platform via the tracking of reflective markers using infrared cameras, and IMUs attached on the user's body. It can also display a virtual 3D animation and 2D kinematic data instantaneously while walking (fig. 4.1b). The treadmill can also measure reaction force from the ground during walking, which can be used to reverse-calculate kinetic data, i.e. force and torque at each joint of the lower limb.

The gait data of a young adult (the author, age 25) was recorded at a comfortable walking speed by the Xsens suit at the Bristol Robotics Laboratory (BRL) in March 2017. Separate movement data was recorded using the CAREN system at the University of Strathclyde in Glasgow during a research visit in April 2017, for walking speeds of 0.75,

1.00 and 1.50 m/s on the CAREN treadmill. The captured knee angles in the sagittal plane is presented, along with data from older people from fig. 2.6, in fig. 4.2.

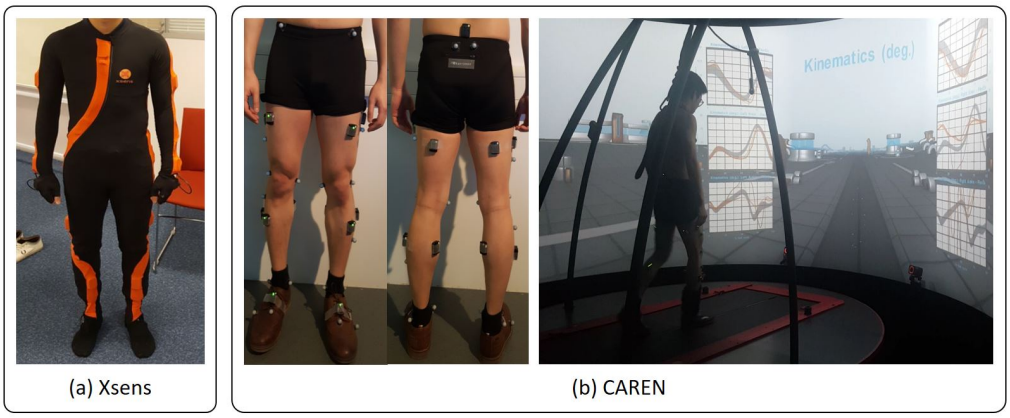

Figure 4.1: Gait measurement from two different body motion capturing technologies: (a) Xsens suit at Bristol Robotics Laboratory, and (b) the CAREN system at the University of Strathclyde.

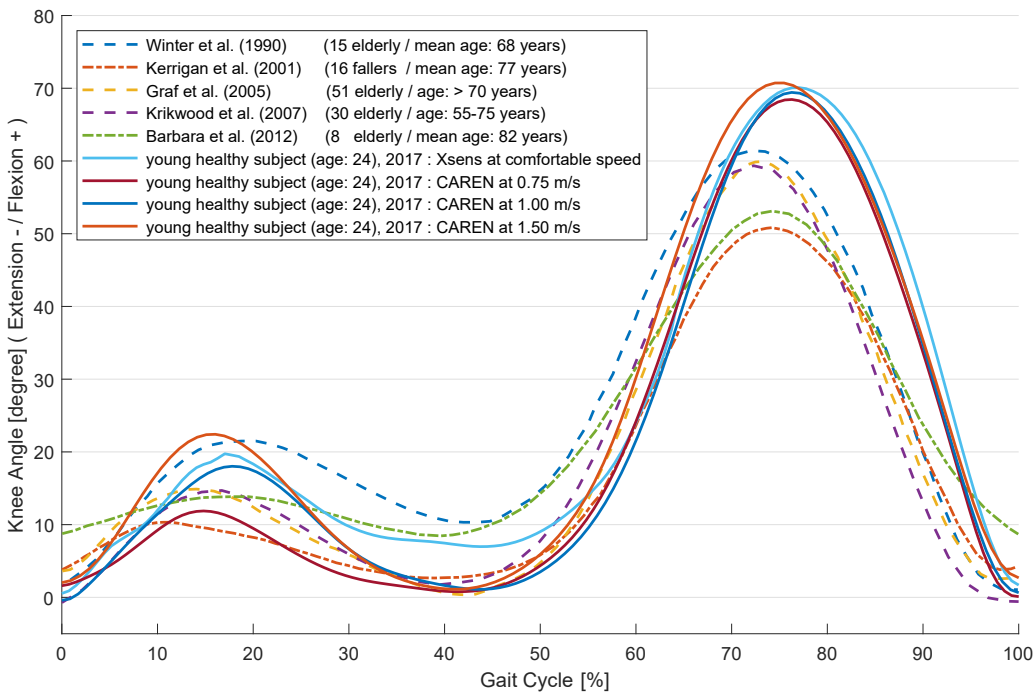

Figure 4.2: Comparison between the author's knee angle during a gait cycle as an example of young healthy subjects and that of elderly subjects taken from fig. 2.6.

According to fig. 4.2, the knee data of the young healthy subject acquired from these two different technologies show similar gait cycle as the data for older people and are in the range of the knee ROM described in fig. 2.5, which was also captured by IMUs [5]. Comparing between these two groups, the reduction of the knee ROM of elderly group is most clearly seen in a swing phase of a gait cycle, especially for knee flexion. The difference

in the peak knee flexion between the young and elderly data in fig. 4.2 is between 10 and 20 degrees. Therefore, this difference can be used as a target increase in knee angle for an orthosis intended for use by older adults.

4.1.2 Leg Pendulum Model

Locomotion, such as walking, stair climbing and running, occurs with the cooperation of the muscles along the hip, knee and ankle. Regarding ground-level walking, muscles are responsible for three major tasks: weight acceptance, single limb support and limb advancement as described in section 2.1. A leg model was designed based on the human leg structure, which can perform limb advancement, especially knee flexion and extension. In order to develop this model, knowledge of leg biomechanics is required.

A typical human is assumed to have the body mass BM of 72.0 kg and height H of 170 cm, based upon average data (BM = 71.78 kg and H = 169 cm) of older adults, beyond the age of 60, that was acquired from several gait analysis studies [25–29, 44, 46]. A segment mass[1], a segment length and the centre of mass of each lower-limb segment can be calculated as a fraction of the total body mass and body height regarding [110], and are summarised in table 4.1.

Table 4.1: Segment mass, segment length and centre of mass of each segment of the lower limb. (modified from chapter 4 in [110])

Segment	Segment mass (m)/ total body mass	Segment length (L)/ total height	Center of mass (COM)/ segment length (from proximal joint)
Total leg	0.161	0.530	0.447
Thigh	0.100	0.245	0.433
shank	0.0465	0.246	0.433
Foot	0.0145	0.152	0.500

For example, given BM = 72 kg, H = 170 cm and the data from table 4.1, the mass, length and centre of mass of the thigh can be calculated as follows.

$$m_{thigh} = 0.10 \times BM = 0.10 \times 72 = 7.20\ [kg]$$
$$L_{thigh} = 0.245 \times H = 0.245 \times 170 = 41.66\ [cm]$$
$$COM_{thigh} = 0.433 \times L_{thigh} = 0.433 \times 41.65 \approx 18.03\ [cm]$$

Using this method, the segment mass, segment length and centre of mass of a typical human's lower limb (i.e. thigh, shank and foot) were calculated and are shown in table 4.2. For the sake of simplicity in building the leg simulation and mechanism, the calculated

[1]In biology, a segment weight or a body weight is measured in kilograms, but in science, they are measured in newtons, whereas a segment mass or a body mass is defined in kilograms.

values were rounded to nearby values, and the centre of mass of each segment was assumed to be half-way along that segment. Values used in the simuated and mechanical model are presented in parenthesis in table 4.2.

Table 4.2: The segment mass, length and centre of mass of thigh, shank and foot of a typical elderly subject with the body mass of 72 kg and height of 170 cm. (Values used in simulated and mechanical model are shown in parenthesis)

Segment	Segment mass [kg]	Segment length [cm]	Center of mass [cm] (from proximal joint)
Thigh	7.20 (7.0)	41.65 (42.0)	18.03 (21.0)
shank	3.39 (3.5)	41.82 (42.0)	18.11 (21.0)
Foot	1.04 (1.0)	25.84 (26.0)	12.92 (13.0)

The biological leg model of a typical human is represented in fig. 4.3a. This was accordingly converted to a simpler leg model, which will be used for testing the performance and assistance of the orthosis on the leg. From the biomechanical perspective, the simpler leg model can be designed based on the pendulum concept since the knee has only one DOF in performing flexing and extending motions.

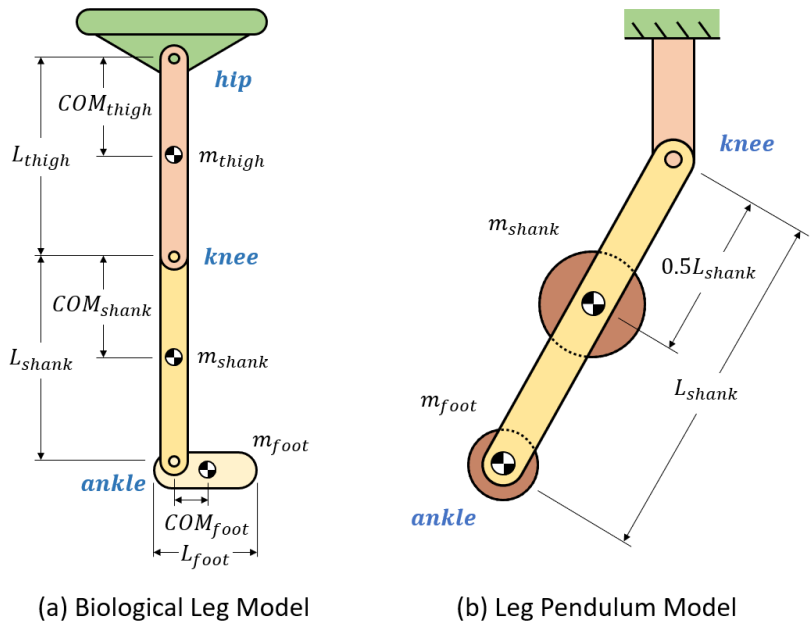

Figure 4.3: (a) The biological leg model that is composed of waist, thigh, shank and foot. (b) The leg pendulum model which is converted from the biological model with some conditions.

The pendulum leg model comprises five components: a vertically fixed linkage as the thigh, a revolute joint as the knee joint, a shank linkage that can rotate about the knee joint, and two masses at the middle and the end of the shank linkage representing the shank and foot masses, respectively (fig. 4.3b). This leg model is intentionally simplified

to minimise complexity of fabrication and experiment. The lengths of the thigh linkage and a shank linkage are both 42 cm, while the mass of the shank and foot are 3.5 and 1.0 kg, respectively, referring to table 4.2. The next section will present how an orthosis can improve knee flexion and extension of a person with restricted movement to match the recorded knee ROM of the young healthy subject, simulated using this leg pendulum model.

4.1.3 Concepts of GLW Assistance

Knee flexion and extension are performed by thigh muscles (fig. 4.4). The hamstrings muscle group is the posterior thigh muscle performing knee flexion, while the rectus femoris is the main anterior thigh muscle performing knee extension. These two muscle groups work cooperatively and antagonistically to generate torques which counteract passive knee stiffness in order to accomplish knee movements during the stance and swing phases of a gait cycle. For example, at the beginning of the swing phase, the hamstrings contract to lift the lower leg through knee flexion. When the leg almost reaches the peak knee flexion, the rectus femoris group contracts to reduce the knee motion, thereby stopping hyperflexion and causing knee extension for limb advancement.

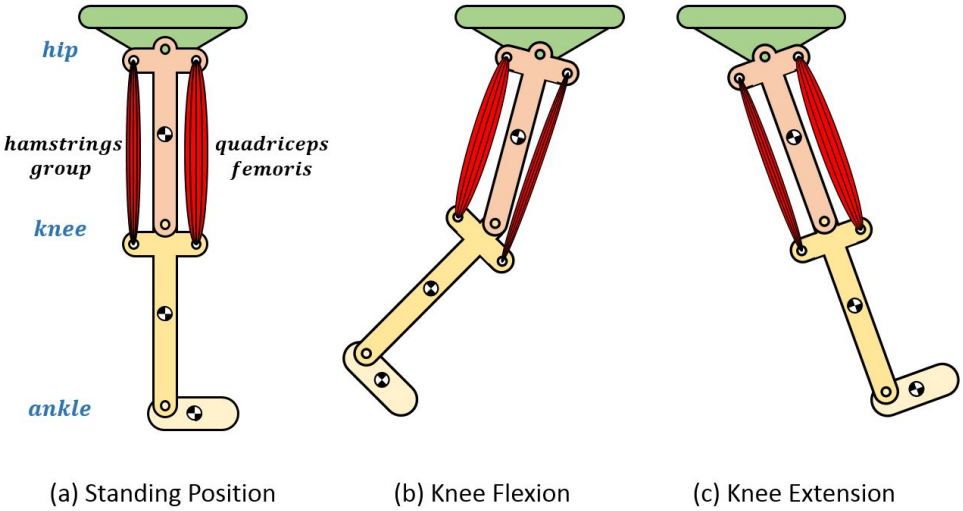

Figure 4.4: Muscle activities of a lower limb when walking. Combination between contraction and extension of hamstrings and rectus femoris muscle groups resulting in (a) standing position (b), knee flexion and (c) knee extension.

The designed leg pendulum can perform both knee flexion and extension using the torque generated by a motor system. A torque profile can be derived to control the leg pendulum model to mimic the knee behaviour of any subject during the swing phase. Regarding fig. 4.3b, the shank linkage is connected by the revolute knee joint and is composed of shank mass (m_{shank} or m_s) and foot mass (m_{foot} or m_f), located at the middle and the end of the leg pendulum (L_{shank} or L_s), respectively. This pendulum model can be converted into a kinetic diagram to calculate the required torque as shown

in fig. 4.5.

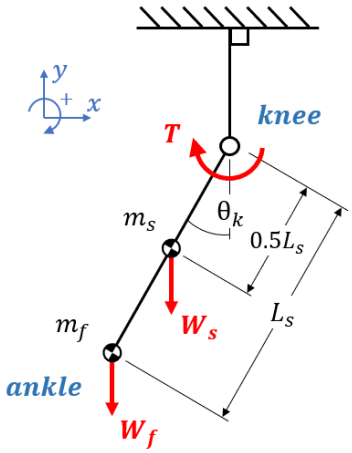

Figure 4.5: Kinetic diagram of the leg pendulum model for calculating the required torque to perform knee flexion and extension.

From this diagram, a knee swing motion can be simulated by applying torque T generated by the motor system to the knee joint to counteract the moment of the shank weight[2] (W_s) and foot weight (W_f). The motor system is therefore required to generate both clockwise and counterclockwise torques (T_{CW} and T_{CCW}), working alternately as hamstring and rectus femoris muscle groups. The knee stiffness can be defined as a spring and a damper [111]. However, this model neglects the effects of the knee stiffness and focuses only on the impact of the leg mass. The resultant knee angle (θ_k) due to a given torque T in fig. 4.5 can be calculated by applying Newton's second law for the dynamic pendulum system as follows.

From Newton's second law:

$$moment\ of\ inertia(I)\ \times angular\ acceleration(\ddot{\theta}) = net\ Torque(T_{net}) \tag{4.1}$$

From eq. (4.1), the leg pendulum system (fig. 4.5) can be derived as follows.

$$I_l\ddot{\theta}_k \ = \ T - W_s \sin\theta_k \cdot \left(\frac{L_s}{2}\right) - W_f \sin\theta_k \cdot (L_s) \tag{4.2}$$

Where the inertia of the leg (I_l) is equal to the sum of shank inertia (I_s) and the foot inertia (I_f). Since the masses of the shank and the foot are defined as point masses on the leg pendulum, their inertia can be calculated using $I = mr^2$.

$$I_l \ = \ I_s + I_f \ = \ m_s\left(\frac{L_s}{2}\right)^2 + m_f {L_s}^2 \tag{4.3}$$

From eq. (4.2), when $W_s = m_s g$ and $W_f = m_f g$,

$$\ddot{\theta}_k \ = \ \frac{1}{I_l} \cdot \left(T - \frac{1}{2} m_s g L_s \sin\theta_k - m_f g L_s \sin\theta_k\right)$$

[2]The weight here is referred to the gravity force (mg) of a mass m when g is 9.81 m/s^2.

$$\ddot{\theta}_k = \left(-\frac{(m_s + 2m_f)\, gL_s}{2I_l}\right) \cdot \sin\theta_k + \frac{1}{I_l} \cdot T \tag{4.4}$$

Set x_1 and x_2 equal to knee angle θ_k and knee angular velocity $\dot{\theta}_k$, respectively, then

$$\dot{x}_1 = x_2 \tag{4.5}$$

$$\dot{x}_2 = \left(-\frac{(m_s + 2m_f)\, gL_s}{2I_l}\right) \cdot \sin x_1 + \frac{1}{I_l} \cdot T \tag{4.6}$$

These nonlinear second order differential equations can be solved using 'ode45' function in MATLAB, a numerical computing software. As a result, the knee angle and velocity at any time t can be calculated from eq. (4.5) and (4.6) when giving a torque (T), physical properties of the leg pendulum (m_s, m_f, L_s, I_l), and the initial condition (x_1, x_2) at $t = 0$. To investigate the assistance of the orthosis in aiding knee flexion and extension, different torque profiles were applied to the leg pendulum model to simulate the resultant knee angles during the swing phase of the gait cycle as shown in fig. 4.6.

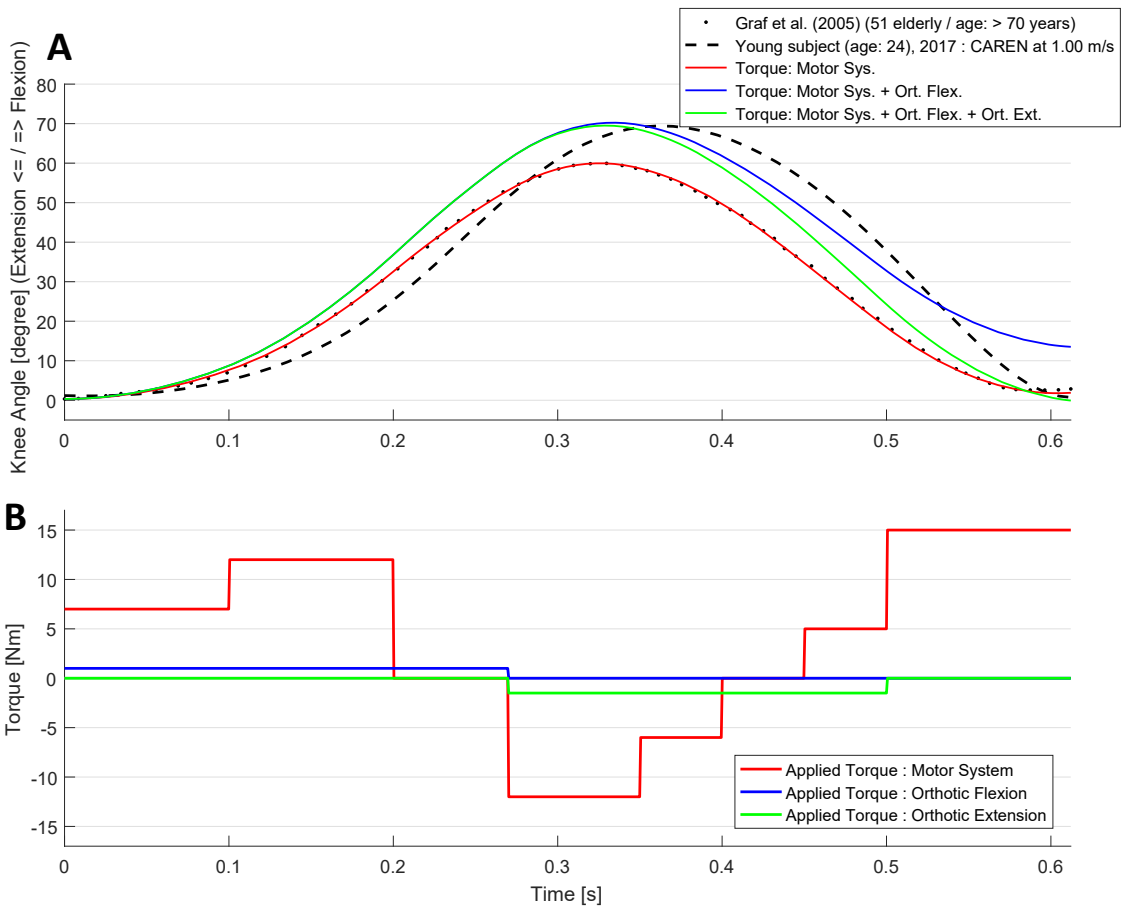

Figure 4.6: The knee-angle simulation of the leg pendulum (A) when applying torque generated from the motor system and additional torques generated from orthotic-driven flexion and extension (B) to improve the knee ROM of elderly subjects.

First, when applying a torque profile generated by the motor system (red line in fig. 4.6B), the leg pendulum performs a knee swing (a red line in fig. 4.6A) which is similar

to the knee swing of the elderly person (black dots in fig. 4.6A) acquired from [44], where their average walking speed and time spent in the swing phase are 1.04 m/s and 0.61 s, respectively. This motor-generated torque represents the torque produced by the thigh muscles of elderly subjects. Their knee pattern during the swing phase was previously presented in fig. 4.2. Next, an additional torque can be applied which simulates the addition of an active orthosis to supplement flexion. This is shown as a blue line in fig. 4.6B together with the motor-generated torque (red line). In this supplemented case, the knee flexion of the simulated elderly subject is increased to the level of a young subject (a blue line in fig. 4.6A). However, the knee cannot swing back within the same period as the original elderly swing. When adding torques generated by both orthotic flexion and orthotic extension (blue and green lines in fig. 4.6B) together with the motor-generated torque, the leg pendulum can reach the peak knee flexion of the young subject and end at the same period as the original elderly data, shown as a green line in fig. 4.6A.

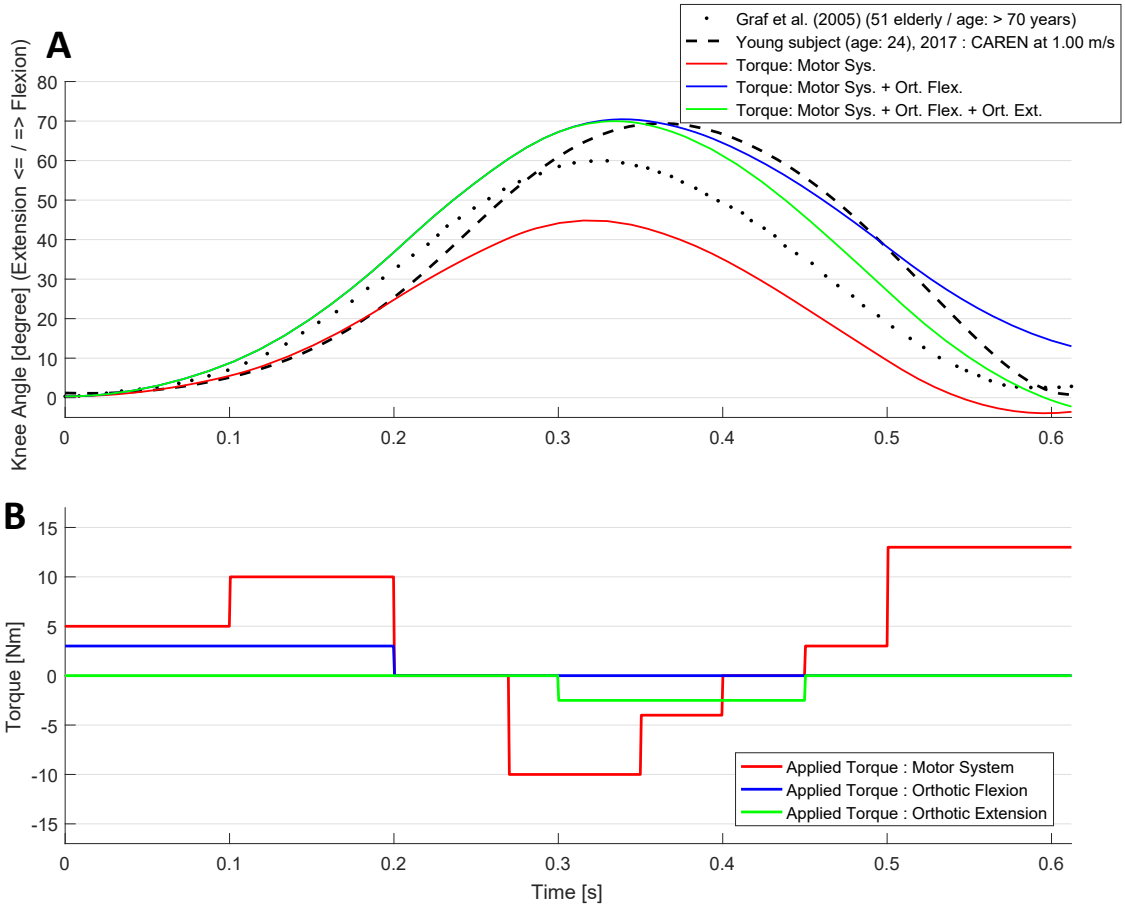

Figure 4.7: The knee-angle simulation of the leg pendulum (A) when applying low torque generated from the motor system, compared to fig. 4.6, and higher additional torques generated from orthotic flexion and orthotic extension (B) to compensate for the reduction of the motor-generated torque and thereby improve the knee ROM of elderly subjects, mimicking that of a young subject.

Considering walking over more than short distances, the elderly person may become tired and generate lower muscle activity, reducing the peak knee flexion. This scenario can be assumed by reducing the entire motor-generated torque profile in fig. 4.6B, which reduces knee flexion of the elderly person at full power, through a redution in torque by a constant 2 Nm, shown as the red line in fig. 4.7B. Consequently, the peak knee flexion of the leg pendulum is reduced to approximately 45 degrees (red line in fig. 4.7A). To improve walking in this condition, the amount of the additional torques generated by the orthotic during both flexion and extension are increased, as in the blue and green lines in fig. 4.7B. As a result, the leg pendulum swing is restored to the same angle as the young healthy knee, shown as a green line in fig. 4.7A. This demonstrates that not only do the knee flexing/extending orthoses fill the gap between young and elderly subjects, but they can also assist the knee to maintain effective walking even if they become weaker by providing higher assistive torques.

4.1.4 Design of a BAM wearable Orthosis

Many conventional orthoses, such as cable-type exosuits [14] and orthoses using straight-fibre PAMs, flat PAMs, pouch motors and PVC gel actuators [19, 51–53], were attached to either the front or back of the user's lower limbs. The rationale behind this design is that the knee has one DOF, performing only flexion and extension in the sagittal plane. Therefore, these orthoses use linear contracting or extending actuators to directly provide additional torques in the same direction as the knee movements, simplifying complexity of the designs. On the other hand, some researchers have developed orthoses to assist on the sides of the knee, with the support extending along lower limbs, for example, KAFO [49] and the orthoses using McKibben PAMs and pneumatic bending actuators [18, 54]. These designs are more complicated and could possibly cause a joint misalignment, leading to impaired gait pattern or joint damage. When the orthoses are misaligned from the centre line of the leg, they must perform both bending and linear motions in order to match the knee joint alignment and maintain an effective walking assistance.

An simple orthotic prototype was designed which is located at the back of the leg, enabling it to lift the leg easily, performing knee flexion as shown in fig. 4.8a. The location of the anchor of any power orthoses on the body is important. Typically anchors are located on human body where the surface is most stable, and typically where the bone is near the surface of the skin, e.g. shoulder, waist and ankle, [14]. These key anchors could carry loads with the least misalignment, resulting in effective force transfer and safe interaction with the body. Therefore, the ends of the orthotic prototype are proposed to be attached to the waist and the calf of the leg so that the prototype can align closely to the thigh when performing swing motion (fig. 4.8a). The orthotic prototype was developed using the Bubble Artificial Muscle to increase knee flexion and thereby restore it to the level of a young subject.

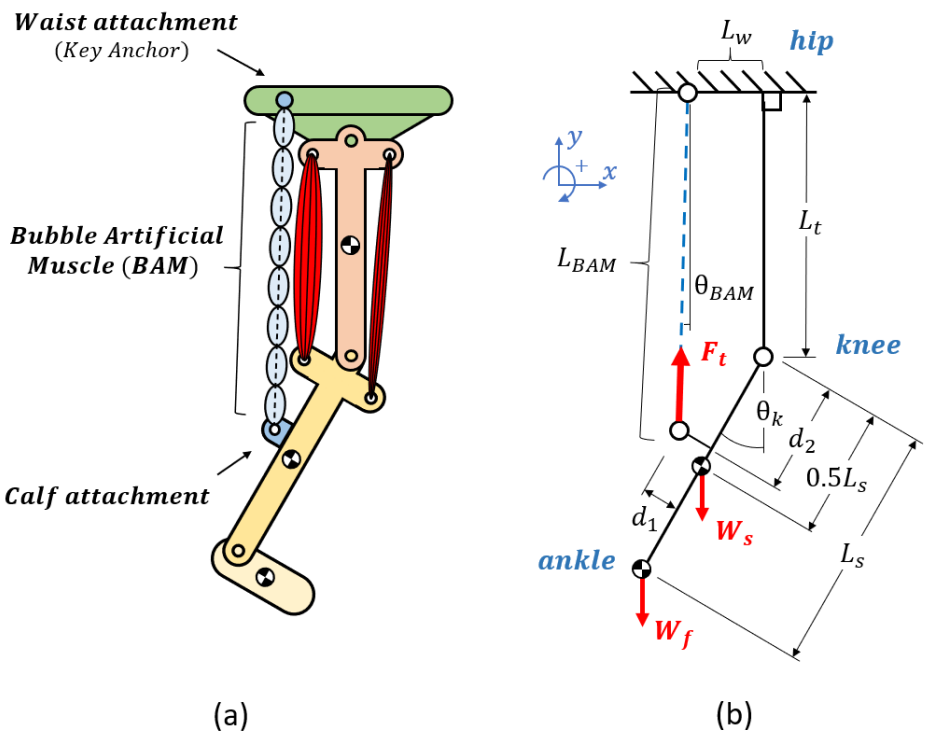

Figure 4.8: (a) Design of the BAM orthosis, composing of waist and calf attachments, and the Bubble Artificial Muscle, and (b) its static force diagram to calculate the required contraction and tensile force.

In reality, the human leg may possibly stop during its swing phase due to some unexpected incident or accident; therefore, an orthosis must be able to support the entire leg mass when it stops. In consequence, we must consider the static situation when we design and build a knee orthosis, and ensure that it can hold the leg mass. A static test was undertaken to evaluate the capability of the BAM orthosis in flexing the leg mechanism and supporting the leg.

4.1.5 Modelling and Analysis of BAM Orthosis

The orthotic model (fig. 4.8a) can be converted into a static force diagram to calculate the required contraction (c) and tensile force (F_t) while holding the leg at certain knee angle (θ_k) as shown in fig. 4.8b. The thigh linkage is fixed in the vertical axis and has a thigh length (L_t), and its weight is neglected. The shank linkage is connected to the thigh at the knee joint and has a shank length (L_s). The shank weight (W_s) and the foot weight (W_f) are located at the middle and end of the shank, respectively. The waist attachment of the BAM orthosis is designed to mount on the waist with a rearward offset (L_w). The point of attachment at the calf must strike a balance between achieving a high torque by having the actuator far from the knee joint and keeping the actuator close to the thigh by having the actuator near the joint, thereby to minimise the impact of the orthosis on the user's outward appearance. The orthosis attaches to the calf at a distance d_2 from

the knee joint and is offset from the centre line at d_1 by a distance corresponding to the thickness of the calf skin and muscle. The length of the BAM orthosis is L_{BAM}, and its centre line is at an angle to the vertical, θ_{BAM}.

The required contraction and tensile force for the orthosis to perform knee flexion are the major criteria in selecting the most suitable design and materials of the BAM, which can be derived as follows. Firstly, consider the length and angle of the orthotic prototype (L_{BAM} and θ_{BAM});

$$L_{BAM} = \sqrt{{L_{BAM,x}}^2 + {L_{BAM,y}}^2} \tag{4.7}$$

$$\theta_k = \tan^{-1}(\frac{L_{BAM,x}}{L_{BAM,y}}) \tag{4.8}$$

Where,

$$L_{BAM,x} = d_2 sin\theta_k + d_1 cos\theta_k - L_w$$

$$L_{BAM,y} = d_2 cos\theta_k - d_1 sin\theta_k + L_t$$

At a given knee angle (θ_k), the contraction (c) can be calculated from the BAM's initial length at zero-degree knee angle, $L_{BAM}(0°)$, and the actuated length, $L_{BAM}(\theta_k)$.

$$c = \frac{L_{BAM}(0°) - L_{BAM}(\theta_k)}{L_{BAM}(0°)} \tag{4.9}$$

The tensile force (F_t) can be calculated by using the moment equilibrium for the static pendulum system as follows.

$$M_{CW} = M_{CCW} \tag{4.10}$$

where,

$$M_{CW} = F_t cos\theta_{BAM} \times (d_2 \sin\theta_k + d_1 \cos\theta_k)$$

$$M_{CCW} = F_t sin\theta_{BAM} \times (d_2 \cos\theta_k - d_1 \sin\theta_k) + W_s \frac{L_s}{2} \sin\theta_k + W_f L_s \sin\theta_k$$

Therefore, the tensile force is a function of θ_{BAM} and θ_k;

$$F_t = f(\theta_{BAM}, \theta_k) \tag{4.11}$$

As a result, the required contraction and tensile force at different knee angles between 0 and 90 degree, for an example elderly subject, are presented in table 4.3. Here, the thickness of the calf muscle and skin (d_1), the location of the calf attachment (d_2) and the waist attachment (L_w) are 8, 21 and 16 cm, respectively. The length of thigh and shank segments (both 42 cm) and the mass of shank and foot (3.5 and 1.0 kg) of the elderly subject can be obtained from table 4.2.

The orthotic prototype is designed to generate a maximum knee angle of 70 degrees, which is in the range of the peak knee flexion of a young healthy subject as shown in fig. 4.2. According to the previous chapter, the BAM made of the thickest material produces

Table 4.3: The required contraction and tensile force at different knee angles for an example elderly subject, used to design the BAM orthosis.

Knee angle (θ_k) [degree]	Orthosis length (L_{BAM}) [cm]	Orthosis angle (θ_{BAM}) [degree]	Contraction (C) [cm (%)]	Tensile force (F_t) [N]
0	63.5	-7.2	0.0 (0.0)	0.0
10	61.5	-4.2	2.1 (3.2)	15.3
20	59.0	-1.3	4.5 (7.1)	25.7
30	56.2	1.5	7.3 (11.5)	33.2
40	53.1	3.9	10.4 (16.4)	38.7
50	49.6	6.0	13.9 (21.8)	42.7
60	46.0	7.7	17.5 (27.6)	45.6
70	42.2	8.8	21.3 (33.6)	47.8
80	38.3	9.1	25.3 (39.8)	49.7
90	34.4	8.4	29.1 (45.9)	51.6

the highest tensile force, comparing to other BAMs made of thinner materials. Higher tensile forces can be generated by using several BAMs aligned in parallel, while their actuation stroke can be increased by using a series of multiple BAM contractile units. Fig. 4.9 presents the tension-contraction relationship required for the orthosis at different knee angles (θ_k) between 0 and 70 degree, obtained from table 4.3, and the performance of parallel BAMs, where N indicates number of BAMs aligned in parallel. A single BAM is made of L_{unit} = 40.5 mm, R_{ring} = 4.5 mm and $s_{material}$ = 0.125 μm, and its empirical performance is acquired from fig. 3.12A.

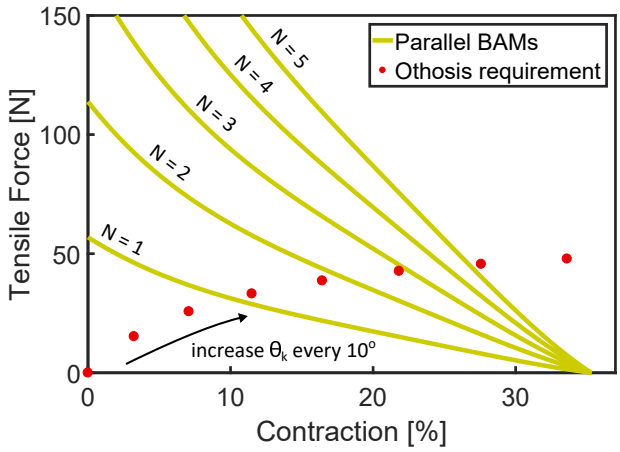

Figure 4.9: The relationship between tensile force and contraction, comparing orthosis requirement at different knee angles (θ_k) between 0 and 70 degree with increments of 10 degree and the performance of parallel BAMs for knee flexion operated at 50 kPa. N indicates number of BAMs aligned in parallel.

From fig. 4.9, five parallel BAMs can produce sufficient tension and contraction for the required working range of up to approximately 60 degree knee angle. Although this knee angle is lower than targeted (70 degree), by adjusting d_1, d_2 and L_w we can balance tension and contraction, changing the workspace of the BAM to fit the requirement. Also, the tension force of the BAM can be increased by operating at higher pressures. The maximum width of the orthosis using five parallel BAMs, when forming a maximum expanding shape, is too wide to be practical (over 17 cm when $R_{material}$ = 17.8 mm), which negatively impacts its appearance. Therefore, only three parallel BAMs were selected to create the orthosis. In this configuration, its width is smaller than that of the calf, enhancing its ability to be used with, or under, normal clothing, while still being able to produce the required tension and contraction up to a useful 50 degree knee angle.

A series BAM was designed in the form of 15 contractile units with L_{unit} = 42 mm, resulting in the total orthosis length of 63 cm, close to the resting orthosis length in table 4.3. Slightly larger rings with R_{ring} = 5 mm were used to fabricate this series BAM. Increasing L_{unit} and R_{ring} results in higher tensile force but lower contraction as investigated and discussed in the previous chapter. The complete BAM orthosis has an extremely light total weight of 206.6 grams, including fittings but excluding air supply (e.g. a pump or a compressor), and each BAM contractile unit weighs only about 3 grams.

4.1.6 Static Knee Flexion Test

The leg pendulum mechanism was constructed to evaluate the performance of the fabricated BAM actuator in assisting knee flexion. It was designed according to the leg model described in section 4.1.2, using Fusion 360, a 3D drawing program, as shown in fig. 4.10. The shank linkage was made of an aluminium plate and connected to a steel shaft passed through bearings mounted on an aluminium frame used as the thigh linkage (fig. 4.10a). Weight plates were used to represent the shank and foot mass, which can be adjusted for different loads (fig. 4.10b).

(a) 3D Drawing Model (b) Physical Pendulum Model

Figure 4.10: The leg pendulum model: (a) a 3D drawing model and (b) the physical pendulum model.

The thigh linkage is fixed in the vertical orientation while the shank linkage, with attached shank and foot masses, can rotate freely as shown in fig. 4.11. The BAM orthosis (comprising three parallel BAMs) was mounted between the centre of the shank linkage and the top of the rig (at a position corresponding to the posterior side of the waist). An air compressor (CW 100/24 AL, Werther International S.p.A., Germany) with two solenoid valves (WZ-98302-46, Cole-Parmer, UK) was used to inflate the orthosis to achieve rapid actuation, and 12V vacuum pump was used to actively deflate the orthosis. A 24-pulse incremental rotary encoder (DPL12SV2424A25K2, TE Connectivity, Switzerland) was connected to the knee joint via 3D printed polylactic acid (PLA) plastic gears to record the knee flexion angle when activating the BAM orthosis. The resolution of a leg pendulum angle sensor was 0.75 degrees. The leg pendulum is set to have 3.5 and 1.0 kg at the middle and end of the shank linkage to represent the shank and foot mass, respectively, as presented in table 4.2.

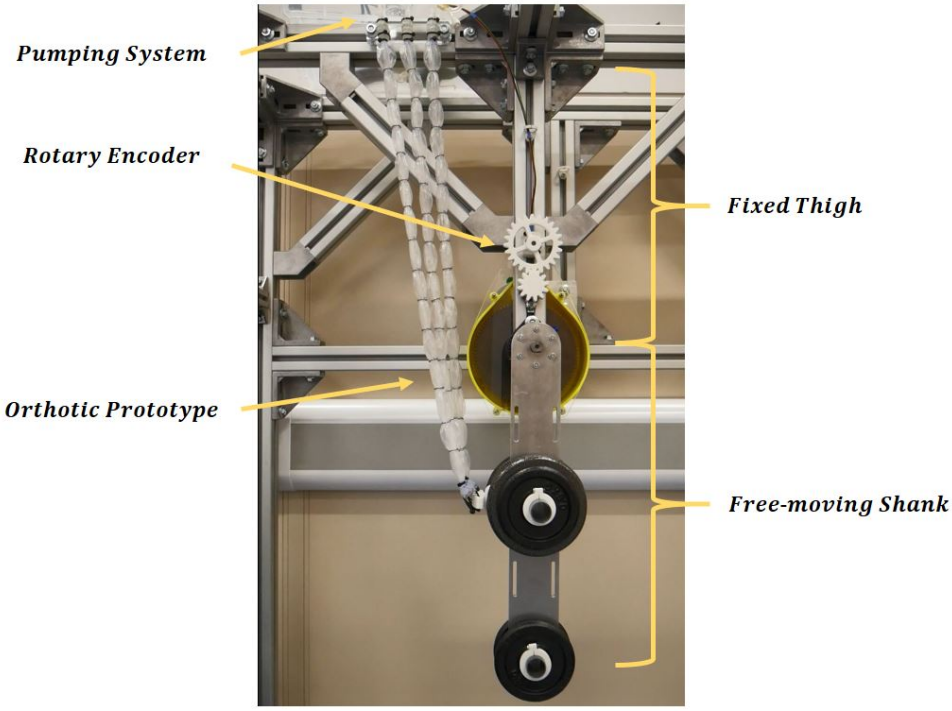

Figure 4.11: The experimental setup of the BAM orthosis mounted on the leg pendulum, ready for static testing.

At the beginning of each experiment, the pendulum leg was set at a zero degree knee angle as the initial angle. This initial knee angle can be changed using a rope with a spring as shown in fig. 4.10b. The rope can set the pendulum at any knee angle and limit it when swinging back after actuation by the orthosis, and the spring removes sudden reaction forces between the rope and the whole aluminium frame. The BAM orthosis was inflated, held at a fixed pressure, and then deflated sequentially for 6, 2 and 12 seconds, respectively. The experiments were performed five times at different operating pressures between 50 and 80 kPa with increments of 10 kPa. The orthosis was set to its full-extended

length before each test. Average and maximum peak knee flexion were 46.35 and 47.25 degrees respectively (fig. 4.12a and 4.13), both occurring within about 5.7 seconds at an applied pressure of 70 kPa. Increasing the applied pressure beyond this point (up to 80 kPa) did not increase knee flexion because the BAM had already fully contracted. In contrast, after the masses on the shank linkage were removed, the leg mechanism could swing up to the peak knee flexion of 60 degree, as shown in fig. 4.12b.

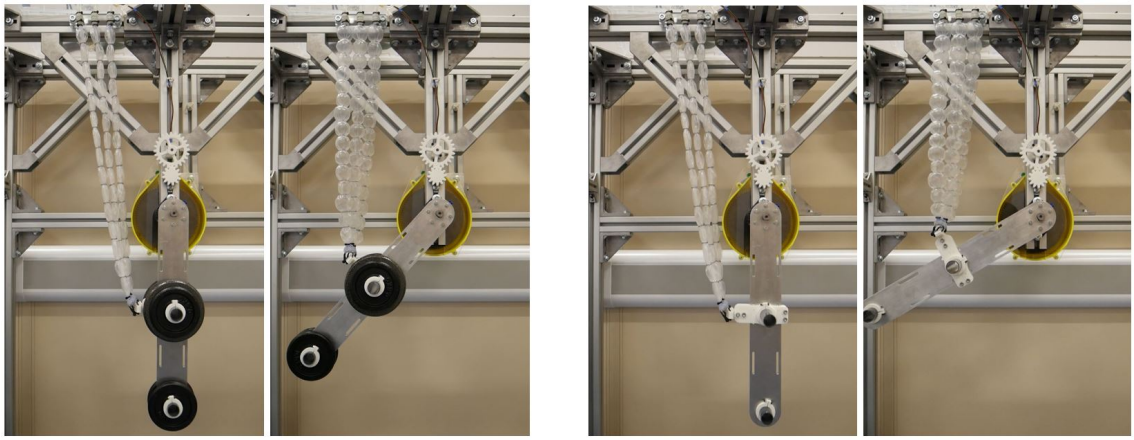

(a) (b)

Figure 4.12: The static pendulum test of the BAM orthosis at zero and maximum inflation: (a) the leg pendulum with the 3.5 kg shank mass and 1.0 kg foot mass and (b) the leg pendulum with no mass. Both experiments were operated at 70 kPa.

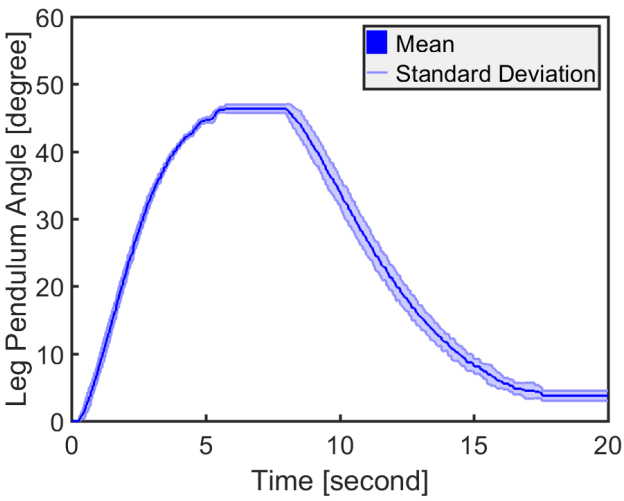

Figure 4.13: The mean knee flexion for five tests performed by the BAM orthosis operated at the pressure of 70 kPa, recorded by the encoder. The shank and foot mass were 3.5 and 1.0 kg. (line and shadow represent mean and standard deviation, respectively).

The developed BAM orthosis was only tested on a human-like leg mechanism to evaluate its efficiency in performing knee flexion. Future experiments can be undertaken by

connecting a motor system at the other end of the steel shaft at the knee joint, allowing the leg mechanism to perform knee flexion when applying a torque generated by the motor. With this setup, the leg mechanism can be controlled to perform knee flexion mimicking that obtained from data obtained from older people, as shown in fig. 4.2, and the BAM orthosis can be simultaneously actuated to investigate its performance in assisting knee flexion for real-world situations.

4.2 BAM Assistance on Sit-to-stand Transition (STS)

This section presents how the Bubble Artificial Muscles (BAMs) can assist sit-to-stand transition (STS). Different designs of leg mechanisms are firstly introduced and discussed, followed by the design and analysis of the BAM orthosis and a standing-assisting test. Similar to the GLW assistance, the BAM orhtosis for STS is proposed to support the functions of the knee.

4.2.1 Design of Leg Mechanism

Initially, a four-bar linkage was designed to lift a wooden dummy from sitting to standing position by attaching the mechanism at the back of the dummy (fig. 4.14). After fixing the position of the dummy's feet, these linkages can constrain the movements of the dummy's trunk while standing. Although this design clearly achieves the basic STS task, it requires a large working space and complicated orthotic attachments to transfer force through the dummy's lower limbs for standing. Consequently, we focused only on a simpler model employing a replica of one human leg.

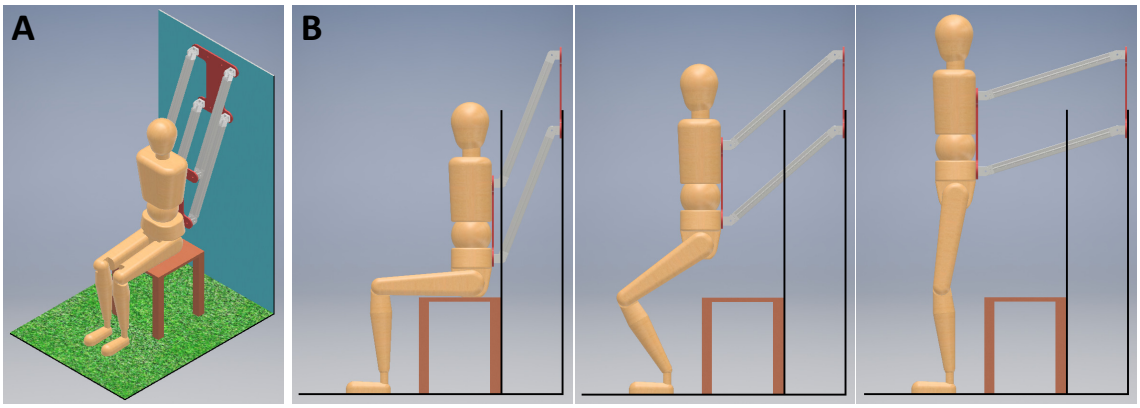

Figure 4.14: Design of a sit-to-stand mechanism using a four-bar linkage to lift a wooden dummy from sitting to standing position.

Similar to the design of the leg mechanism for walking motion previously presented, a sit-to-stand leg mechanism can be designed based on one human leg, consisting of three main components: thigh, shank and foot, connected through knee and ankle joints. Fig. 4.15 shows the design of one leg mechanism including an example of the BAM orthosis as

well as its attachments along the leg. The entire mechanism was built using aluminium profiles (KJN Automation Ltd., UK). All lower limbs, such as thigh, shank and foot, were connected using revolute joints at the knee and ankle. The hip motion is constrained by using a plastic shaft, connected at the end of the shank linkage as the hip joint, to support and remain inside an acrylic profile which defined a specific trajectory (fig. 4.15B). This shaft can also be loaded with an additional mass, which is assumed to be less than the mass of the human trunk. Two different hip trajectories were designed and built to observe the leg movements during a standing task: curve and straight trajectories, as shown in fig. 4.16, A and B. When constraining the hip trajectory and fixing a position of the foot, the thigh and shank linkages can freely move, mimicking human's standing motion.

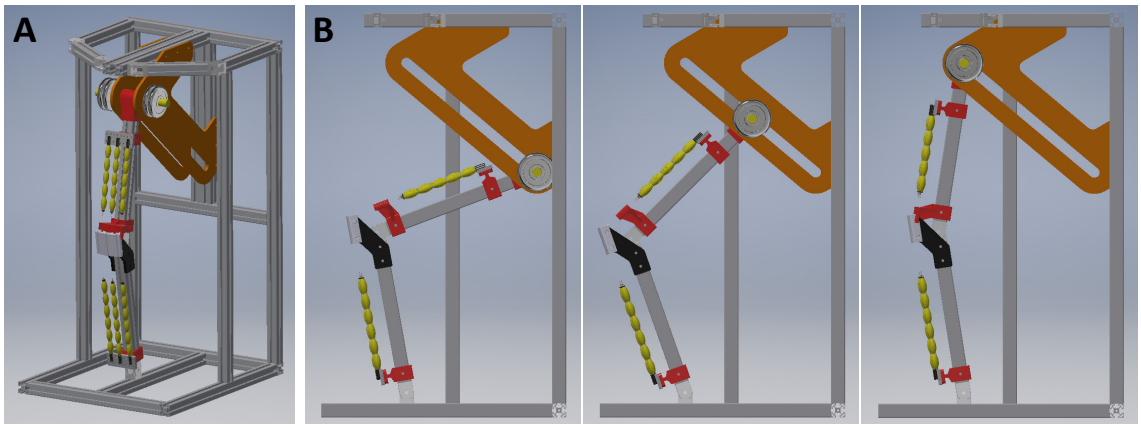

Figure 4.15: Design of a leg mechanism using two linkages to perform sit-to-stand transition. Three series BAMs are mounted on the leg mechanism using three attachments along the leg mechanism.

In practice, the leg failed to stand when applying forces over the knee for standing in the cases where the trajectory was defined by the acrylic plate. This is because the freely-moving thigh and shank linkages tended to extend, pushing the hip into the top part of an acrylic profile, generating significant friction which restricted movement along the designed routes. This issue can be solved by removing the acrylic trajectory profile, fixing the position of the foot and shank linkages (meaning that an angle of the ankle joint is fixed) and only freeing the thigh linkage, as shown in fig. 4.16C. This approach allows the leg model to perform the STS when an assistive force is applied. Therefore, design C was used to build the leg mechanism and design a wearable orthosis.

4.2.2 Design of a BAM wearable Orthosis

A BAM wearable orhtosis was designed and attached to the sit-to-stand leg mechanism as shown in fig. 4.17A. The STS leg mechanism consists of three segments: a foot base, a shank linkage and a thigh linkage, which are connected via two revolute joints as a knee and an ankle. It was designed so that the shank linkage can be fixed with an adjustable ankle angle and an external load can be added to the hip joint (fig. 4.17B).

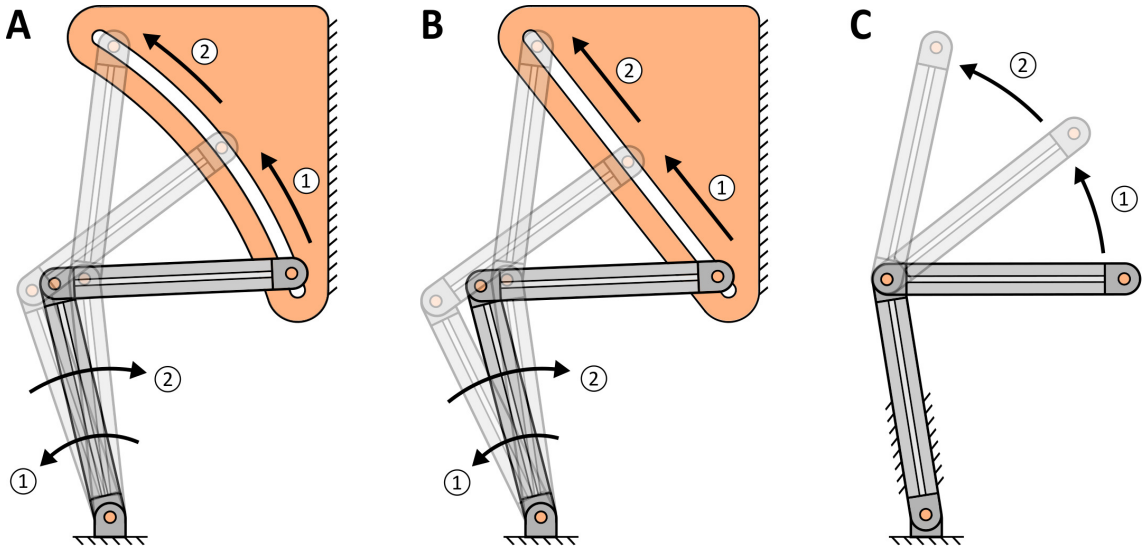

Figure 4.16: Three different trajectories of lower-limb joints of the leg mechanism while performing sit-to-stand transition. (A-B) Both thigh and shank linkages are free-moving, and the hip joint are constrained in (A) curve or (B) straight trajectories. (C) The shank linkage is fixed at a given ankle angle, allowing only the thigh linkage to freely move to perform STS. Numbers indicate sequences of STS movements.

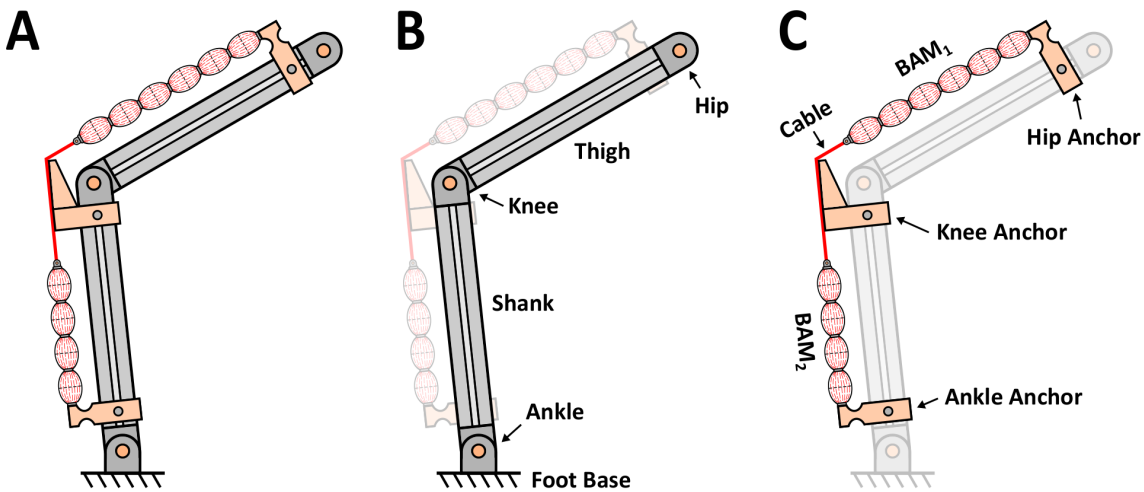

Figure 4.17: The experimental setup for the sit-to-stand motion (A) is composed of two main parts: the leg mechanism (B) and the BAM orthosis (C).

The BAM orthosis was created using three pairs of BAMs aligned in parallel (fig. 4.17C). In each pair, two BAM chains (each with seven actuator elements) are connected in series by cables and mounted to the thigh and shank linkages using three anchors. The ends of BAM_1 and BAM_2 connect to the hip and ankle anchors and the connecting cables, which pass through the knee anchor.

4.2.3 Modelling and Analysis of BAM Orthosis

Mathematical diagrams of the sit-to-stand leg mechanism were built to calculate the required contraction and tensile force for the BAM orthosis in order to perform a standing motion (fig. 4.18). The shank segment in fig. 4.18B is shortened, and the thigh segment is set at a higher knee angle comparing to fig. 4.18A to illustrate the orthosis angle γ, referred to the thigh segment (the angle between $\overline{hk}$ and $\overline{HK}$). Hip, knee and ankle joints are defined as H, K and A. h and a are hip and ankle anchors for the BAM orthosis, and k is the location on the knee anchor, where the connecting cables always touch. All relevant parameters are defined in table 4.4.

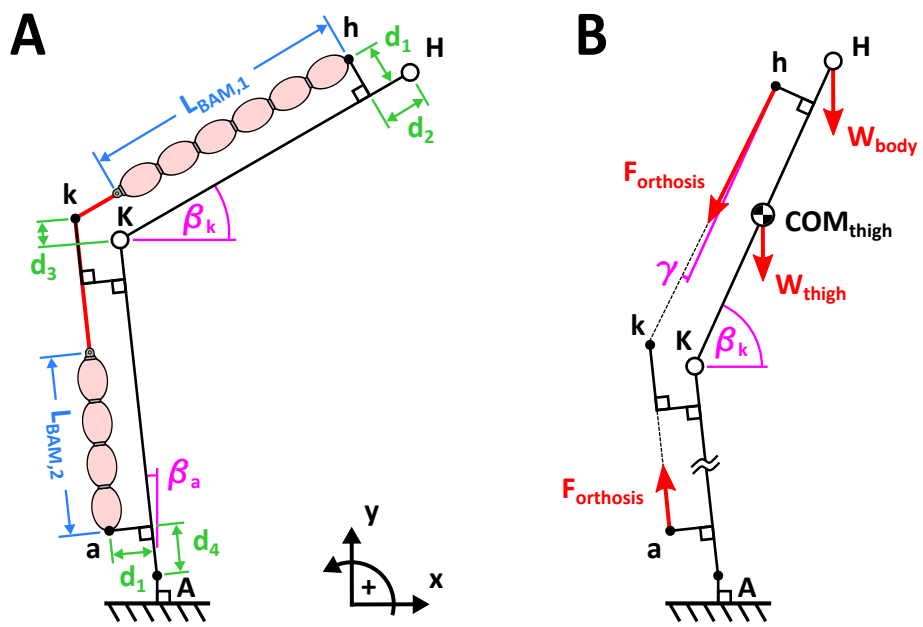

Figure 4.18: Diagrams of the sit-to-stand leg mechanism presenting all parameters used to calculate the required contraction (A) and tensile force (B) of the BAM orthosis.

To simplify the complex standing movement of the lower limbs, the shank segment is fixed at an ankle angle β_a. The thigh segment is freely-moving from horizontal level ($\beta_k = 0°$) to a limited standing posture ($\beta_k = 90°–\beta_a$), where the hip was vertically aligned with the ankle, meaning that thigh and shank segments are symmetrical. As a result, the BAM orthosis were simply used to pull and rotate the thigh segment at the revolute knee joint with an additional body weight W_{body} at the hip joint. The weight of the thigh segment W_{thigh} is assumed as a point load at the middle of the thigh segment as its centre of mass COM_{thigh} for ease of calculating othorsis requirements. According to fig. 4.18A, the coordinate of each joint and anchor can be derived as listed in table 4.5, and the required contraction $c_{orthosis}$ and tensile force $F_{orthosis}$ can be derived as follows. $c_{orthosis}$ can be calculated from the change in $\overline{hk}$ and $\overline{ka}$, and $F_{orthosis}$ is parallel to $\overline{hk}$ and $\overline{ka}$.

Table 4.4: Definition of all parameters used to calculate the required contraction and tensile force of the BAM orthosis.

Parameter	Definition	Unit
$\overline{HK}$	Length of the thigh between hip and knee joints.	mm
$\overline{KA}$	Length of the shank between knee and ankle joints.	mm
$\overline{hk}$	Available length for the BAM orthosis on the thigh.	mm
$\overline{ka}$	Available length for the BAM orthosis on the shank.	mm
$L_{BAM,1}$	Length of the first BAM of the orthosis on the thigh.	mm
$L_{BAM,2}$	Length of the second BAM of the orthosis on the shank.	mm
d_1	Distance of the anchors from leg segments ($\overline{HK}$ and $\overline{KA}$).	mm
d_2	Distance of the anchor point from the hip joint.	mm
d_3	Offset height of the knee anchor from the knee joint.	mm
d_4	Distance of the anchor point from the ankle joint.	mm
β_k	Angle of the knee referred to the horizontal axis.	degree
β_a	Angle of the ankle referred to the vertical axis.	degree
γ	Angle of the BAM orthosis referred to the thigh axis.	degree
W_{thigh}	Gravity force of the thigh mass.	N
W_{body}	Gravity force of an external load at the hip, proportional to human body weight.	N
$F_{orthosis}$	Orthosis tension to perform standing at knee angle β_k.	N
$c_{orthosis}$	Orthosis contraction to perform standing at knee angle β_k.	%

Table 4.5: Coordinate (x, y) of all joints, i.e. hip, knee and ankle, and key anchors of the sit-to-stand mechanism.

Joint	Coordinate	
	x	y
A	x_0	y_0
K	$x_0 - \overline{KA}sin\beta_a$	$y_0 + \overline{KA}cos\beta_a$
H	$x_0 - \overline{KA}sin\beta_a + \overline{HK}cos\beta_k$	$y_0 + \overline{KA}cos\beta_a + \overline{HK}sin\beta_k$
a	$x_0 - d_4sin\beta_a - d_1cos\beta_a$	$y_0 + d_4cos\beta_a - d_1sin\beta_a$
k	$x_0 - \left(\overline{KA} + d_3\right) sin\beta_a - d_1cos\beta_a$	$y_0 + \left(\overline{KA} + d_3\right) cos\beta_a - d_1sin\beta_a$
h	$x_0 - \overline{KA}sin\beta_a + \left(\overline{HK} - d_2\right) cos\beta_k$ $-d_1sin\beta_k$	$y_0 + \overline{KA}cos\beta_a + \left(\overline{HK} - d_2\right) sin\beta_k$ $+d_1cos\beta_k$

The length for the orthosis $L_{orthosis}$ to achieve standing motion at given knee angle β_k can be derived from eq. (4.12), where $\overline{ka}$ and $\overline{hk}$ are the distance between the ankle and knee anchors and distance between the knee and hip anchors, respectively.

$$L_{orthosis}(\beta_k) = \overline{ka} + \overline{hk} \tag{4.12}$$

These two distances can be calculated using the following equations and coordinate values from table 4.5.

$$\overline{ka} = \sqrt{(x_k - x_a)^2 + (y_k - y_a)^2}$$
$$\overline{hk} = \sqrt{(x_h - x_k)^2 + (y_h - y_k)^2}$$

The stroke $\Delta L_{orthosis}(\beta_k)$ and contraction $c_{orthosis}(\beta_k)$ of the orthosis at a given knee angle β_k can be derived as follows.

$$\Delta L_{orthosis}(\beta_k) = L_{orthosis}(0°) - L_{orthosis}(\beta_k) \tag{4.13}$$

$$c_{orthosis}(\beta_k) = \frac{\Delta L_{orthosis}(\beta_k)}{L_{BAM,1}(0°) + L_{BAM,2}(0°)} \tag{4.14}$$

Where $L_{BAM,1}$ and $L_{BAM,2}$ are the actual length of the BAM orthosis. From fig. 4.18B, the required torque can be calculated by using the equilibrium of moments when considering the thigh segment and the knee revolute joint.

$$F_{orthosis}(\beta_k) = \frac{\left(\frac{W_{thigh}}{2} + W_{body}\right) \cdot \overline{HK} cos\beta_k}{d_1 cos\gamma + \left(\overline{HK} - d_2\right) sin\gamma} \tag{4.15}$$

The relationship between the contraction and the tensile force associated with the knee angle can be demonstrated in fig. 4.19. The dimension of the sit-to-stand leg mechanism is provided in table 4.6. The ankle angle is fixed at $\beta_a = 10°$, and the knee angle β_k starts at 0° and is limited at 80°. W_{thigh} and W_{body} are the gravity forces of the thigh mass of 1.5 kg (an aluminium frame) and an external load of 1.0 kg (weight plates) when $g = 9.81$ m/s^2.

The orthosis was designed to have three pairs of BAMs aligned in parallel, located over the thigh segment (BAM_1) and shank segment (BAM_2) as shown in fig. 4.17. Both BAM_1 and BAM_2 contain seven contractile units in series, where each unit is made using $L_{unit} = 40.5$ mm, $R_{ring} = 4.5$ mm and $s_{material} = 125.0$ μm, leading to a total length of 28.4 cm (as shown in table 4.6). According to fig. 4.19, the orthosis consisting of three parallel BAMs will achieve a standing angle β_k up to 80 degree with zero additional mass, and about 50 degree when an external load at the hip of 1 kg is applied, when actuated at 50 kPa.

Table 4.6: Sizes of the components of the leg mechanism and the BAM orthosis.

Parameter	Dimension [cm]	Parameter	Dimension [cm]
$\overline{HK}$	48.0	d_1	7.5
$\overline{KA}$	46.0	d_2	14.5
$L_{BAM,1}$	28.4	d_3	6.0
$L_{BAM,2}$	28.4	d_4	5.5

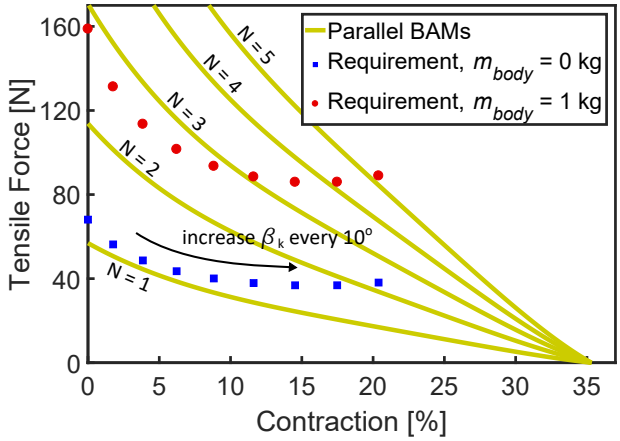

Figure 4.19: The relationship between tensile force and contraction, comparing orthosis requirement at different knee angles (θ_k) between 0 and 80 degree with increments of 10 degree and the performance of parallel BAMs for sit-to-stand transition operated at 50 kPa. N indicates number of BAMs aligned in parallel, and two orthosis requirements are plotted for body masses of 0 and 1 kg, shown as blue square and red circle marks, respectively.

4.2.4 Standing-assisting Test

A leg mechanism was built to evaluate the BAM performance in assisting human mobility in the task of standing up from a sitting position as shown in fig. 4.20. The BAM orthosis was able to perform sit-to-stand transition up to a maximum knee angle of 80 degree within 5 s, supplied by an air compressor at $P = 50$ kPa when there is no external load (fig. 4.20). When an additional mass of 1 kg is attached at the hip joint, the orthosis can lift the thigh segment up to approximately 45 degree at 50 kPa, but was able to deliver full standing when the pressure was increased to 70 kPa.

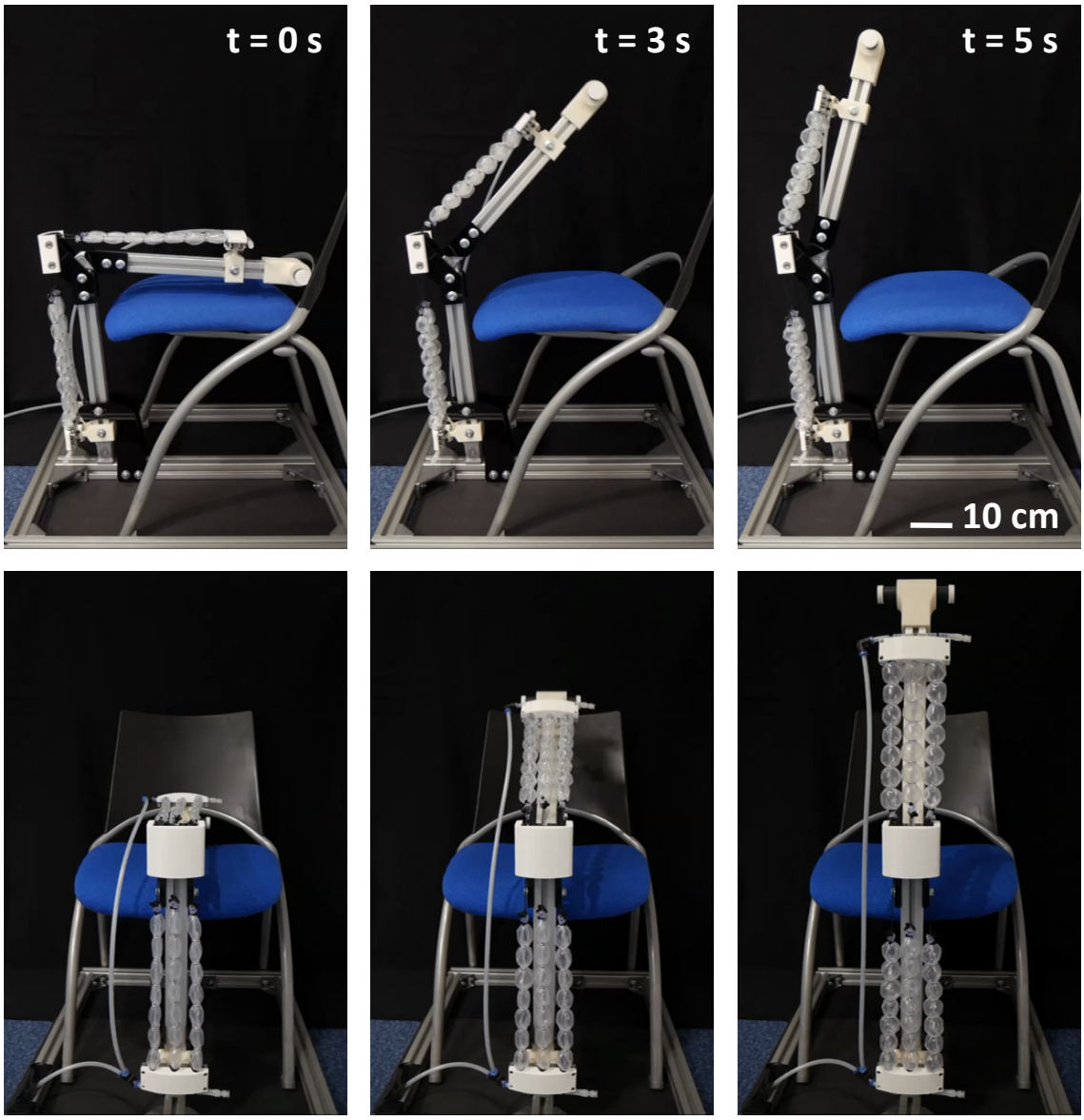

Figure 4.20: Actuation of the BAM orthosis on the human-like leg mechanism to perform standing motion, operated at 50 kPa (no additional load).

4.3 Discussion

The concept of mobility assistance was defined, and it was shown that an effective orthosis could improve and replace work generated by weakened human muscles. This orthosis could perform and maintain high-performance locomotions, potentially solving the problem of mobility impairment for older people. Two types of assistive orthoses were presented in this chapter, demonstrating the capabilities of the Bubble Artificial Muscles (BAMs) in producing mechanical work on human-scale leg mechanisms, attaining essential knee functions for ground-level walking (GLW) and sit-to-stand transition (STS). Two human-scale leg mechanisms were designed and built to assess the performance of the developed BAM orthoses in mobility assistance. The orthoses were designed to attach along the leg

over the knee joint at the front and back of lower limbs for knee extension and flexion, respectively.

Based upon the achieved knee flexion for GLW, the BAM orthosis was able to exert a maximum torque of 8.32 Nm at a maximum knee flexion of 47.25 degrees. This knee angle is approximately 70% of the peak knee flexion acquired from young healthy subjects with age under 30 (67.8 degrees) [5]. The typical exerted moment during knee flexion has been recorded at 25 Nm (for a healthy young subject with body weight 79 kg and height 1.75 m) [14]. As such, the BAM orthosis can deliver 33.3% of the required knee flexion torque. The BAM orthosis created for STS accomplished a standing task on a replicate leg mechanism loaded with an additional mass of 1 kg, starting from a stable sitting position. It exerted a maximum torque of 8.24 Nm, equal to 7.4% of the peak required torque during slow STS without additional supports (111 Nm, acquired from [35]).

The presented BAM orthoses are extremely lightweight and flexible, making them suitable for wearable assistive robotic clothing. They could be attached to a subject using tight straps, or to a passive orthotic such as a knee-brace to convert them to an assistive device. Both orthoses for knee flexion and extension can be combined to create a compact orthosis which can function to fully aid the mobility of the knee joint. Ideally, the size of BAMs should be miniaturised, making them possible to be integrated with normal clothing to create an advanced smart assistive suit. This would controllably change its morphology and function from a normal passive fabric to an assitive system, ready to work and exert supporting forces to supplement human mobility when required. Future experiments can be undertaken involving a human subject to evaluate the performance of the orthoses in assisting human mobile tasks and to develop the orthoses further.

The drawback of the presented BAM orthoses is that, since they are pneumatically-driven, they require a portable pumping system or source of high pressure air to operate. Although the presented BAM orthoses exhibited promising potential in assisting human mobilities, their actuation is slower than that required to assist the dynamic locomotions of young and elderly subjects, particularly the knee swing which occurs in less than one second. The next chapter will introduce an alternative soft robotic technology, an electrically-driven actuator, which has been developed to address the major issue of reliance on conventional pneumatic power sources, resulting in fast, silent and lightweight actuation (Chapter 5).

In addition to limited actuation speed, the most important characteristics of assistive devices are safety and reliability, since for all users, and especially for elderly and disabled people, improper actuation could inhibit their locomotions or even encourage falling. To prevent these, a portable air supply is required to be reliably controlled to inflate and deflate the pneumatic orthosis at the correct time. This system was invented and is presented in Chapter 6. Moreover, sophisticated sensing mechanisms and gait-prediction models are necessary to correctly interpret the user's intention while walking or standing, which can be studied as a next step of this research (see future work in Chapter 7).

Chapter 5

Development of Electro-ribbon Actuator

Parts of the work described in this chapter has been submitted to the following peer-reviewed venue as:

- **Diteesawat RS**, Fishman A, Helps T, Taghavi M, Rossiter J. Closed-loop Control of Electro-ribbon Actuators. Submitted to *Frontier in Robotics and AI* under the research topic of "Advances in Modelling and Control of Soft Robot", in April 2020. *Diteesawat RS and Fishman A contributed equally in this work.*

The previous chapters introduced a novel lightweight, inexpensive pneumatic actuator, namely Bubble Artificial Muscle (BAM), and presented its capabilities in human mobility assistance for walking motion and sit-to-stand transition. The BAM can be optimised to deliver either high contraction or high tension, easily tuned to suit various applications, especially for human mobilities. However, the BAM requires a noisy and heavy pump or compressor as its air-supplying system to operate as a muscle. This limits the use of BAM in portable and high-speed wearable applications.

This chapter discusses the electro-ribbon actuator (ERA) [105], an electrically-driven actuator which has high potential to be implemented in wearable assistive devices thanks to its high actuation response, silent operation and low weight, enabling portability and addressing the major limitations of pneumatic actuators. The ERA applies the actuation concept of Dielectrophoretic Liquid Zipping (DLZ) to significantly amplify the electrostatic force, resulting in high-stress and high-strain performance. Control algorithms were developed to increase its capability, leading to various actuation profiles. Novel fabrication processes of ERAs using low-cost materials were explored, resulting in a simpler fabrication method and the possibility to introduce new designs and morphologies of the ERAs, widening their applications. Several conceptual designs for different configurations and functions are presented in this chapter as some examples demonstrating their versatility.

5.1 Dielectrophoretic Liquid Zipping (DLZ)

Dielectrophoretic Liquid Zipping (DLZ) is an actuation concept recently introduced in [105], which uses dielectric liquid to dramatically amplify electrostatic zipping force. Electrostatic zipping actuation has been previously demonstrated in several zipping devices [112–114]. When two electrodes are oppositely charged, a strong electric field is developed between them, inducing a strong electrostatic attractive force that closes the electrodes like a zipper. However, zipping devices are mostly designed for microelectromechanical systems (MEMS) since the electrostatic force is stronger at small displacements. When scaled up, they can not produce a useful force even with the application of high voltage. DLZ improves this zipping force by adding dielectric liquid between two electrodes, which significantly amplifies electrostatic force and increases zipping performance in macro scale.

While this force amplification can be achieved by submerging the entire actuator in the dielectric liquid, only a tiny droplet at each zipping point is sufficient. This is because coincidentally occurring dielectrophoretic force (drawing higher-permittivity materials respect to the medium towards strong electric fields) help to retain the dielectric liquid at the zipping point [105]. An actuation of a simple electro-origami fold (featuring one zipping corner of the ERA) is demonstrated in fig. 5.1, A and B. When charging opposite electrodes, the fold starts zipping from the corner, causing the flow of dielectric liquid along with zipping direction to consistently amplify electrostatic force at an attracting area, and eventually fully zips. Fig. 5.1C shows the difference of isometric tensile forces between an actuation with and without an addition of dielectric liquid.

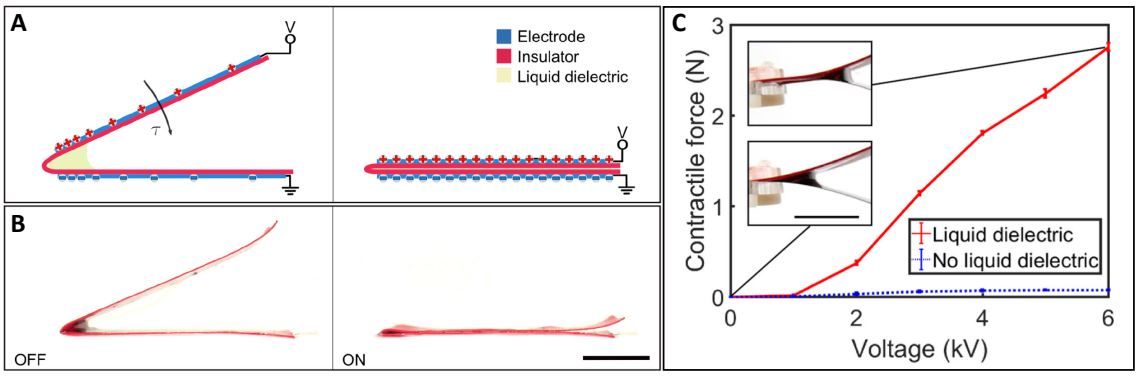

Figure 5.1: (A-B) Simple configuration of two electrodes with a tiny droplet of dielectric liquid, demonstrating Dielectrophoretic Liquid Zipping (DLZ) when oppositely charging two electrodes, showing as (A) diagrams and (B) photographs of an actuated electro-origami fold. (C) Improvement of contractile force when adding dielectric liquid to the ERA and when increasing applied voltage during isometric tests. Photographs of electro-origami zipping are inset. Reproduced with permission from [105]

The added liquid dielectric not only has a higher permittivity but also a considerably higher breakdown strength compared with air, allowing stronger electric fields to be sustained with associated stronger electrostatic zipping forces. The electrostatic force between the two electrodes is related to Maxwell pressure, $P = \varepsilon E^2$, where ε is the permittivity of the dielectric liquid and E is the electric field [115]. Silicone oil, for example, whose respective permittivity and breakdown strength are around 2.7 and 6.7 times greater than air, theoretically implies up to 120-fold amplification of electrostatic force [105].

5.2 Electro-ribbon Actuators (ERAs)

The electro-ribbon actuator is a complaint, low-mass, high-performance electrostatic actuator driven by Dielectrophoretic Liquid Zipping (DLZ) [105]. This actuator can lift 1,000 times their own weight and contract up to 99.8%; it has high specific energy and specific power equivalent to human muscle. It is made of two opposite electrodes individually seperated by an insulator and mechanically arranged in a zipping configuration, creating two zipping corners (fig. 5.2A). The ERA extends under an external load and contracts due to the attraction of opposite electric charges. When the applied voltage exceeds the critical voltage, pull-in instability occurs, resulting in full zipping.

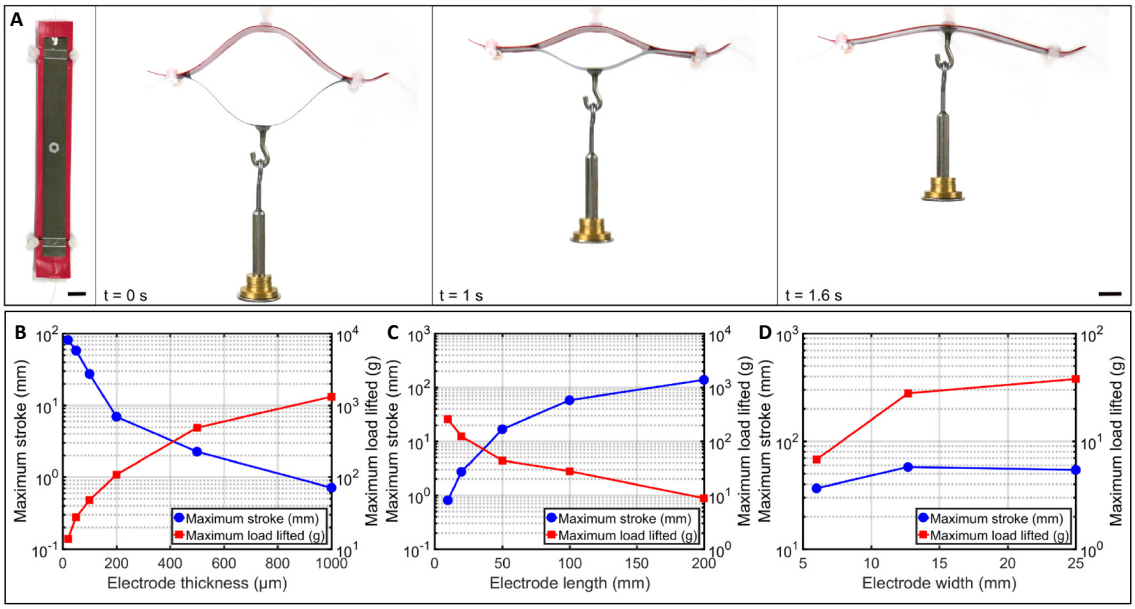

Figure 5.2: (A) Actuation of the standard Electro-ribbon actuator (ERA). Scale bars, 10 mm. (B-D) Performance of ERAs when varying electrode's dimensions: (B) thickness, (C) length and (D) width while the other parameters are fixed. Reproduced with permission from [105]

The standard electro-ribbon actuator [105] uses flat steel strips (1.1274 carbon steel, h+s präzisionsfolien GmbH, Germany) as the electrodes due to their conductive property. The beam provides stiffness to the actuator, allowing either high-stress or high-strain ac-

tuation when using thick and thin steels, respectively. The insulator is required to possess high permittivity while that of the dielectric liquid is recommended to be lower, since electrostatic field is stronger in a medium with lower permittivity. Both must have high breakdown strength to withstand high applied voltage for the actuation. PVC electrical insulation tape (AT7 PVC Electrical Insulation Tape, Advance Tapes, UK) and 50-cSt silicone oil (#378356, Sigma-Aldrich, USA) were used as the insulator and dielectric liquid for the standard ERA, of which permittivity are 4.62 and 2.7, respectively [105].

The dimension of the electrodes, i.e. length, width and thickness, showed major effects on the performance of the ERAs (fig. 5.2B). Wider electrodes have a larger zipping surface area at the zipping corners, generating higher electrostatic force for the given voltage. Variations of length and thickness of the electrodes lead to different actuator's stiffness and performance. The ERA made of short and thick steel beams delivers high stress, whereas that made of long and thin steel beams delivers high strain [105].

Besides high-stroke and high-force capabilities of a single-unit ERA, it can be designed to achieve multiactuator lattices with a combination of the ERAs arranged in series, parallel or both, improving their contraction and tension (fig. 5.3). Complex electro-origami designs made of three electrodes attached on a single strip were also demonstrated in [105] to build useful electro-origami devices such as solenoids, adaptive grippers, robotic cilia and locomoting robots as shown in fig. 5.4.

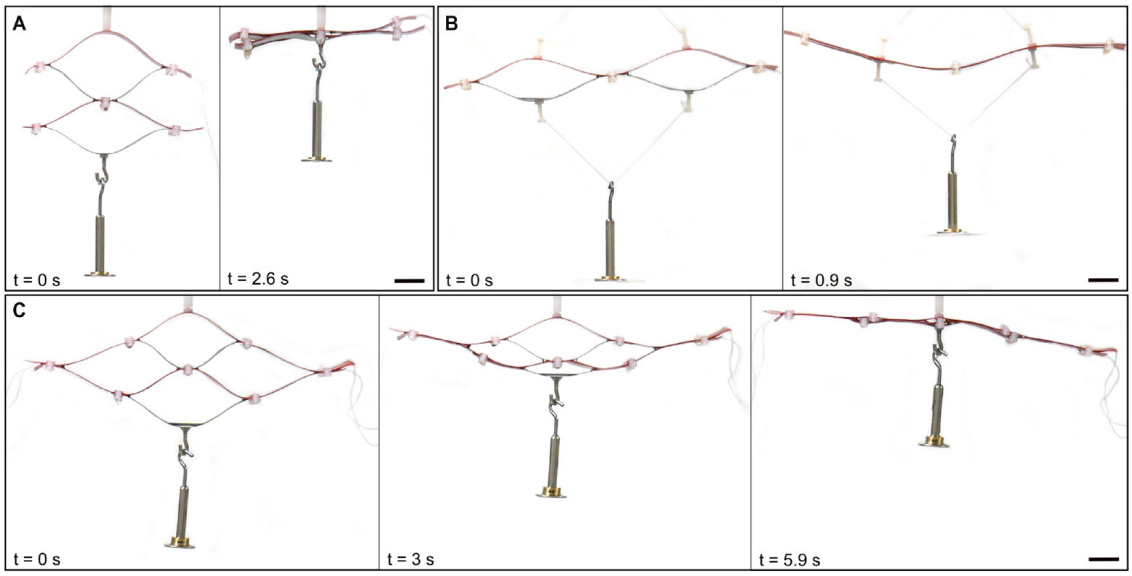

Figure 5.3: Multiactuator structures of the ERAs: (A) series, (B) parallel and (C) lattice. Scale bars, 20 mm. Reproduced with permission from [105]

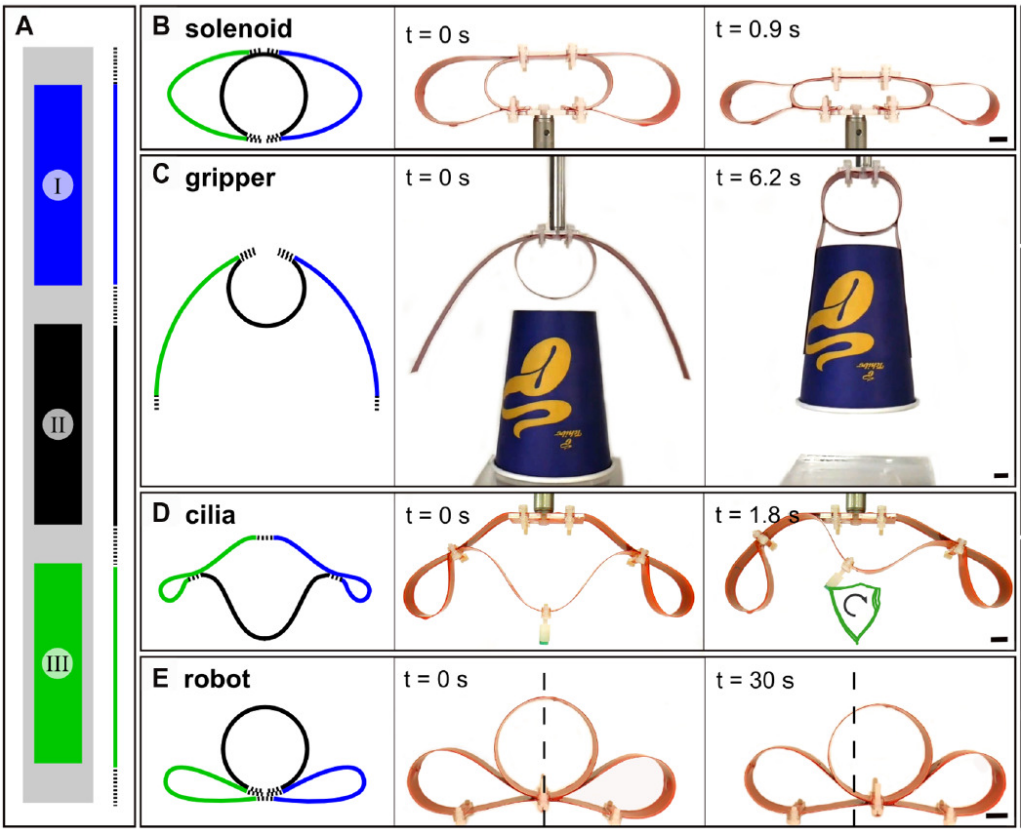

Figure 5.4: Complex electro-origami devices made from a single strip containing three electrodes: (A) solenoids (B), adaptive grippers (C), robotic cilia (D) and locomoting robots (E). Scale bars, 10 mm. Reproduced with permission from [105]

5.3 Control of ERAs

Control of soft robots is typically a challenging task due to their continuum structure and inherent compliance when interacting with the environment [116]. Conventional control strategies that assume rigid joints tend to be ineffective at controlling soft robots [83]. Closed-loop control of electrically-driven actuators, for example, Dielectric Elastomer Actuators (DEAs), has been demonstrated using capacitive self-sensing [117]. Self-sensing has also been demonstrated in liquid-filled flexible fluidic actuators [118] and electrically-driven HASEL [106] and Peano-HASEL [119] actuators, although full closed-loop control was not achieved. Closed-loop control in pneumatic bending actuators has also been demonstrated, using both flex bending sensors and hall effect sensors [120, 121].

This section will investigate closed-loop control for electro-ribbon actuators. Open-loop control is limited with these actuators because pull-in instability occurs when the applied voltage reaches a certain voltage threshold, causing instant full zipping. They have an extremely small range of travel where position may be reliably controlled. This nonlinearity makes the control of the ERAs challenging. However, by modulating the input voltage, a much larger region of stable positions can be achieved. A closed-loop (Boost-PI) controller is introduced, exploring the effect of system gains upon output parameters,

and selecting gains based on a multi-objective (Pareto) optimisation. Demonstrators are developed to show the control performance, including setpoint tracking of predetermined trajectories and sinusoidal signals, typical behaviours needed for the actuation and control of soft robots.

5.3.1 Experimental Setup

The ERA was made from two electrode ribbons, each of which was comprised of a 50-μm-thick, 10-cm-long, 2.5-cm-wide steel strip. Each electrode ribbon was insulated using PVC tapes, and their ends were attached to one another using custom-made plastic clips to ensure a tight zipping point (fig. 5.5). A drop of silicone oil with viscosity of 50 cSt was added to each zipping point prior to each test. High voltage was applied to the ERAs using a high voltage amplifier (5HVA24-BP1, UltraVolt, USA). Inputs were controlled, and data was recorded using a National Instrument device (NI USB-6343, National Instruments, USA). A laser displacement sensor (LK-G402, Keyence, Japan) was used to measure actuator displacement, by measuring the height of a suspended mass. The measured height was used as the feedback variable for closed-loop height control, operating at a sampling frequency of 32 Hz.

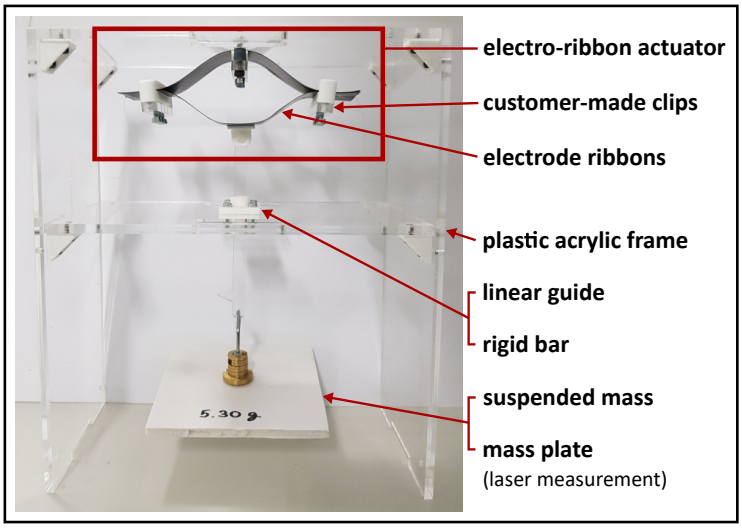

Figure 5.5: Experimental setup of an electro-ribbon actuator for testing control algorithm.

Isotonic testing was used to investigate the controllability of an electro-ribbon actuator. A rigid acrylic frame was built for the experiments. The centre of the upper ribbon of the ERA was clamped to the top of the rigid frame (fig. 5.5). The bottom ribbon was connected to a rigid bar, prescribed to move vertically by a custom-made linear guide, ensuring symmetrical zipping of the ERA. To apply load to the ERA, an external mass was hung at the bottom of the rigid bar.

5.3.2 Step Response and Pull-in Instability

To investigate the effects of electrical charging, we performed a step-response test by applying a constant voltage, $V_{constant}$, across the electrodes of the electro-ribbon actuator. Each test started from resting height, where the actuator was flexed and opened by hanging a constant mass. The applied voltage was gradually increased by 100 V increments until reaching pull-in voltage. For example, for the actuator loaded with a constant mass of 10.18 g, when the $V_{constant}$ reached 6300 V, pull-in instability resulted in the actuator undergoing full zipping (fig. 5.6). In this case, pull-in voltage $V_{pull-in}$ was 6,300 V. This pull-in instability causes rapid full zipping because the generated electrostatic force at the moving zipping points consistently and increasingly overcomes the gravitational force transferred from the external load, which is highest at zipping corners and decreases along the actuator to the centre. As a result, when the electrostatic force at the zipping corners is increased above the gravitational load, the actuator will always fully zip. Fig. 5.6 demonstrates how traditional actuation strategies for electro-ribbon actuators provide a very small controllable range. Since greater loads applied to the actuator induce larger extensions and require greater electrostatic force to initiate full zipping, $V_{pull-in}$ increases with an external load.

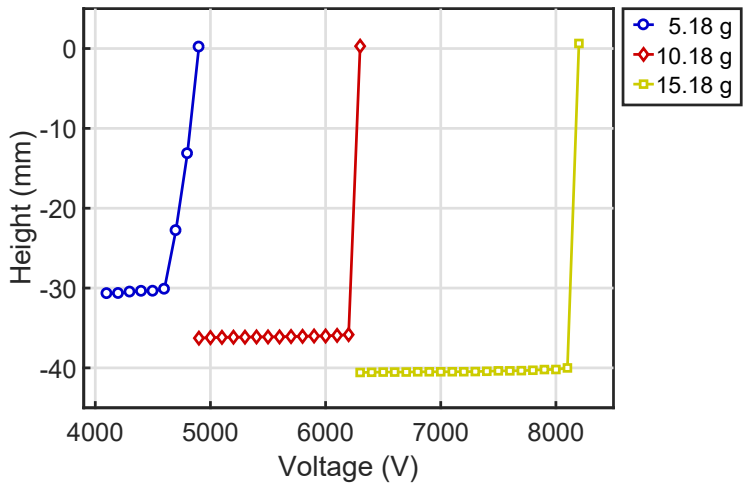

Figure 5.6: Height variation with voltage for the ERA loaded masses of 5.18 g, 10.18 g and 15.18 g.

5.3.3 Time-varying voltage Profiles

A more complex approach was explored by applying a time-varying voltage profile to the ERA (fig. 5.7A). In this experiment, the actuator began to zip when applying voltage $V \geq V_{pull-in}$. After some time, V was reduced to a constant value below $V_{pull-in}$, which allowed the actuator to be held at a new steady state height greater than the pull-in height in the previous step-response experiment. By increasing or reducing V for a short time and then setting new constant voltages below $V_{pull-in}$, the ERA was able to move its position

to multiple heights, which are not accessible by the traditional actuation strategies (fig. 5.7B). This implies that the system has multiple stable steady states depending on whether contraction has already been facilitated by exceeding $V_{pull-in}$. This could be because of the complex non-linearities associated with the electrostatic force and beam deformation.

For example, as shown in fig. 5.7A at $t = 12$ s, the voltage was increased from 2 kV to 3 kV, and the actuator thus contracted by roughly 5 mm. After decreasing the voltage to 1.7 kV, this steady-state position was maintained. Although this approach enables a wider range of accessible steady-state contractions, challenges remain because the steady-state contraction reached depends on not only the applied voltage profile but also the previous steady-state contraction. This finding highlights the need for the design of a closed-loop controller such that we can control the actuator displacement of the ERAs in this larger controllable range.

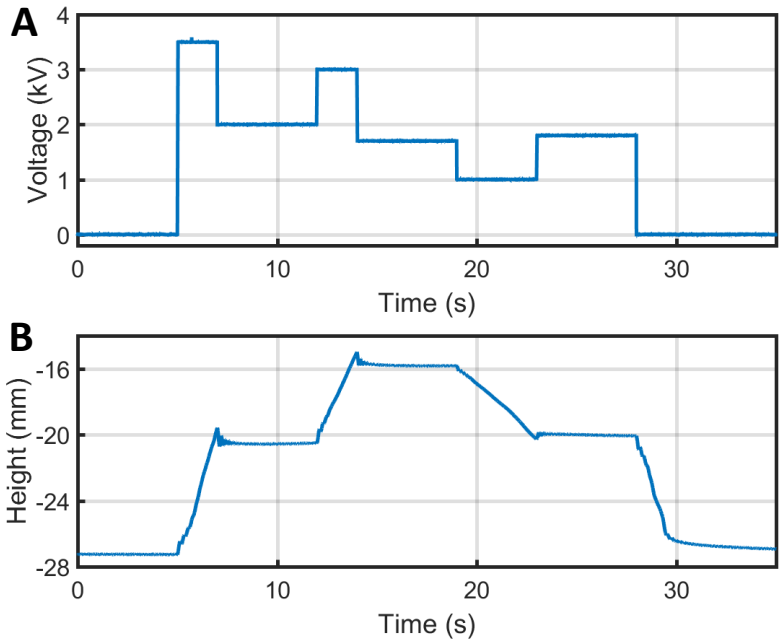

Figure 5.7: (A) Voltage and (B) height output of the time-varying voltage profile applied to the ERA loaded with a mass of 7.05 g.

5.3.4 Closed-loop Control

Having found evidence of complex non-linearities affecting actuator stability within the system, a modified closed-loop proportional-integrator (PI) controller, termed the Boost-PI controller, was developed to control the position of electro-ribbon actuators. The control law took the form of the following equations:

$$e(t) = h(t) - h_s, \tag{5.1}$$

where e is an input error, which is the difference between the current measured height h and the setpoint height h_s of the ERA. The input voltage V can be derived as follows when t is time:

$$V(t) = K_p e(t) + \int K_i e(t) dt + V_c. \tag{5.2}$$

The Boost-PI controller with an additional term consists of three parts as follows:

- K_p: a proportional term, providing a large initial voltage proportional to the error. This term acts to rapidly initiate zipping.
- K_i: an integral term, which acts to minimise the steady-state error.
- V_c: a constant voltage equal to 90% of $V_{pull-in}$, the voltage at which the actuator overcomes the load and begins to contract. This term acts to prime, or boost, the actuator for zipping, reducing rise time.

In general, the voltage applied to the electro-ribbon actuator needs to exceed $V_{pull-in}$ in order to initiate zipping. If only proportional and integral terms are used (standard PI controller), the actuator can experience large integration timescales, causing a long delay to reach this $V_{pull-in}$. For example, if the proportional term is much lower than $V_{pull-in}$, the integral term will take long time to accumulate until the total input voltage V reaches $V_{pull-in}$. In this regard, V_c is set as 90% of $V_{pull-in}$, ensuring the actuator is immediately almost at the point zipping begins. The maximum voltage applied to the actuator is limited to 9,000 V to prevent damage to the actuator or electric breakdown of the nearby air. An example actuation of the ERA under an external load of 8.04 g using the Boost-PI controller is shown in fig. 5.8.

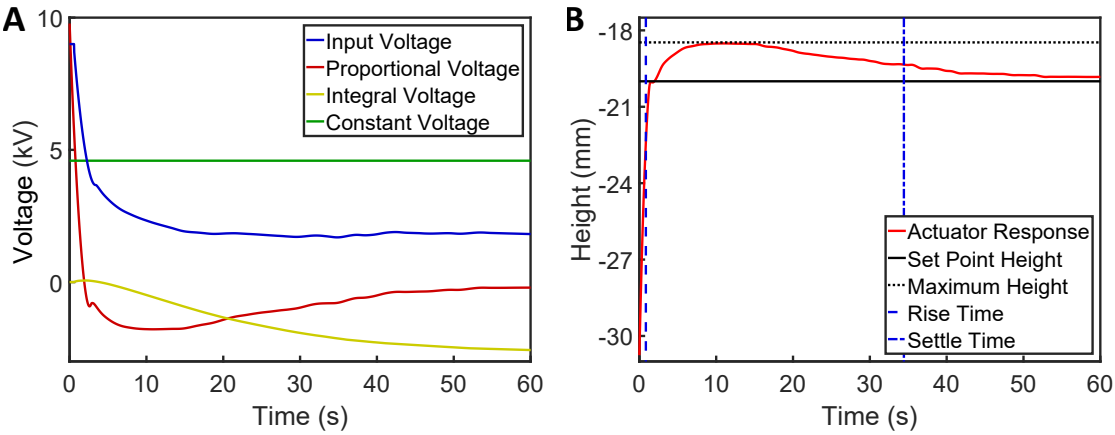

Figure 5.8: An example step-response control task of the ERA actuated using a closed-loop Boost-PI controller ($K_p = 1200$ and $K_i = 60$) while loaded with a mass of 8.04 g, showing (A) the controlled voltage input to the actuator (a combination of the proportional, integral and the constant voltage terms of the controller) and (B) the actuator response with setpoint, maximum height, rise time and settle time.

The gains of the Boost-PI controller were manually selected using a multi-objective (Pareto) optimisation approach. K_p was varied from 0 to 1200 with increments of 200, and K_i was varied from 0 to 60 with increments of 20 for each K_p value. Increasing either gain above these maximum values resulted in oscillation or instability. V_c was set at 4,590 V (90% of $V_{pull-in}$ for an actuator loaded with a mass of 8.04 g). Step-response control tasks (as the same as shown in fig. 5.8) were preformed for different control values; the experimental results can be concluded as follows:

- When K_p and K_i were both equal to zero (i.e. using only V_c without a PI controller), the actuator remained at the resting height without any zipping motion since the input voltage $V = V_c < V_{pull-in}$.
- When $K_i = 0$ (i.e. using the controller with only K_p and V_c), when K_p was between 200 and 600, the actuator overshot the setpoint considerably, and zipped fully. With $K_p \geq 800$, the proportional term was large enough to quickly reduce applied voltage after overshoot, preventing full zipping. This causes the actuator height to approach the setpoint, although large steady-state error was present. Increasing K_p reduced the steady-state error but could negatively cause oscillation around the setpoint.
- When $K_p = 0$ (i.e. using the controller with only K_i and V_c), the integral term slowly increased until the sum of the integral term and V_c exceeded $V_{pull-in}$ to initialise actuation. At this point, full zipping occurred, because the integral term did not reduce applied voltage quickly enough to prevent full zipping.
- Using a controller with non-zero values of K_p, K_i and V_c allowed the actuator to converge to the setpoint at different velocities, apart from the controller with K_p = 200, for which the actuator fully zipped (again, the proportional term was not large enough to reduce applied voltage after overshoot quickly enough to prevent full zipping).

The performance of the Boost-PI controller was evaluated by assessing performance metrics of steady state error, overshoot, rise time and settle time as benchmarks to select Boost-PI gains (fig. 5.9). Steady state error is defined as the difference between steady state height and setpoint height, while overshoot is the difference between maximum height and setpoint height. Rise time is the time until current height h reaches 90% of the setpoint height h_s; settle time is the time until h remains within 5% of the setpoint height. It is not possible to select gains which optimise all performance metrics, instead gains should be chosen that provide an appropriate compromise. In practice, the relative importance of each metric is problem-dependent, and thus the Boost-PI gains should be selected according to the task at hand.

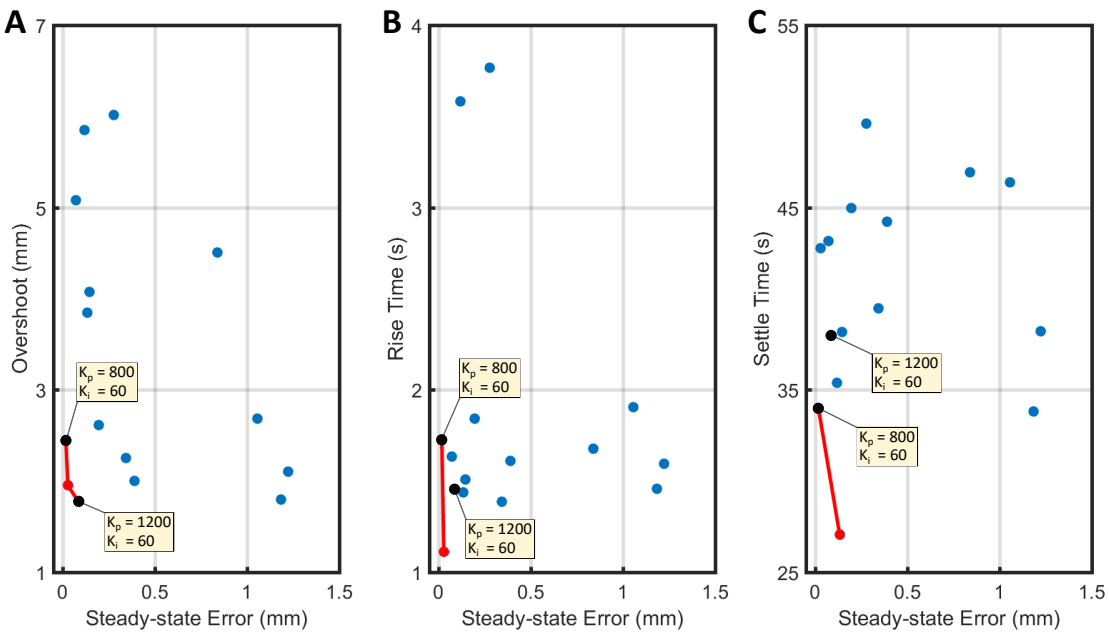

Figure 5.9: Multi-objective (Pareto) optimisation approach to select Boost-PI gains: the relationship between steady-state error and (A) rise time, (B) overshoot and (C) settle time. Blue dots indicate the actuation results of the ERA controlled by different P and I gains; red lines indicate the Pareto front of each relationship for selecting optimal Boost-PI gains. Red dots indicate trails residing on the Pareto front, and black dots indicate trails for which K_p and K_i are provided in the figure.

Fig. 5.9 shows that $K_p = 800$ and $K_i = 60$ were found to reside at the Pareto front for three conditions (overshoot, rise time and settle time relative to steady-state error). However, $K_p = 1200$ and $K_i = 60$, despite higher settle time, resulted in faster rise time (1.45 s or 5.89 mm/s) and lower overshoot (1.77 mm), performance metrics that were prioritised for closed-loop control. Hence, $K_p = 1200$ and $K_i = 60$ were selected as task-appropriate general-use gains for this controller.

In traditional PID control systems, overshoot may be reduced by the addition of a derivative term (K_d). In these initial experiments, when a derivative term was added to the controller, considerable oscillation and instability exist. This is attributed as the inherent compliance of the ERAs. Small high-frequency oscillations tended to be amplified by a derivate term, resulting in further self-perpetuating oscillations. For systems where a very low rise time is not required, a form of damping could be included to smooth movement of the ERAs, allowing the addition of a derivative term, which could promote smaller overshoot and provide improved stability.

The versatility of this developed Boost-PI controller can be demonstrated by performing three setpoint tracking tasks: a ramp task, a staircase task and an oscillatory task (fig. 5.10). The controller exhibited better performance for the ramp task (fig. 5.10A) than the step-response task (fig. 5.8); the actuator had less overshoot and lower steady-state error for the same testing period.

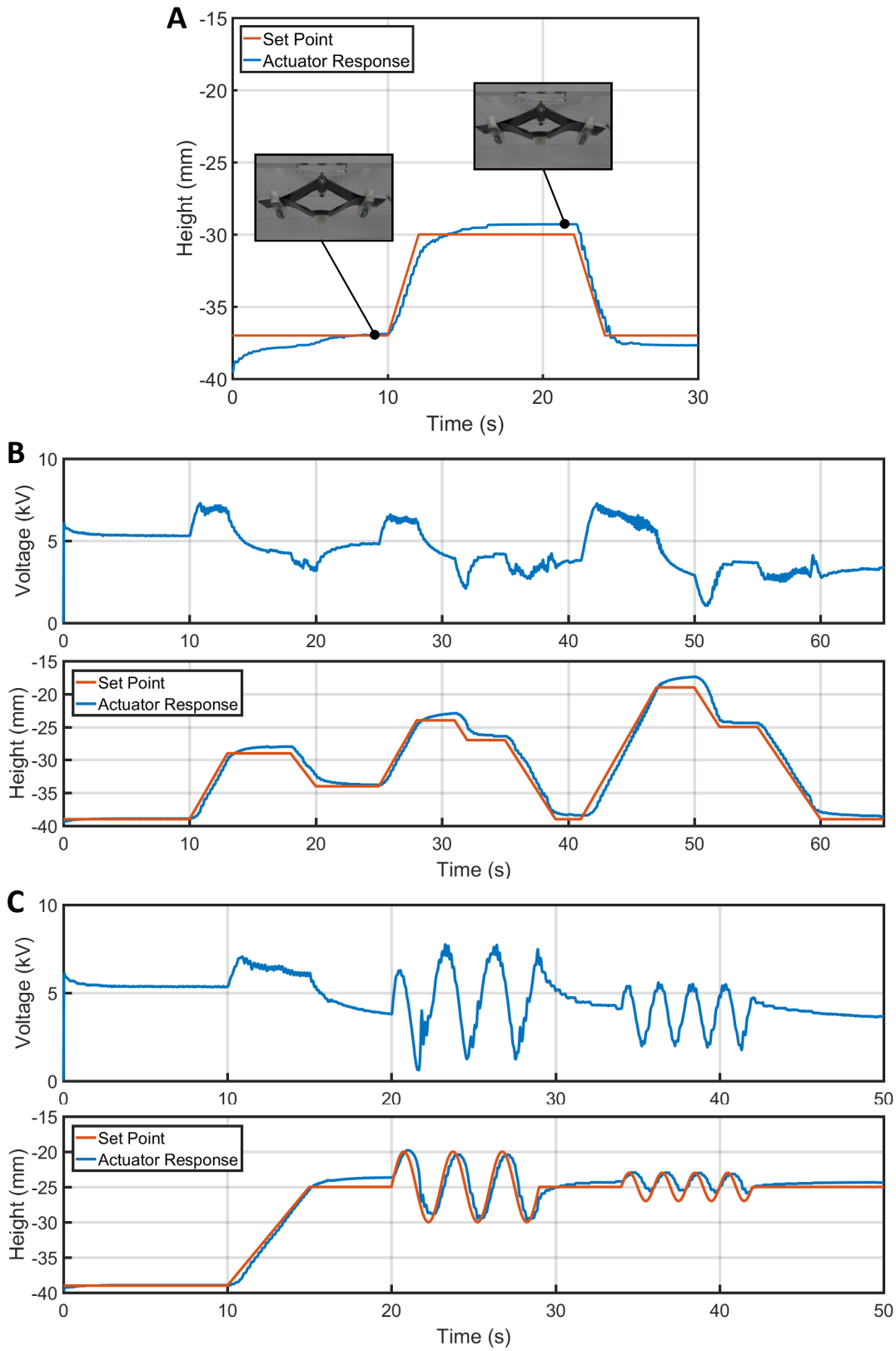

Figure 5.10: Controlled height output of an electro-ribbon actuator actuated using a closed-loop Boost-PI controller ($K_p = 1200$ and $K_i = 60$) while loaded with a mass of 18.04 g, for different setpoint tracking tasks: (A) ramp, (B) mountain and (C) sinewave.

Although complex non-linearities clearly exist for the electro-ribbon actuator, it can be effectively controlled using the presented Boost-PI controller. In conclusion, the demonstrated Boost-PI controller enables closed-loop, high-accuracy, high-working-range displacement control of electro-ribbon actuators. This considerably extends the range of applications for this type of DLZ actuators, allowing it to be included in a wide range of soft robotic systems including wearables assistive devices, autonomous rescue robots and soft robots for space exploration. The next two sections will introduce a new ERA made of alternative materials, leading to a simpler, low-cost fabrication and expansion of ERA designs and applications.

5.4 Material Adaptation of ERAs

As described in Section 5.2, the standard Electro-ribbon Actuator (ERA) is made of two steel strips insulated by a PVC tape and attached together from two ends to create zipping corners using plastic custom-made clips. Despite versatility in designing multi-actuator lattices and various active origami structures, this fabrication method requires tightening clips to create zipping configurations. It unnecessarily increases the thickness of the actuator and limit ERA designs when multiple joints are necessary. Glue-bonding, on the other hand, either weakens the electrostatic force by adding a thick intermediate layer at the zipping point or fails to withstand high peeling force applied to the actuator. In addition, size, thickness and shape of steel strips are limited depending on the commercial availability. To tackle these challenges, alternative materials for fabricating the ERA were explored to achieve simpler, low-cost fabrication and expanding the variety of ERA designs and applications.

5.4.1 Alternative Materials for Simpler Fabrication

Flat steel strip, used as an electrode in the ERA, not only acts as conductive electrodes but also provides stiffness to the actuator, causing a proper curved structure under various external loads (as previously shown in fig. 5.2). These two features can be replaced by other thin conductive materials with an addition of a backing layer. The backing material can be used to vary stiffness of the electrode ribbons to deliver either high contraction or high force generation similar to the steel strip.

A polyvinyl chloride (PVC) sheet was found to be suitable as the backing material since different thicknesses are commercially available at low price, and PVC sheets can be adhered together simply by a heat-sealing method using an impulse hand sealer (HS300C, Polybags Ltd, UK). Copper tape (AT525, Advance Tapes, UK) was used to provide conductivity to PVC sheets by attaching to their surface. The insulator and dielectric liquid with high primitivity and electrical breakdown strength were recommended since they cause high electrostatic zipping force between two electrodes [105]. Therefore, PVC tape and silicone oil were selected as an insulator and dielectric liquid, matching the standard

ERA (section 5.2). All components, fabrication process and configuration of the new ERA are presented in fig. 5.11.

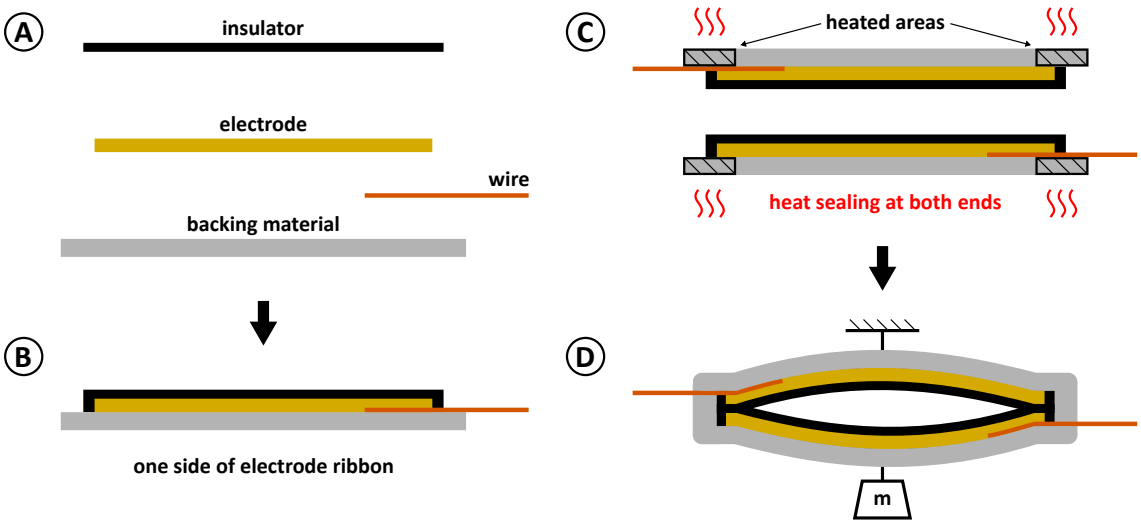

Figure 5.11: Components, fabrication process and configuration of the ERA consisting of new materials.

This new ERA was created using two identical insulated electrodes, composed of a PVC tape, a copper tape and a PVC sheet as an insulator, an electrode and a backing material, respectively. Its fabrication process is presented in fig. 5.11, as explained below: The copper tape is adhered to the PVC sheet and covered by the PVC tape to create an electrode ribbon (fig. 5.11, A and B). An enamelled copper wire (CUL 100/0,15, BLOCK Transformatoren-Elektronik GmbH, Germany) was added between the copper tape and the PVC sheet, making a connection to the high voltage amplifier for electrical charging. The area of the PVC tape is necessarily larger than the copper tape to cover the entire conductive area to prevent from an electrical arc and short circuit between two electrodes under high-voltage actuation. The PVC sheet is also cut larger than both electrode and insulator to provide sufficient area for heat-melting attachment at the two ends of the ERA.

Two insulated electrode ribbons are sealed together by a heat sealer over the conductive area at both ends of the actuator to create zipping corners and ensure tight bonding between two insulated electrodes (fig. 5.11C). The heat-sealing method causes the PVC sheets of both actuator sides to melt together, forming a tight connection instead of using clips. When one side of the ERA is fixed and the other is loaded with a mass, it extends and forms an effective bow-shaped structure (fig. 5.11D). These new materials and fabrication process allow for simpler, low-cost fabrication to create a practical electro-ribbon actuator. The copper tape and PVC sheet, both of which are commercially available in different sizes, can be easily cut by a blade or a cutting machine, enabling various new designs of the ERA. A typical ERA developed using this method, made of electrodes with 10 cm length and 4 cm width, and actuated with the application of high voltage are presented in fig.

5.12. The ERA is highly flexible, and its total thickness is less than 1 mm. Removing the plastic clips from two ends of the actuator makes it flat when fully zips, with no bending due to gravity, as can be observed with standard ERAs.

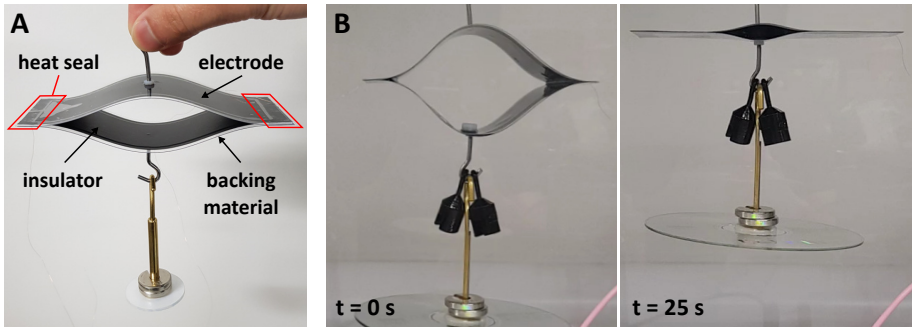

Figure 5.12: Photographs of the new ERA, showing (A) its components and (B) a resting state under the load of 86 g and a fully-zipped state when electrically charged, delivering an actuation stroke of 52 mm.

5.5 Conceptual Designs of ERAs for Various Applications

This section presents various conceptual designs of the ERAs following the presented fabrication technique, for multiple robotic applications. Thanks to the simplicity of the fabrication based on cutting thin layers and heat-sealing (fig. 5.11), three different designs were presented: (1) a stacked ERA for linear actuation, (2) a donut-shaped ERA for linear and bending actuation and (3) a pre-bent ERA and a pre-formed ERA for a pre-extended contractile structure. These designs enable 3-dimensional motions, making ERAs suitable to be used in various Soft Robotic applications.

5.5.1 Stacked ERA for Linear Actuation

A stacked ERA was introduced for linear actuation (fig. 5.13). Typically, to achieve a high contractile stroke, a single ERA requires long electrode strips to be extended under external loading. This causes larger zipping angles, reducing the resultant electrostatic force, and an unnecessary large working space. In contrast, this long stroke can be easily attained by stacking multiple ERAs with shorter electrodes, which also increases zipping efficiency and decreases the working space. The stacked ERA contains many contractile units aligned in series, each of which is connected to the adjacent actuator from the actuator centre using a heat-sealing method.

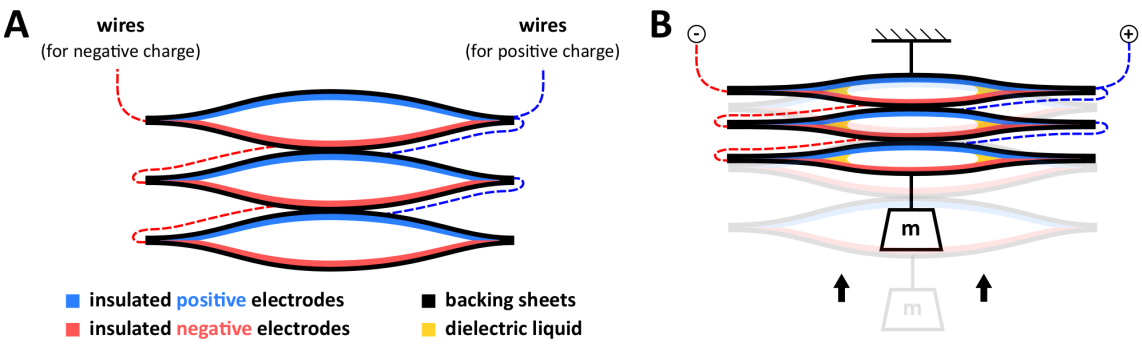

Figure 5.13: Conceptual design of the stacked ERA consisting of three ERAs aligned in series, showing (A) components and configuration of the stacked ERA when extended and (B) actuation of the stacked ERA loaded with an external mass. Three ERA units are connected by heat sealing at their centres, and wires (dashed lines) are connected separately for different charges (blue and red).

The same-pole electrodes of each unit are connected through copper wires (blue and red dashed lines), routed separately for different charges as shown as in fig. 5.13A. This wire routing is for avoiding electrical short circuit due to accidental connection between opposite electrodes. The wires are hidden behind PVC sheets. When adding dielectric liquid to each ERA unit and electrically charged, they all contract simultaneously, lifting an external mass (fig. 5.13B).

The fabrication process of this stacked ERA is illustrated in fig. 5.14. This approach starts by preparing a backing structure, followed by assembling electrodes and insulators to the backing structure and finalised by sealing each ERA unit together layer-by-layer. Following this fabrication method, a single stacked ERA was built, and its actuation is shown in fig. 5.15A. A linear actuator was developed by using a pair of stacked ERAs (fig. 5.15B). This system consists of a rigid frame, shafts, linear bearings and a connecting carriage. One end of each identical stacked ERA is fixed to the rigid frame; the other end is attached to the carriage. The carriage can slide left and right on double supporting shafts through bearings, depending on which stacked ERA is activated by applying high voltage (fig. 5.15B).

This linear mechanism was designed and built as a compact demonstrator of a linear actuator (applied to the rigid red pin in fig. 5.15C) driven by the ERAs and enclosed in an electrical safety box. The negative poles of the two stacked ERAs were connected together while the positive poles were separated to control the motion direction, resulting in the three channels to be connected to a portable power supply. This linear actuator is used to demonstrate the versatility of the ERAs for a wide range of robotic and industrial applications.

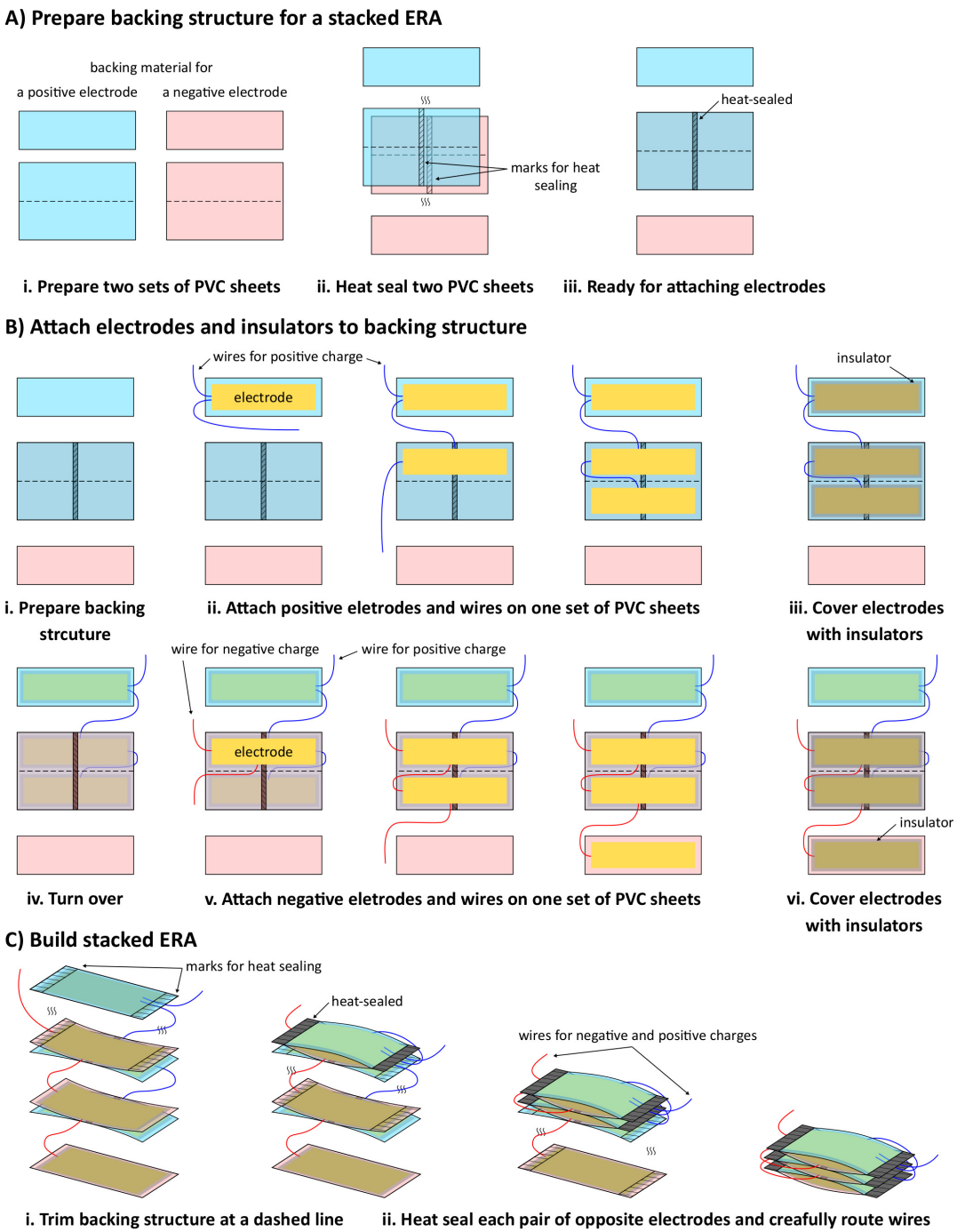

Figure 5.14: Fabrication process of the stacked ERA: (A) preparing backing structure for a stacked ERA using two identical sets of PVC sheets for positive and negative electrodes, each of which includes three rectangles (one piece is cut and the other two pieces remains connected, shown by a dashed line), (B) attaching both electrodes and insulating tapes to backing structures using copper and PVC tapes, respectively, while placing the electrical wires under the Copper tape; two sides of the backing material are reserved for two opposite electrodes and wiring, and (C) trimming backing structures on the dashed line, aligning the backing structure in a way that opposite electrodes face each other and heat sealing at both ends of the backing materials, ensuring that opposite electrodes are attached together.

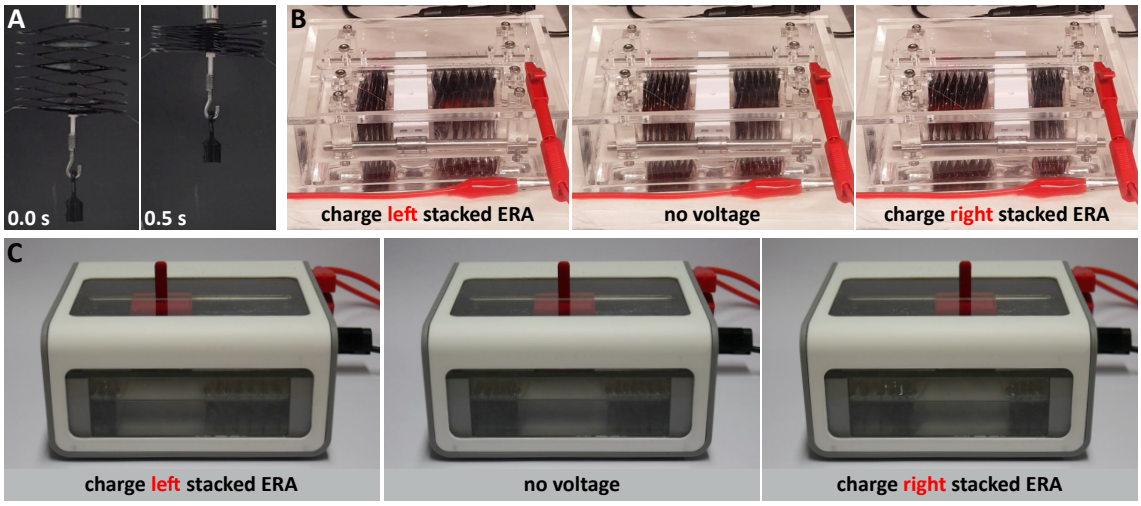

Figure 5.15: Actuation of (A) a single stacked ERA achieving full zipping within 0.5 second at 8 kV and (B-C) a pair of stacked ERAs used as a linear actuator to (B) show a proof of concept mechanism, and (C) build a compact demonstrator.

5.5.2 Donut-shaped ERA for Linear and Bending Actuation

A donut-shaped ERA was designed to achieve linear, i.e. contraction and extension, and bending actuation, resulting in 3-dimensional motions. It is fabricated using several electrode layers similar to the stacked ERA, shown in fig. 5.16. The shape of all components can be easily customised using the above-mentioned cutting-sealing method. Opposite C-shape electrodes are attached to donut-shape backing materials in different orientations, on both top and bottom sides, covered by insulators (fig. 5.16A). Electrode layers are aligned and sealed in series side-by-side, where opposite electrodes facing each other, resulting in a donut-shaped ERA (fig. 5.16B). The C-shape electrodes from different layers which have the same orientation are connected together using copper wires as the same approach used in the stacked ERA. These wires remain separated from the other electrodes on the same layer side. This leads to the total four voltage channels, each of which includes positive and negative connections (fig. 5.16, C and D).

As a result, a continuum electrically-driven robotic arm can be created as shown in fig. 5.17A. The top and bottom layers of the donut-shape ERA are mounted on rigid frames (grey rectangles), which can also be used for making a connection to the similar units, creating a series of a continuum robot. This actuator is required to be extended to initialise its actuation simply by the use of an external load or an additional spring attached between top and bottom rigid frames through the centre of the actuators. This approach allows for the actuator to deliver 3-dimensional motions by controlling the input voltage pattern applied to the four voltage channels. For example, the actuator can contract vertically when applying voltage to all four channels (fig. 5.17B) and can bend in one direction when applying voltage to one or two adjacent channels (fig. 5.17, B and C).

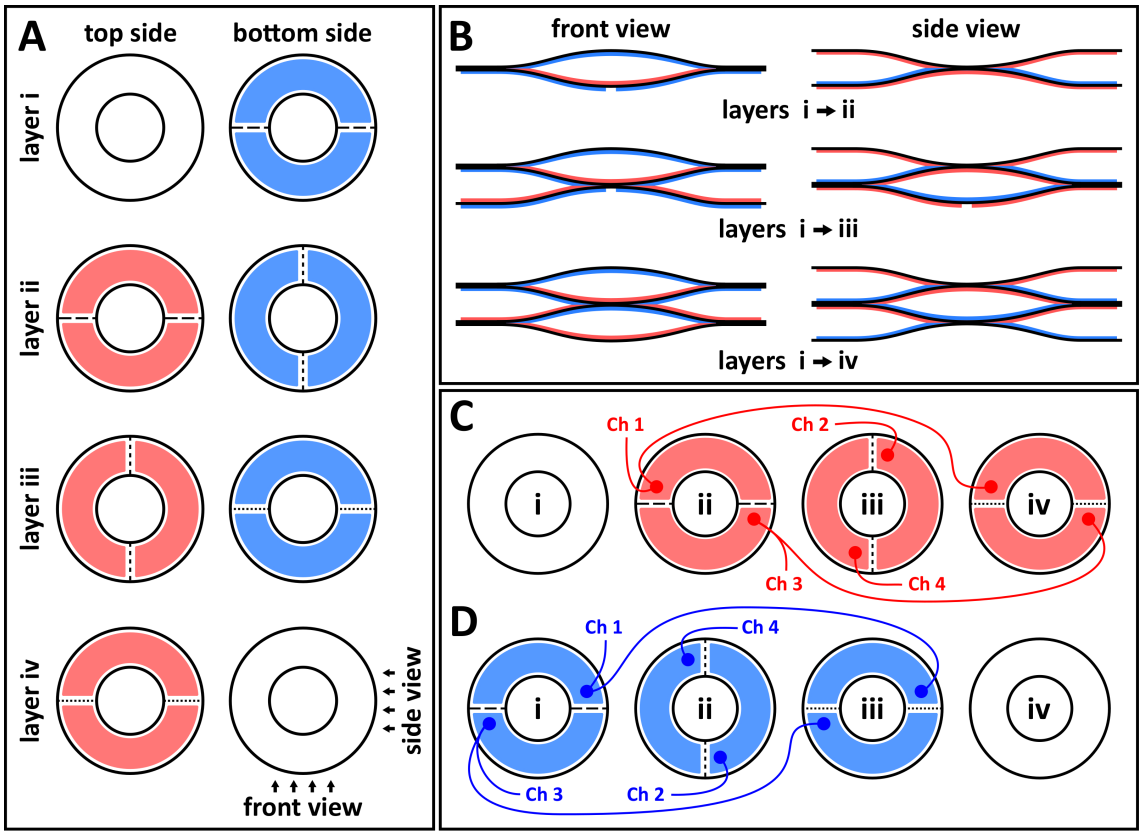

Figure 5.16: (A) Top and bottom views of electrode layers used to create a donut-shape ERA. Each layer consists of a backing material (clear donut shapes) and two sets of opposite insulated C-shape electrodes (red and blue areas) attached to the backing layer in different orientations. (B) Front and side views of the donut-shape ERA, showing the heat-sealing process. (C-D) Approaches to connect wires for (C) negative and (D) positive poles to each C-shape electrodes, shown as red and blue lines.

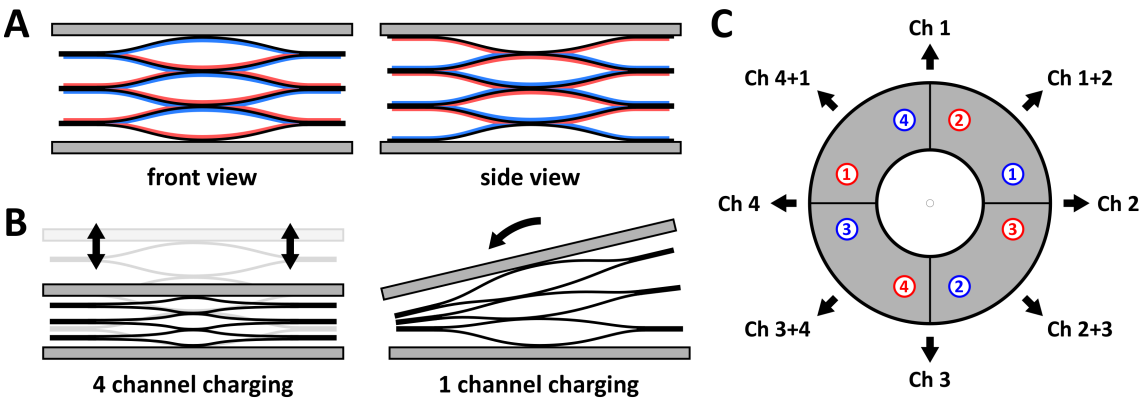

Figure 5.17: (A) Front and side views of a donut-shape ERA. (B) Contraction and bending motion when applying voltage to four or one voltage channels. (C) Top view of the donut-shape ERA showing 2D bending motions at vertical, horizontal and diagonal directions, when applying voltage to a single channel or two adjacent channels.

5.5.3 Pre-bent ERA and Pre-formed ERA

In general, the standard ERA needs to be extended, for example, by loading with an external weight, enabling its contraction by the application of high voltage (fig. 5.2A or 5.18A). A pre-bent ERA, forming the initial extension without loading, was achieved by using deformed electrodes as presented in [105]. This actuator contracts when voltage is applied and naturally extends when voltage is removed. Two new approaches are introduced in this section, which simplifies the fabrication of a pre-bent ERA as follows.

First, adding spring at the centre between opposite electrode ribbons can extend the actuator to a certain height, and this pre-bent ERA contract when charged (fig. 5.18B). Following this approach, the actuator will partially zip because of an inclusion of the spring at the centre. The spring's stiffness affects the actuation stroke, compromising between the electrostatic contractile force and the resistive extension force from the spring. To actuate the ERA, an applied voltage is required to be high enough such that a generated electrostatic force overcomes the extension force of the spring.

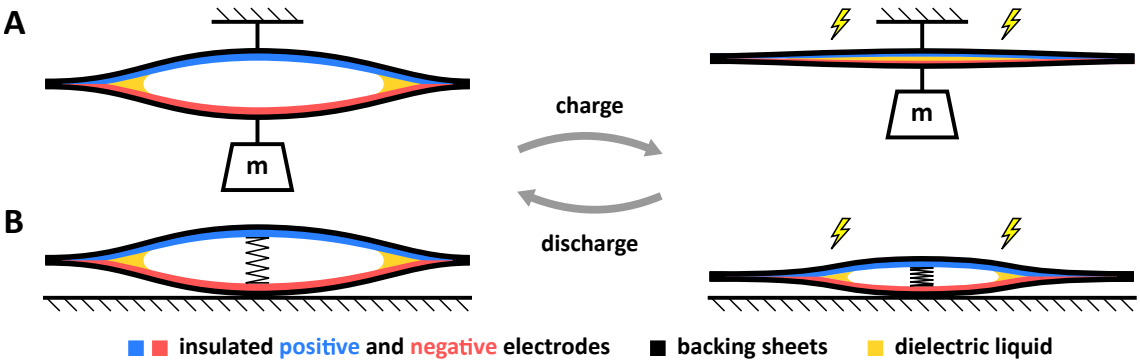

Figure 5.18: Schematic diagram showing the resting state at no voltage and the maximum contracted state of (A) a standard ERA and (B) a pre-bent ERA with the use of a spring. The spring is attached at the centre of the actuator.

This actuator can be used to actuate a normally-closed mechanism. For example, a solenoid valve was developed using a pair of standard ERAs made of steel strips as electrodes with an additional spring, connected to a plunger, replacing the electromagnetic mechanism of a commercial solenoid valve (fig. 5.19). The actuator was compressed to increase the extensive force generated by the spring. This force was necessarily higher than the fluidic pressured, forcing to push the plunger, to close the normally-closed valve. A thickness of the electrodes with sufficient stiffness was selected to maintain an effective zipping structure containing small initial zipping angles. These pre-bent ERAs result in a very thin actuating mechanism, which can lead to a much smaller and lighter solenoid valve, with extremely low power consumption (over ten times less than the commercial valve). In addition to steel springs, a sponge can be used as a soft spring, which increases actuator's contraction because of its much lower compressed thickness compared to that of the spring.

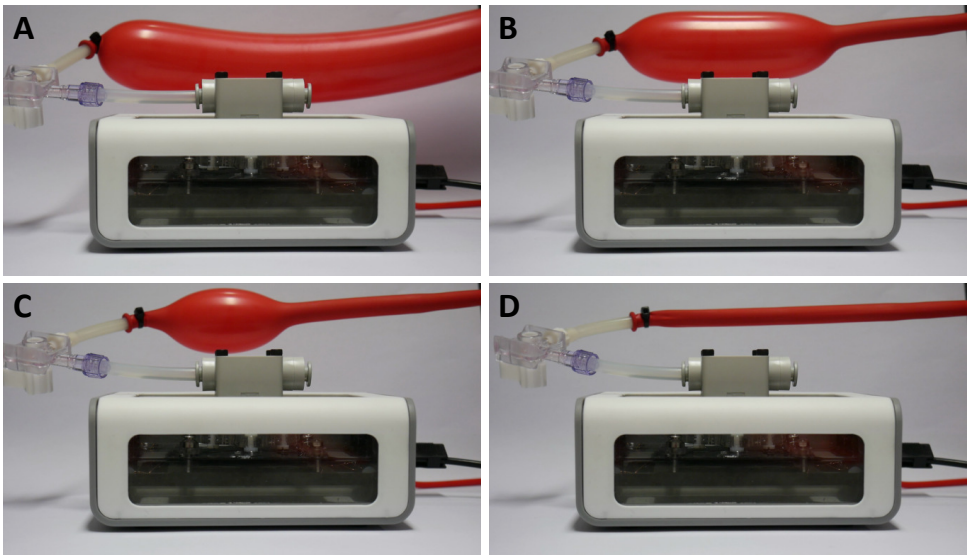

Figure 5.19: A solenoid valve made of a pair of pre-bent ERAs with the use of an additional spring, connected to a commercial valve, at (A) a resting state, working as a normally-closed valve, and (B-D) actuation steps every two-seconds, releasing air trapped inside the connected balloon.

As the second approach for developing a pre-bent ERA, the PVC sheet, used as the backing material of the new ERA, can be pre-formed by heating. The ERA (fig. 5.11D) can be shaped by putting it in a mould and heating up to the temperature around 70°C in the oven (fig. 5.20). The mould can be customised to define a new natural shape for the ERA. Heating the actuator for 10 minutes, followed by cooling them gradually at the room temperature, leads to a new natural shape of the actuator matching the mould's shape as shown in fig. 5.21A.

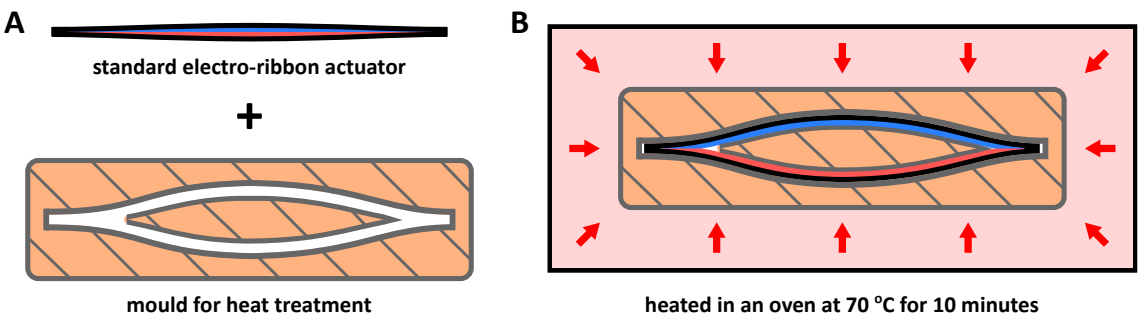

Figure 5.20: Fabrication of the pre-bent ERA using heat treatment: (A) embedding the standard ERA in a customised mould and (B) putting them in an oven at 70°C for 10 minutes, followed by cooling gradually at the room temperature, resulting in changing the shape of the actuator permanently .

This actuator can fully contract when applying voltage across the opposite electrodes and will relax back to its natural curved shape when voltage is removed (fig. 5.21A). The fabrication of the ERA using plastic backing materials together with this heat-shaping

method enables a contractile lattice structure consisting of multiple ERA units as shown in fig. 5.21B.

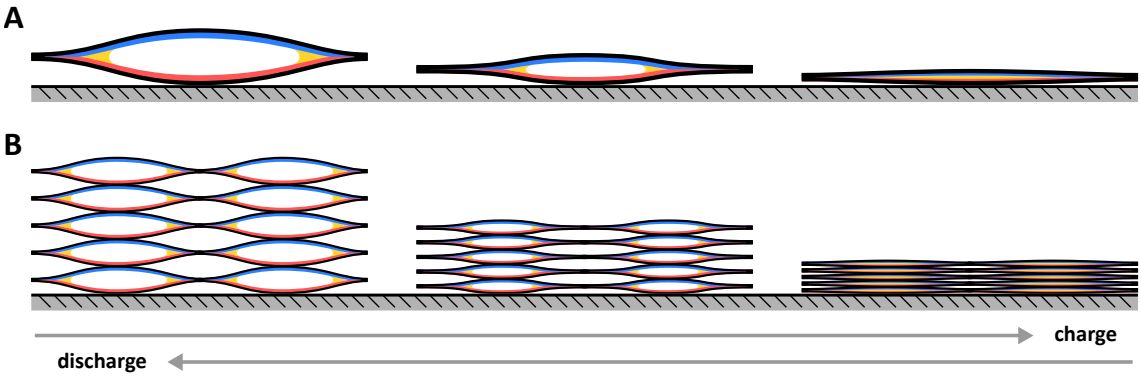

Figure 5.21: Schematic diagram comparing actuation of (A) a single pre-bent ERA and (B) multiple pre-bent ERA units attached in both series and parallel arrangements. The actuators contract and passively return to their initial state when charged and discharged, respectively.

5.6 Discussion

The electro-ribbon actuator (ERA) is an electrostatic zipping actuator which uses Dielectrophoretic Liquid Zipping phenomena to amplify the electrostatic force between two opposite electrodes, closing the actuator like a zipper. It is capable of applying extremely high contraction, fast actuation response, silent operation and low power consumption.

However, the ERA is limited by a very small controllable range due to its pull-in instability and non-linear actuation behaviour. When the supplied voltage reaches the point where the generated electrostatic force overcomes the gravity force exerted by the external load, the actuator starts closing, which always ends up with fully zipping. This challenging non-linear behaviour was controlled by developing a closed-loop Boost-PI controller with an additional constant term. This control method increases a working range of the ERA allowing for the actuator to access many intermediate contractile heights rather than resting at initial extended or fully contracted states. The additional term was used to prepare the actuator ready for zipping and raise its actuation response. Three different tracking tasks were performed demonstrating the high accuracy of the presented controller, expanding the application range of the electro-ribbon actuator.

The ERA was also improved by exploiting alternative materials, resulting in a simpler, low-cost fabrication using a heat-sealing method. This approach replaces the rigid clamps used to bond the actuator ends, leading to a totally flexible and thin electro-ribbon actuator. It also increases the adaptability of the actuator to create more designs for various applications. Three different conceptual designs were presented in this chapter, which can enable the ERA to accomplish 3-dimensional motions, i.e. contraction, extension and

bending motions. A compact linear actuator using a pair of antagonistic stacked ERAs and a solenoid valve driven by pre-bent ERAs were built showing their possibility as future robotic and industrial technologies replacing conventional devices due to their flexibility and low power consumption.

One remaining challenge of using ERA in portable applications is dielectric liquid since it can leak from the actuator when fully zipped, reducing its electrostatic force for the next actuation round. Although cyclic testing over 100,000 cycles was undertaken for partial zipping with the modified ERA containing a liquid reservoir as presented in [105], the dielectric liquid must be re-applied to the standard ERA when it has been at rest for a long time. The next chapter will present a solution to the leakage of dielectric liquid by encapsulating the ERA, resulting in a new application (Chapter 6). A pouch containing an electrical zipping structure, dielectric liquid and air is introduced, creating an air-pumping system which can actuate a typical pneumatic actuator. For example, this new device can inflate, deflate and control the actuation of the Bubble Artificial Muscle (presented in Chapter 3), improving actuation speed of the pneumatic actuator. This new air supply highlights its portability and silent operation, paving the way for future wearable assistive devices.

Chapter 6

Electro-pneumatic Pump

The work described in this chapter has been submitted to the following peer-reviewed venue as:

- **Diteesawat RS**, Helps T, Taghavi M, Rossiter J. Electro-pneumatic Pumps for Soft Robotics. Submitted to *Science Robotics* in April 2020.

This chapter will introduce a novel lightweight air source for pneumatic actuators, called Electro-pneumatic Pump (EPP). It was developed from the electro-ribbon actuators (Chapter 5) by encapsulating and improving the zipping mechanism while containing a small volume of dielectric liquid for Dielectrophoretic Liquid Zipping (DLZ) actuation. This EPP addresses the major drawbacks of typical pneumatic actuators, for example, Bubble Artificial Muscles (Chapter 3), leading to fast actuation speed, silent operation and portability.

Pneumatic artificial muscles (PAMs) have been developed for decades and used in a wide range of applications including: soft actuators [55,94,108,122,123], wearable assistive devices [14, 18, 51, 67, 72], robot grippers [124, 125], soft manipulators [126, 127], smart skins [128], locomotion [129–131], navigation [132] and soft-bodied robots [86]. PAMs exert high forces while contracting or extending under air pressure. However, they often require a large, heavy and noisy air supply, which limits their portability [3, 82, 133, 134].

Conventional electromagnetic (motor-driven) pumps can be used to actuate typical pneumatic actuators, but these are bulky and rigid. A range of novel pumps have been developed as active air sources to address these issues, exploiting non-electromagnetic methods to generate air pressure. Dielectric elastomer (DE) pumps [135–137] have been shown to pump fluids, however these employ rigid frames, which limits their flexibility and suitability for Soft Robotics applications. Recently a stretchable electrohydrodynamic pump capable of pumping liquid [138], a soft combustion-driven pump [139] and a soft pneumatic pump activated using low-boiling point fluids [140] were developed to drive soft actuators, but their low flow rates can limit their applications.

Dielectric fluid actuators, such as electro-ribbon actuators (ERAs) [105] and hydraulically amplified self-healing electrostatic (HASEL) actuators [106, 141], have recently been developed, which exploit the electrical and hydraulic properties of a dielectric liquid. In these devices, the dielectric liquid amplifies the electrostatic force of attraction between two electrodes, resulting in high-performance actuation. HASEL actuators encapsulate the dielectric liquid within the actuator and exhibit high stress up to 0.3 MPa for standard actuators and up to 6 MPa for Peano-HASEL actuators [119]. As presented in the previous chapter, ERAs are zipping structures which only require a tiny droplet of dielectric liquid at the point(s) where the two electrodes are closest, reducing total actuator mass. When electrically charged, the two electrodes progressively zip together, in a process of Dielectrophoretic Liquid Zipping (DLZ), resulting in high-contraction (>99%) actuation.

In this chapter, we present the Electro-pneumatic Pump (EPP), a flexible, high-performance pneumatic pump driven by DLZ actuation that overcomes the limitations of conventional electromagnetic pneumatic power sources. We evaluate the pressure-generating capabilities of the EPP and its behavior when driving a typical pneumatic actuator. We demonstrate a range of EPP applications: antagonistic actuation, a wearable robotic device for the arm, and a continuous pumping system, showing the EPP's versatility and potential to be used as a silent, lightweight, fast-response pump. These characteristics endow the EPP with the potential to impact widely across robotics and enable a new generation of entirely soft robots.

6.1 Principal Concepts

The Electro-pneumatic Pump (EPP) is an active air-transferring device driven by electrostatic zipping. It consists of a flexible air-filled pouch with a pair of insulated electrodes integrated into its sides (fig. 6.1). These electrodes form a zipping structure when the pouch contains internal air volume, which, upon electrical stimulation, acts to reduce the volume of the pouch and thereby generate pressure. The EPP is flexible and can be easily bent as shown in fig. 6.1C.

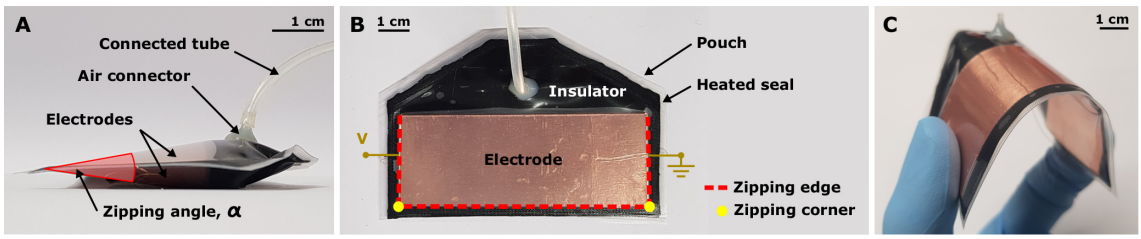

Figure 6.1: Photographs of the Electro-pneumatic Pumps (EPP), showing (A) the inflated EPP, (B) terminology describing zipping components, and (C) flexibility of the EPP.

The EPP is fabricated using two identical pouch sides (as shown in fig. 6.2), each comprising an insulated electrode, a backing material and an outer pouch wall. The

pouch sides are then heat-sealed around their edges to form a sealed pouch (fig. 6.1B). The pouch is typically larger than the electrodes in at least one direction, allowing the actuator to deform when filled with air. An air connector is added to one side of the EPP to permit air flow into and out of the actuator. The facile structure of the EPP allows simple, low-cost fabrication of a wide variety of functional soft pumps.

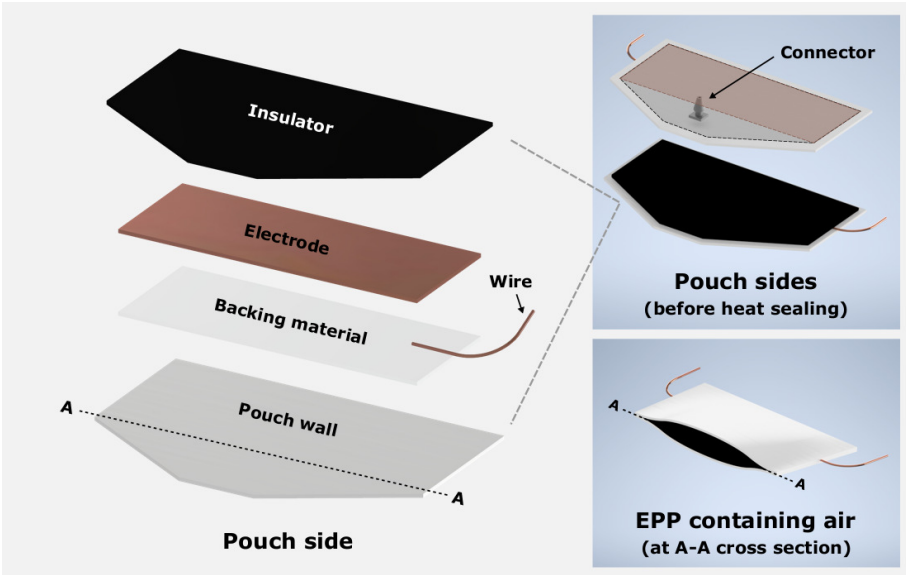

Figure 6.2: Exploded-view schematic diagram showing components of one pouch side of the EPP, two identical pouch sides with an air connector before heat sealing, and cross-section view of the EPP at electrode end when inflated.

A typical EPP is made using electrodes of dimensions 8 cm x 3 cm. Actuation of the EPP is defined by three adjacent *zipping edges* and two *zipping corners* where the zipping edges meet (fig. 6.1B). The *zipping angle* (α) defines the angle between two electrodes (fig. 6.1A). In its fabricated state, the EPP has zero internal volume and $\alpha = 0$ (fig. 6.3). For the EPP to actuate, it must contain an internal air volume, and α must be greater than zero. To achieve this, air must be injected into the EPP through the air connector. The injected air volume (v_{in}) refers to the volume of air at atmosphere pressure (P_{atm}) and at room temperature that is injected into the pneumatic system. As the EPP is inflated (increasing v_{in}), it deforms and α increases (fig. 6.3). As v_{in} increases, the pressure and volume of the whole pneumatic system changes, since air is compressible. Initial pressure (P_i) is the pressure of the system with no EPP actuation (0 kV), and actuated pressure, $P_a(V)$, is the pressure at applied voltage V.

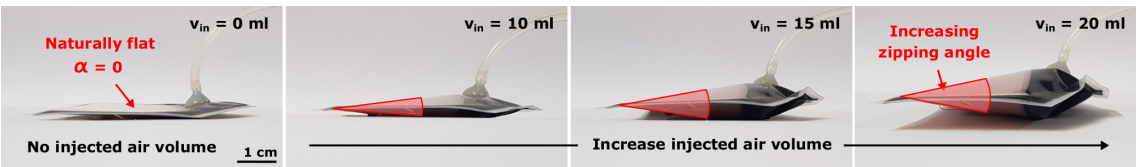

Figure 6.3: Photographs of the EPP containing different injected air volume v_{in}.

EPP actuation employs the concept of Dielectrophoretic Liquid Zipping (DLZ) [105] in a closed system: the electrodes are oppositely charged, and the small droplet of liquid dielectric contained inside the pouch amplifies electrostatic force, allowing for high-force, progressive electrostatic zipping that acts to close the pouch and transfers compressed air to a connected pneumatic device (fig. 6.4). This electrostatic force decreases monotonically as zipping angle α increases at constant applied voltage.

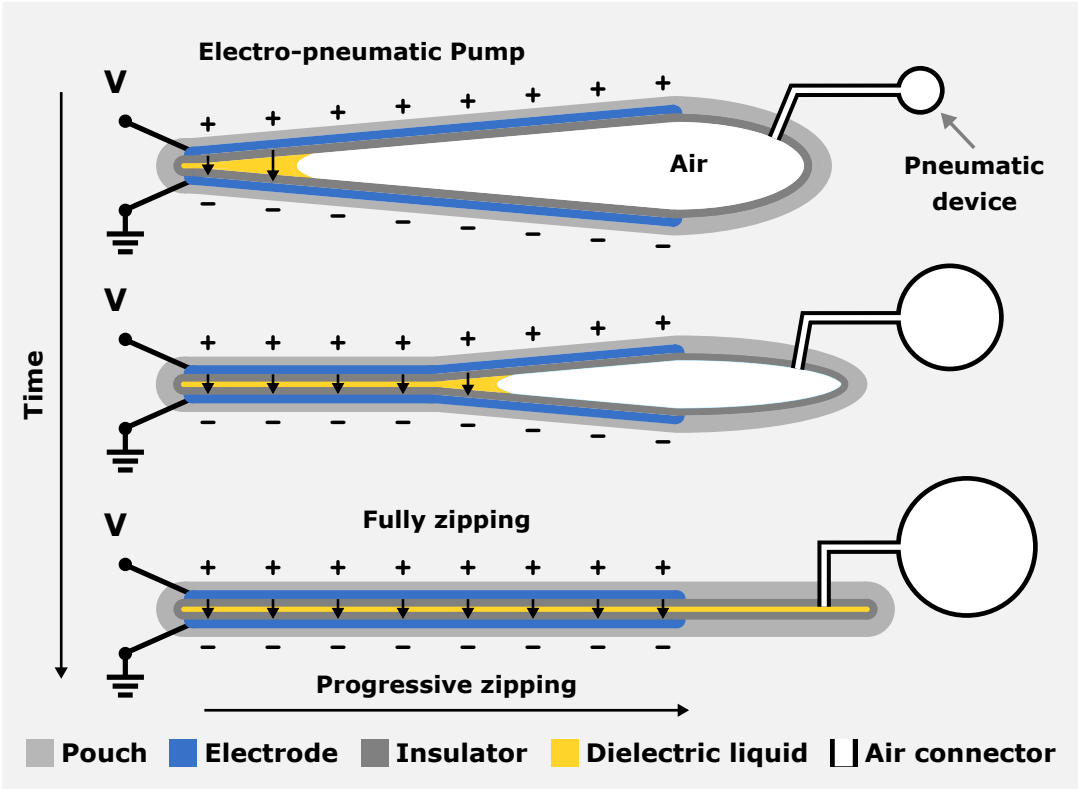

Figure 6.4: Conceptual diagram of Dielectrophoretic Liquid Zipping used in the EPP. When applying a constant voltage V, the opposite electrodes progressively zip, compressing the pouch and transferring its internal air volume to inflate a connecting pneumatic device.

A typical EPP was fabricated and tested to characterise its pressure-generating capabilities. Actuated pressure (P_a) increased with applied voltage for each given v_{in} (fig. 6.5A). When increasing v_{in}, initial pressure (P_i) increased (blue plot in fig. 6.5B) while pressure change ΔP, the difference between P_a and P_i ($\Delta P = P_a - P_i$), decreased, as shown in fig. 6.5B. At low v_{in}, the EPP fully zipped ($\alpha \rightarrow 0$), resulting in a strong electrostatic force and associated high pressure generation. In contrast, at high v_{in}, the EPP partially zipped since the larger air volume resisted compression, resulting in a larger zipping angle and lower electrostatic force. Further increasing v_{in} prevented the EPP from zipping, for instead, the EPP containing v_{in} of 16 ml, which produces almost zero pressure change (black plot in fig. 6.5A).

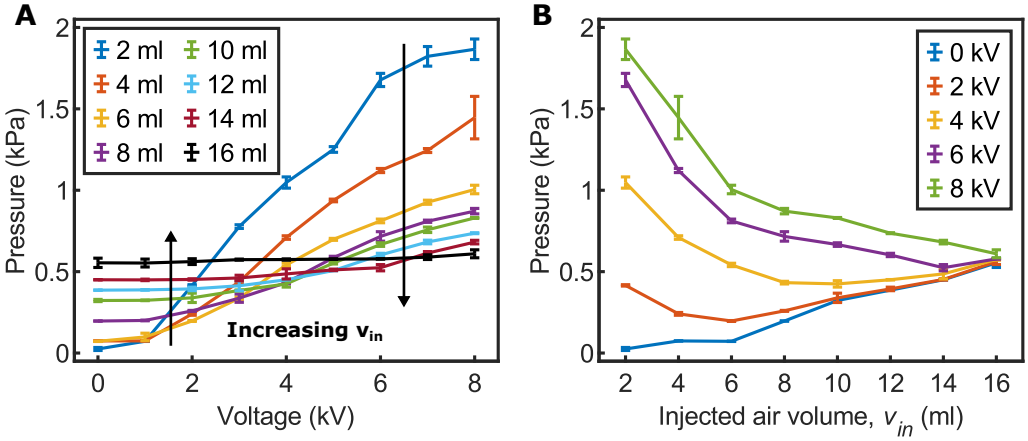

Figure 6.5: Capability of the EPP made of 8 cm x 3 cm electrodes in generating pressure while containing different injected air volumes v_{in} and actuated at different voltages V, showing the relationship between (A) pressure and voltage, and (B) pressure and injected air volume. Points are averages of three trials, and error bars show ± 1 standard deviation.

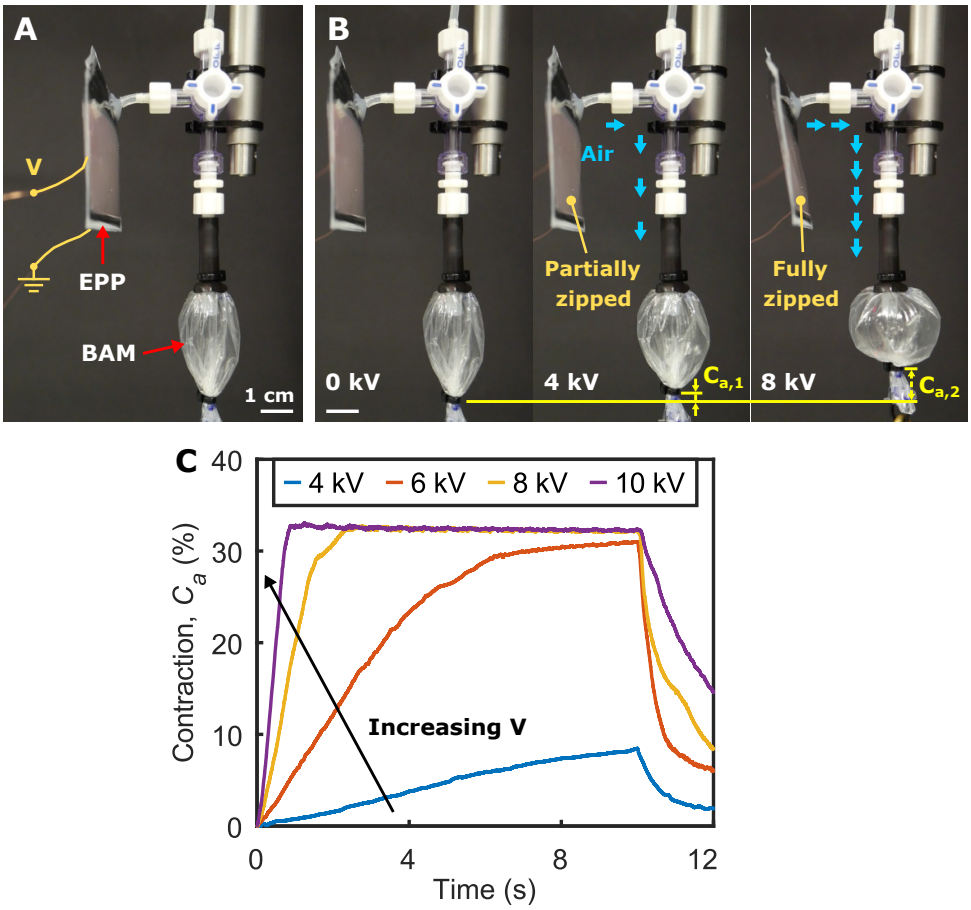

Figure 6.6: (A) Photograph of the EPP connected to a connected pneumatic actuator (Bubble Artificial Muscle (BAM)). (B) Actuation of the EPP-BAM system at 0, 4 and 8 kV (blue arrows denote the amount of air volume transferred from the EPP to the BAM). (C) Active contraction C_a of the BAM actuated by the EPP at different voltages.

To demonstrate the efficacy of the EPP in transferring air, it was used to actuate a typical pneumatic contractile actuator, a Bubble Artificial Muscle (BAM) [122], which was made from 30 μm thick, 17 mm radius plastic tubing and had length 40 mm and unactuated radius 3 mm, loaded with an external mass of 26.5 g. The EPP was connected through a three-way valve to the BAM and a syringe, allowing for control of initial air volume (v_{in}) (fig. 6.6A). BAM contraction (C) is inflated actuator length subtracted from extended length, divided by extended length, expressed as a percentage. C is equal to 0% at no inflation (full extension). Passive contraction (C_p) is the BAM contraction at no EPP actuation (0 kV) and pressure P_i, when v_{in} is injected to the EPP-BAM system. Active contraction (C_a) is defined as further BAM contraction from C_p when the EPP is charged at voltage V and the EPP-BAM system is at pressure $P_a(V)$. The sum of C_p and C_a is the maximum BAM contraction from full extended length. As voltage applied to the EPP was increased, C_a increased up to a maximum of 32.40%. Full zipping of the EPP occurred at a voltage of 8 kV (fig. 6.6, B and C).

When a voltage is applied, the EPP starts zipping from the zipping corners, which have the shortest distance between two electrodes, resulting in the highest electric field. As the EPP zips, the dielectric liquid is squeezed along in the same direction, such that it is always coincident with the zipping point. This ensures that it amplifies electrostatic force as the EPP progressively zips (fig. 6.7).

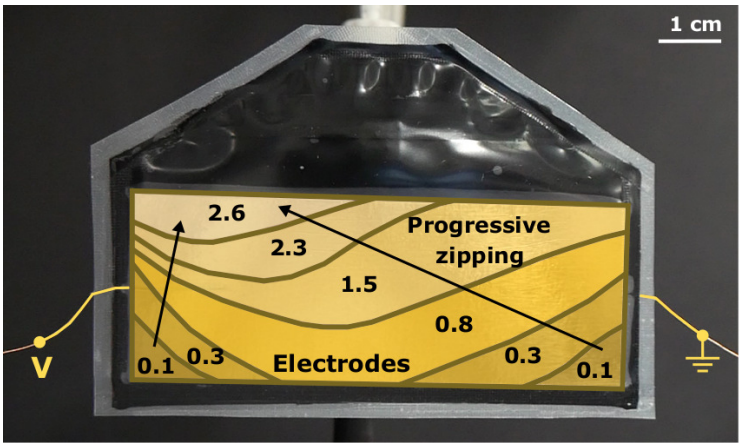

Figure 6.7: Progressive zipping of the EPP actuated at 8 kV (numbers indicate time in seconds; different shades of yellow areas indicate the progressive zipped region of the electrodes at actuation time, defined by numbers where they are in).

The following sections will present materials and fabrication of the ERA and BAM and an experimental setup used to characterise and evaluate performance of the EPP-BAM system, including investigations of actuation behaviour and the effect of varying electrodes' dimension of the EPP. Its capabilities are presented by performing different types of experiments, such as actuation at different frequencies, actuation using open-loop voltage control and cyclic durability tests over ten thousand cycles, as well as three

demonstrators driven by the EPP, showing its versatility and suitable to be adapted for Soft Robotics applications and wearable devices.

6.2 Methodology

6.2.1 Material and Fabrication

Electro-pneumatic Pump

EPPs were fabricated from two identical pouch sides; each side included an insulated electrode, a backing material and an outer pouch wall, as shown in fig. 6.2. 130 μm thickness polyvinyl chloride (PVC) tape (AT7, Advance Tapes, UK) was used as an insulator. 35 μm thickness copper tape (AT525, Advance Tapes, UK) formed the electrode, attached to a 240 μm thickness PVC backing sheet (A4 Clear PVC Covers, Binding Store Ltd., UK). The backing material provided stiffness to the actuator, ensuring an effective zipping structure when the EPP is filled with air. Electrical connections were made using enameled copper wires (CUL 100/0,15, BLOCK Transformatoren-Elektronik GmbH, Germany). 125 μm thickness low-density polyethylene (LDPE) layflat tubing (LFT9500STK, Polybags Ltd, UK) was used as a pouch material, and pouch sides were heat-sealed around their edges, using an impulse heat sealer (HS300C, Polybags Ltd, UK), to form an EPP. A 1/16 inch diameter polypropylene straight connector (#06365-11, Cole Parmer, UK) was attached to one side of the pouch by hot glue. A small volume of silicone oil with low viscosity of 5 cSt (#317667, Sigma-Aldrich, USA) was injected into the pouch to act as the dielectric liquid. Low viscosity benefits flow of the dielectric liquid along with zipping points (fig. 6.7). The total thickness of the empty EPP was 1.10 mm.

Bubble Artificial Muscle

BAMs (fig. 6.6) were made from 30 μm thick low-density polyethylene (LDPE) layflat tubing (LFT2120STK, Polybags Ltd, UK) as an actuator membrane. One actuator end was connected to a polyurethane tube with outer radius 3 mm (197377, FESTO, Germany) for air input/output, and heat shrink was used to seal the layflat tubing to the polyurethane tube. The heat sealer was used to seal the other end of the BAM, and both ends were further secured using cable ties.

6.2.2 Experimental Setup

An experimental setup was built to evaluate the performance of the EPP (fig. 6.8). By changing the position of the three-way valve, three different experiments were conducted:

- EPP only (EPP pressure generation)
- BAM only (BAM manual inflation)
- EPP-BAM system (BAM actuation by the EPP)

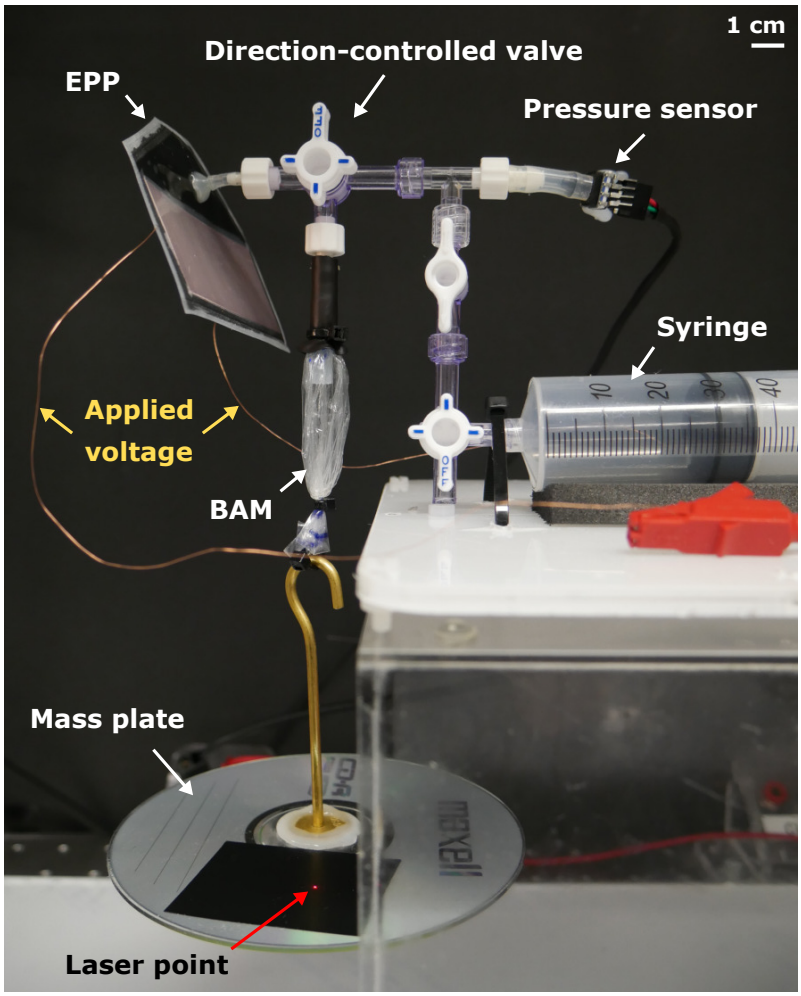

Figure 6.8: Three different experiments were undertaken by changing the position of the three-way valve: EPP only (valve OFF downwards), BAM only (valve OFF to the left) and the EPP-BAM system (valve OFF upwards; all ports open). The pressure sensor recorded the system pressure in all cases. The EPP was activated by a high voltage amplifier, and v_{in} was controlled by the syringe. The BAM was loaded with an external mass, and the laser displacement sensor was used to measure the movement of the mass plate to infer the contraction of the BAM.

First, the EPP was evaluated by measuring the air pressure when a fixed volume of air at atmospheric pressure (v_{in}) was injected into the system, and a voltage was applied across the two electrodes. The EPP was connected to a pressure sensor (HSCDANN030PGAA5, Honeywell, US) to measure internal pressure, and a standard 60 ml syringe was used to inject a known air volume (v_{in}) through the three-way valve (Cole Parmer, UK). The EPP was charged using a high voltage amplifier (5HVA24-BP1, UltraVolt, USA) at a range of input voltages, controlled by a computer running MATLAB. A National Instruments data acquisition device (NI USB-6343, National Instruments, USA) was used to control the input voltage and to record output data at a sampling frequency of 1,000 Hz. Each test was repeated three times.

Second, the contraction-pressure relationship of the BAM was determined by measuring contractile displacement and internal pressure while adjusting v_{in} using the syringe. Different external loads were suspended from the BAM. A laser displacement sensor (LK-G152, Keyence, Japan) was used to measure the displacement of the load. Each test was repeated three times for a range of loads.

Third, the performance of the EPP in inflating the BAM was assessed by connecting the EPP and BAM together. The EPP was actuated, and the pressure of the EPP-BAM system and BAM contraction were recorded. The syringe was used to control injected air volume v_{in} of the EPP-BAM system. Each experiment was repeated three times at a range of v_{in} and loads.

Data Acquisition and Analysis

For visualisation, all data was smoothed using the MATLAB "smooth" function with span of 0.01 and method of 'rloess'. In some experiments, the EPP pressure under actuation either increased asymptotic to a stable value or retained a small oscillatory component. In all cases, the average data in the stable region was used as the recorded value.

6.3 Characterisation of the combined EPP and BAM system

The BAM previously described in section 6.1 was used to evaluate the performance of the EPP in an isotonic experimental setup (fig. 6.8). Actuation of this 2-g BAM under different loads is shown in fig. 6.9.

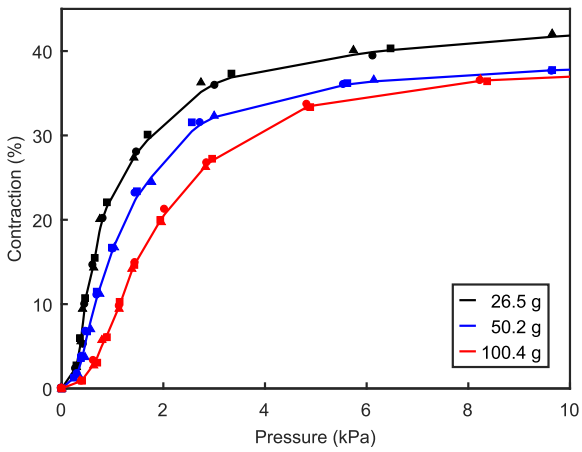

Figure 6.9: Isotonic contraction of a BAM under loads of 26.5, 50.2 and 100.4 g. The BAM was inflated manually using a syringe during three separate trials for each load. Colors indicate different tested loads, and markers indicate different trials. For each trial, interpolated data was generated using the MATLAB *interp1* function, and this data was averaged across three trials to generate the three lines plotted in the figure.

Various air volumes (v_{in}) were injected into the EPP-BAM system, and a voltage of 8 kV was applied to the EPP (8 cm x 3 cm). At a given voltage, the maximum amount of zipping in the EPP and active contraction (C_a) of the BAM were dependent upon v_{in} (fig. 6.10). For each load, there was a v_{in} that maximised BAM contraction (fig. 6.11). Below this v_{in}, the EPP fully zipped, but did not displace enough air to maximally contract the BAM. Above this v_{in}, the injected air resisted EPP actuation, causing partial zipping as in the case of the EPP pressure experiments (fig. 6.6), where zipping angle α is too large, reducing electrostatic force and impairing zipping. This resulted in less displaced air and lower C_a. At 8 kV EPP actuation, the BAM delivered maximum C_a of 31.48%, 29.05% and 18.29% under loads of 26.5 g, 50.2 g and 100.4 g, respectively (fig. 6.11). Both maximum BAM contraction, and the injected air v_{in} at which BAM contraction was maximum, decreased with increasing load.

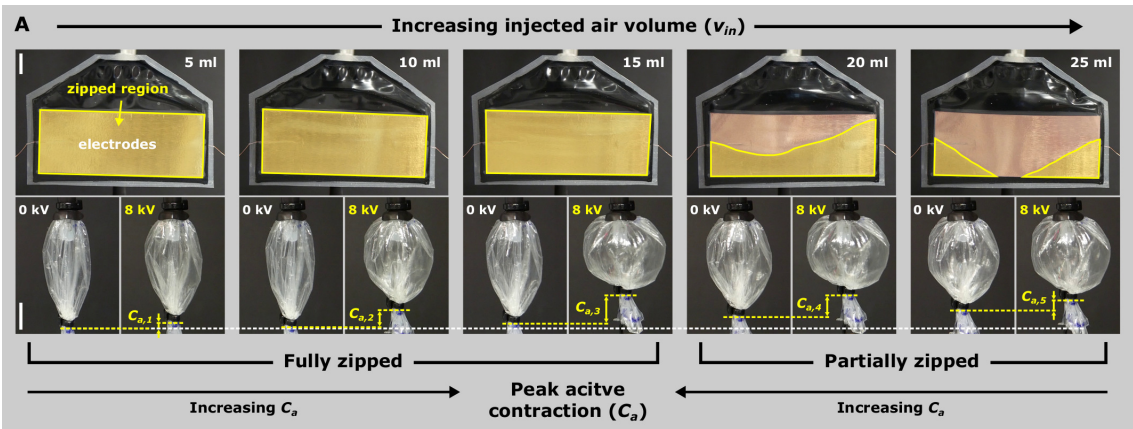

Figure 6.10: Zipping behaviour when increasing v_{in}, showing maximally zipped state and active contraction C_a when actuated at 8 kV. Photographs of the EPP show the zipped region of the electrodes at 8 kV in yellow, and the BAM at 0 kV (C_p) and 8 kV. The white dashed line shows the passive contraction C_p of the BAM at v_{in} = 5 ml and 0 kV; yellow dashed lines show C_a of the BAM at different v_{in}. Scale bars, 1 cm.

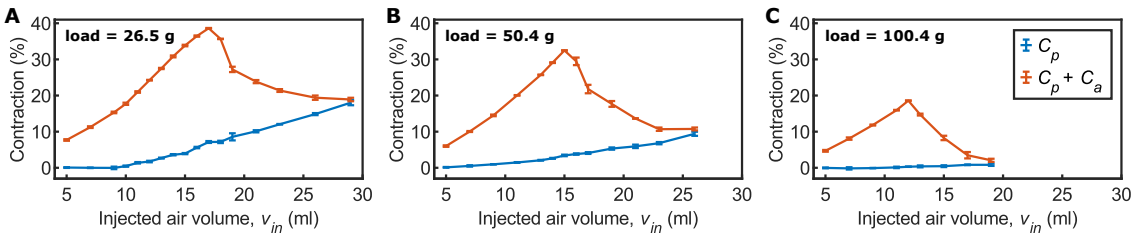

Figure 6.11: Passive contraction (C_p) and maximum contraction ($C_p + C_a$) at different v_{in} under different applied loads. Points are averages of three trials, and error bars show ± 1 standard deviation.

The EPP-BAM system with an external load of 26.5 g, containing v_{in} of 17 ml (the injected air volume that maximised C_a at this load) was studied further to observe change

in BAM contraction, pressure of the EPP-BAM system and BAM actuation velocity at different voltages between 0 and 10 kV (fig. 6.12). BAM contraction started at 4 kV and reached a maximum at 7 kV, whereas the actuation velocity continuously increased with applied voltage as electrostatic force increased and reached a maximum of 54.43%/s at 10 kV.

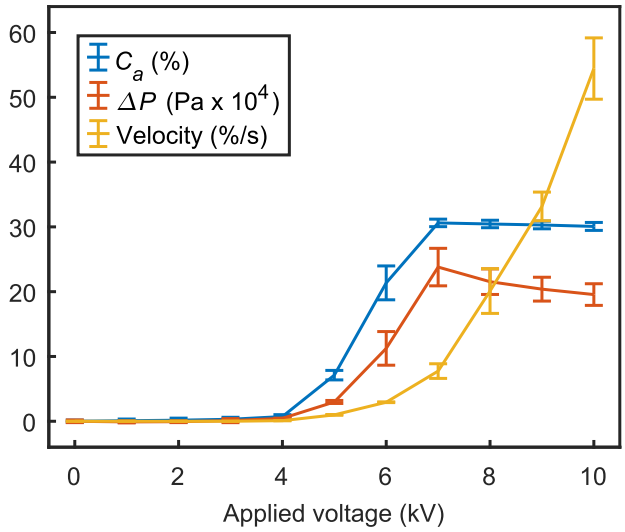

Figure 6.12: Active contraction C_a, pressure change ΔP and actuation velocity of the BAM under a load of 26.5 g when v_{in} = 17 ml, actuated at increasing applied voltages. Points are averages of three trials, and error bars show ± 1 standard deviation.

The BAM actuated by the EPP at different voltages showed the same contraction-pressure relationship as that of a syringe-actuated BAM (fig. 6.13A). Variation between three EPP-BAM systems featuring different EPPs with the same electrode dimensions when actuated at 8 kV is shown in fig. 6.13B.

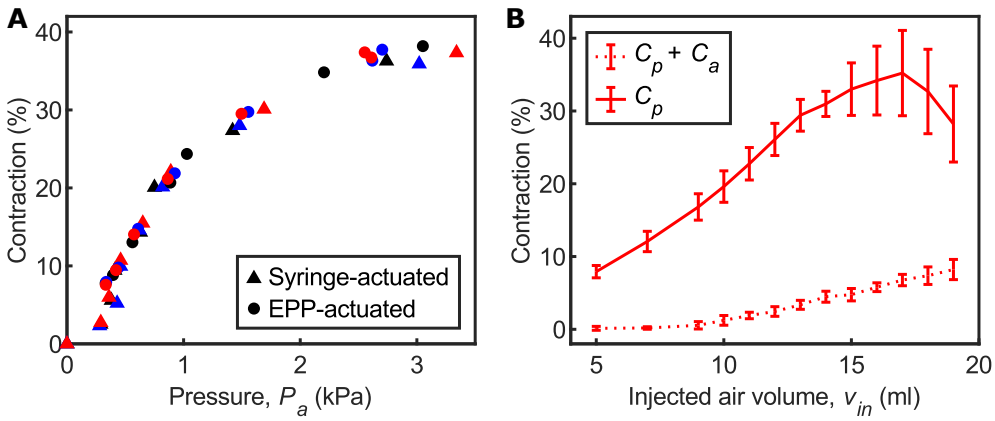

Figure 6.13: (A) Comparison of syringe-actuated and EPP-actuated BAM (different colors indicate different experimental trials). (B) Sample variation of BAM contraction when actuated by three EPPs of the same dimensions. In (B), points are averages of three trials from three EPPs (nine trials total), and error bars show ± 1 standard deviation.

6.4 Design Characterisation and Effect of Actuator's Stiffness

To explore the effect of different designs on the performance of the EPP, three additional EPP designs with different dimensions were fabricated and tested (varying electrode length and width while conserving total electrode area). We refer to these EPP designs as D2, D3 and D4; the EPP design previously presented is D1 (table 6.1 and fig. 6.14). These four EPPs have different total lengths of the zipping edges but have similar weight between 4.9 and 5.3 g. The volume of dielectric liquid injected into each EPP was kept to a minimum and was between 1-2% of the maximum volume of the EPPs (table 6.1). The inflation stiffness of each EPP design is different due to their different geometry, as can be observed by the change of initial pressure (P_i) when inflating them with a certain v_{in} (fig. 6.14B). EPP stiffness increases from design D1 to design D4.

Table 6.1: Design detail of four fabricated EPPs. The zipping edge length is the total length of the adjacent zipping edges. The dielectric liquid volume fraction is the ratio of the used dielectric liquid and the maximum liquid which could be contained within the actuator.

Actuator Design	D1	D2	D3	D4
Electrode length [cm]	8	6	4	3
Electrode width [cm]	3	4	6	8
Zipping edge length [cm]	14	14	16	19
Actuator Weight [g]	5.280	5.190	5.100	4.961
Dielectric liquid volume fraction [%]	1.062	1.708	1.157	1.937
Used dielectric liquid [g]	0.306	0.534	0.342	0.467
Maximum dielectric liquid [g]	28.810	31.273	29.552	24.115

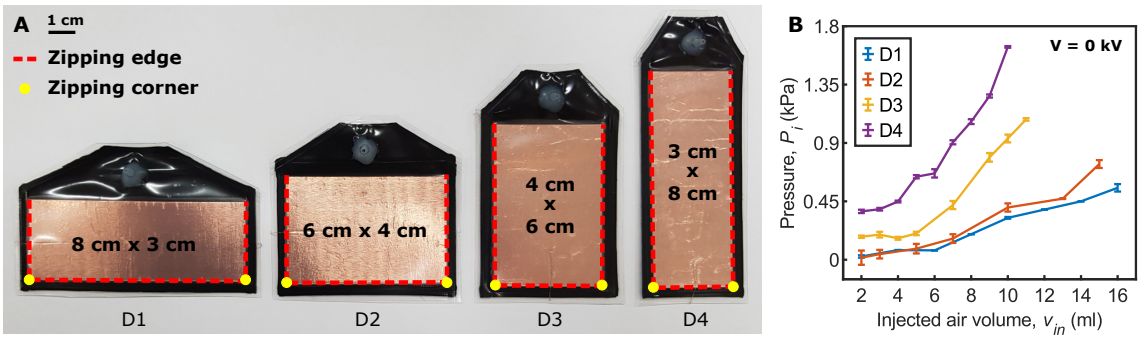

Figure 6.14: (A) Photographs of four EPP designs with different dimensions, length and width, but the same total electrode area. (B) Initial pressure P_i of the four EPPs when increasing v_{in}.

These four EPPs were tested to investigate their pressure-generating capabilities by injecting increasing air volume v_{in} and applying voltages of 2, 4, 6 and 8 kV for each v_{in}; the experiments of each EPP were stopped when their actuated pressure changes (ΔP) were nearly zero. The experimental results are illustrated in fig. 6.15. Higher applied voltage resulted in higher generated pressure. The maximum ΔP occurred when the EPPs contained low v_{in} and almost fully zipped, except for EPP D3, for which there was intermediate v_{in} that maximised ΔP. We attribute this to buckling and creasing effects associated with this design. ΔP decreased with increasing v_{in} and reduced to zero at different v_{in} for different designs. EPP D4 generated the highest ΔP of 2.34 kPa.

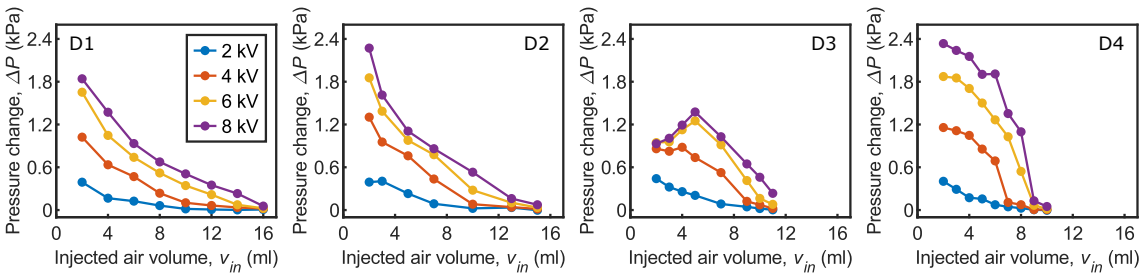

Figure 6.15: Pressure change ΔP of the four EPPs directly connected to the pressure sensor when containing different v_{in} and actuated at different voltages for each v_{in}.

Each EPP was tested to inflate the previously described BAM in order to observe their zipping behaviour and BAM contraction, as the same as in fig. 6.11. When increasing v_{in} at 0 kV (no EPP actuation), the BAM connected to the stiffest EPP D4 had a larger passive contraction C_p compared with the BAM connected to the softest EPP D1 (fig. 6.16A), since the stiffer EPP implies a lower ratio of injected air between EPP and BAM. When the EPP is stiffer than the BAM, most of v_{in} will remain in the BAM. When the load was increased, more air was pushed into the EPP, reducing C_p (fig. 6.16B).

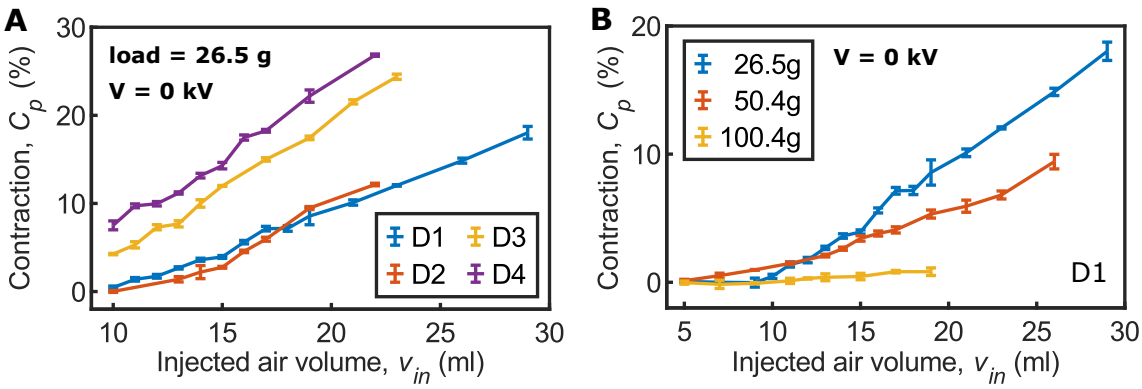

Figure 6.16: Passive contraction C_p of the BAM connected to (A) each EPP when loaded with a 26.5 g mass or (B) EPP D1 when loaded with different masses. $V = 0$ kV in (A) and (B).

When actuating the EPP, for each EPP design and each tested load, there was v_{in} that maximised C_a while the EPP fully zipped. Fig. 6.17 shows key performance metrics of each EPP-BAM system under different loads of 26.5, 50.2 and 100.4 g when containing v_{in} maximising C_a and actuated at $V = 8$ kV.

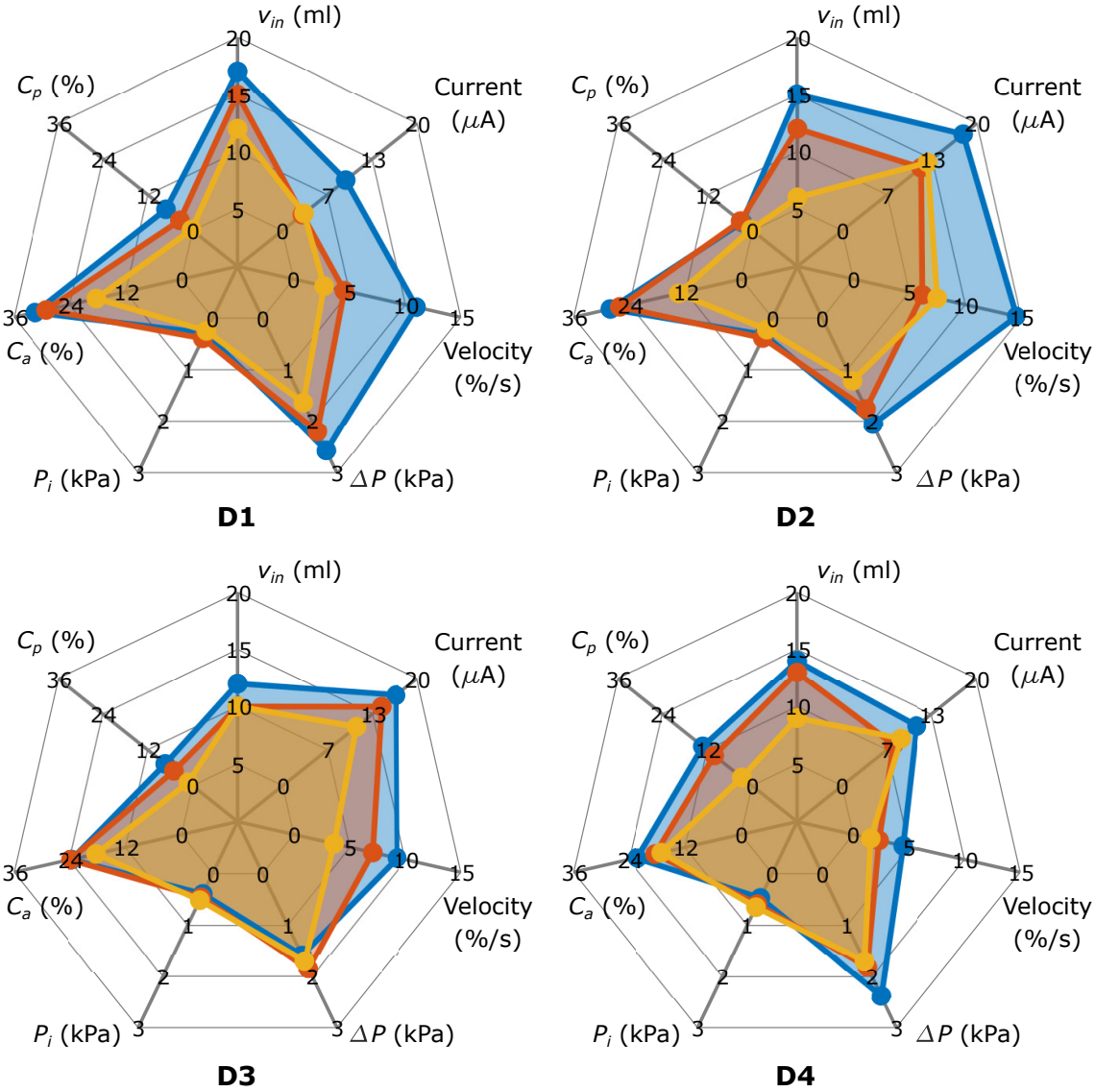

Figure 6.17: Spider plots of each EPP design's key performance metrics when actuating a BAM under different loads at an applied voltage of 8 kV while containing v_{in} which maximising C_a. Loads were 26.5 g (blue area), 50.2 g (red area) and 100.4 g (yellow area). Current describes the continuous current draw of the EPP when in its actuated state (while maintaining pressure). Velocity describes the average velocity of the BAM during contraction.

EPP D1 was found to produce the highest active contraction C_a, among all EPPs and loads tested (fig. 6.17 and 6.18). This was because the softest EPP (D1) contained the largest air volume at 0 kV and thus transferred the highest air volume to the BAM when actuated. All EPPs required very low currents to deliver actuation; maximum current

draw for all EPPs was less than 100 μA, and continuous current draw in their actuated state (while maintaining pressure) was less than 20 μA at 8 kV (fig. 6.17), implying low power consumption less than 0.16 W. In addition, although increasing v_{in} caused higher C_a, the actuation velocity of each EPP decreased with an increasing v_{in} for all tested loads.

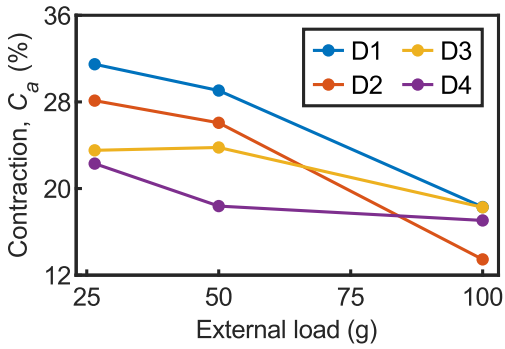

Figure 6.18: Active contraction C_a of the EPP-BAM system under different loads when containing v_{in} that maximised C_a and actuated at 8 kV.

6.5 EPP-BAM Capabilities

Several experiments were performed to demonstrate the versatility of this novel soft pump. EPP D1 was connected to the previously described BAM, loaded with a mass of 26.5 g. The EPP-BAM system contained v_{in} = 15 ml, and the EPP was actuated at different frequencies between 0.1 and 2.0 Hz at V = 8 kV (fig. 6.19). The highest frequency that allowed for full contraction of the BAM was 0.2 Hz; the interpolated -3dB cutoff frequency was at 0.38 Hz (fig. 6.20).

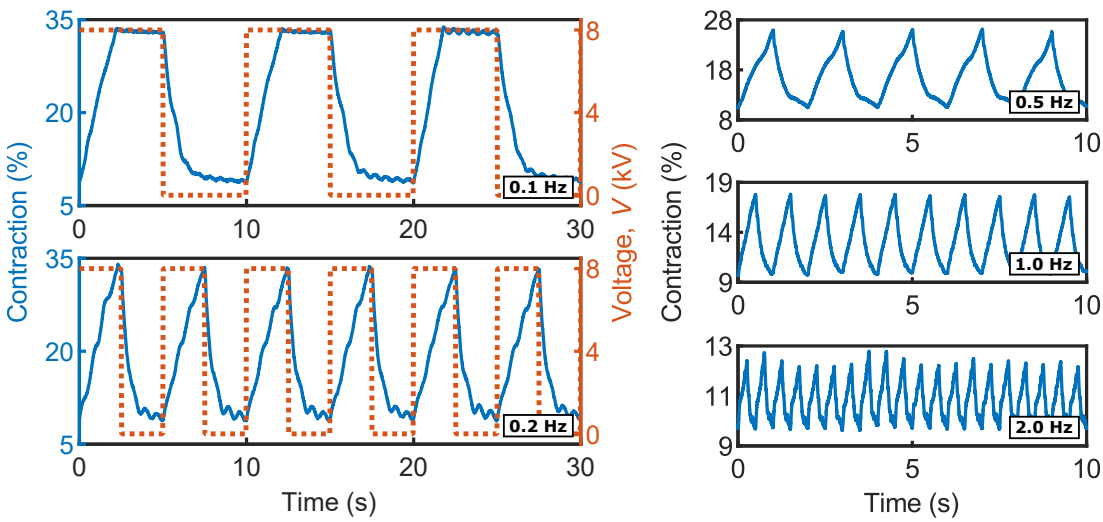

Figure 6.19: EPP-BAM actuation at frequencies of 0.1, 0.2, 0.5, 1.0 and 2.0 Hz at V = 8 kV.

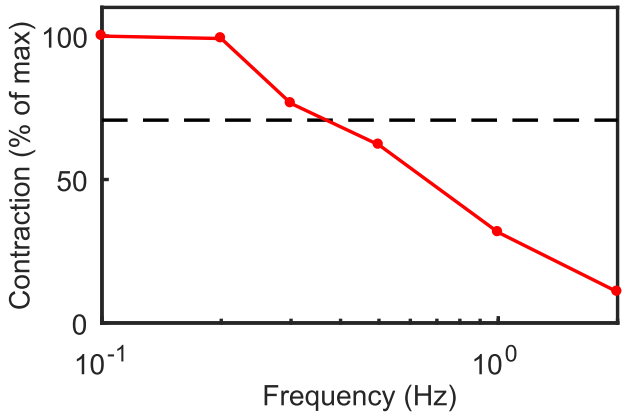

Figure 6.20: Bode plot of actuator frequency response at V = 8 kV (The dashed line indicates -3 dB).

Open-loop voltage control of the EPP-BAM system was implemented; fig. 6.21 shows EPP D1 holding the BAM at various intermediate contractions, reachable by adjusting voltage. To increase and decrease BAM contraction, voltages of 8 kV and 1 kV, respectively, were applied momentarily. To hold BAM at different contraction, a holding voltage in the range of 3.7-4.7 kV was applied depending on the amount of contraction. This provides a promising possibility for the EPP pump to be readily controllable.

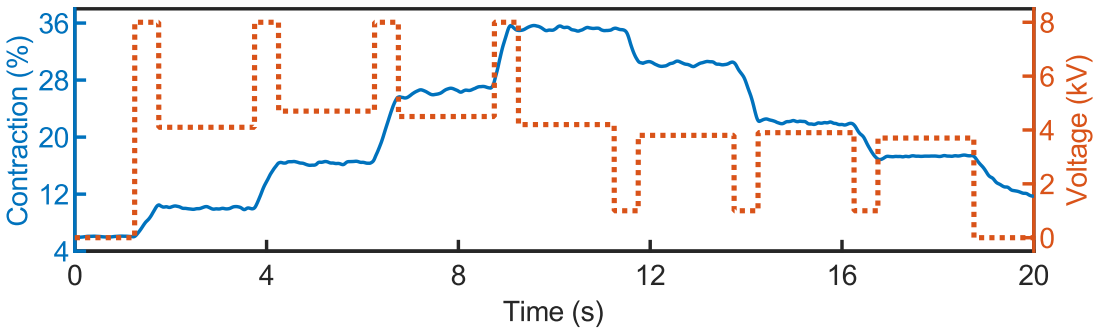

Figure 6.21: Open-loop voltage control allowing the EPP D1 to hold the BAM at different intermediate contraction values.

Cyclic testing was undertaken over ten thousand cycles at a frequency of 1 Hz (fig. 6.22A). EPP D1 was actuated at a voltage of 8 kV, while the BAM was loaded with a mass of 70 g. The EPP-BAM system contained v_{in} of 7 ml, less than in the experiments for fig. 6.19, to enable full zipping at 1 Hz actuation. After 8,000 cycles, the contraction (C_a) reduced by 1.17% (fig. 6.22B).

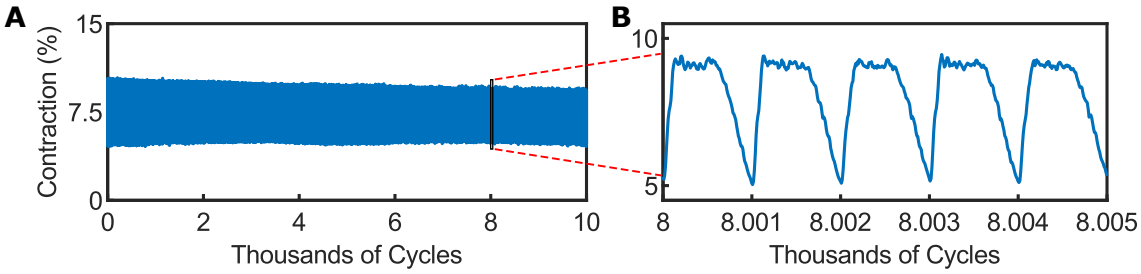

Figure 6.22: (A) Cyclic test of the EPP-BAM system, over ten thousand cycles at a frequency of 1 Hz and at voltage of 8 kV. (B) Five actuation cycles after 8,000 cycles.

These three experiments show different aspects of the capabilities of the EPP in actuating a typical pneumatic actuator, increasing its suitability as a future air power source. It was able to be controllable, and closed-loop control for the EPP is possible. It has high durability despite being handmade; improving fabrication can even increase its life time and actuation performance. Next section will present three demonstrators showing the versatility of the EPP for use in real-world applications.

6.6 Demonstrators

6.6.1 Antagonistic Mechanism

Using a pair of EPP-BAM systems (design D1) allows for an antagonistic mechanism, connecting each end of the BAMs to a connecting bar (fig. 6.23). Each EPP-BAM system was injected air volume v_{in} up to where the BAM delivered maximum contraction. The EPPs were actuated with a 180° out of phase square voltage wave at a range of frequencies and at 10 kV. The system moved the connecting bar at frequencies up to 5 Hz. Full stroke of the connecting bar was achieved when the frequency was equal or lower than 0.2 Hz.

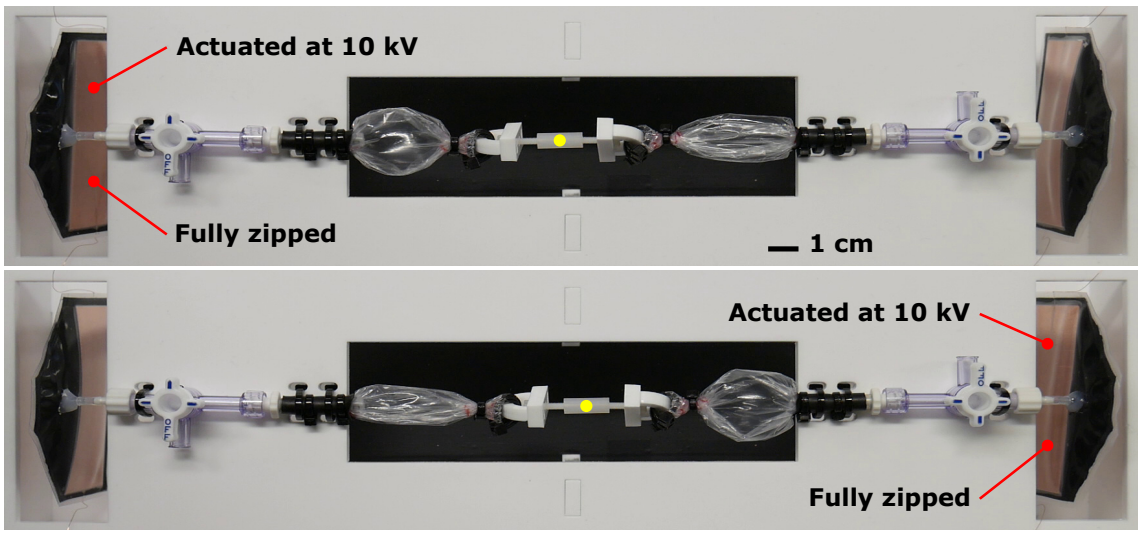

Figure 6.23: Antagonistic mechanism featuring two identical EPP-BAM systems (EPP D1) actuated at 10 kV (yellow dots indicate the center of the connecting bar).

6.6.2 Arm-flexing Assistive Device

An arm-flexing wearable robotic device was designed as shown in fig. 6.24. The device consisted of two EPPs (design D1) connected in parallel, a BAM with three contractile units, and a plastic skeleton arm to represent a human arm. The skeleton has a 12.5 cm long upper arm and a 22 cm long forearm and hand. For the BAM, two metal retaining rings with inner radius 2 mm (MM Watch Co. Limited, UK) were added to create three series contractile units to increase its actuation stroke. The BAM has a total extended length of 11.5 cm and unactuated radius of 2 mm. It was anchored to a rigid mount near the shoulder, and to the forearm 4 cm from the elbow. Actuation of the BAM lifted the 18.62 g forearm. Injected air volume v_{in} was adjusted to deliver the highest flexion. The weight of the series BAM and two EPP units were 2.48, 5.72 and 5.82 g respectively, resulting in a total weight of the wearable robotic device of 14.02 g.

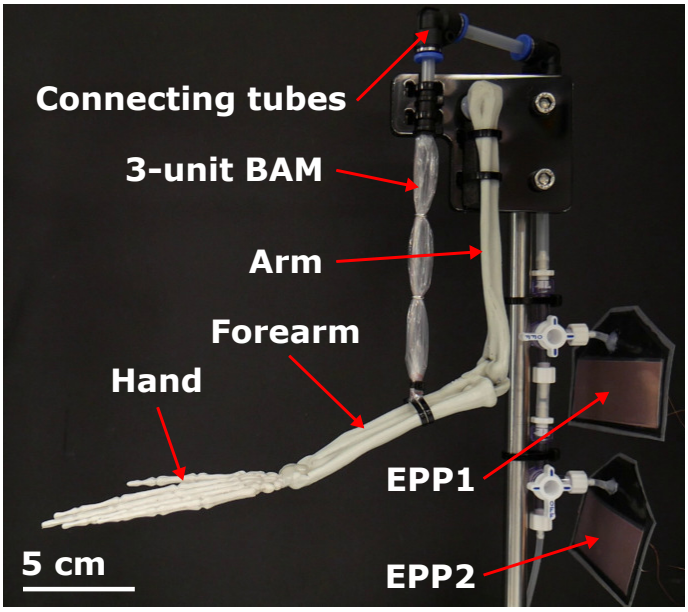

Figure 6.24: Experimental setup of the wearable robotic device, driven by two parallel EPPs (design D1).

Both EPPs were actuated simultaneously at 10 kV, causing the BAM to contract and the arm to lift. A maximum stroke of 23.0 cm was achieved at v_{in} = 40 ml (fig. 6.25, A-D). When deactivating the EPPs, the arm lowered due to gravity; an antagonistic mechanism for both flexion and extension could be applied to the arm to increase the speed at which the arm lowered. The wearable robotic device can also deliver an arm stroke of approximately 3.2 cm when actuated at a frequency of 1 Hz. The arm was able to contract up to 15.1 cm and 9.6 cm stroke while it was loaded with a 4.8-g toy duck and a 20-g mass, respectively (fig. 6.25, E-H).

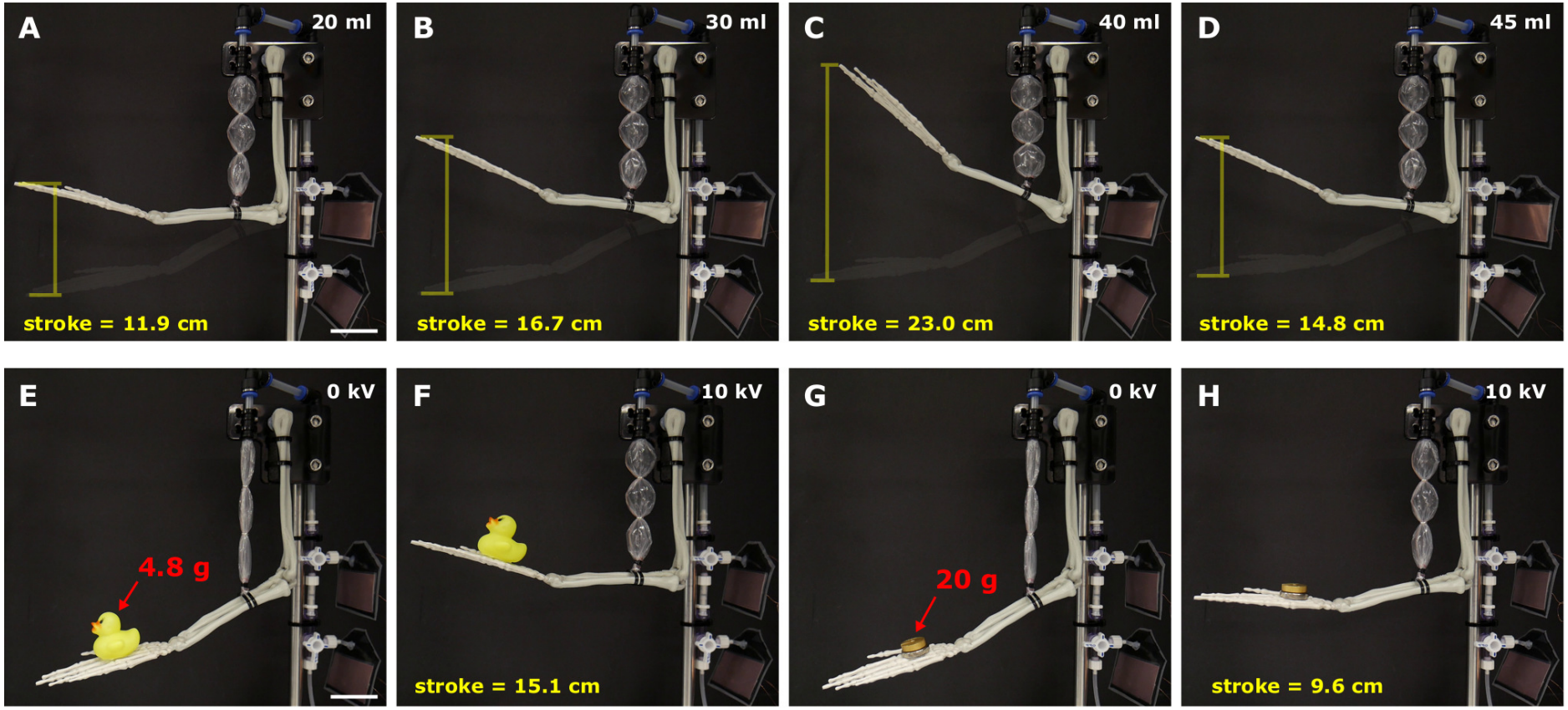

Figure 6.25: (A-D) Motion of the arm when actuating the EPPs at 10 kV, but with different v_{in} for the EPP-BAM system of 20, 30, 40 and 45 ml, respectively. (E-H) Resting and actuation states of the arm while holding a 4.8 g toy duck (E-F) and a 20 g load (G-H).

6.6.3 Continuous-pumping System

To create continuous pumping, the EPP must be returned to its resting state to restore atmospheric air into the pouch for transferring air during its actuation state. The pumping EPP was fabricated by adding a sponge between the two electrodes at the center of the EPP (design D1, fig. 6.26a). This sponge acts as a soft spring, generating a sufficient restoring force to open the EPP at 0 kV. A sponge with dimensions 10 x 10 x 12 mm (103-4073, RS Components Ltd., UK) was inserted into the EPP prior to final sealing. The EPP was connected to two one-way valves for passive control of air input and output, ensuring directional pumping and allowing the EPP to work as a continuous pump.

Experiments were performed by linking the EPP to a volume measurement setup, comprising a water trough and a measuring cylinder, through a pumping tube (fig. 6.26b). Pumped air volume was measured by observing the change in water level in a 10-ml measuring cylinder (#11517832, Fisher Scientific UK Ltd, UK). For each experiment, the water level was reset using a syringe through an adjusting tube.

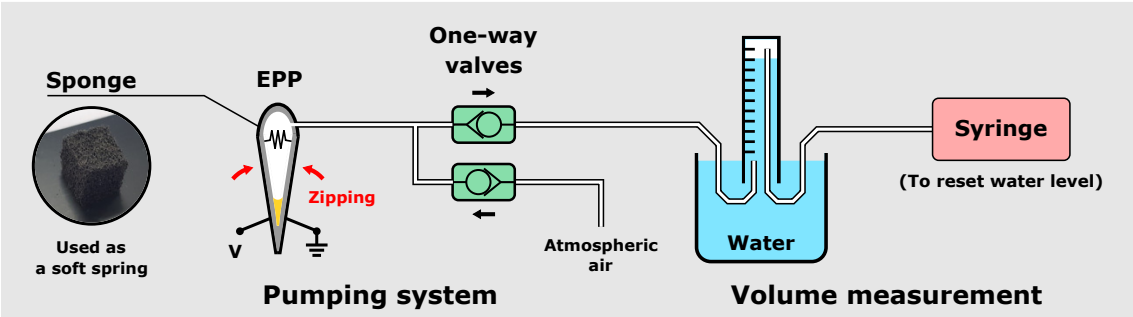

(a)

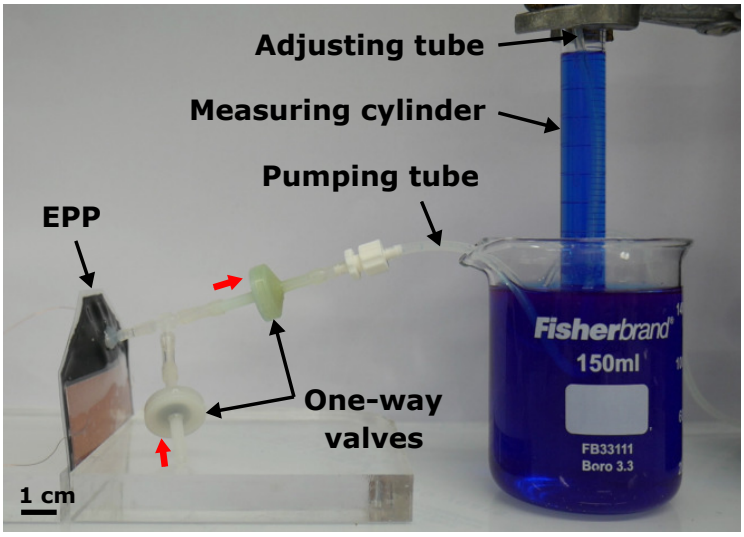

(b)

Figure 6.26: Experimental design (a) and setup (b) to evaluate the performance of a continuous-pumping system driven by the EPP D1 with an additional sponge.

Two types of experiments were undertaken while actuating the EPP at a control voltage of 10 kV at different frequencies: measuring pumped air volume while actuating the pump for two cycles (fig. 6.27), and measuring flow rate while actuating for two seconds (fig. 6.28). When actuating the EPP pump for two cycles, the pumped air volume decreased with increasing frequency (fig. 6.27). When actuating the EPP pump for two seconds, peak average flow rates of 2.65 and 2.68 ml/s were delivered at 2 and 25 Hz (fig. 6.28). Although pumped air volume of the EPP was lower at higher frequency when actuating for the same period, the EPP can generate a similar flow rate over 2 ml/s between 0 and 30 Hz. The high flow rate achieved at high frequency and associated small EPP contractions suggests the possibility of creating an extremely small EPP pump which retains the high performance of the EPP demonstrated here.

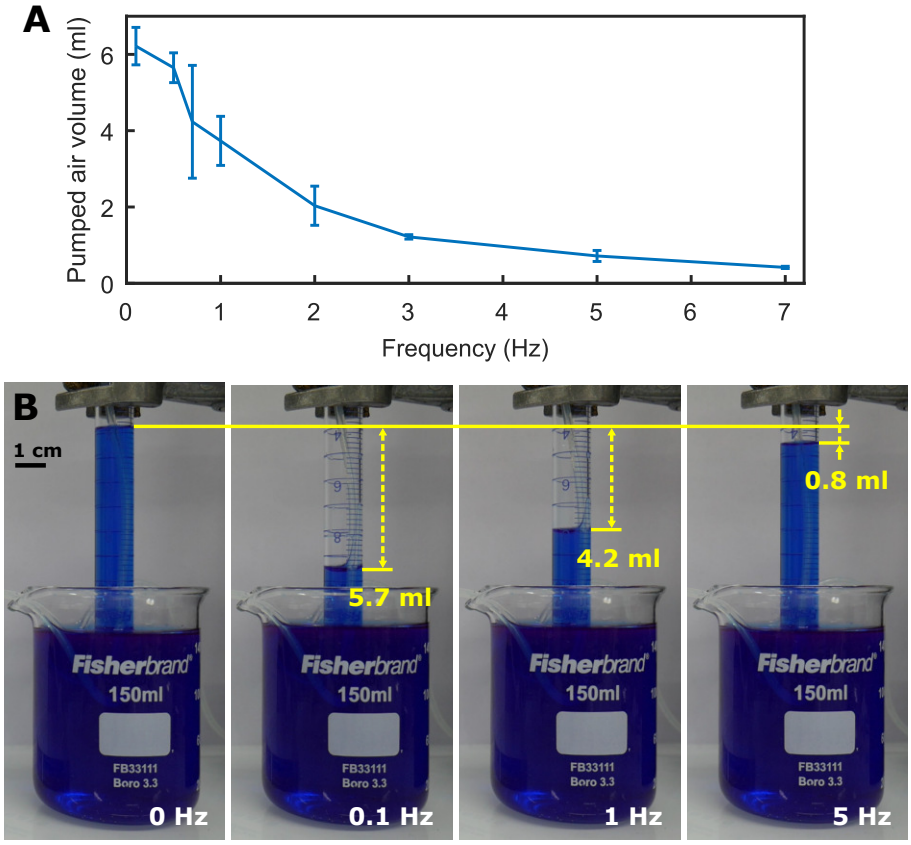

Figure 6.27: (A) Variation in pumped air volume during two actuation cycles at different frequencies. Points are averages of three trials, and error bars show ± 1 standard deviation. (B) Actuation of the pumping system for two actuation cycles at frequencies of 0.1, 1 and 5 Hz, respectively.

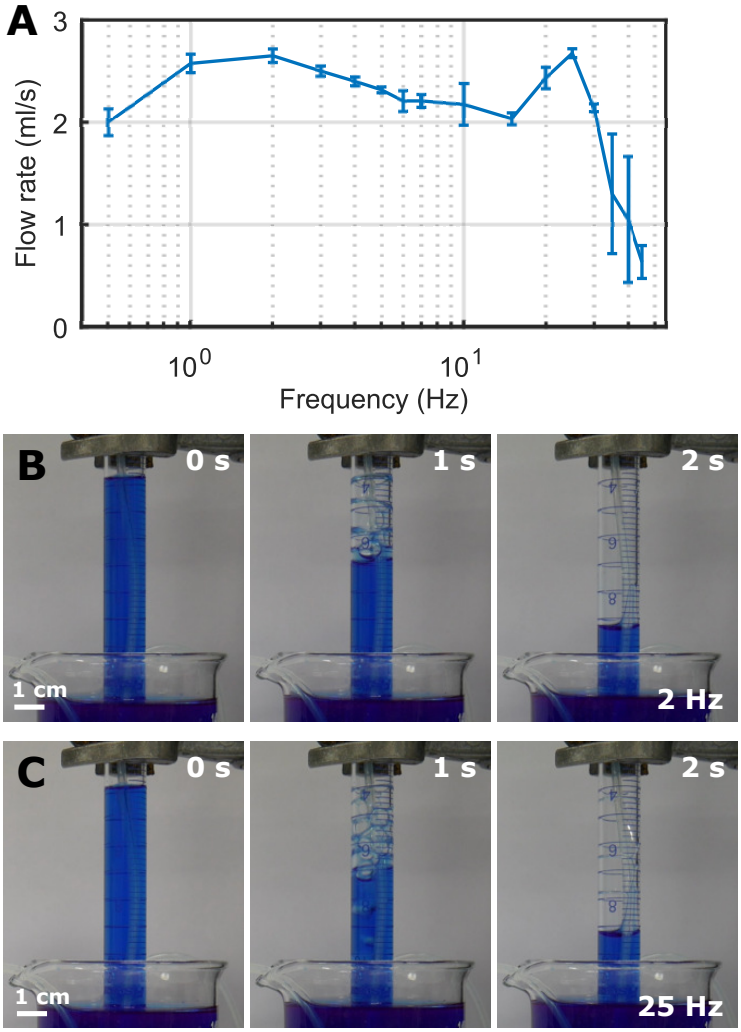

Figure 6.28: (A) Variation in average flow rate during two seconds of cyclic actuation at different actuation frequencies. Points are averages of three trials, and error bars show ± 1 standard deviation. (B-C) Actuation of the pumping system for two seconds of cyclic actuation at frequencies of 2 and 25 Hz, respectively.

6.7 Discussion

Soft Robotics has applications in myriad fields from assistive wearables to autonomous exploration. Currently, the portability and performance of many devices is limited by their associated pneumatic energy source, requiring either large, heavy pressure vessels or noisy, inefficient air pumps. In this chapter, we present a lightweight, inexpensive, flexible Electro-pneumatic Pump (EPP), which can silently control volume and pressure, enabling portable, local energy provision for soft robotic applications and wearable devices, overcoming the limitations of existing pneumatic power sources.

The EPP is actuated using dielectric-fluid-amplified electrostatic zipping. It can generate pressure and transfer air when electrically charged. Its stiffness depends on its geometry and the materials used in its fabrication; stiff EPPs generated high pressure,

while soft EPPs transferred high air volumes. EPP maximum pressure change was 2.34 kPa, lower than the 14 kPa delivered by the stretchable liquid pump presented in [138]. However the EPP is also capable of pumping air rather than liquid, making it suitable for driving pneumatic artificial muscles. Its highest continuous pumping air flow rate was 2.68 ml/s (161 ml/min), considerably higher than the fluidic flow rate of that pump (6 ml/min), and the combustion-driven pump (40 ml/min) presented in [139]. The EPP-BAM system delivered a maximum C_a of 32.4% (load 26.5 g) and lifted a maximum load of 100.4 g (corresponding to 0.98 N), which compares favorably with the maximum C_a of 2.2% and maximum blocking force of 0.84 N reported for thin McKibben muscles actuated by the stretchable pump [142]. The maximum actuation velocity of the BAM is 54.43%/s when actuating the EPP at 10 kV. The EPP-BAM system is also open-loop controllable, enabling applications where precise pumping behavior is required, and has high durability, delivering over 10,000 actuation cycles despite being handmade.

Although the EPP is driven by high voltage, no conductors are exposed to the outside of the pump other than insulated wires, which limits the possibility of exposure to high voltage. Furthermore, the maximum current delivered to the EPPs demonstrated here was less than 100 μA, considerably lower than the 20 mA maximum permitted by Underwriters Laboratories (UL) and International Electrotechnical Commission (IEC) consumer electronics safety standards [143]. EPPs require low power consumption (< 0.16 W) during actuation to maintain generated pressure and contraction of a connecting pneumatic actuator.

A typical EPP has an extremely low thickness of 1.1 mm and weight of 5.3 g, and smaller, lighter EPPs are achievable by better fabrication quality. The performance of EPPs can be improved by optimising their design or altering their fabrication process, for example by using origami structures or different electrode shapes. EPPs can be used as a portable pump for soft robotics when paired with a portable, lightweight high-voltage supply as in [138], demonstrating their potential for wearable robotics applications. The EPP-BAM wearable robotic device was able to drive an arm to exert force and do work, suggesting it can generate useful forces for wearable applications. In the future, the EPP-BAM system can be miniaturised and integrated into assistive clothing, containing several units in an array, which can be actuated to assist body movement when required.

We highlight the versatility of this technology by presenting three EPP-driven embodiments: an antagonistic mechanism, an arm-flexing wearable robotic device and a continuous-pumping system. This research shows the wide applicability of the EPP across robotics and autonomous systems. As a flexible, silent, lightweight, fast-response pump, it has the potential to enable advanced wearable assistive devices and a new generation of entirely soft, mobile, multifunctional robots.

Chapter 7

Conclusion and Future Work

This thesis describes novel artificial muscles that have been developed for use in a wearable assistive device to improve human mobility. The developed soft actuators successfully meet the general requirements of wearable assistive devices. This chapter summarises the main contributions of the work, discusses limitations of developed technologies and introduces guidelines for future research.

7.1 Conclusions

The goal of this research is to create new technology towards the development of a future smart assistive suit, which can autonomously provide extra power for healthy people to effectively perform and prolong their locomotion with less fatigue, achieving daily activities with more ease and comfort, leading to better quality of life and independent living. Soft pneumatic and electrical actuators were studied and developed according to inherent advantages that benefit wearable assistive devices. A novel electro-pneumatic actuator was developed, combining the advantages of these two soft technologies and addressing their independent limitations. As a result, this actuator has high potential for the next generation of soft robotics and wearable assistive technology.

All three developed actuators are lightweight, flexible, compact, simply fabricated and made of readily available, inexpensive materials. They can produce excellent actuation performance and have high reliability (controllability) and durability (minimal performance reduction after 10,000 actuation cycles). With higher fabrication quality, these actuators can be portable and operate more safely. They overcome current challenges in creating wearable assistive devices and address the orthosis stakeholder needs (table 2.1). The advantages and limitations of each developed actuator are summarised as follows.

Bubble Artificial Muscles

The Bubble Artificial Muscle (BAM) is a lightweight, flexible pneumatic actuator, capable of producing high stress and strain, greater than human muscle performance (table 3.3). BAMs can generate higher contraction than typical soft pneumatic actuators and have high force- and power-to-weight ratios. The approach to design the optimal BAM producing the highest contraction and its actuation model were derived for reproduction and practical usage in robotic applications.

The BAM was designed to be used as a wearable assistive device to aid human mobility. Knee motions was primarily selected and studied to develop orthotic prototypes, since it was found to be the dominant joint in performing human locomotion, and is the easiest joint to be assisted (one DOF in a sagittal plane). A dynamic leg model was derived and revealed that a knee assistive device could improve the walking performance of older adults, to reach that of young healthy individuals, especially when they generated less muscle power, which was assumed as a result of tiredness from long walking.

Two BAM orthoses were created to assist knee flexion and extension for a swing leg motion during ground-level walking and for sit-to-stand transitions, respectively. They generated assistive torques exceeding 8 Nm, resulting in sufficient assistance for both knee flexion and extension, while being aesthetic, slim and unobtrusive, not larger than the leg width. They were able to lift a human-scale leg mechanism with actual human leg weight up to 70% of the peak knee flexion of young subjects and achieve standing motion, rising from a chair, lifting 1 kg hip weight. They also possess inherent backdrivability since they are pneumatic-driven. They behave as a soft spring, allowing natural human body movements. Moreover, they operated at air pressures under 70 kPa, implying safe interaction with human body. A downside of BAMs is that they are powered by pneumatic sources; as such they exhibit slow actuation due to high air volume, and heavy, bulk, noise air supplies, e.g. a compressor and pump, limiting portability.

Electrostatic Actuators

The electro-ribbon actuator (ERA) is an electrical zipping actuator using the concept of Dielectrophoretic Liquid Zipping (DLZ) where dielectric liquid amplifies electrostatic attractive forces between two electrodes, resulting in high stress and strain actuation. DLZ exhibits fast and silent actuation, low power consumption and high efficiency (up to 70% as studied in [105]). These features address the limitations of soft pneumatic actuators; therefore, the ERA were selected to study in this research. It was improved to increase controllability, simplify fabrication and enable a wider range of actuator designs and applications.

The ERA typically experiences nonlinear actuation behaviour due to its pull-in instability, leading to a narrow controllable range between resting and full-zipping states. A Boost-PI controller was developed to efficiently control the ERA, allowing the actuator to

access multiple intermediate contractions and demonstrate a range of contracting profiles with low error. Although the presented work used actuator contraction measured by a laser displacement sensor as an input parameter for the controller, the ERA was recently found to possess a self-sensing ability thanks to its fundamental structure as a variable capacitor [144]. Using the developed controller with a self-sensing ERA could result in a compact, self-contained ERA-based actuation-control system.

A new ERA using alternative materials was designed, leading to a simpler fabrication process. Originally, ERAs used clips or magnets fix together each zipping corner, which unnecessarily increased the actuator thickness and weight. With alternative materials, ERAs can be made using a heat-sealing method to attach opposing electrodes together, resulting in a very thin zipping actuator. This fabrication method allows wider variety of the ERA designs and applications. Three different conceptual designs of the new ERA were presented: a stacked ERA for a linear actuation, a donut-shaped ERA for a 3-dimensional motion and a pre-bent ERA for a pre-deformed structure. The concepts of the stacked ERA and pre-bent ERA were implemented, creating a linear actuator using stacked ERAs and a solenoid valve using pre-bent ERAs with additional springs. These demonstrators show the high potential of the electro-ribbon actuator as a promising technology for future robotics due to its extremely low power consumption compared to currently available technologies. However, the ERA requires high-voltage actuation, which could lead to safety issues. The leakage of dielectric liquid is another problem experienced in the ERA, which decreases zipping efficiency. These two issues were solved in the electro-pneumatic pump by encapsulating the entire zipping mechanism.

Electro-pneumatic Pumps

The electro-pneumatic pump (EPP) is an active air-transferring pouch, driven by the DLZ actuation concept. This device was designed to address limitations of both pneumatic and electrostatic actuators. It was developed from the newly-designed ERA by encapsulating the zipping mechanism, resulting in a hybrid hydraulic-pneumatic system containing dielectric liquid for high-stress electrostatic zipping actuation and air as a pneumatic source. When charged, the EPP's electrodes progressively zip and the pouch squeezes, resulting in compression of air and air-transfer to a connected pneumatic device.

Different geometries of the EPP's electrodes were characterised, concluding that a stiffer EPP generated higher pressure while a softer EPP transferred a larger air volume. The EPP was used to actuate the Bubble Artificial Muscle (BAM), achieving high contraction and fast contraction rate up to 32.4% and 54.4%/s, respectively. The EPP-BAM system was capable of being controllable, operating at different frequencies and having long lifetime with low output change, whilst being lightweight. Three demonstrators were built showing the EPP's versatility for robotic applications: an antagonistic mechanism, an arm-flexing device and a continuous-pumping system. The EPP-BAM system achieved

high stroke, exceeding 45 degree arm flexion and was able to lift a heavier load than its own weight; both arm flexion and extension can be actively performed by using the antagonistic mechanism. The EPP achieved a pumped air flow rate of 161 ml/min at high frequency, associated with a small zipping region, raising the potential of creating a much small, soft, high flow rate air pump.

The EPP consumes low power, at less than 0.16 W. Although the EPP-BAM system successfully delivered high BAM contraction, the current EPP has low efficiency in actuating a connected pneumatic actuator due to parasitic current leakage and shape deformation of the pneumatic actuator driven by compressible air. Parasitic current leakage can be minimised by using different insulated materials as suggested in [105]. The presented work is the first workable version of the electro-pneumatic pump; more improvements are required. For example, optimising the electrodes' geometry, not restricted to only a rectangular shape, exploiting insulating materials and dielectric liquid to increase electrostatic force amplification and decrease current leakage (possibly up to 10 times less as reported in [105]), and removing unproductive EPP region, so as to increase its pressure-generating capability, air volume transfer and tensile force generation in a connected pneumatic actuator. Moreover, since the EPP was designed to actuate a pneumatic device, its transferred air volume reduced while zipping, causing energy loss to air compression. Alternatively, when fully filled with incompressible dielectric liquid, its efficiency can be increased as the transferred volume remains constant and the dielectric liquid can further increase electrostatic zipping force, as in the HASEL actuator [106]. However, this will significantly increase the actuator's weight.

High-voltage actuation is another drawback of the EPP. This issue can be improved by replacing a single, large EPP with multiple smaller EPPs. With a multi-layer EPP matrix (where each layer contains many small identical EPPs), each EPP can have smaller zipping angles, while the combined filled air volume of the small EPPs can equal that of the single, large EPP. In theory, the EPP matrix will exhibit higher electrostatic force because of the small angles, implying a lower voltage required to exert the same air pressure. However, a multi-layer EPP matrix will have a larger total electrode area than the single EPP, and thus its current draw will be higher, which could result in higher power requirement, despite the lower voltage requirement. This system could be more suitable to conventional energy sources such as lithium-ion batteries, which can deliver comparatively low voltages (< 100 V) and high currents (> 1 A). In addition, the electrostatic force can be increased by using higher dielectric EPP materials, resulting in a lower required voltage for the same force generation.

Overall, the electro-pneumatic pump overcomes the limitations of the BAM and ERA. Although the current EPP-BAM system produced low tensile force, it allows fast BAM contraction and works as a lightweight compressed air supply, enabling portability when using a small portable power source. As discussed above, increasing fabrication quality can improve its efficiency in delivering higher pressure generation and air volume transferring,

leading to higher BAM contraction and tension, and can reduce required operating voltage and power consumption. The EPP also solved the leakage of dielectric liquid, a major drawback of the ERA, enhancing its durability. As a result, this compact, lightweight, portable pneumatic system is the first successful step in developing novel technology towards a desired flexible assistive suit.

7.2 Future Work

The developed technologies successfully delivered against all orthosis stakeholder's needs and actuator requirements; however, further developments are required to achieve the ultimate goal of innovating a smart assistive suit. The scope of improvements of each technology are discussed regarding material, design and fabrication for better actuation performance, sensing capability and controllability as follows.

Bubble Artificial Muscles

The BAM was made of an inelastic material folded and inserted into retaining rings, used as actuator ends. A flexible, thin membrane allowed the BAM to easily unfold and bend and thus contract significantly, whereas a stiffer or thick membrane caused it to withstand high pressure, resulting in high force generation but at the expense of reduced contraction. Employing a flexible, thin material with high tensile strength, for example, a TPU-coated nylon fabric (used in [69, 70]), can enable the BAM to deliver both high contraction and tensile force, improving its actuation performance. Different designs of pneumatic shape-changing actuators made of various heat sealable inextensible materials, e.g. paper, plastics and fabrics, and fabrication methods using these materials were investigated in [145], which can be a guideline for implementing new materials for the BAM.

The BAM membrane is non-uniformly folded, which increases friction in expending and bending, limiting BAM contraction and causing deviation from theoretical predictions. Different folding patterns or approaches are required to explore in order to create uniform folds with a simple fabrication. In particular, origami and kirigami methods could be used to achieve uniform folding. Moreover, rigid retaining rings were used in construction, but they added rigidity to the actuator. Removing these rings is another challenge to be addressed so as to fabricate an entirely soft BAM for safe interaction with human body.

Miniaturising the actuator size by reducing material radius can considerably benefit the BAM in many aspects. Although the BAM will become small, its contractile performance can be maintained by fixing the ratio between material and ring radii, and using design optimisation to obtain the optimal length for the selected material and ring radii. Compared to a large single-contractile-unit BAM sharing the same total inflated cross-section area and total actuator length, higher force generation can be achieved by a pack of several miniature multiple-contractile-unit BAMs aligned in parallel with an offset in

vertical direction, making use of the available space. In this configuration, each bubble of one BAM fits into the space between bubbles of the adjacent BAM. The miniature BAM also enhances its aesthetics and appearance for easy integration with normal clothing. For example, combining several small multiple-contractile-unit BAMs, parallelly aligned in a single row, will create a flexible, flat planar, muscle textile producing high contraction and tensile force. Consequently, a 2-dimensional-actuating matrix of BAMs can be implemented by layering two planar BAM units. This BAM matrix can be used as a future active pneumatic clothing, enabling desired surface deformation or shape changing and specific local force generation when applying a combination of actuation patterns between individual miniature BAMs in each layer and between two layers of BAM textiles.

The BAM actuation model presented in this research was derived based on experimental results, considering loss due to the effect of material thickness. A theoretical model derived from first principles is required to simulate actual BAM performance from selected actuator materials, size and actuated pressure. Integrating force and contraction sensors into the BAM is another field to explore, for example, by connecting a load cell in series with the actuator and embedding a stretchable capacitive-base linear sensor at the actuator core or a bending sensor on the actuator membrane for measuring total displacement or shape changing of each contractile unit. Using the data acquired from these sensors with an accurate model will facilitate a precise low-level actuation control.

Electro-ribbon Actuators

The Boost-proportional-and-integral (Boost-PI) closed-loop controller was developed for the ERAs, shortening initial zipping time and enabling precise actuation across the contraction range. Traditional closed-loop control using self-sensing has been demonstrated in the ERAs over a small displacement range of approximately 3 mm [144]. Employing self-sensing with the Boost-PI controller is the next step to investigate larger controllable contractions. In addition, the leakage of dielectric liquid should be addressed for real-world robotic applications. Although the ERA made of a modified insulator, used as a liquid reservoir, successfully ran over 100,000 cyclic actuations, the dielectric liquid can possibly leak when operated in different orientations. The concept of adding additional conductive fabric materials between two electrodes for containing dielectric liquid was tested and showed promising results. However, more investigations are required to evaluate the actuation performance and durability. With these two improvements, a self-contained electro-ribbon actuator can be created.

Electro-pneumatic Pumps

Both EPPs and ERAs are limited to low tensile force generation and efficiency although higher performance can be accomplished using alternative materials [105]. Exploring new insulators and dielectric liquids, considering their permittivity and electric breakdown, can decrease current leakage (possibly up to 10 times less as reported in [105]) and increase electrostatic force amplification, leading to higher efficiency and low voltage requirement.

The EPP can be improved by optimising the electrodes' geometry, not restricted to only a rectangular shape, and removing any unproductive non-zipping region, so as to increase its pressure-generating capability, air volume transfer and tensile force generation in a connected pneumatic actuator, causing higher actuation efficiency. In addition, stiffer backing materials can possibly allow the EPP to operate at a higher pressure range and the connecting pneumatic actuator to generate higher tensile force or contract while lifting a heavier load. This can also increase the EPP-BAM efficiency since internal air compresses at high pressure. According to the continuous-pumping system, the EPP was able to pump a high air flow rate at high frequency, associated with a small zipping region. Consequently, a much smaller soft pump can be fabricated, and multiple EPPs can be combined and connected in either series or parallel for higher pressure and flow rate generation.

The EPP-BAM system has the possibility to be controllable by applying lower voltages to achieve stable intermediate BAM contractions. A Boost-PI closed-loop controller may be implemented with the EPP-BAM system, using either BAM contraction or the self-sensing capability of the EPP, as in the ERA, for sensing feedback.

Wearable Assistive Prototype

The BAM was demonstrated as a soft actuator suitable for building wearable assistive devices because of its light weight, compliance, flexibility, high force-to-weight ratio and high contractile ability. Two orthotic BAM prototypes demonstrated knee flexion and extension for the swing motion of ground-level walking, and sit-to-stand transition. They were able to partially perform these locomotions, based upon human data acquired from other research, which is sufficient to assist healthy able-bodied people as required. However, they were tested only on human-scale leg mechanisms and used rigid attachments.

The new version of the BAM orthoses can be integrated with soft fabric-based attachments as used in cable-driven exosuits [59, 60] and soft pneumatic exoskeletons [70, 71]. A high-level controller is required to calculate pressure inputs for the BAMs, to deliver tensile force and contraction requirements at different lower-limb positions during human locomotions. An example of the simple high-level control was introduced in [71] by converting a linear relationship between tensile force F_t and pressure input P to a linear equation, $P = K(c) \cdot F_t$, where $K(c)$ is a variable varied depending on the actuator's contraction c. This approach can also be implemented with the BAM since it shares similar actuation behaviour. That is, generated tensile force and pressure of the BAMs have a

linear relationship in a certain pressure range at given contraction, and its gradient decreases with contraction (fig. 3.7). At a specific knee angle, tensile force and contraction requirements can be calculated using a human model and data measured from sensors, and thus required pressure input can be easily and reversely calculated from this tensile force and pressure relationship used in low-level actuation control.

Advanced Smart Assistive Suit

According to the concept of a future smart assistive suit, the EPP-BAM system has high potential to be developed to meet this target. When a much smaller EPP-BAM system can be manufactured, a matrix of multiple identical EPP-BAM units can be designed and created. For example, each EPP can be surrounded by BAMs made of fabric-like materials, resulting in a slim, compliant, assistive mesh prototype with capability of two-dimensional-motion actuation. At a resting state, a certain air volume is contained inside EPPs. When electrically charging the EPP, the air volume will be transferred to the surrounding BAMs, causing BAM contraction and shape deformation. This air volume will return to the EPPs when they are discharged. With this design, the EPP-BAM mesh can actively adjust its shape to fit an arbitrary shape, enabling self-fitting ability and increasing ease of donning/doffing for the wearable device. Stiffness variability could also be achieved when BAMs contain lightweight jamming elements. The EPP-BAM mesh can become stiffer when removing air from the BAMs, causing the BAM membrane to compress internal small jamming elements to stick together and form a rigid structure, and can become softer when injecting a small air volume into the BAMs.

Each EPP-BAM unit is self-contained since it is capable of being self-sensing and controllable, delivering accurate actuation with low power consumption. To initialise actuation, the entire EPP-BAM mesh will store air as a restoring energy source without additional weight to the assistive suit. Cooperating between the self-sensing capability and an advanced, high-level controller can result in specific local deformation by transferring air volume between two or more selected locations on the suit. This enables multidirectional tasks, for example, local stiffening of one leg for standing support, antagonistic contractions for bidirectional motions, and stiffness exchanging between two legs during walking to independently assist leg advancement. When unpredicted falling is detected by motion sensors, internal air volume can be transferred to inflate BAMs so as to absorb impact forces, reducing injuries.

In addition, since the EPP is a capacitor, it can harvest mechanical energy when it is deformed by the user's body movements. This could allow the smart assistive suit to harvest mechanical energy and charge itself when the user is doing an energetically easy task, such as descending stairs or a hill (this could also be used to slow the user's descent). This harvested energy could then be used when the user wishes to do an energetically intensive task, such as sit-to-stand, stair- or hill-climbing.

Human Locomotion Experiments

Future research will involve testing the orthotic prototypes with real human subjects at a clinical level. The assistance of an orthosis can be assessed by measuring the metabolic cost, especially for walking motions on a treadmill, or muscle activities using sEMG sensors for various human body movements, for example, sit-to-stand transitions and different body postures, as in [61–63, 70, 71].

Besides well-performing and accurate actuation units and sensing systems, a sophisticated high-level controller is required to achieve high overall system performance. It should be adaptable to adjust its assisting strategy in real time to match the user's body condition, e.g. different locomotion speeds and patterns or tiredness of the user, in order to maximise assistance, minimise muscle energy consumption and maintain high locomotion performance.

In conclusion, this thesis describes research developing novel artificial muscles, providing noteworthy contributions to soft robotics. They all have high potential to be developed further and deliver a future generation of wearable assistive devices, to achieve the ultimate goal in creating a smart assistive suit.

Bibliography

[1] T. Yan, M. Cempini, C. M. Oddo, and N. Vitiello, "Review of assistive strategies in powered lower-limb orthoses and exoskeletons," *Robotics and Autonomous Systems*, vol. 64, pp. 120–136, 2015.

[2] B. S. Rupal, S. Rafique, A. Singla, E. Singla, M. Isaksson, and G. S. Virk, "Lower-limb exoskeletons: Research trends and regulatory guidelines in medical and non-medical applications," *International Journal of Advanced Robotic Systems*, vol. 14, no. 6, p. 1729881417743554, 2017.

[3] W. Huo, S. Mohammed, J. C. Moreno, and Y. Amirat, "Lower limb wearable robots for assistance and rehabilitation: A state of the art," *IEEE systems Journal*, vol. 10, no. 3, pp. 1068–1081, 2014.

[4] G. F. Anderson and P. S. Hussey, "Population aging: A comparison among industrialized countries: Populations around the world are growing older, but the trends are not cause for despair.," *Health affairs*, vol. 19, no. 3, pp. 191–203, 2000.

[5] M. Monda, A. Goldberg, P. Smitham, M. Thornton, and I. McCarthy, "Use of inertial measurement units to assess age-related changes in gait kinematics in an active population," *Journal of aging and physical activity*, vol. 23, no. 1, pp. 18–23, 2015.

[6] W. J. Chodzko-Zajko, D. N. Proctor, M. A. F. Singh, C. T. Minson, C. R. Nigg, G. J. Salem, and J. S. Skinner, "Exercise and physical activity for older adults," *Medicine & science in sports & exercise*, vol. 41, no. 7, pp. 1510–1530, 2009.

[7] A. M. Dollar and H. Herr, "Lower extremity exoskeletons and active orthoses: challenges and state-of-the-art," *IEEE Transactions on robotics*, vol. 24, no. 1, pp. 144–158, 2008.

[8] J. E. Pratt, B. T. Krupp, C. J. Morse, and S. H. Collins, "The roboknee: an exoskeleton for enhancing strength and endurance during walking," in *IEEE International Conference on Robotics and Automation, 2004. Proceedings. ICRA'04. 2004*, vol. 3, pp. 2430–2435, IEEE, 2004.

[9] A. B. Zoss, H. Kazerooni, and A. Chu, "Biomechanical design of the berkeley lower extremity exoskeleton (bleex)," *IEEE/ASME Transactions On Mechatronics*, vol. 11, no. 2, pp. 128–138, 2006.

[10] G. Colombo, M. Joerg, R. Schreier, and V. Dietz, "Treadmill training of paraplegic patients using a robotic orthosis," *Journal of rehabilitation research and development*, vol. 37, no. 6, p. 693, 2000.

[11] S. K. Banala, S. H. Kim, S. K. Agrawal, and J. P. Scholz, "Robot assisted gait training with active leg exoskeleton (alex)," *IEEE Transactions on Neural Systems and Rehabilitation Engineering*, vol. 17, no. 1, pp. 2–8, 2009.

[12] J. F. Veneman, R. Kruidhof, E. E. Hekman, R. Ekkelenkamp, E. H. Van Asseldonk, and H. Van Der Kooij, "Design and evaluation of the lopes exoskeleton robot for interactive gait rehabilitation," *IEEE Transactions on Neural Systems and Rehabilitation Engineering*, vol. 15, no. 3, pp. 379–386, 2007.

[13] A. Esquenazi, M. Talaty, A. Packel, and M. Saulino, "The rewalk powered exoskeleton to restore ambulatory function to individuals with thoracic-level motor-complete spinal cord injury," *American journal of physical medicine & rehabilitation*, vol. 91, no. 11, pp. 911–921, 2012.

[14] M. Wehner, B. Quinlivan, P. M. Aubin, E. Martinez-Villalpando, M. Baumann, L. Stirling, K. Holt, R. Wood, and C. Walsh, "A lightweight soft exosuit for gait assistance," in *Robotics and Automation (ICRA), 2013 IEEE International Conference on*, pp. 3362–3369, IEEE, 2013.

[15] A. T. Asbeck, R. J. Dyer, A. F. Larusson, and C. J. Walsh, "Biologically-inspired soft exosuit," in *Rehabilitation robotics (ICORR), 2013 IEEE international conference on*, pp. 1–8, IEEE, 2013.

[16] S. Kim, C. Laschi, and B. Trimmer, "Soft robotics: a bioinspired evolution in robotics," *Trends in biotechnology*, vol. 31, no. 5, pp. 287–294, 2013.

[17] A. T. Asbeck, S. M. De Rossi, I. Galiana, Y. Ding, and C. J. Walsh, "Stronger, smarter, softer: next-generation wearable robots," *IEEE Robotics & Automation Magazine*, vol. 21, no. 4, pp. 22–33, 2014.

[18] Y.-L. Park, B.-r. Chen, C. Majidi, R. J. Wood, R. Nagpal, and E. Goldfield, "Active modular elastomer sleeve for soft wearable assistance robots," in *2012 IEEE/RSJ International Conference on Intelligent Robots and Systems*, pp. 1595–1602, IEEE, 2012.

[19] T. Kawamura, K. Takanaka, T. Nakamura, and H. Osumi, "Development of an orthosis for walking assistance using pneumatic artificial muscle: A quantitative

assessment of the effect of assistance," in *Rehabilitation Robotics (ICORR), 2013 IEEE International Conference on*, pp. 1–6, IEEE, 2013.

[20] A. Kharb, V. Saini, Y. Jain, and S. Dhiman, "A review of gait cycle and its parameters," *IJCEM International Journal of Computational Engineering & Management*, vol. 13, pp. 78–83, 2011.

[21] J. Rose and J. G. Gamble, *Human walking.* Williams & Wilkins, 1994.

[22] M. Schenkman, R. A. Berger, P. O. Riley, R. W. Mann, and W. A. Hodge, "Whole-body movements during rising to standing from sitting," *Physical therapy*, vol. 70, no. 10, pp. 638–648, 1990.

[23] E. R. Ikeda, M. L. Schenkman, P. O. Riley, and W. A. Hodge, "Influence of age on dynamics of rising from a chair," *Physical therapy*, vol. 71, no. 6, pp. 473–481, 1991.

[24] N. B. Alexander, A. B. Schultz, and D. N. Warwick, "Rising from a chair: effects of age and functional ability on performance biomechanics," *Journal of gerontology*, vol. 46, no. 3, pp. M91–M98, 1991.

[25] R. W. Bohannon, A. W. Andrews, and M. W. Thomas, "Walking speed: reference values and correlates for older adults," *Journal of Orthopaedic & Sports Physical Therapy*, vol. 24, no. 2, pp. 86–90, 1996.

[26] R. W. Bohannon, "Comfortable and maximum walking speed of adults aged 20—79 years: reference values and determinants," *Age and ageing*, vol. 26, no. 1, pp. 15–19, 1997.

[27] T. Troosters, R. Gosselink, and M. Decramer, "Six minute walking distance in healthy elderly subjects," *European Respiratory Journal*, vol. 14, no. 2, pp. 270–274, 1999.

[28] K. M. Ostrosky, J. M. VanSwearingen, R. G. Burdett, and Z. Gee, "A comparison of gait characteristics in young and old subjects," *Physical Therapy*, vol. 74, no. 7, pp. 637–644, 1994.

[29] D. A. Winter, A. E. Patla, J. S. Frank, and S. E. Walt, "Biomechanical walking pattern changes in the fit and healthy elderly," *Physical therapy*, vol. 70, no. 6, pp. 340–347, 1990.

[30] M. E. Chamberlin, B. D. Fulwider, S. L. Sanders, and J. M. Medeiros, "Does fear of falling influence spatial and temporal gait parameters in elderly persons beyond changes associated with normal aging?," *The Journals of Gerontology Series A: Biological Sciences and Medical Sciences*, vol. 60, no. 9, pp. 1163–1167, 2005.

[31] L. A. Talbot, R. J. Musiol, E. K. Witham, and E. J. Metter, "Falls in young, middle-aged and older community dwelling adults: perceived cause, environmental factors and injury," *BMC public health*, vol. 5, no. 1, p. 86, 2005.

[32] M. F. Reelick, M. B. van Iersel, R. P. Kessels, and M. G. O. Rikkert, "The influence of fear of falling on gait and balance in older people," *Age and ageing*, vol. 38, no. 4, pp. 435–440, 2009.

[33] J. Munton, M. Ellis, M. A. CHAMBERLAIN, and V. Wright, "An investigation into the problems of easy chairs used by the arthritic and the elderly," *Rheumatology*, vol. 20, no. 3, pp. 164–173, 1981.

[34] Y. Pai and M. W. Rogers, "Control of body mass transfer as a function of speed of ascent in sit-to-stand.," *Medicine and Science in Sports and Exercise*, vol. 22, no. 3, pp. 378–384, 1990.

[35] Y.-C. Pai and M. W. Rogers, "Speed variation and resultant joint torques during sit-to-stand," *Archives of physical medicine and rehabilitation*, vol. 72, no. 11, pp. 881–885, 1991.

[36] S. J. Fleckenstein, R. L. Kirby, and D. A. MacLeod, "Effect of limited knee-flexion range on peak hip moments of force while transferring from sitting to standing," *Journal of biomechanics*, vol. 21, no. 11, pp. 915–918, 1988.

[37] W. Mathiyakom, J. McNitt-Gray, P. Requejo, and K. Costa, "Modifying center of mass trajectory during sit-to-stand tasks redistributes the mechanical demand across the lower extremity joints," *Clinical Biomechanics*, vol. 20, no. 1, pp. 105–111, 2005.

[38] D. W. Vander Linden, D. Brunt, and M. U. McCulloch, "Variant and invariant characteristics of the sit-to-stand task in healthy elderly adults," *Archives of physical medicine and rehabilitation*, vol. 75, no. 6, pp. 653–660, 1994.

[39] M. Kouta and K. Shinkoda, "Differences in biomechanical characteristics of sit-to-walk motion between younger and elderly males dwelling in the community," *Journal of physical therapy science*, vol. 20, no. 3, pp. 185–189, 2008.

[40] H. Sadeghi, P. Allard, F. Barbier, S. Sadeghi, S. Hinse, R. Perrault, and H. Labelle, "Main functional roles of knee flexors/extensors in able-bodied gait using principal component analysis (i)," *The Knee*, vol. 9, no. 1, pp. 47–53, 2002.

[41] S. J. Piazza and S. L. Delp, "The influence of muscles on knee flexion during the swing phase of gait," *Journal of biomechanics*, vol. 29, no. 6, pp. 723–733, 1996.

[42] H. Sadeghi, F. Prince, K. Zabjek, S. Sadeghi, and H. Labelle, "Knee flexors/extensors in gait of elderly and young able-bodied men (ii)," *The Knee*, vol. 9, no. 1, pp. 55–63, 2002.

[43] D. C. Kerrigan, L. W. Lee, J. J. Collins, P. O. Riley, and L. A. Lipsitz, "Reduced hip extension during walking: healthy elderly and fallers versus young adults," *Archives of physical medicine and rehabilitation*, vol. 82, no. 1, pp. 26–30, 2001.

[44] A. Graf, J. O. Judge, S. Õunpuu, and D. G. Thelen, "The effect of walking speed on lower-extremity joint powers among elderly adults who exhibit low physical performance," *Archives of physical medicine and rehabilitation*, vol. 86, no. 11, pp. 2177–2183, 2005.

[45] R. N. Kirkwood, H. d. A. Gomes, R. F. Sampaio, E. Culham, and P. Costigan, "Biomechanical analysis of hip and knee joints during gait in elderly subjects," *Acta Ortopédica Brasileira*, vol. 15, no. 5, pp. 267–271, 2007.

[46] R. Bárbara, S. M. Freitas, L. B. Bagesteiro, M. R. Perracini, and S. R. Alouche, "Gait characteristics of younger-old and older-old adults walking overground and on a compliant surface," *Brazilian Journal of Physical Therapy*, vol. 16, no. 5, pp. 375–380, 2012.

[47] M. del Carmen Sanchez-Villamañan, J. Gonzalez-Vargas, D. Torricelli, J. C. Moreno, and J. L. Pons, "Compliant lower limb exoskeletons: a comprehensive review on mechanical design principles," *Journal of neuroengineering and rehabilitation*, vol. 16, no. 1, p. 55, 2019.

[48] "Rewalk more than walking." Available from: `https://rewalk.com/`. [Accessed July 2017].

[49] G. S. Sawicki and D. P. Ferris, "A pneumatically powered knee-ankle-foot orthosis (kafo) with myoelectric activation and inhibition," *Journal of neuroengineering and rehabilitation*, vol. 6, no. 1, p. 23, 2009.

[50] Y.-L. Park, B.-r. Chen, D. Young, L. Stirling, R. J. Wood, E. Goldfield, and R. Nagpal, "Bio-inspired active soft orthotic device for ankle foot pathologies," in *Intelligent Robots and Systems (IROS), 2011 IEEE/RSJ International Conference on*, pp. 4488–4495, IEEE, 2011.

[51] Y.-L. Park, J. Santos, K. G. Galloway, E. C. Goldfield, and R. J. Wood, "A soft wearable robotic device for active knee motions using flat pneumatic artificial muscles," in *Robotics and Automation (ICRA), 2014 IEEE International Conference on*, pp. 4805–4810, IEEE, 2014.

[52] S.-Y. Chang, K. Takashima, S. Nishikawa, R. Niiyama, T. Someya, H. Onodera, and Y. Kuniyoshi, "Design of small-size pouch motors for rat gait rehabilitation device," in *2015 37th Annual International Conference of the IEEE Engineering in Medicine and Biology Society (EMBC)*, pp. 4578–4581, IEEE, 2015.

[53] Y. Li and M. Hashimoto, "Design and prototyping of a novel lightweight walking assist wear using pvc gel soft actuators," *Sensors and Actuators A: Physical*, vol. 239, pp. 26–44, 2016.

[54] A. Wilkening, S. Hacker, H. Stöppler, L. Dürselen, and O. Ivlev, "Experimental and simulation-based investigation of polycentric motion of an inherent compliant pneumatic bending actuator with skewed rotary elastic chambers," *Robotics*, vol. 6, no. 1, p. 2, 2017.

[55] R. Niiyama, D. Rus, and S. Kim, "Pouch motors: Printable/inflatable soft actuators for robotics," in *Robotics and Automation (ICRA), 2014 IEEE International Conference on*, pp. 6332–6337, IEEE, 2014.

[56] R. Niiyama, X. Sun, C. Sung, B. An, D. Rus, and S. Kim, "Pouch motors: printable soft actuators integrated with computational design," *Soft Robotics*, vol. 2, no. 2, pp. 59–70, 2015.

[57] A. J. Veale, S. Q. Xie, and I. A. Anderson, "Modeling the peano fluidic muscle and the effects of its material properties on its static and dynamic behavior," *Smart Materials and Structures*, vol. 25, no. 6, p. 065014, 2016.

[58] Y. Li, Y. Maeda, and M. Hashimoto, "Lightweight, soft variable stiffness gel spats for walking assistance," *International Journal of Advanced Robotic Systems*, vol. 12, no. 12, p. 175, 2015.

[59] B. Quinlivan, S. Lee, P. Malcolm, D. Rossi, M. Grimmer, C. Siviy, N. Karavas, D. Wagner, A. Asbeck, I. Galiana, *et al.*, "Assistance magnitude versus metabolic cost reductions for a tethered multiarticular soft exosuit," *Science Robotics*, vol. 2, no. 2, p. eaah4416, 2017.

[60] L. N. Awad, J. Bae, K. O'donnell, S. M. De Rossi, K. Hendron, L. H. Sloot, P. Kudzia, S. Allen, K. G. Holt, T. D. Ellis, *et al.*, "A soft robotic exosuit improves walking in patients after stroke," *Science translational medicine*, vol. 9, no. 400, p. eaai9084, 2017.

[61] J. Zhang, P. Fiers, K. A. Witte, R. W. Jackson, K. L. Poggensee, C. G. Atkeson, and S. H. Collins, "Human-in-the-loop optimization of exoskeleton assistance during walking," *Science*, vol. 356, no. 6344, pp. 1280–1284, 2017.

[62] Y. Ding, M. Kim, S. Kuindersma, and C. J. Walsh, "Human-in-the-loop optimization of hip assistance with a soft exosuit during walking," *Science Robotics*, vol. 3, no. 15, p. eaar5438, 2018.

[63] K. Schmidt, J. E. Duarte, M. Grimmer, A. Sancho-Puchades, H. Wei, C. S. Easthope, and R. Riener, "The myosuit: Bi-articular anti-gravity exosuit that reduces hip

extensor activity in sitting transfers," *Frontiers in neurorobotics*, vol. 11, p. 57, 2017.

[64] T. Poliero, C. Di Natali, M. Sposito, J. Ortiz, E. Graf, C. Pauli, E. Bottenberg, A. De Eyto, and D. G. Caldwell, "Soft wearable device for lower limb assistance: assessment of an optimized energy efficient actuation prototype," in *2018 IEEE International Conference on Soft Robotics (RoboSoft)*, pp. 559–564, IEEE, 2018.

[65] V. Bartenbach, K. Schmidt, M. Naef, D. Wyss, and R. Riener, "Concept of a soft exosuit for the support of leg function in rehabilitation," in *2015 IEEE International Conference on Rehabilitation Robotics (ICORR)*, pp. 125–130, IEEE, 2015.

[66] S. Kurumaya, K. Suzumori, H. Nabae, and S. Wakimoto, "Musculoskeletal lower-limb robot driven by multifilament muscles," *Robomech Journal*, vol. 3, no. 1, p. 18, 2016.

[67] T. Abe, S. Koizumi, H. Nabae, G. Endo, and K. Suzumori, "Muscle textile to implement soft suit to shift balancing posture of the body," in *2018 IEEE International Conference on Soft Robotics (RoboSoft)*, pp. 572–578, IEEE, 2018.

[68] J. C. Case, J. Booth, D. S. Shah, M. C. Yuen, and R. Kramer-Bottiglio, "State and stiffness estimation using robotic fabrics," in *2018 IEEE International Conference on Soft Robotics (RoboSoft)*, pp. 522–527, IEEE, 2018.

[69] S. Sridar, P. H. Nguyen, M. Zhu, Q. P. Lam, and P. Polygerinos, "Development of a soft-inflatable exosuit for knee rehabilitation," in *2017 IEEE/RSJ International Conference on Intelligent Robots and Systems (IROS)*, pp. 3722–3727, IEEE, 2017.

[70] S. Sridar, Z. Qiao, N. Muthukrishnan, W. Zhang, and P. Polygerinos, "A soft-inflatable exosuit for knee rehabilitation: Assisting swing phase during walking," *Frontiers in Robotics and AI*, vol. 5, p. 44, 2018.

[71] J. Fang, J. Yuan, M. Wang, L. Xiao, J. Yang, Z. Lin, P. Xu, and L. Hou, "Novel accordion-inspired foldable pneumatic actuators for knee assistive devices," *Soft Robotics*, vol. 7, no. 1, pp. 95–108, 2020.

[72] M. A. M. Dzahir and S.-i. Yamamoto, "Recent trends in lower-limb robotic rehabilitation orthosis: Control scheme and strategy for pneumatic muscle actuated gait trainers," *Robotics*, vol. 3, no. 2, pp. 120–148, 2014.

[73] A. J. Veale and S. Q. Xie, "Towards compliant and wearable robotic orthoses: A review of current and emerging actuator technologies," *Medical engineering & physics*, vol. 38, no. 4, pp. 317–325, 2016.

[74] T. Helps, M. Taghavi, S. Manns, A. J. Turton, and J. Rossiter, "Easy undressing with soft robotics," in *Annual Conference Towards Autonomous Robotic Systems*, pp. 79–90, Springer, 2018.

[75] A. Schiele and F. C. van der Helm, "Influence of attachment pressure and kinematic configuration on phri with wearable robots," *Applied Bionics and Biomechanics*, vol. 6, no. 2, pp. 157–173, 2009.

[76] K. Junius, M. Degelaen, N. Lefeber, E. Swinnen, B. Vanderborght, and D. Lefeber, "Bilateral, misalignment-compensating, full-dof hip exoskeleton: design and kinematic validation," *Applied bionics and biomechanics*, vol. 2017, 2017.

[77] L. Saccares, I. Sarakoglou, and N. G. Tsagarakis, "it-knee: An exoskeleton with ideal torque transmission interface for ergonomic power augmentation," in *2016 IEEE/RSJ International Conference on Intelligent Robots and Systems (IROS)*, pp. 780–786, IEEE, 2016.

[78] U. Martinez-Hernandez, I. Mahmood, and A. A. Dehghani-Sanij, "Simultaneous bayesian recognition of locomotion and gait phases with wearable sensors," *IEEE Sensors Journal*, vol. 18, no. 3, pp. 1282–1290, 2017.

[79] U. Martinez-Hernandez and A. A. Dehghani-Sanij, "Adaptive bayesian inference system for recognition of walking activities and prediction of gait events using wearable sensors," *Neural Networks*, vol. 102, pp. 107–119, 2018.

[80] U. Martinez-Hernandez and A. A. Dehghani-Sanij, "Probabilistic identification of sit-to-stand and stand-to-sit with a wearable sensor," *Pattern Recognition Letters*, vol. 118, pp. 32–41, 2019.

[81] F. Shahmiri and P. H. Dietz, "Sharc: A geometric technique for multi-bend/shape sensing," in *Proceedings of the 2020 CHI Conference on Human Factors in Computing Systems*, pp. 1–12, 2020.

[82] J. Zhang, J. Sheng, C. T. O'Neill, C. J. Walsh, R. J. Wood, J.-H. Ryu, J. P. Desai, and M. C. Yip, "Robotic artificial muscles: Current progress and future perspectives," *IEEE Transactions on Robotics*, vol. 35, no. 3, pp. 761–781, 2019.

[83] D. Rus and M. T. Tolley, "Design, fabrication and control of soft robots," *Nature*, vol. 521, no. 7553, pp. 467–475, 2015.

[84] C. Laschi, B. Mazzolai, and M. Cianchetti, "Soft robotics: Technologies and systems pushing the boundaries of robot abilities," *Sci. Robot*, vol. 1, no. 1, p. eaah3690, 2016.

[85] J. M. McCracken, B. R. Donovan, and T. J. White, "Materials as machines," *Advanced Materials*, p. 1906564, 2020.

[86] M. Wehner, R. L. Truby, D. J. Fitzgerald, B. Mosadegh, G. M. Whitesides, J. A. Lewis, and R. J. Wood, "An integrated design and fabrication strategy for entirely soft, autonomous robots," *Nature*, vol. 536, no. 7617, pp. 451–455, 2016.

[87] S. Tibbits, "4d printing: multi-material shape change," *Architectural Design*, vol. 84, no. 1, pp. 116–121, 2014.

[88] D. Correa, A. Papadopoulou, C. Guberan, N. Jhaveri, S. Reichert, A. Menges, and S. Tibbits, "3d-printed wood: Programming hygroscopic material transformations," *3D Printing and Additive Manufacturing*, vol. 2, no. 3, pp. 106–116, 2015.

[89] C. S. Haines, M. D. Lima, N. Li, G. M. Spinks, J. Foroughi, J. D. Madden, S. H. Kim, S. Fang, M. J. De Andrade, F. Göktepe, *et al.*, "Artificial muscles from fishing line and sewing thread," *science*, vol. 343, no. 6173, pp. 868–872, 2014.

[90] C. S. Haines, N. Li, G. M. Spinks, A. E. Aliev, J. Di, and R. H. Baughman, "New twist on artificial muscles," *Proceedings of the National Academy of Sciences*, vol. 113, no. 42, pp. 11709–11716, 2016.

[91] L. Wu, M. J. de Andrade, L. K. Saharan, R. S. Rome, R. H. Baughman, and Y. Tadesse, "Compact and low-cost humanoid hand powered by nylon artificial muscles," *Bioinspiration & biomimetics*, vol. 12, no. 2, p. 026004, 2017.

[92] L. Saharan, M. J. de Andrade, W. Saleem, R. H. Baughman, and Y. Tadesse, "igrab: hand orthosis powered by twisted and coiled polymer muscles," *Smart materials and structures*, vol. 26, no. 10, p. 105048, 2017.

[93] B. Tondu and P. Lopez, "Modeling and control of mckibben artificial muscle robot actuators," *IEEE control systems Magazine*, vol. 20, no. 2, pp. 15–38, 2000.

[94] F. Daerden and D. Lefeber, "Pneumatic artificial muscles: actuators for robotics and automation," *European journal of mechanical and environmental engineering*, vol. 47, no. 1, pp. 11–21, 2002.

[95] W. F. Carlo Ferraresi, W. Walter Franco, and A. Bertetto, "Flexible pneumatic actuators: a comparison between the mckibben and the straight fibres muscles," *J. Rob. Mechatronics*, vol. 13, no. 1, pp. 56–63, 2001.

[96] T. Nakamura, N. Saga, and K. Yaegashi, "Development of a pneumatic artificial muscle based on biomechanical characteristics," in *IEEE International Conference on Industrial Technology, 2003*, vol. 2, pp. 729–734, IEEE, 2003.

[97] H. Tomori and T. Nakamura, "Theoretical comparison of mckibben-type artificial muscle and novel straight-fiber-type artificial muscle," *International Journal of Automation Technology*, vol. 5, no. 4, pp. 544–550, 2011.

[98] F. Durante, M. G. Antonelli, P. B. Zobel, and T. Raparelli, "Development of a straight fibers pneumatic muscle," *International Journal of Automation Technology*, vol. 12, no. 3, pp. 413–423, 2018.

[99] F. Daerden, "Conception and realization of pleated pneumatic artificial muscles and their use as compliant actuation elements," *Vrije Universiteit Brussel, Belgium*, 1999.

[100] F. Daerden, D. Lefeber, B. Verrelst, and R. Van Ham, "Pleated pneumatic artificial muscles: actuators for automation and robotics," in *2001 IEEE/ASME International Conference on Advanced Intelligent Mechatronics. Proceedings (Cat. No. 01TH8556)*, vol. 2, pp. 738–743, IEEE, 2001.

[101] N. Saga and T. Saikawa, "Development of a pneumatic artificial muscle based on biomechanical characteristics," *Advanced Robotics*, vol. 22, no. 6-7, pp. 761–770, 2008.

[102] A. O'Halloran, F. O'malley, and P. McHugh, "A review on dielectric elastomer actuators, technology, applications, and challenges," *Journal of Applied Physics*, vol. 104, no. 7, p. 9, 2008.

[103] S. Rosset and H. R. Shea, "Small, fast, and tough: Shrinking down integrated elastomer transducers," *Applied Physics Reviews*, vol. 3, no. 3, p. 031105, 2016.

[104] G.-Y. Gu, J. Zhu, L.-M. Zhu, and X. Zhu, "A survey on dielectric elastomer actuators for soft robots," *Bioinspiration & biomimetics*, vol. 12, no. 1, p. 011003, 2017.

[105] M. Taghavi, T. Helps, and J. Rossiter, "Electro-ribbon actuators and electro-origami robots," *Science Robotics*, vol. 3, no. 25, p. eaau9795, 2018.

[106] E. Acome, S. Mitchell, T. Morrissey, M. Emmett, C. Benjamin, M. King, M. Radakovitz, and C. Keplinger, "Hydraulically amplified self-healing electrostatic actuators with muscle-like performance," *Science*, vol. 359, no. 6371, pp. 61–65, 2018.

[107] J. D. Greer, T. K. Morimoto, A. M. Okamura, and E. W. Hawkes, "Series pneumatic artificial muscles (spams) and application to a soft continuum robot," in *Robotics and Automation (ICRA), 2017 IEEE International Conference on*, pp. 5503–5510, IEEE, 2017.

[108] F. Daerden and D. Lefeber, "The concept and design of pleated pneumatic artificial muscles," *International Journal of Fluid Power*, vol. 2, no. 3, pp. 41–50, 2001.

[109] J. D. Madden, N. A. Vandesteeg, P. A. Anquetil, P. G. Madden, A. Takshi, R. Z. Pytel, S. R. Lafontaine, P. A. Wieringa, and I. W. Hunter, "Artificial muscle technol-

ogy: physical principles and naval prospects," *IEEE Journal of oceanic engineering*, vol. 29, no. 3, pp. 706–728, 2004.

[110] D. A. Winter, *Biomechanics and motor control of human movement.* John Wiley & Sons, 2009.

[111] K. Endo, D. Paluska, and H. Herr, "A quasi-passive model of human leg function in level-ground walking," in *Intelligent Robots and Systems, 2006 IEEE/RSJ International Conference on*, pp. 4935–4939, IEEE, 2006.

[112] L. Maffli, S. Rosset, and H. Shea, "Zipping dielectric elastomer actuators: characterization, design and modeling," *Smart Materials and Structures*, vol. 22, no. 10, p. 104013, 2013.

[113] A. S. Chen, H. Zhu, Y. Li, L. Hu, and S. Bergbreiter, "A paper-based electrostatic zipper actuator for printable robots," in *2014 IEEE International Conference on Robotics and Automation (ICRA)*, pp. 5038–5043, IEEE, 2014.

[114] J. Li, H. Godaba, Z. Zhang, C. Foo, and J. Zhu, "A soft active origami robot," *Extreme Mechanics Letters*, vol. 24, pp. 30–37, 2018.

[115] Z. Suo, "Theory of dielectric elastomers," *Acta Mechanica Solida Sinica*, vol. 23, no. 6, pp. 549–578, 2010.

[116] D. Trivedi, C. D. Rahn, W. M. Kier, and I. D. Walker, "Soft robotics: Biological inspiration, state of the art, and future research," *Applied bionics and biomechanics*, vol. 5, no. 3, pp. 99–117, 2008.

[117] S. Rosset, B. M. O'Brien, T. Gisby, D. Xu, H. R. Shea, and I. A. Anderson, "Self-sensing dielectric elastomer actuators in closed-loop operation," *Smart Materials and Structures*, vol. 22, no. 10, p. 104018, 2013.

[118] T. Helps and J. Rossiter, "Proprioceptive flexible fluidic actuators using conductive working fluids," *Soft robotics*, vol. 5, no. 2, pp. 175–189, 2018.

[119] N. Kellaris, V. G. Venkata, G. M. Smith, S. K. Mitchell, and C. Keplinger, "Peano-hasel actuators: Muscle-mimetic, electrohydraulic transducers that linearly contract on activation," *Science Robotics*, vol. 3, no. 14, 2018.

[120] S. Ozel, E. H. Skorina, M. Luo, W. Tao, F. Chen, Y. Pan, and C. D. Onal, "A composite soft bending actuation module with integrated curvature sensing," in *2016 IEEE International Conference on Robotics and Automation (ICRA)*, pp. 4963–4968, IEEE, 2016.

[121] G. Gerboni, A. Diodato, G. Ciuti, M. Cianchetti, and A. Menciassi, "Feedback control of soft robot actuators via commercial flex bend sensors," *IEEE/ASME Transactions on Mechatronics*, vol. 22, no. 4, pp. 1881–1888, 2017.

[122] R. S. Diteesawat, T. Helps, M. Taghavi, and J. Rossiter, "High strength bubble artificial muscles for walking assistance," in *2018 IEEE International Conference on Soft Robotics (RoboSoft)*, pp. 388–393, IEEE, 2018.

[123] S. Kurumaya, H. Nabae, G. Endo, and K. Suzumori, "Design of thin mckibben muscle and multifilament structure," *Sensors and Actuators A: Physical*, vol. 261, pp. 66–74, 2017.

[124] F. Ilievski, A. D. Mazzeo, R. F. Shepherd, X. Chen, and G. M. Whitesides, "Soft robotics for chemists," *Angewandte Chemie International Edition*, vol. 50, no. 8, pp. 1890–1895, 2011.

[125] Y. Hao, Z. Gong, Z. Xie, S. Guan, X. Yang, Z. Ren, T. Wang, and L. Wen, "Universal soft pneumatic robotic gripper with variable effective length," in *2016 35th Chinese control conference (CCC)*, pp. 6109–6114, IEEE, 2016.

[126] M. Cianchetti, T. Ranzani, G. Gerboni, T. Nanayakkara, K. Althoefer, P. Dasgupta, and A. Menciassi, "Soft robotics technologies to address shortcomings in today's minimally invasive surgery: the stiff-flop approach," *Soft robotics*, vol. 1, no. 2, pp. 122–131, 2014.

[127] P. Ohta, L. Valle, J. King, K. Low, J. Yi, C. G. Atkeson, and Y.-L. Park, "Design of a lightweight soft robotic arm using pneumatic artificial muscles and inflatable sleeves," *Soft Robotics*, vol. 5, no. 2, pp. 204–215, 2018.

[128] J. W. Booth, D. Shah, J. C. Case, E. L. White, M. C. Yuen, O. Cyr-Choiniere, and R. Kramer-Bottiglio, "Omniskins: Robotic skins that turn inanimate objects into multifunctional robots," *Science Robotics*, vol. 3, no. 22, p. eaat1853, 2018.

[129] R. F. Shepherd, F. Ilievski, W. Choi, S. A. Morin, A. A. Stokes, A. D. Mazzeo, X. Chen, M. Wang, and G. M. Whitesides, "Multigait soft robot," *Proceedings of the national academy of sciences*, vol. 108, no. 51, pp. 20400–20403, 2011.

[130] D. T. Kühnel, T. Helps, and J. Rossiter, "Kinematic analysis of vibrobot: a soft, hopping robot with stiffness-and shape-changing abilities," *Frontiers in Robotics and AI*, vol. 3, p. 60, 2016.

[131] H.-Y. Chen, R. S. Diteesawat, A. Haynes, A. J. Partridge, M. F. Simons, E. Werner, M. Garrad, J. Rossiter, and A. T. Conn, "Rubic: An untethered soft robot with discrete path following," *Frontiers in Robotics and AI*, vol. 6, p. 52, 2019.

[132] E. W. Hawkes, L. H. Blumenschein, J. D. Greer, and A. M. Okamura, "A soft robot that navigates its environment through growth," *Science Robotics*, vol. 2, no. 8, p. eaan3028, 2017.

[133] S. M. Mirvakili and I. W. Hunter, "Artificial muscles: Mechanisms, applications, and challenges," *Advanced Materials*, vol. 30, no. 6, p. 1704407, 2018.

[134] M. Wehner, M. T. Tolley, Y. Mengüç, Y.-L. Park, A. Mozeika, Y. Ding, C. Onal, R. F. Shepherd, G. M. Whitesides, and R. J. Wood, "Pneumatic energy sources for autonomous and wearable soft robotics," *Soft robotics*, vol. 1, no. 4, pp. 263–274, 2014.

[135] C. Cao, X. Gao, and A. T. Conn, "A magnetically coupled dielectric elastomer pump for soft robotics," *Advanced Materials Technologies*, vol. 4, no. 8, p. 1900128, 2019.

[136] J. J. Loverich, I. Kanno, and H. Kotera, "Concepts for a new class of all-polymer micropumps," *Lab on a Chip*, vol. 6, no. 9, pp. 1147–1154, 2006.

[137] Z. Li, Y. Wang, C. C. Foo, H. Godaba, J. Zhu, and C. H. Yap, "The mechanism for large-volume fluid pumping via reversible snap-through of dielectric elastomer," *Journal of Applied Physics*, vol. 122, no. 8, p. 084503, 2017.

[138] V. Cacucciolo, J. Shintake, Y. Kuwajima, S. Maeda, D. Floreano, and H. Shea, "Stretchable pumps for soft machines," *Nature*, vol. 572, no. 7770, pp. 516–519, 2019.

[139] C. Stergiopulos, D. Vogt, M. T. Tolley, M. Wehner, J. Barber, G. M. Whitesides, and R. J. Wood, "A soft combustion-driven pump for soft robots," in *ASME 2014 Conference on Smart Materials, Adaptive Structures and Intelligent Systems*, American Society of Mechanical Engineers Digital Collection, 2014.

[140] M. Garrad, G. Soter, A. T. Conn, H. Hauser, and J. Rossiter, "Driving soft robots with low-boiling point fluids," in *2019 2nd IEEE International Conference on Soft Robotics (RoboSoft)*, pp. 74–79, IEEE, 2019.

[141] S. K. Mitchell, X. Wang, E. Acome, T. Martin, K. Ly, N. Kellaris, V. G. Venkata, and C. Keplinger, "An easy-to-implement toolkit to create versatile and high-performance hasel actuators for untethered soft robots," *Advanced Science*, vol. 6, no. 14, p. 1900178, 2019.

[142] V. Cacucciolo, H. Nabae, K. Suzumori, and H. Shea, "Electrically-driven soft fluidic actuators combining stretchable pumps with thin mckibben muscles," *Frontiers in Robotics and AI*, vol. 6, no. ARTICLE, 2020.

[143] S. Pourazadi, A. Shagerdmootaab, H. Chan, M. Moallem, and C. Menon, "On the electrical safety of dielectric elastomer actuators in proximity to the human body," *Smart Materials and Structures*, vol. 26, no. 11, p. 115007, 2017.

[144] S. Bluett, T. Helps, M. Taghavi, and J. Rossiter, "Self-sensing electro-ribbon actuators," *IEEE Robotics and Automation Letters*, vol. 5, no. 3, pp. 3931–3936, 2020.

[145] J. Ou, M. Skouras, N. Vlavianos, F. Heibeck, C.-Y. Cheng, J. Peters, and H. Ishii, "aeromorph-heat-sealing inflatable shape-change materials for interaction design," in *Proceedings of the 29th Annual Symposium on User Interface Software and Technology*, pp. 121–132, 2016.